Higgs physics as a window to the electroweak epoch

Dissertation

zur Erlangung des Doktorgrades
an der Fakultät für Mathematik,
Informatik und Naturwissenschaften

Fachbereich Physik

der Universität Hamburg

vorgelegt von

MARÍA OLALLA OLEA ROMACHO

Hamburg

2022

Gutachter/innen der Dissertation:	Prof. Dr. Georg Weiglein Prof. Dr. Géraldine Servant
Zusammensetzung der Prüfungskommission:	Prof. Dr. Georg Weiglein Prof. Dr. Géraldine Servant Prof. Dr. Freya Blekman Prof. Dr. Günter H. W. Sigl Prof. Dr. Florian Grüner
Vorsitzender der Prüfungskommission:	Prof. Dr. Florian Grüner
Datum der Disputation:	19.09.2022
Vorsitzender Fach-Promotionsausschusses PHYSIK:	Prof. Dr. Wolfgang J. Parak
Leiter des Fachbereichs PHYSIK:	Prof. Dr. Günter H. W. Sigl
Dekan der Fakultät MIN:	Prof. Dr. Heinrich Graener

To the unsung female presences of the past
who paved the way for today's women scientists.

También a mis padres,
Ventura y Olalla,
y a mi hermano Miguel.

Abstract

This dissertation investigates three well-motivated scalar extensions of the Standard Model and shows that the combination of constraints from collider experiments, from the evolution of the early Universe, and from future astrophysical experiments, such as GW interferometers, will be very valuable for probing the parameter space of those models. In particular, extensions of the Higgs sector of the Standard Model allow for a rich cosmological history around the electroweak scale. In the two-Higgs-doublet model (2HDM) and its real singlet extension (the N2HDM), we determine the parameter regions featuring a first-order EW phase transition (FOEWPT), but also the regions where other effects occur such as electroweak symmetry non-restoration (SnR) at high temperature. We further show that the presence of vacuum trapping can impede a strong FOEWPT in parameter space regions that previously were considered promising for the realisation of electroweak baryogenesis. We analyse these phenomena and in particular their relation to each other, and discuss their connection to the predicted phenomenology at the LHC. Specifically for the 2HDM, we study whether the parameter space region featuring a strong FOEWPT can be probed in the future with the space-based gravitational-wave (GW) telescope LISA via the detection of the associated stochastic GW background. We find that only very contrived regions of the parameter space can give rise to GW signals that are detectable at LISA. We point out that these regions predict indications of new physics at energy scales that will already be probed at the HL-LHC by means of searches for new physics at the TeV scale or the experimental information on the self-coupling of the Higgs boson at 125 GeV. We also investigate a complex singlet extension of the 2HDM, the S2HDM, which contains a pseudo-Nambu-Goldstone dark matter (DM) candidate. In this model, the cross sections for the scattering of the DM on nuclei vanish at tree-level in the limit of zero momentum-transfer due to a U(1) symmetry. However, this symmetry is softly broken in order to give a mass to the DM particle. As a consequence, non-vanishing scattering cross sections arise at the loop level. On one hand, we confront the model with a multitude of theoretical and experimental constraints and discuss the complementarity between constraints related to the DM sector and to the Higgs sector. On the other hand, we calculate the leading radiative corrections to the DM-nucleon scattering in the S2HDM, and we find that the current cross-section limits from DM direct-detection experiments can hardly constrain the parameter space of the S2HDM. However, the loop-corrected predictions for the scattering cross sections can be well within the reach of future direct-detection experiments.

Zusammenfassung

Diese Dissertation untersucht drei auf verschiedene Weise motivierte skalare Erweiterungen des Standardmodells und zeigt, dass die Kombination von Einschränkungen aus Teilchenbeschleuniger-Experimenten, aus der Entwicklung des frühen Universums und aus zukünftigen astrophysikalischen Experimenten, zum Beispiel Gravitationswellen (GW)-Interferometern, von großem Wert sein werden, um die Parameterraum dieser Modelle einzuschränken. Erweiterungen des Higgs-Sektors des Standardmodells ermöglichen eine vielfältige kosmologische Entwicklung rund um die elektroschwache (EW) Skala. Im Zwei-Higgs-Dublett-Modell (2HDM) und seiner Erweiterung um ein weiteres reales Singletfeld (dem N2HDM) bestimmen wir die Parameterregionen, die einen EW Phasenübergang erster Ordnung (FOEWPT), aber auch andere Effekte wie die Nichtrestauration der EW Symmetrie (SnR) bei hohen Temperaturen, vorhersagen. Wir zeigen ferner, dass das Vorhandensein von 'vacuum trapping' eine starke FOEWPT in Parameterraumregionen verhindern kann, die zuvor als vielversprechend für die Realisierung von EW Baryogenese angesehen wurden. Wir analysieren diese Phänomene und insbesondere ihre Beziehung zueinander und diskutieren ihre Verbindung zur vorhergesagten Phänomenologie am LHC. Speziell für das 2HDM betrachten wir, ob die Regionen des Parameterraums mit einem starken FOEWPT in Zukunft mit dem weltraumgestützten GW-Teleskop LISA durch durch die Beobachtung eines zugehörigen stochastischen GW-Hintergrunds getested werden können. Wir finden, dass nur sehr eingeschränkte Bereiche des Parameterraums GW-Signale hervorrufen können, die durch LISA nachweisbar sind. Wir zeigen außerdem auf, dass diese Parameterregionen Indizien für neuartige Physik bei Energieskalen vorhersagen, die bereits am HL-LHC durch Suchen nach neuartiger Physik an der TeV-Skala oder durch die Messungen der Selbstkopplung des Higgs-Bosons bei 125 GeV experimentell untersucht werden. Wir analysieren desweiteren eine Erweiterung des 2HDMs, das ein komplexes Singletfeld enthält, das S2HDM. Dieses Modell sagt ein Teilchen voraus, das als sogenanntes pseudo-Nambu-Goldstone ein Kandidat für dunkle Materie darstellt. Im S2HDM verschwinden aufgrund einer U(1)-Symmetrie auf klassischer Ebene und im Limes von verschwindendem Impulstransfer die Wirkungsquerschnitte für die Streuung der Dunklen Materie an Atomkernen. Die U(1)-Symmetrie ist jedoch sanft gebrochen, um dem Dunkle-Materie-Teilchen eine Masse zu verleihen. Als Folge dessen entstehen nicht-verschwindende Wirkungsquerschnitte auf Schleifen-Niveau. Einerseits konfrontieren wir das Modell mit einer Vielzahl theoretischer und experimenteller Randbedingungen und diskutieren die Komplementarität zwischen den Randbedingungen im Zusammenhang mit dem Sektor der Dunklen Materie und dem Higgs-Sektor. Andererseits berechnen wir die führenden Strahlungskorrekturen der Streuung der dunkler Materie an Nukleonen im S2HDM und stellen fest, dass die aktuellen Obergrenzen an die Wirkungsquerschnitte ermittelt mit Hilfe der Experimenten zur direkten Detektion dunkler Materie den Parameterraum des S2HDMs kaum einschränken können. Im Gegensatz dazu können die strahlungskorrigierten Vorhersagen für die Streuquerschnitte jedoch über den Obergrenzen zukünftiger Experimente zur direkten Detektion dunkler Materie liegen.

List of publications

This thesis is based on the following scientific articles.

Journal articles:

[1] T. Biekötter, S. Heinemeyer, J. M. No, M. O. Olea and G. Weiglein, *Fate of electroweak symmetry in the early Universe: Non-restoration and trapped vacua in the N2HDM*, *JCAP* **06** (2021) 018 [`2103.12707`].

[2] T. Biekötter and M. O. Olea-Romacho, *Reconciling Higgs physics and pseudo-Nambu-Goldstone dark matter in the S2HDM using a genetic algorithm*, *JHEP* **10** (2021) 215 [`2108.10864`].

Preprints:

[3] T. Biekötter, P. Gabriel, M. O. Olea-Romacho and R. Santos, *Direct detection of pseudo-Nambu-Goldstone dark matter in a two Higgs doublet plus singlet extension of the SM*, `2207.04973`.

[4] T. Biekötter, S. Heinemeyer, J. M. No, M. O. Olea-Romacho and G. Weiglein, *The trap in the early Universe: impact on the interplay between gravitational waves and LHC physics in the 2HDM*, `2208.14466`.

Contents

I Prologue 1

1 Introduction 3

2 The need for BSM physics 9
- 2.1 The Standard Model Higgs sector 10
- 2.2 Unsolved problems of the Standard Model 15
  - 2.2.1 The electroweak phase transition 16
  - 2.2.2 Dark matter 17

3 Extended scalar sectors 19
- 3.1 Models 20
  - 3.1.1 Five fundamental scalars: The 2HDM 20
  - 3.1.2 Six fundamental scalars: The N2HDM 25
  - 3.1.3 Seven fundamental scalars: The S2HDM 28
- 3.2 Theoretical and experimental constraints 30
  - 3.2.1 Theoretical constrains 30
  - 3.2.2 Experimental constraints 37

II The EW symmetry in the early Universe 43

4 Extended scalar sectors at finite-temperature 45
- 4.1 The finite-temperature scalar potential 46
- 4.2 Thermal evolution 57
  - 4.2.1 The EWPT 57
  - 4.2.2 Vacuum trapping 62
  - 4.2.3 EW symmetry non-restoration 62
- 4.3 Cosmological gravitational wave backgrounds 63
  - 4.3.1 Characterisation of a stochastic GW background 63
  - 4.3.2 Stochastic GW background from FOEWPTs 65

5 Interplay between gravitational waves and LHC physics in the 2HDM 71
- 5.1 The 2HDM: an overview 72
  - 5.1.1 The zero-temperature 2HDM effective potential 72
  - 5.1.2 Scale dependence and perturbativity of scalar couplings 73
- 5.2 The finite-temperature 2HDM effective potential 73

5.3 2HDM thermal history and phenomenological implications 74
  5.3.1 The cosmological evolution of the vacuum in the 2HDM 75
  5.3.2 Phenomenological consequences of vacuum trapping 80
  5.3.3 Interplay between the LHC and LISA 90

6 EW symmetry non-restoration and trapped vacua in the N2HDM 97
6.1 The N2HDM at zero-temperature 98
6.2 Constraints 99
6.3 The N2HDM at finite-temperature 102
6.4 Symmetry non-restoration at high T 104
  6.4.1 Analytical considerations 104
  6.4.2 Numerical Analysis 110
  6.4.3 The EW phase transition and SnR 115
6.5 Trapped metastable singlet vacua 118
  6.5.1 Case 1: Singlet admixture in H 119
  6.5.2 Case 2: Singlet admixture in h_{125} 123

III Dark matter 129

7 Dark matter direct-detection 131
7.1 Pseudo-Nambu Goldstone dark matter 131
7.2 Dark matter direct detection 132

8 Pseudo-Nambu Goldstone dark matter in the S2HDM 137
8.1 Constraints 138
  8.1.1 Theoretical constraints: vacuum stability and unitarity 138
  8.1.2 Experimental constraints 139
8.2 Numerical analysis 143
  8.2.1 pNG DM in the Higgs funnel region 145
  8.2.2 pNG DM and a Higgs boson at 96 GeV 159

9 Direct detection of pNG DM in the S2HDM 165
9.1 Calculation of DM-nucleon scattering cross section 166
  9.1.1 One-loop contributions to Wilson coefficients 166
  9.1.2 From amplitudes to cross sections 170
9.2 Numerical impact in light of current and future experiments 170
  9.2.1 General considerations 170
  9.2.2 Parameter scans in type I and type II 175

10 Conclusions 181
10.1 The electroweak symmetry in the early Universe 182
10.2 Pseudo-Nambu-Goldstone dark matter 184

A Change of basis in the S2HDM **187**

References **189**

Part I

Prologue

Chapter 1

Introduction

> The Brain -is wider than the Sky-
> For -put them side by side-
> The one the other will contain
> With ease -and You- beside
>
> Emily Dickinson

Physical cosmology is a relatively new Science [5]. In the fall of 1916, Willem de Sitter (1872-1934) and Albert Einstein (1879-1955) met to discuss the newly born theory of General Relativity (GR) [6]. In these meetings the idea of using GR as a theoretical framework to study the large-scale Universe was conceived. In 1917, Einstein published his article "Kosmologische Betrachtungen zur allgemeinen Relativitätstheorie" [7], in which he proposed a model for a finite, static, spherically curved universe with a non-vanishing matter density. A few years later, Edwin Hubble (1889-1953) observed that nearby galaxies are moving away from Earth at speeds proportional to their distance [8], thus giving rise to the first observational evidence that any acceptable model of the Universe had to accommodate. We owe the first theory of an expanding universe to Georges Lemaître (1894-1966), who would later be known as the father of the Big Bang theory. He did not only claim that the Universe was expanding but, furthermore, he postulated its abrupt origin [9]. Based on those early considerations and further developed, physical cosmology has accomplished a consensus standard model, the ΛCDM (see e.g. Ref. [10] for a review). It has been built in meticulous detail and can be considered as well-substantiated by a growing body of observations[1]. Relying on extrapolating the well-tested local physics governing gravity and the other fundamental forces to large scales, it describes the overall structure of the Universe and its evolution. This paradigm is based on the classical description of gravity provided by GR and on the Standard Model (SM) of the strong and electroweak (EW) interactions. It additionally requires novel ingredients of unknown nature such as dark energy and dark matter (DM).

According to the ΛCDM cosmology, the Universe was once in an extremely hot early state. It evolved by expanding, cooling, and developing structures at various scales, such as galaxies and stars. Because radiation, matter, and a cosmological constant term (or dark energy) dilute with expansion at different rates, an expanding universe naturally falls into separate epochs. Shortly after the Big Bang, most of the energy was in the

---

[1] See Ref. [11] for a comprehensive review of its shortcomings.

form of radiation, which set the dynamics of the Universe by controlling the expansion. A radiation-dominated epoch transitioned to a matter-dominated phase at a later time, and it was followed eventually by a dark-energy-dominated phase that persisted until the present time. During most part of the radiation-domination epoch, the interactions among elementary particles were efficient enough to keep the primordial plasma in thermal equilibrium, whose state was then solely determined by the temperature. However, the turning points in our early Universe's evolution happened due to a series of departures from thermal equilibrium during its hot thermal phase, which allowed some particle species to acquire a significant cosmological abundance. When the interactions that coupled a particle to the thermal plasma fell out of equilibrium, it decoupled and streamed freely across the Universe, carrying valuable information about the moment of decoupling, and bearing the traces of the most distant past.

The deepest reliable probe of the Universe dates back to Big Bang nucleosynthesis (BBN), when the light element abundances froze in within the "first three minutes" after the Big Bang, at a temperature of ~ 0.1 MeV [10]. Prior stages to BBN are so far not supported by observational evidence, and the theoretical extrapolation becomes increasingly uncertain, in view of shortcomings of the SM which require new physics beyond the SM (BSM). Experimentally probing those earlier instants could shed light on the precise BSM model realised in nature, and those experimental probes receive valuable feedback from high energy experiments, such as the Large Hadron Collider (LHC).

Among other deficiencies, the ingredients of the SM are not sufficient to generate the observed baryon asymmetry (BAU) of the Universe [12–14], and the SM lacks a particle candidate to explain the observed cosmological abundance of DM [15]. Another mystery lies in the nature of the EW phase transition (EWPT), the cosmological realisation of electroweak symmetry breaking (EWSB). Feasible in minimal extensions of the SM [16–23], a first-order EW phase transition (FOEWPT) is a particularly attractive scenario that provides the necessary out-of-equilibrium conditions needed to generate the observed BAU [24]. Such a transition has also the remarkable feature of sourcing a stochastic gravitational wave (GW) background that may be detectable with future space-based GW interferometers [25, 26] such as LISA [27].

This dissertation is an effort toward a better understanding of the evolution of our Universe before BBN. On one hand, the focus is placed on the EWPT, happening naturally at $T \sim \mathcal{O}(100\ \text{GeV})$, and more generally on the cosmological evolution of the vacuum structure. On the other hand, we study a scalar weakly-interacting massive particle (WIMP), a DM candidate with weak couplings to the SM particles and a mass around the EW scale that decouples from the thermal plasma at $T \sim \mathcal{O}(1 - 100\ \text{GeV})$. This yields an overall structure for the manuscript divided into two big blocks, Part II gathers the discussions concerning the cosmological evolution of the vaccuum structure, and Part III contains the analyses focusing on DM.

All the BSM scenarios explored in this dissertation bear in common the sensitive dependence on the precise structure of the Higgs sector, containing additional scalar states apart from the discovered Higgs boson with a mass of about 125 GeV at the LHC [28, 29]. Within the current experimental and theoretical uncertainties, the properties of the detected particle agree with the predictions of the SM [30–32]. However, they are also compatible with a wide variety of BSM scalar extensions. We analyse three well-motivated scalar extensions of the SM, exploiting the strong interplay between collider measurements and present or projected output from dedicated DM or GW experiments. Such a complementarity constrains the physically allowed parameter space of the models or allows making projections in order to distinguish between them in the future. The detailed structure of this thesis is described in the following.

Part I discusses Higgs sectors as the basic framework for further discussions in this dissertation. In Chapter 2, we review the Higgs sector of the SM (Sect. 2.1), as well as several aspects of its phenomenology at colliders. We also illustrate how the present composition of the Universe calls for BSM physics (Sect. 2.2). In Chapter 3, we motivate extended Higgs sectors in view of the aforementioned shortcomings. In particular, we introduce the three models analysed in upcoming chapters (Sect. 3.1): the two-Higgs-doublet model (2HDM), the next-to-two-Higgs-doublet model (N2HDM) and the singlet-extended 2HDM (S2HDM). All of them share the characteristic of containing at least one additional EW doublet. Finally, we describe the constraints that shape the physically allowed parameter space of those models in Sect. 3.2.

In part II the focus is placed on the fate of the EW symmetry in the early Universe. It is has been shown that adding further Higgs doublets to the SM [33–35] makes it possible to realise a FOEWPT [36–39]. Other interesting features in models with extended Higgs sectors are related to the vacuum structure. In the SM, the EW symmetry is broken spontaneously at zero-temperature by a non-vanishing vacuum expectation value (vev) for the Higgs field. Due to the measured value of the Higgs boson mass, the ΛCDM cosmology follows the commonly expected picture in which the gauge symmetry is restored at high temperatures, and is broken dynamically via a cross over as the Universe cools down to temperatures below 160 GeV [40–44]. This intuitive picture, even though commonly taken for granted, is not generically present in extensions of the SM, as it was already pointed out in Ref. [45]. The presence of additional scalar fields can give rise to much richer symmetry-breaking patterns. For instance, a symmetry might remain broken at all temperatures, or only be restored in an intermediate temperature region. These two scenarios feature the so-called "symmetry non-restoration" (SnR) [45–51], which would require other mechanisms than EW baryogenesis [52] to yield the observed BAU. A further possibility in the thermal history of the universe is vacuum trapping: at zero temperature the EW vacuum exists as the deepest minimum of the potential. However, if the conditions for the on-set of the FOEWPT were never fulfilled, the Universe would be trapped in a higher-energetic non-EW vacuum.

In Chapter 4, we present the background material needed for these related discussions: basics on finite temperature Quantum Field Theory, cosmological phase transitions and the associated GW production are therein reviewed. In Chapter 5, we discuss the 2HDM, for which all the features described above (FOEWPT, stochastic GWs, SnR, vacuum trapping) can be present and give rise to an interesting interplay between the early Universe physics and the collider phenomenology. In Chapter 6, we study scenarios with a FOEWPT, EW symmetry-non-restoration and vacuum trapping in the N2HDM, as well as the connection of such early Universe processes to possible signatures at the LHC. Our results illustrate the plurality of thermal histories that can be realised in extended Higgs sectors, as well as the phenomenological impact of these different histories. In particular, we demonstrate that the results for the thermal history of the early Universe can rule out large parts of the otherwise unconstrained N2HDM parameter space.

Finally, Part III focuses on the study of WIMP scalar DM. We explore a complex singlet extension of the 2HDM that respects a softly broken global U(1) symmetry, the S2HDM. In view of the fact that the DM particle(s) might not be charged under the SM gauge groups, the possibility of coupling the DM to the SM only via the Higgs sector, often called Higgs portal [53, 54], is an interesting scenario. Many extended Higgs sectors provide a (pseudo)scalar DM candidate fitting the WIMP paradigm. However, they are stringently constrained by DM direct-detection (DD) experiments [55]. A way to evade those constraints can be achieved by means of momentum-suppressed tree-level DM-nucleon cross sections. A particle that naturally has this feature is the so-called pseudo-Nambu-Goldstone boson (pNG) DM [23, 56–61]. As a result, BSM models including a pNG DM candidate and accounting for the DM relic abundance have recently gained a lot of attention [62–71]. In Chapter 7, we provide the needed background material for further discussions on DM DD.

In Chapter 8, we study a relatively light pNG DM candidate in the S2HDM, which suggest an interesting interplay of collider phenomenology and astrophysics. In particular, we focus on DM masses between 40 and 80 GeV. In scenarios of this kind, the DM relic abundance [72] can occur via the freeze-out mechanism through resonantly enhanced annihilations mediated by the SM-like Higgs boson. As for the rest of the analyses presented in this thesis, we constrain the parameter space by various experimental requirements coming from flavour physics, EW precision observables, searches for additional scalars and measurements of the properties of the 125 GeV Higgs boson. Additionally, there are experimental constraints arising from cosmological and astrophysical sources. In particular, the limitation imposed by the measured DM relic abundance and indirect-detection limits from the observation of dwarf spheroidal galaxies by the Fermi-LAT space telescope [73] play an important role. We also take into account several theoretical constraints to ensure the validity of the perturbative treatment of the theory and the stability of the EW vacuum. Furthermore, we note that the corresponding parameter space is suitable for explaining the excess of gamma rays from the galactic centre observed by the Fermi Large Area Telescope (LAT) [74, 75]. It has been argued that these observations could be due to DM annihilations in the galactic centre [76–82], where a large concentration of DM is expected to reside [83, 84]. At the same time, the Alpha Magnetic Spectrometer (AMS) [85], onboard the International Space Station, reported an excess over the expected flux of cosmic ray antiprotons consistent with DM annihilating into b-quark pairs with a similar range of DM masses [86–91]. In Chapter 8, we address the question whether the DM candidate of the S2HDM can account for the two cosmic-ray excesses in combination with a Higgs boson at roughly 96 GeV that could explain the so-called LEP [92] excess in the $b\bar{b}$ final state, and an excess observed by CMS in the diphoton final state [93].

In Chapter 9, we calculate the leading radiative corrections to the DM-nucleon scattering in the S2HDM. As mentioned above, pNG DM models have the distinct feature of having a negligible DM DD cross section at leading order (LO) as first reported in Ref. [58]. The first relevant contribution to the cross section comes from the one-loop EW corrections to the DM-nucleon cross section. In order to unmistakably observe a DM candidate, one needs DD experiments that probe the mass and couplings of the DM particle with the SM particles via its interactions with known objects such as nuclei. This motivates the need of understanding in great detail the DM-nucleon cross sections in the different proposed models. If we confine ourselves to the mass region of WIMPs the most restrictive and up-to-date DD constraints were obtained by the PandaX-4T [94], the XENON1T [95] and the LZ [96, 97] collaborations. Our calculation of the next-to leading order (NLO) EW corrections to the DM DD cross section shows that, even though the current experimental sensitivities by XENON1T, PandaX-4T and LZ are not sufficient to probe the S2HDM parameter space in a notable way, a significant portion of the parameter space will be probed in near-future DD experiments.

In Chapter 10, we conclude and summarise our results. Furthermore, we give an outlook as to the possible directions into which the analyses presented in this thesis could be extended.

Chapter 2

The need for BSM physics

Symmetry, tightly related to the concepts of unity, beauty, and harmony, has served as a guiding principle to understanding the Cosmos already since Classical antiquity. In Plato's *Timaeus*, the regular polyhedra are granted a central role in the doctrine of the natural elements for their harmonious proportions and the beauty of their forms. Aristotle described symmetry as one of the greatest forms of beauty to be found in the mathematical sciences. Another characteristic example of the essential role of symmetry in the understanding of the cosmic structure is Kepler's 1596 *Mysterium Cosmographicum*, which presented a planetary system based on the five regular solids [98]. The ancient notion of symmetry used by the Greeks and Romans has evolved into the concept found today in modern science, in which the underlying symmetry patterns that govern the elementary particles and their interactions are described mathematically with group theory. In particular, gauge invariance has taken a central role in providing the architecture of the fundamental laws.

The SM is the gauge theory of the EW and strong interactions of elementary particles. It describes the structure of the subatomic world with an unprecedented level of precision, achieving predictions in agreement with experimental measurements up to the level of one part in 10^{13} [99]. The EW theory [100–102] is a Yang-Mills [103] theory based on the gauge symmetry group $\mathrm{SU}(2)_L \times \mathrm{U}(1)_Y$ which describes the electromagnetic [104–109] and weak [110, 111] interactions acting on quarks and leptons. Together with Quantum Chromodynamics (QCD) [112–117], the theory of strong interactions based on the $\mathrm{SU}(3)_c$ symmetry group, the model provides a unified framework to describe all the known forces of nature except for gravity. One of the pillars of the SM is the mechanism of EWSB [118–122], the Brout-Englert-Higgs (BEH) mechanism, whose relic, the Higgs boson, is a central piece to the consistency of the SM since it ensures the unitarity of the theory beyond the TeV scale and permits the existence of massive gauge bosons and fermions while respecting gauge invariance. Despite of the excellent agreement between the SM predictions and the experiments, important questions remain unanswered. Some of the solutions might be deeply connected to the structure of the scalar sector and the precise properties of the Higgs boson discovered in 2012. Exploring such a connection is the central goal of this dissertation.

In this chapter, we briefly review the mechanism of EWSB and several aspects of the SM Higgs phenomenology that will be useful in the discussions of the upcoming chapters (Sect. 2.1). Furthermore, we illustrate the unsolved problems of the SM, paying special attention to those that concern the results presented in this thesis (Sect. 2.2).

2.1 The Standard Model Higgs sector

The EW sector of the SM is described by the gauge symmetry group $\mathrm{SU}(2)_L \times \mathrm{U}(1)_Y$ of weak left-handed isospin and hypercharge (see e.g. Refs. [10, 123–126] for reviews on EW and Higgs physics). We will first recapitulate the consequences of EWSB for the bosonic sector of the SM, which is specified by the bosonic piece of the EW Lagrangian,

$$\mathcal{L}_{\mathrm{EW}} = -\frac{1}{4} B_{\mu\nu} B^{\mu\nu} - \frac{1}{4} W^a_{\mu\nu} W^{\mu\nu}_a + |D_\mu \Phi|^2 - V(\Phi), \tag{2.1}$$

$$V(\Phi) = \mu^2 |\Phi|^2 + \lambda |\Phi|^4 . \tag{2.2}$$

The field Φ is a complex scalar doublet under $\mathrm{SU}(2)_L$ with weak hypercharge $Y = 1$ for a singlet doublet field. The postulated scalar potential $V(\Phi)$ is the most general renormalisable potential. The covariant derivative D_μ and the field strength tensors $B_{\mu\nu}$ and $W^a_{\mu\nu}$ read

$$D_\mu = \partial_\mu + ig\frac{\tau^a}{2} W_{\mu a} + ig'\frac{Y}{2} B_\mu, \tag{2.3}$$

$$B_{\mu\nu} = \partial_\mu B_\nu - \partial_\nu B_\mu, \tag{2.4}$$

$$W^a_{\mu\nu} = \partial_\mu W^a_\nu - \partial_\nu W^a_\mu - g f^{abc} W_{\mu b} W_{\nu c}, \tag{2.5}$$

where the fields W^a_μ $(a = 1, 2, 3)$ and B_μ are the respective gauge fields of the symmetry groups SU(2) and U(1). Here $\tau^a = \sigma^a$ are the Pauli matrices, i.e. the SU(2) group generators in their fundamental representation, f^{abc} are the SU(2) structure constants, and g and g' are the $\mathrm{SU}(2)_L$ and $\mathrm{U}(1)_Y$ gauge couplings, respectively. Here Y is understood as a diagonal matrix proportional to the identity matrix. However, throughout this discussion, loosely speaking it will be also understood as its eigenvalue. If the quadratic term in the scalar potential is negative, $\mu^2 < 0$, the minimum of the potential is found at

$$\langle \Phi \rangle = \frac{1}{\sqrt{2}} \begin{pmatrix} 0 \\ v \end{pmatrix} \quad \text{with} \quad v := \sqrt{\frac{-\mu^2}{\lambda}}. \tag{2.6}$$

The vev, $v \approx 246$ GeV, can be extracted experimentally through measurements of the Fermi constant G_F in muon decay. After spontaneous symmetry breaking, the electric charge, $Q = (\tau^3 + Y)/2$, remains as the sole unbroken generator, i.e. $Q \langle \Phi \rangle = 0$. Therefore, electromagnetism is left unbroken by the vev, which yields the desired symmetry breaking scheme,

$$\mathrm{SU}(2)_L \times \mathrm{U}(1)_Y \to \mathrm{U}(1)_{\mathrm{em}}. \tag{2.7}$$

To guarantee the stability of the scalar potential, λ should be positive. The doublet Φ can be expanded about the ground state and be expressed in terms of the BEH field h and three Goldstone boson fields $\phi_{1,2,3}$ as

$$\Phi = \frac{1}{\sqrt{2}} \begin{pmatrix} \phi_1 + \mathrm{i}\phi_2 \\ v + h + \mathrm{i}\phi_3 \end{pmatrix}. \tag{2.8}$$

Field	SU(3)	SU(2)$_L$	U(1)$_Y$
$Q_L = \begin{pmatrix} u_L \\ d_L \end{pmatrix}$	3	2	$\frac{1}{3}$
u_R	3	1	$\frac{4}{3}$
d_R	3	1	$-\frac{2}{3}$
$L_L = \begin{pmatrix} \nu_L \\ e_L \end{pmatrix}$	1	2	-1
e_R	1	1	-2
$\Phi = \begin{pmatrix} \phi^+ \\ \phi^0 \end{pmatrix}$	1	2	1

Table 2.1: Representations of the SM gauge groups to which the first generation of quarks and leptons belong.

In the unitary gauge, the three Goldstone bosons disappear from the mass spectrum and they transform into the longitudinal components of the three massive weak vector bosons, $W_\mu^\pm$ and Z_μ. The photon A_μ, being the gauge field corresponding to an unbroken symmetry, remains massless. The EW gauge boson mass eigenstates are

$$W_\mu^\pm = \frac{1}{\sqrt{2}}(W_\mu^1 \mp iW_\mu^2), \tag{2.9}$$

$$Z_\mu = c_w W_\mu^3 - s_w B_\mu, \tag{2.10}$$

$$A_\mu = s_w W_\mu^3 + c_w B_\mu. \tag{2.11}$$

Here we have defined the weak mixing angle $\theta_w = \arctan g'/g$, and the short-hand notation $s_w = \sin\theta_w$ and $c_w = \cos\theta_w$. The Higgs-gauge boson interactions are described by

$$\begin{aligned}\mathcal{L}_{\text{hGB}} = &\left[M_W^2 W_\mu^+ W^{-\mu} + \frac{1}{2}M_Z^2 Z_\mu Z^\mu\right]\left(1+\frac{h}{v}\right)^2 \\ &- \frac{1}{2}M_h^2 h^2 - \frac{\lambda_{hhh}^{\text{SM}}}{3!}h^3 - \frac{\lambda_{hhhh}^{\text{SM}}}{4!}h^4,\end{aligned} \tag{2.12}$$

with

$$M_W = \frac{1}{2}gv, \quad M_Z = \frac{1}{2}\sqrt{g^2+g'^2}v, \quad M_h = \sqrt{2\lambda}v, \tag{2.13}$$

$$\lambda_{hhh}^{\text{SM}} = 3\frac{m_h^2}{v}, \quad \lambda_{hhhh}^{\text{SM}} = 3\frac{m_h^2}{v^2}. \tag{2.14}$$

We now turn to briefly illustrate the implications of the BEH mechanism for the SM fermions. In Tab. 2.1, we show the representations of the SM gauge groups to which the first generation of quarks and leptons belong, together with their charges. It is found experimentally that right-handed fields do not interact with the $W^\pm$ boson, implying that the right-handed quarks and leptons are $\mathrm{SU}(2)_L$ singlets. The Yukawa interaction terms for the first generation of fermions read

$$\mathcal{L}_Y = y_u \bar{Q}_L \Phi_c u_R + y_d \bar{Q}_L \Phi d_R + y_e \bar{L}_L \Phi e_R + \text{h.c.}, \tag{2.15}$$

where $\Phi_c \equiv -i\tau_2 \Phi^*$. An SU(2) transformation brings Φ in Eq. (2.8) to the unitary gauge

$$\Phi = \frac{1}{\sqrt{2}} \begin{pmatrix} 0 \\ v + h \end{pmatrix}. \tag{2.16}$$

Inserting Eq. (2.16) in Eq. (2.15), we obtain

$$\mathcal{L}_Y = m_u \bar{u} u \left(1 + \frac{h}{v}\right) + m_d \bar{d} d \left(1 + \frac{h}{v}\right) + m_e \bar{e} e \left(1 + \frac{h}{v}\right), \tag{2.17}$$

with the definitions $\bar{f} f = f_L^\dagger f_R + f_R^\dagger f_L$ and $m_f = y_f v/\sqrt{2}$ with $f = u, d, e$.

These terms are esily extended to the three-family case, where the Yukawa couplings y_d, y_u and y_e become 3×3 matrices

$$\mathcal{L}_Y = \frac{(v + h)}{\sqrt{2}} \left\{ \sum_{j,k} \bar{u}_L^j y_u^{jk} u_R^k + \bar{d}_L^j y_d^{jk} d_R^k + \bar{e}_L^i y_e^{jk} e_R^k + \text{h.c.} \right\}. \tag{2.18}$$

Given that y_u and y_d cannot be simultaneously diagonalised, there is a net effect of the basis change on the charged current interaction, which couples u-type and d-type quarks. Thus, charged-current interactions mediated by the $W^\pm$ boson acquire a flavour structure encoded in the Cabbibo-Kobayashi-Maskawa (CKM) matrix [127, 128]. In the SM, CP-violation originates from the single phase naturally occurring in the CKM matrix. Since the Yukawa matrices and the fermion mass matrices are proportional to each other, the interactions of the Higgs boson with the fermion mass eigenstates are flavour diagonal, and the Higgs boson does not mediate flavour changing interactions.

Custodial symmetry The masses of the weak vector bosons (Eq. (2.13)) satisfy the following tree-level relation,

$$\rho \equiv \frac{M_W^2}{c_w^2 M_Z^2} = 1, \quad \text{with} \quad c_w^2 = \frac{g^2}{g^2 + g'^2}, \tag{2.19}$$

which is protected by the custodial symmetry. The Higgs potential has a global approximate symmetry $\mathrm{SU}(2)_L \times \mathrm{SU}(2)_R$, which is explicitly broken by the EW hypercharge and the hierarchy between the fermion masses. After EWSB, the global symmetry spontaneously breaks down to the custodial symmetry group $\mathrm{SU}(2)_C$. In the limit of $g' \to 0$, the three gauge fields W_μ^a belong to a triplet representation of $\mathrm{SU}(2)_C$, meaning that their masses are degenerate. Due to the small value of the hypercharge, there exists a relatively small difference between the masses of the weak vector bosons. The custodial symmetry gives rise to the relation in Eq. (2.19) at lowest order, and the leading radiative corrections vanish in the limit $g' \to 0$ and $m_t \to m_b$.

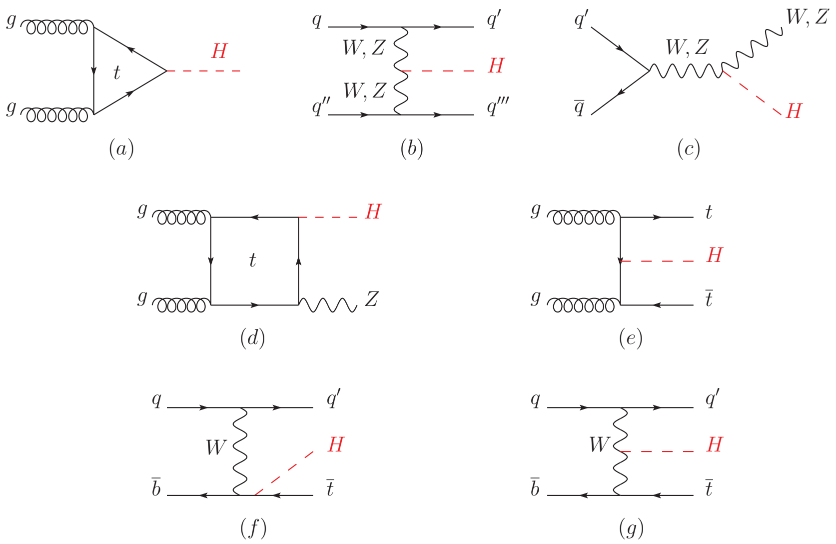

Figure 2.1: Main leading Feynman diagrams contributing to the Higgs boson production at the LHC via a) gluon fusion, b) weak-boson fusion, (c-d) associated production with a gauge boson, e) associated production with a pair of quarks, (f-g) production in association with a single top quark [10]. H in the image stands for h in the text.

Higgs boson production and decays The Higgs boson couplings to the fundamental particles are determined by their masses. Consequently, the dominant channels for the Higgs boson production and decay involve the coupling of h to $W^{\pm}$, Z and/or the third generation of fermions. The main production mechanisms at the LHC and the Tevatron collider are gluon fusion (ggF), weak-boson fusion (VBF), associated production with a gauge boson (Vh), and associated production with a pair of tt quarks (tth), or with a single top quark (th) [10]. The most relevant leading order Feynman diagrams contributing to the different production mechanisms are shown in Fig. 2.1 [10]. In Fig. 2.2 (left), we display their contribution to the SM Higgs boson production cross section as a function of the centre-of-mass energy for pp collisions [129]. The blue line corresponds to the total production cross section due to gluon fusion exclusively. The red one indicate the same for the weak-boson fusion mechanism. The green and grey lines show the total cross section for the associated production with a W and a Z boson, respectively. Finally, the pink and dark violet lines coincide with the cross section for the associated production with a pair of bottom and top quarks, respectively, whereas the light violet curve shows the cross section for Higgs production in association with a single top. All these processes have been computed including important QCD and EW radiative corrections at different levels of accuracy, which are correspondingly indicated in the lines labels (see Ref. [129] for further details on those corrections). The Higgs boson production mechanism with the largest cross section is gluon-fusion and, in particular, the largest contribution to gluon fusion is mediated by a virtual top quark.

In Fig. 2.2 (right), we show the branching ratios including QCD and EW radiative

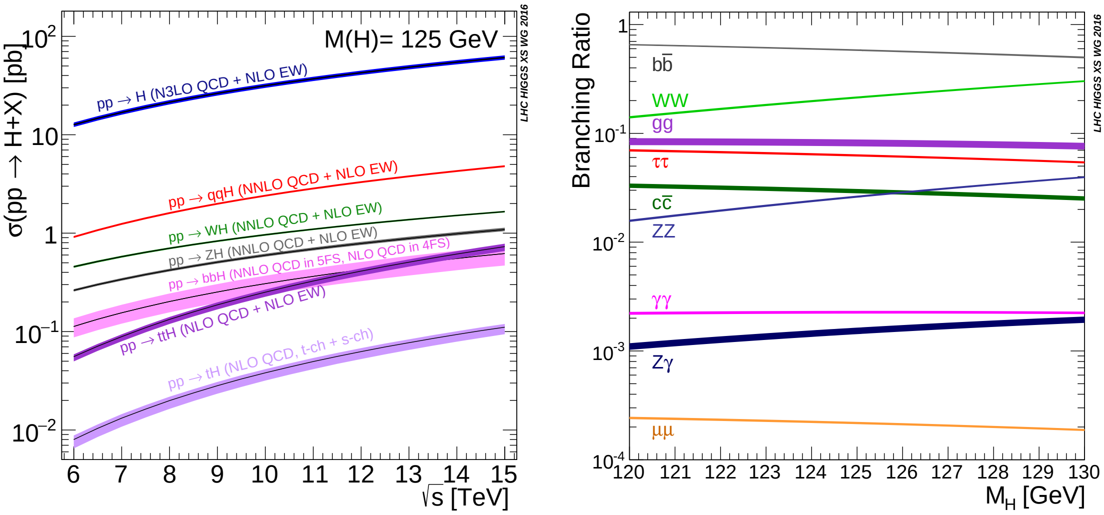

Figure 2.2: Left [129]: Production cross sections for a SM Higgs boson at $M_h = 125$ GeV in pp collisions as a function of the centre-of-mass energy $\sqrt{s}$. Lines labelled as $pp \to X$ refer to ggF for $X = h$, VBF for $X = qqh$, Vh for $X = Wh$ and $X = Zh$. Right [129]: Branching ratios for the main decays of the SM Higgs boson near $m_h = 125$ GeV. Uncertainties are indicated as bands. H in the image stands for h in the text.

corrections for the decay of a SM Higgs boson of mass around 125 GeV [130]. The dominant decay modes are $h \to b\bar{b}$, $h \to WW^*$, $h \to gg$, $h \to \tau\bar{\tau}$, $h \to c\bar{c}$ and $h \to ZZ^*$. With smaller decay rates follow $h \to \gamma\gamma$, $h \to Z\gamma$ and $h \to \mu\bar{\mu}$.

Higgs self couplings Measuring the Higgs boson trilinear and quartic self couplings is an extremely important direct probe of the SM. The SM tree-level predictions of these couplings are shown in Eq. (2.14). Reconstructing the Higgs scalar potential is a crucial long-term experimental goal that will deepen our understanding of the mechanism of EWSB. The cubic and quartic Higgs couplings could be directly measured using double- and triple-Higgs production processes, respectively. However, constraints from the hhh final state on the quartic Higgs self coupling are inaccessible to current and near-future colliders due to the intricate final states and the small production rates [131]. On the other hand, the Higgs triple self-interaction can be constrained through the measurement of double Higgs production either at hadron colliders, where the production is dominated by gluon fusion, $gg \to hh$, or at lepton colliders via double Higgs-strahlung, $e^+e^- \to Zhh$, particularly relevant at low energies, or via VBF, $e^+e^- \to hh\nu_e\bar{\nu}_e$, more important at centre-of-mass energies of 1 TeV and above [132]. The currently strongest bound at the 95% C.L.on the trilinear Higgs self coupling λ_{hhh} has been reported by ATLAS [133],

$$-1.1 < \kappa_\lambda < 6.3, \tag{2.20}$$

where $\kappa_\lambda \equiv \lambda_{hhh}/\lambda_{hhh}^{\mathrm{SM}}$. In the future, the sensitivity will further improve [132]. At the high-luminosity LHC (HL-LHC), the projected sensitivity for the trilinear Higgs coupling will be

$$0.1 < \kappa_\lambda < 2.3 \tag{2.21}$$

at 95% C.L. with 3 ab^{-1} data [134] (assuming SM rates), whereas the prospects for the ILC and the FCC-*hh* point towards $\mathcal{O}(10\%)$ experimental precision [135–137].

2.2 Unsolved problems of the Standard Model

Despite its enormous success in describing very accurately the vast majority of measurements of particle physics experiments performed in the last decades, the SM cannot be the ultimate theory of nature. There is a variety of theoretical open questions and experimental anomalies which strongly suggests the existence of physics BSM.

On the **theory side**, the first shortcoming concerns *gravity*, which is described at the classical level by GR and for which a consistent quantum theory has not been framed yet. The SM does not incorporate gravity, implying that its validity is limited at most by the Planck scale $M_P \sim \mathcal{O}(10^{19})$ GeV, where gravitational effects are expected to be of comparable strength as the other interactions. There is also the question whether the converging behaviour of the gauge couplings at a high scale signifies the *unification of the fundamental forces*, in which case all SM fermions should fit (ideally) in a representation of a larger symmetry group containing the SM gauge group as a subgroup. Besides that, we have no explanation to the apparent absence of CP-violation in the QCD sector (*strong CP problem*), which otherwise would be permitted by gauge invariance. We also do not know what protects the Higgs mass and the cosmological constant from Planck-scale radiative corrections, often referred to as the *hierarchy problem* [138–140], and the *cosmological constant problem*, respectively. Furthermore, we are ignorant of the mechanism that is driving the *accelerated expansion of the Universe.* Another important set of issues bears on the question why the SM has such a *flavour structure.* Finally, the scalar potential in the SM is postulated *ad hoc* and the dynamics by which the Higgs acquired its vev in the early Universe remains still a mystery. The *nature of the EW phase transition* (EWPT) is one of the enigmas that contextualises a large part of the results presented in this dissertation.

On the **experimental side**, neutrino oscillations [141] infer the existence of *neutrino masses*, which are not accommodated in the SM. In addition, the observed *matter-antimatter asymmetry* [72] of the Universe requires additional sources of CP violation beyond the CP-violating phase in the CKM matrix and the departure from thermal equilibrium in the early Universe in order to meet the Sakharov conditions [24] to accomplish baryogenesis. Another prominent cosmological question, which also frames large parts of the results of this thesis, is the nature of the *dark matter* that constitutes some 80% of the matter in the Universe [72].

In the following, we will expand on the need to study the EWPT and the nature of dark matter.

2.2.1 The electroweak phase transition

Since the SM scalar potential is an *ad hoc* choice in order to trigger EWSB while respecting gauge invariance and renormalisability, its origin remains a mystery. The nature of the EW phase transition and the generation of mass in the early Universe are still a conundrum.

The SM predicts that the spontaneous breaking of the EW symmetry set in smoothly, i.e. through a mild cross over, as the Universe cooled down to temperatures below 160 GeV. This would imply that the bulk motion of the primordial plasma did not depart from thermal equilibrium and, hence, did not generate cosmological relics. Interactions could have been out of thermal equilibrium in the primordial Universe by means of a FOEWPT, which is a crucial element for EW baryogenesis. In a FOEWPT, the Universe transitions from a metastable EW symmetric vacuum into a (meta)stable symmetry-breaking vacuum, through a process of bubble nucleation, growth, and merger. The collision of bubble walls naturally leads to the production of an stochastic GW background whose peak frequency overlaps with the sensitivity of next generation GW experiments [142]. Independently of baryogenesis, the EWPT is an interesting issue to study in its own right that compels the research program of high energy physics and GW astronomy. We will expand on the details of a FOEWPT and the generation of gravitational waves in Chapter 4.

While the SM is found to feature no FOEWPT, such a transition can be achieved via minimal extensions such as introducing additional scalar particles with masses around the EW scale or modifying the scalar potential [143, 144].

Concerning the latter possibility, a first-order phase transition can be realised through a sufficiently large Wilson coefficient of the effective operator $(\Phi\Phi^\dagger)^3$ [143]. This can be viewed as one of the main motivations to look for large deviations at the HL-LHC and future colliders of the trilinear Higgs coupling with respect to the SM prediction and confirm or rule out the possibility of EW baryogenesis in a rather model-independent way [126].

Many extensions of the SM can accommodate a FOEWPT, for instance models containing additional EW singlets [16–23] or additional doublets (see e.g. [39, 145, 146]). Such extensions would not only achieve the realisation of a FOEWPT but could also give rise to a rich variety of patterns in the thermal evolution of the scalar fields in the early Universe, differing significantly from the commonly expected scenario of EWSB around a temperature T of $\mathcal{O}(100\text{ GeV})$. For instance, it is well-known that the EW symmetry can be broken already at temperatures much larger than the EW scale, resulting in EW SnR up to these (possibly very high) temperatures, or even in no restoration at all. In view of these kind of scenarios, the question concerning the order of the phase transition can be replaced by an even more fundamental question. Did an EWPT ever occur in the early Universe?. This thesis is concerned with the implications on the thermal evolution of the vacuum configuration caused by including, at least, one additional EW doublet in the Higgs sector. The EWPT as well as non-standard cosmological histories will be some of the topics studied in the upcoming chapters (see Chapter 4).

2.2.2 Dark matter

Another experimental milestone consists of various indications for the existence of dark matter (DM) through a conjoint of data gathered from, among others, rotation curves of spatial galaxies [147, 148], gravitational lensing [149], and the Bullet cluster merger [150]. The Planck collaboration [72], using the precise map of the cosmic microwave background (CMB), reports the most precise measurement of today's DM relic abundance Ωh^2,

$$(\Omega h^2)_{\text{Planck}} = 0.119 \pm 0.003. \tag{2.22}$$

Hence, the DM sector constitutes about 26% of the energy-matter content of the Universe. Apart from the incontestable astrophysical evidence, there are cosmological indications for the existence of DM. For instance, it is widely accepted that DM played a crucial role in structure formation [151]. In the absence of DM, any density perturbation would have been washed out during the era of radiation domination. Since DM does not interact with radiation, the DM gravitational wells were required to form galaxies and clusters sufficiently fast.

Even though there are many indirect indications for the existence of DM via gravitational effects, so far there has not been any direct discovery of a DM particle that could give rise to more information about the attributes of DM. The elusive nature of DM has opened up an interesting landscape of BSM theories that can provide one or more DM candidates. A good candidate must account for the following properties:

- A detailed analysis of the anisotropies in the CMB spectrum demonstrates that approximately 26% of the matter-energy content of the Universe is constituted by DM [72].
- DM is electrically neutral, except for a possible millicharge [152].
- DM interacts gravitationally. This is clear by all the evidence listed above.
- DM must interact only very feebly with the SM particles.
- DM must be stable or have a lifetime of at least the age of the Universe.
- DM is most likely ”cold” (non-relativistic) and pressureless.

One of the most studied scenarios in such SM extensions is the weakly-interacting massive particle (WIMP), a particle with weak couplings to the SM particles and a mass around the EW scale whose existence could potentially be probed also at present or future colliders. In view of the fact that the DM particle(s) might not be charged under the SM gauge groups, in which case they are also not coupled directly to the quarks and leptons, the possibility of coupling the DM to the SM only via the Higgs sector, often called Higgs portal [53, 54], is an interesting scenario.

Chapter 3

Extended scalar sectors

Except for the SM-like Higgs boson discovered in 2012, all the SM particles either have spin 1/2 (fermions) or spin 1 (gauge bosons). Lorentz invariance, on the other hand, demands that the Higgs field be scalar. All other known scalar particles are composed of more fundamental particles, i.e the mesons are composed of quarks. Hence, this raises the question: is the discovered Higgs boson the sole fundamental scalar particle that populates our Universe? Or is there a scalar *particle zoo* that awaits to be discovered? Thinking of the SM Higgs boson as the one and only fundamental scalar particle existing might be perplexing on its own, but there are more reasons to motivate the existence of additional scalar states. The precisely measured value [10] of the ρ parameter, defined in Eq. (2.19),

$$\rho = 1.00038 \pm 0.00020 \tag{3.1}$$

is compatible with additional EW doublets and singlets, since their structure of weak isospin and hypercharge leads to the same SM tree-level prediction, i.e. $\rho = 1$. In particular, the 2HDM addresses some of the shortcomings listed in Sect. 2.2, while being one of the minimal extensions of the SM Higgs sector. As mentioned in Sect. 2.2.1, 2HDMs can accommodate a FOEWPT, which is interesting because of its crucial role in EW baryogenesis and its capability to source a GW stochastic background. Furthermore, supersymmetric extensions of the SM, in which the hierarchy problem can be addressed [138–140], require the existence of at least two Higgs doublet fields in order to account for the masses of all quarks and leptons. Also the most commonly studied solutions to the strong CP-problem incorporating the so-called QCD axion require the presence of two doublet fields [153]. Moreover, new axially coupled U(1) interactions, resulting in extra gauge bosons weakly coupled to standard model particles and which behave very much as axion-like particles, provide a possible bridge to a new dark sector and also demand an additional EW doublet [154]. Other models to solve the hierarchy problem rely on a unification of the gauge interactions and the fact that the discovered Higgs boson at 125 GeV, h_{125}, arises as a (composite) pNG, but where also additional (potentially stable) pNGs can be present [155]. Such models could resemble at low energy a model with two Higgs doublets [156–159]. Finally, 2HDMs and extensions thereof can provide scalar DM candidates [160, 161], scalar mediators as a portal to a more complex dark matter sector[162, 163] and be linked to neutrino masses [164].

Furthermore, adding a second EW doublet leads to a rich phenomenology. It permits experimental signatures that are impossible within the SM, such as several Higgs bosons, charged and neutral, modifications of the SM-like Higgs couplings and additional forms of CP-violation from the scalar sector. The latter was the reason for T. D. Lee to introduce the 2HDM in 1973 [33]. We will concentrate on the phenomenology of the 2HDM and real and complex scalar extensions thereof, the N2HDM and the S2HDM, respectively. We will explore their role in confronting problems of cosmological relevance, such as the EW phase transition and the elusive nature of DM.

In this chapter, we present the 2HDM (Sect. 3.1.1), the N2HDM (Sect. 3.1.2) and the S2HDM (Sect. 3.1.3), illustrating some of their general phenomenological consequences. We will also explicitly review the theoretical and experimental constraints to which these models are subjected (Sect. 3.2).

3.1 Models

Here we present the basic characteristics of the 2HDM, the N2HDM and the S2HDM, which will be analysed in Chapter 5, Chapter 6 and Chapters 8 and 9, respectively. The three models include at least an additional $\mathrm{SU}(2)_L$ doublet and therefore share multiple features. In particular, they all share the same mechanism to avoid the existence of flavour-changing neutral currents (FCNCs) at tree-level, which results in four different configurations. For the three models, we will only explore the so-called Yukawa type II (see the definition below).

3.1.1 Five fundamental scalars: The 2HDM

The tree-level potential of the CP-conserving 2HDM[1] with a softly broken $\mathbb{Z}_2$ is given by

$$\begin{aligned} V_{\text{tree}} = {} & m_{11}^2 \left|\Phi_1\right|^2 + m_{22}^2 \left|\Phi_2\right|^2 - m_{12}^2 \left(\Phi_1^\dagger \Phi_2 + \text{h.c.}\right) + \frac{\lambda_1}{2} \left(\Phi_1^\dagger \Phi_1\right)^2 + \frac{\lambda_2}{2} \left(\Phi_2^\dagger \Phi_2\right)^2 \\ & + \lambda_3 \left(\Phi_1^\dagger \Phi_1\right) \left(\Phi_2^\dagger \Phi_2\right) + \lambda_4 \left(\Phi_1^\dagger \Phi_2\right) \left(\Phi_2^\dagger \Phi_1\right) + \frac{\lambda_5}{2} \left[\left(\Phi_1^\dagger \Phi_2\right)^2 + \text{h.c.}\right] , \end{aligned} \tag{3.2}$$

where all the parameters are real as a result of imposing hermiticity and CP-conservation. The $\mathbb{Z}_2$ symmetry of the 2HDM potential in Eq. (3.2),

$$\Phi_1 \to \Phi_1 ,\ \Phi_2 \to -\Phi_2 \ , \tag{3.3}$$

is softly broken by the m_{12}^2 term. The most general [165] vacuum configuration allows for the spontaneous breaking of CP and electric charge,

$$\langle \Phi_1 \rangle = \frac{1}{\sqrt{2}} \begin{pmatrix} v_{\text{C}} \\ v_1 + \mathrm{i} v_{\text{CP}} \end{pmatrix} \ , \quad \langle \Phi_2 \rangle = \frac{1}{\sqrt{2}} \begin{pmatrix} 0 \\ v_2 \end{pmatrix} , \tag{3.4}$$

where $v_{1,2}$, v_{C}, v_{CP} are real values. A charge-breaking vacuum with $v_{\text{C}} \neq 0$, resulting in a non-zero photon mass, must be avoided for phenomenological reasons. We will not consider

---

[1] See Ref. [165] for a comprehensive review of the 2HDM and its phenomenology.

spontaneous charge- and CP-violation at the physical EW minimum, meaning that in the following we use $v_{\mathrm{C}} = v_{\mathrm{CP}} = 0$. In principle, charge-breaking and CP-breaking vacua could coexist in the potential together with the physical vacuum, raising the possibility of tunneling between different minima, which will be discussed in Sect. 3.2.1. We can expand the fields around the EW vacuum as follows,

$$\Phi_1 = \begin{pmatrix} \phi_1^+ \\ (v_1 + \rho_1 + \mathrm{i}\eta_1)/\sqrt{2} \end{pmatrix}, \quad \Phi_2 = \begin{pmatrix} \phi_2^+ \\ (v_2 + \rho_2 + \mathrm{i}\eta_2)/\sqrt{2} \end{pmatrix}, \tag{3.5}$$

where $v_1, v_2 > 0$ are the field vevs for the Higgs doublets at zero temperature, where the EW scale is defined as $v = \sqrt{v_1^2 + v_2^2} \approx 246$ GeV. Minimising the tree-level potential with respect to the two fields that acquire a vev, ρ_1 and ρ_2, leads to the minimisation (or tadpole) equations,

$$m_{11}^2 + \frac{\lambda_1 v_1^2}{2} + \frac{\lambda_3 v_2^2}{2} = m_{12}^2 \frac{v_2}{v_1} - (\lambda_4 + \lambda_5)\frac{v_2^2}{2}, \tag{3.6}$$

$$m_{22}^2 + \frac{\lambda_2 v_2^2}{2} + \frac{\lambda_3 v_1^2}{2} = m_{12}^2 \frac{v_1}{v_2} - (\lambda_4 + \lambda_5)\frac{v_1^2}{2}. \tag{3.7}$$

After spontaneous symmetry breaking, the CP-conserving 2HDM gives rise to five physical mass eigenstates in the scalar sector: two CP-even neutral scalars h and H, one CP-odd neutral pseudoscalar A and a pair of charged states $H^\pm$. In addition, there are one neutral and two charged massless Goldstone bosons G^0 and $G^\pm$, respectively, which are absorbed into longitudinal polarisations of the gauge bosons Z and $W^\pm$, respectively. With the above minimum, the mass matrix for the charged scalars reads,

$$M_{\mathrm{C}}^2 = \left[m_{12}^2 - \frac{1}{2}(\lambda_4 + \lambda_5) v_1 v_2\right] \begin{pmatrix} v_2/v_1 & -1 \\ -1 & v_1/v_2 \end{pmatrix}. \tag{3.8}$$

For the charged and, as we will see, for the CP-odd scalar sectors, the mass eigenstates are related to the gauge eigenstates by an orthogonal rotation defined by the angle

$$\tan\beta = v_2/v_1. \tag{3.9}$$

The zero eigenvalue corresponds to the mass of the charged Goldstone boson $G^\pm$. The mass squared of the charged Higgs boson $H^\pm$ is

$$m_{H^\pm}^2 = M^2 - \frac{1}{2}(\lambda_4 + \lambda_5) v^2, \tag{3.10}$$

with the mass scale $M^2 = m_{12}^2 / s_\beta c_\beta$. Analogously, the mass matrix for the pseudoscalar sector is expressed as

$$M_\eta^2 = \left[\frac{m_{12}^2}{v_1 v_2} - \lambda_5\right] \begin{pmatrix} v_2^2 & -v_1 v_2 \\ -v_1 v_2 & v_1^2 \end{pmatrix}. \tag{3.11}$$

This yields an additional massless Goldstone mode G^0 together with the mass squared of the pseudoscalar state,

$$m_A^2 = M^2 - \lambda_5 v^2. \tag{3.12}$$

Finally the mass matrix for the CP-even states is given by

$$M_\rho^2 = \begin{pmatrix} m_{12}^2 \frac{v_2}{v_1} + \lambda_1 v_1^2 & -m_{12}^2 + \lambda_{345} v_1 v_2 \\ -m_{12}^2 + \lambda_{345} v_1 v_2 & m_{12}^2 \frac{v_1}{v_2} + \lambda_2 v_2^2 \end{pmatrix} , \tag{3.13}$$

with $\lambda_{345} = \lambda_3 + \lambda_4 + \lambda_5$. The CP-even sector is diagonalised by the rotation angle α. The masses of the CP-even states are expressed as

$$m_h^2 = \frac{1}{2}\left((M_\rho)_{11} - \sqrt{4(M_\rho)_{12}^2 + ((M_\rho)_{11} - (M_\rho)_{22})^2} + (M_\rho)_{22} \right), \tag{3.14}$$

$$m_H^2 = \frac{1}{2}\left((M_\rho^2)_{11} + \sqrt{4(M_\rho^2)_{12} + ((M_\rho^2)_{11} - (M_\rho^2)_{22})^2} + (M_\rho^2)_{22} \right), \tag{3.15}$$

where the $(M_\rho^2)_{ij}$ denote the matrix elements of M_ρ^2. The state h is conventionally chosen as the lightest CP-even scalar and, throughout this thesis, plays the role of the discovered Higgs boson h_{125} at $m_h = 125$ GeV and should resemble the properties of a SM Higgs boson. The parameters α and β control the coupling strengths of the scalar particles to fermions and gauge bosons. The neutral Higgs couplings to vector bosons $V \equiv W, Z$, normalised to the respective SM Higgs couplings, read

$$C_{hVV} = \sin(\beta - \alpha), \quad C_{HVV} = \cos(\beta - \alpha), \quad C_{AVV} = 0. \tag{3.16}$$

Note that the sum rule $\sum_i (C_{h_i VV})^2 = 1$ holds as a consequence of unitarity [166]. In the limit $\beta - \alpha \to \frac{\pi}{2}$, the lightest CP-even state h is SM-like and can be identified with the experimentally observed Higgs boson h_{125} within the present experimental and theoretical uncertainties. The heavier state H decouples from the gauge boson pairs in this limit. This is the so-called *alignment limit* [167], where the couplings of h to all SM particles are precisely as predicted by the SM, whereas $\cos(\alpha - \beta) \neq 0$ give rise to deviations of the couplings of h compared to the SM. The alignment limit has also been motivated by employing different global symmetries of the scalar potential [168, 169]. It is convenient to reconstruct the scalar potential in terms of quantities with a direct phenomenological meaning, i.e. particle masses of the Higgs sector and the mixing angles. We choose the following set of independent parameters:

$$t_\beta (:= \tan\beta) \ , \ m_{12}^2 \ , \ v \ , \ \cos(\beta - \alpha) \ , \ m_h \ , \ m_H \ , \ m_A \ , \ m_{H^\pm} \ . \tag{3.17}$$

The relations between the set of input parameters shown in Eq. (3.17) and the Lagrangian parameters shown in Eq. (3.2) can be found in Ref. [165].

Concerning the Yukawa structure, the 2HDM faces the dangerous possibility of FCNCs at tree-level, which are severely experimentally constrained [10]. To illustrate the problem,

	u_R	d_R	e_R	Q_L, L_L	Φ_1	Φ_2
Type-I	$-$	$-$	$-$	$+$	$+$	-
Type II	$-$	$+$	$+$	$+$	$+$	-
Type III or LS (lepton-specific)	$-$	$-$	$+$	$+$	$+$	-
Type-IV or F (flipped)	$-$	$+$	$-$	$+$	$+$	-

Table 3.1: Models that lead to the absence of FCNC at lowest order in the 2HDM. $\mathbb{Z}_2$ charge assignments of the different fermionic multiplets.

consider the most general form of the Yukawa interactions for down-type quarks in the 2HDM,

$$y^1_{dij}\bar{Q}_{Li}d_{Rj}\Phi_1 + y^2_{dij}\bar{Q}_{Li}d_{Rj}\Phi_2, \tag{3.18}$$

where i, j are the generation indices. The mass matrix is then

$$M_{ij} = y^1_{dij}\frac{v_1}{\sqrt{2}} + y^2_{dij}\frac{v_2}{\sqrt{2}}. \tag{3.19}$$

In the 2HDM, the transformation that diagonalises M (Eq. (3.19)) will not, in general, simultaneously diagonalise y^1_d and y^2_d, and the Yukawa couplings will not be flavour diagonal. This opens the possibility of FCNC at tree-level mediated by the scalars. FCNC are absent at tree-level in the SM and highly suppressed in loop corrections by the GIM (Glashow–Iliopoulos–Maiani) mechanism [170]. A way to address this problem in the 2HDM is to extend the $\mathbb{Z}_2$ symmetry defined in Eq. (3.3) to the Yukawa sector in such a way that, if all fermions with the same quantum numbers, which therefore mix with each other, couple to the same Higgs multiplet, FCNC will be absent. The two fields Φ_1 and Φ_2 transform differently under the $\mathbb{Z}_2$ symmetry, resulting in four configurations or types that avoid FCNCs at tree-level depending on the $\mathbb{Z}_2$ charge assignment of the fermionic fields (Tab. 3.1). In the following, we will concentrate on the Yukawa type II, which provides the same Yukawa couplings as the original Peccei–Quinn models as well as supersymmetric models. The discrete $\mathbb{Z}_2$ symmetry leads to the following Yukawa interactions,

$$\mathcal{L}_Y^{\mathrm{2HDM}} = -\sum_{f=u,d,e}\frac{m_f}{v}\left(C_{hff}\bar{f}fh + C_{Hff}\bar{f}fH - iC_{Aff}\bar{f}\gamma^5 fA\right) \tag{3.20}$$

$$-\left\{\frac{\sqrt{2}V_{ud}}{v}\bar{u}\left(m_u C_{Auu}P_L + m_d C_{Add}P_R\right)dH^+ + \frac{\sqrt{2}m_e C_{Aee}}{v}\bar{\nu}_L e_R H^+ + \text{h.c.}\right\}. \tag{3.21}$$

In the Lagrangian u, d, e stand for the three generations, $P_{L/R}$ are the projection operators for left-handed/right-handed fermions, and V_{ud} is the CKM matrix element that mixes the up-type quark u with the down-type quark d in charged-current interactions. The factors C in the Yukawa type II are given by

$$C_{huu} = \cos\alpha/\sin\beta, \quad C_{hdd} = -\sin\alpha/\cos\beta \quad C_{hee} = -\sin\alpha/\cos\beta, \tag{3.22}$$

$$C_{Huu} = \sin\alpha/\sin\beta, \quad C_{Hdd} = \cos\alpha/\cos\beta \quad C_{Hee} = \cos\alpha/\cos\beta \tag{3.23}$$

$$C_{Auu} = \cot\beta, \quad C_{Add} = \tan\beta \quad C_{Aee} = \tan\beta. \tag{3.24}$$

We see that the only source of flavour changing couplings is given by the CKM matrix, which controls the quark interactions with W bosons and with charged scalars $H^{\pm}$.

Collider phenomenology The type II 2HDM parameter space that concerns our study features low $\tan\beta$ values and large splittings among the CP-even states masses and the CP-odd and charged scalar masses, i.e. $M \sim v \sim m_H \ll m_A \sim m_{H^\pm}$. We will also focus on the alignment limit where $\cos(\beta - \alpha) = 0$. In the following, we will go through some of the potential manifestations at colliders of this specific scenario.

The neutral Higgs bosons in the 2HDM are produced [165] via the same production mechanisms as the SM Higgs Boson (gluon fusion, weak vector fusion, etc.). In the regime of low $\tan\beta$ values, the main loop production channel is still gluon fusion mediated by top quark (see Fig. 2.1), which is modified with respect to the SM by the factors $(C_{huu})^2$, $(C_{Huu})^2$, and $(C_{Auu})^2$ for the production of h, H and A, respectively. Considering the other production mechanisms, those that involve couplings to gauge bosons are absent for the CP-odd state A and change with respect to the SM-Higgs production by the factors $(C_{hVV})^2$ and $(C_{HVV})^2$ for the production of h and H, respectively. Consequently, in the alignment limit where $C_{HVV} = 0$, vector boson fusion and Higgsstrahlung are suppressed for the heavy CP-even scalar. As for the top-pair associated production, the 2HDM Yukawa type II prediction is modified by $(C_{huu})^2$, $(C_{Huu})^2$, and $(C_{Auu})^2$ for the production of h, H and A, respectively. Therefore the two relevant production channels to probe the heavy neutral CP-even Higgs boson within the parameter region analysed in this thesis are gluon fusion and top quark associated production. Here we should note the importance of the bottom-pair associated production in the high $\tan\beta$ region. Regarding the charged Higgs production, if it is heavier than the top quark, the most important production mode in the region of low $\tan\beta$ is usually [171]

$$pp \to H^{\pm}tb. \tag{3.25}$$

As for the decays, for masses beyond the di-top quark threshold and low $\tan\beta$ values, the neutral Higgs bosons will decay predominantly into top quark pairs. Besides the decays into SM particles, processes involving BSM scalars can occur. In particular, the cascade decay

$$A \to ZH \tag{3.26}$$

is particularly important to probe at the LHC the hierarchical pattern in which we are interested leading to a FOEWPT [172]. This signal will be called in the following the *smoking-gun* signature. Regarding the current status of LHC searches of this kind, ATLAS and CMS have searched for the $A \to ZH$ signature within their 8 TeV [173] and 13 TeV [174, 175] data sets, assuming that the Higgs boson H decays into a pair of bottom quarks or a pair of τ-leptons.

In general, the 2HDM can be probed at colliders by directly producing BSM states or searching for rare 125 GeV Higgs boson decays. One can also look for deviations of the decay rates of the h_{125} as compared to the SM predictions. Both strategies are complementary and correlated probes of the model since the same interactions can affect the signals involving new scalars and the measured Higgs properties. Even though no current experimental anomaly clearly points towards a 2HDM interpretation, one can limit the parameter space of the model, which has 7 independent parameters in the CP-conserving version. In Sect. 3.2, all the relevant experimental but also theoretical constraints will be described in detail.

3.1.2 Six fundamental scalars: The N2HDM

In the N2HDM, the tree-level scalar potential of the two $\mathrm{SU}(2)_L$ Higgs doublets Φ_1 and Φ_2 and the real singlet field Φ_S is given by [176]

$$\begin{aligned} V_{\text{tree}} = {}& m_{11}^2 \left|\Phi_1\right|^2 + m_{22}^2 \left|\Phi_2\right|^2 - m_{12}^2 \left(\Phi_1^\dagger \Phi_2 + \text{h.c.}\right) + \frac{\lambda_1}{2} \left(\Phi_1^\dagger \Phi_1\right)^2 + \frac{\lambda_2}{2} \left(\Phi_2^\dagger \Phi_2\right)^2 \\ &+ \lambda_3 \left(\Phi_1^\dagger \Phi_1\right) \left(\Phi_2^\dagger \Phi_2\right) + \lambda_4 \left(\Phi_1^\dagger \Phi_2\right) \left(\Phi_2^\dagger \Phi_1\right) + \frac{\lambda_5}{2} \left[\left(\Phi_1^\dagger \Phi_2\right)^2 + \text{h.c.}\right] \\ &+ \frac{1}{2} m_S^2 \Phi_S^2 + \frac{\lambda_6}{8} \Phi_S^4 + \frac{\lambda_7}{2} \left(\Phi_1^\dagger \Phi_1\right) \Phi_S^2 + \frac{\lambda_8}{2} \left(\Phi_2^\dagger \Phi_2\right) \Phi_S^2 . \end{aligned} \tag{3.27}$$

Here the terms that only involve the two Higgs doublets are identical to the 2HDM scalar potential in Eq. (3.2) and, therefore the $\mathbb{Z}_2$ symmetry defined in Eq. (3.3) and extended to the Yukawa sector also prevents the occurrence of FCNCs at lowest order in the N2HDM. The third line of the tree-level potential includes the contribution of the singlet field. Here an extra discrete $\mathbb{Z}_2'$ symmetry is imposed,

$$\Phi_1 \to \Phi_1 \;, \qquad \Phi_2 \to \Phi_2 \;, \qquad \Phi_S \to -\Phi_S \;, \tag{3.28}$$

which is not explicitly broken. The original motivation to introduce this symmetry for the N2HDM was the fact that, when not spontaneously broken, it will give rise to a DM candidate after EWSB (see e.g. [177–184]). In this work we do not restrict to such a scenario, but study the case where Φ_S does acquire a vacuum expectation value, which makes it unstable and permits its decay and enables the possibility of mixing with the other two CP-even Higgs bosons. The most general vacuum configuration corresponds to

$$\langle \Phi_1 \rangle = \begin{pmatrix} 0 \\ v_1/\sqrt{2} \end{pmatrix} , \quad \langle \Phi_2 \rangle = \begin{pmatrix} v_{\mathrm{C}}/\sqrt{2} \\ \left(v_2 + \mathrm{i} v_{\mathrm{CP}}\right)/\sqrt{2} \end{pmatrix} , \quad \langle \Phi_S \rangle = v_S, \tag{3.29}$$

where we removed redundant degrees of freedom via an $\mathrm{SU}(2)_L \times \mathrm{U}(1)_Y$ gauge transformation. In the physical vacuum, charge-breaking and CP-breaking vevs are both required to vanish, i.e. $v_{\mathrm{C}} = v_{\mathrm{CP}} = 0$. A discussion on the stability of the EW minimum is reserved to Sect. 3.2.1. The vevs $v_1, v_2, v_S > 0$ are the field vevs for the Higgs doublets and the singlet field, respectively, at zero temperature. We expand the fields around the EW minimum as follows,

$$\Phi_1 = \begin{pmatrix} \phi_1^+ \\ \frac{1}{\sqrt{2}} \left(v_1 + \rho_1 + \mathrm{i}\eta_1\right) \end{pmatrix} , \quad \Phi_2 = \begin{pmatrix} \phi_2^+ \\ \frac{1}{\sqrt{2}} \left(v_2 + \rho_2 + \mathrm{i}\eta_2\right) \end{pmatrix} , \quad \Phi_S = v_S + \rho_3 . \tag{3.30}$$

The doublet vevs v_1 and v_2 define the EW scale $v = \sqrt{v_1^2 + v_2^2} \approx 246$ GeV. The minimization (or tadpole) equations for v_1, v_2 and v_S read

$$\frac{v_2}{v_1} m_{12}^2 - m_{11}^2 = \frac{1}{2}\left(v_1^2 \lambda_1 + v_2^2 \lambda_{345} + v_S^2 \lambda_7\right) \,, \tag{3.31}$$

$$\frac{v_1}{v_2} m_{12}^2 - m_{22}^2 = \frac{1}{2}\left(v_1^2 \lambda_{345} + v_2^2 \lambda_2 + v_S^2 \lambda_8\right) \,, \tag{3.32}$$

$$-m_S^2 = \frac{1}{2}\left(v_1^2 \lambda_7 + v_2^2 \lambda_8 + v_S^2 \lambda_6\right) , \tag{3.33}$$

with $\lambda_{345} \equiv \lambda_3 + \lambda_4 + \lambda_5$.

Since, in the physical vacuum, the CP symmetry and the electric charge are conserved, the (squared-)mass matrix for the fields $\Phi_{1,2}^{\pm}$, $\eta_{1,2}$, $\rho_{1,2,3}$ can be split into three blocks: a 3×3 matrix M_ρ^2 for the CP-even states $\rho_{1,2,3}$, a 2×2 matrix M_η^2 for the CP-odd states $\eta_{1,2}$, and a 2×2 matrix M_C^2 for the charged scalars $\Phi_{1,2}^{\pm}$. The matrices M_η^2 and M_C^2 correspond to the ones obtained in the 2HDM (see Eqs. (3.11) and (3.8)). They can be diagonalised via the rotation matrix

$$R_\beta = \begin{pmatrix} c_\beta & s_\beta \\ -s_\beta & c_\beta \end{pmatrix} , \tag{3.34}$$

with $t_\beta \equiv \tan\beta \equiv v_2/v_1$. After diagonalization we are left with the charged and neutral massless Goldstone bosons, $G^{\pm}$ and G^0, and the charged and neutral CP-odd physical mass eigenstates, $H^{\pm}$ and A, with masses $m_{H^{\pm}}$ and m_A.

The neutral CP-even sector of the N2HDM is modified with respect to that of the 2HDM by the presence of the singlet ρ_3. The mass matrix M_ρ^2 in the basis $\rho_{1,2,3}$ can be expressed as

$$M_\rho^2 = \begin{pmatrix} v^2 \lambda_1 c_\beta^2 + m_{12}^2 t_\beta & v^2 \lambda_{345}\, c_\beta\, s_\beta - m_{12}^2 & v\, v_S \lambda_7\, c_\beta \\ v^2 \lambda_{345}\, c_\beta\, s_\beta - m_{12}^2 & v^2 \lambda_2\, s_\beta^2 + m_{12}^2/t_\beta & v\, v_S \lambda_8\, s_\beta \\ v\, v_S \lambda_7\, c_\beta & v\, v_S \lambda_8\, s_\beta & v_S^2\, \lambda_6 \end{pmatrix} . \tag{3.35}$$

In the physical basis $h_{1,2,3}$, the mass matrix M_ρ^2 is diagonal. The rotation matrix R between the $h_{1,2,3}$ and $\rho_{1,2,3}$ bases satisfies $R\, M_\rho^2\, R^T = \mathrm{diag}\left(m_{h_1}^2, m_{h_2}^2, m_{h_3}^2\right)$, where $m_{h_i}^2$ denotes the squared tree-level mass for h_i. The matrix R can be parametrised in terms of the angles $\alpha_{1,2,3}$ as

$$R = \begin{pmatrix} c_{\alpha_1} c_{\alpha_2} & s_{\alpha_1} c_{\alpha_2} & s_{\alpha_2} \\ -\left(c_{\alpha_1} s_{\alpha_2} s_{\alpha_3} + s_{\alpha_1} c_{\alpha_3}\right) & c_{\alpha_1} c_{\alpha_3} - s_{\alpha_1} s_{\alpha_2} s_{\alpha_3} & c_{\alpha_2} s_{\alpha_3} \\ -c_{\alpha_1} s_{\alpha_2} c_{\alpha_3} + s_{\alpha_1} s_{\alpha_3} & -\left(c_{\alpha_1} s_{\alpha_3} + s_{\alpha_1} s_{\alpha_2} c_{\alpha_3}\right) & c_{\alpha_2} c_{\alpha_3} \end{pmatrix} . \tag{3.36}$$

Without loss of generality, the angles $\alpha_{1,2,3}$ are defined in the range $-\pi/2 \leq \alpha_i < \pi/2$, and we choose the convention that the mass eigenstates are ordered by ascending mass as $m_{h_1} < m_{h_2} < m_{h_3}$. The singlet composition of the mass eigenstates h_i will be denoted by

$$\Sigma_{h_i} = R_{i3}^2 . \tag{3.37}$$

	u-type	d-type	leptons
Type II	R_{i2}/s_β	R_{i1}/c_β	R_{i1}/c_β

Table 3.2: N2HDM coupling factors C_{h_iff} of the CP-even Higgs bosons to fermions as defined in Eq. (3.40), for the Yukawa type II.

The singlet field ρ_3 does not couple directly to the SM fermions and gauge bosons. As a result, any change in the couplings of the CP-even Higgs bosons to the SM particles with respect to the ones from the 2HDM is due to the mixing between the fields $\rho_{1,2}$ and ρ_3. The Feynman rules for the couplings of the states h_i to the massive gauge bosons $V \equiv W, Z$ are

$$i\, g_{\mu\nu}\, C_{h_iVV}\, g^{\mathrm{SM}}_{hVV}\,, \tag{3.38}$$

where $g_{\mu\nu}$ denotes the Minkowski metric. Here C_{h_iVV} are the N2HDM coupling factors of the CP-even Higgs bosons h_i to the massive SM gauge bosons, and g^{SM}_{hVV} is the corresponding SM Higgs–gauge coupling, $g^{\mathrm{SM}}_{hWW} = g\, M_W$ and $g^{\mathrm{SM}}_{hZZ} = \sqrt{g^2 + g'^2}\, M_Z$ (see Eq. (2.12)). The coupling factors C_{h_iVV} are given in terms of the mixing matrix elements R_{ij}, and the mixing angle β as

$$C_{h_iVV} = c_\beta R_{i1} + s_\beta R_{i2}, \tag{3.39}$$

and, consequently, in terms of the mixing angles α_i if we replace the R_{ij} by their corresponding parametrisation shown in Eq. (3.36).

As in the 2HDM, the $\mathbb{Z}_2$ symmetry in Eq. (3.27) may be extended to the Yukawa sector of the theory in order to avoid tree-level FCNCs. As the two fields Φ_1 and Φ_2 transform differently under the $\mathbb{Z}_2$ symmetry, they cannot be coupled both to the same SM fermions. The flavour-conserving Yukawa-types of the N2HDM are those of the 2HDM (see e.g. [165]). We will focus exclusively on type II. The Yukawa interactions involving the CP-even Higgs bosons h_i can be written as

$$\mathcal{L}_Y^{\mathrm{N2HDM}} = -\sum_{i=1}^{3} \frac{\sqrt{2}\, m_f}{v}\, C_{h_iff}\, \bar{f}\, f\, h_i\,, \tag{3.40}$$

with the N2HDM coupling factors C_{h_iff} given in Table 3.2. The Feynman rule for the h_i coupling to the CP-odd A and the Z boson is given by

$$\lambda_\mu(h_iZA) = \frac{\sqrt{g^2 + g'^2}}{2}\, (p_{h_i} - p_A)_\mu\, \tilde{c}(h_iV), \tag{3.41}$$

where p_{h_i} and p_A denote the incoming four-momenta of h_i and A, respectively. The effective coupling $\tilde{c}(h_iV)$ is not normalised to a corresponding SM coupling, since there is no SM counterpart. The coupling factors $\tilde{c}(h_iV)$ can be found in Tab. 3.3. The alignment limit in the N2HDM is defined through $C^2_{h_iVV} = C^2_{h_iuu} = C^2_{h_idd} = 1$, where h_i is identified with the observed scalar at 125 GeV, i.e $h_i \equiv h_{125}$. In this limit, the interactions involving h_{125}, the CP-odd scalar A and the Z boson vanish at tree-level, i.e. $\lambda_\mu(h_{125}ZA) = 0$.

We also note that any coupling not involving the CP-even neutral Higgs bosons remains unchanged with respect to the 2HDM and may be found in [165].

	$\tilde{c}(h_i V)$
h_1	$-c_{\alpha_2} s_{\beta-\alpha_1}$
h_2	$s_{\beta-\alpha_1} s_{\alpha_2} s_{\alpha_3} + c_{\alpha_3} c_{\beta-\alpha_1}$
h_3	$c_{\alpha_3} s_{\beta-\alpha_1} s_{\alpha_2} - s_{\alpha_3} c_{\beta-\alpha_1}$

Table 3.3: The couplings factors $\tilde{c}(h_i V)$ as defined in Eq. (3.41).

Collider phenomenology In the N2HDM, we are also interested in exploring a hierarchical spectrum among the scalar masses and low $\tan\beta$ values. As previously mentioned, the decay $A \to ZH$ (Eq. (3.26)) has emerged as a smoking-gun collider signature [172] of a FOEWPT in the 2HDM. Also in the N2HDM such a type of signature is linked to the possible presence of a FOEWPT, but the collider phenomenology related to this class of processes in the N2HDM is much richer than in the 2HDM. In the 2HDM in the alignment limit, only the decay $A \to ZH$ is possible if kinematically allowed, whereas in the N2HDM the two decays, $A \to Zh_2$ and $A \to Zh_3$, can occur. Those branching ratios depend on both the singlet component and the masses of $h_{2,3}$.

3.1.3 Seven fundamental scalars: The S2HDM

The scalar sector of the S2HDM consists of two SU(2) doublets and a complex gauge singlet field, which can be expressed as

$$\Phi_1 = \begin{pmatrix} \phi_1^+ \\ (\rho_1 + \mathrm{i}\eta_1)/\sqrt{2} \end{pmatrix} , \quad \Phi_2 = \begin{pmatrix} \phi_2^+ \\ (\rho_2 + \mathrm{i}\eta_2)/\sqrt{2} \end{pmatrix} , \quad \Phi_S = (\rho_3 + \mathrm{i}\chi)/\sqrt{2} , \tag{3.42}$$

where the imaginary component χ gives rise to the DM candidate of the model. Assuming the absence of explicit CP violation, the scalar potential of the S2HDM is given by

$$\begin{aligned} V = {}& \mu_{11}^2 \left(\Phi_1^\dagger \Phi_1\right) + \mu_{22}^2 \left(\Phi_2^\dagger \Phi_2\right) - \mu_{12}^2 \left(\left(\Phi_1^\dagger \Phi_2\right) + \left(\Phi_2^\dagger \Phi_1\right)\right) + \frac{1}{2}\mu_S^2 \left|\Phi_S\right|^2 - \frac{1}{4}\mu_\chi^2 \left(\Phi_S^2 + (\Phi_S^*)^2\right) \\ & + \frac{1}{2}\lambda_1 \left(\Phi_1^\dagger \Phi_1\right)^2 + \frac{1}{2}\lambda_2 \left(\Phi_2^\dagger \Phi_2\right)^2 + \lambda_3 \left(\Phi_1^\dagger \Phi_1\right)\left(\Phi_2^\dagger \Phi_2\right) + \lambda_4 \left(\Phi_1^\dagger \Phi_2\right)\left(\Phi_2^\dagger \Phi_1\right) \\ & + \frac{1}{2}\lambda_5 \left(\left(\Phi_1^\dagger \Phi_2\right)^2 + \left(\Phi_2^\dagger \Phi_1\right)^2\right) + \frac{1}{2}\lambda_6 \left(|\Phi_S|^2\right)^2 + \lambda_7 \left(\Phi_1^\dagger \Phi_1\right)|\Phi_S|^2 + \lambda_8 \left(\Phi_2^\dagger \Phi_2\right)|\Phi_S|^2 . \end{aligned} \tag{3.43}$$

Here the terms that exclusively involve the doublet fields are identical to the scalar potential of the 2HDM, where a $\mathbb{Z}_2$ symmetry defined by the transformations $\Phi_1 \to \Phi_1$, $\Phi_2 \to -\Phi_2$ and $\Phi_S \to \Phi_S$ is only softly broken by the terms proportional to μ_{12}. One can define the usual four Yukawa types depending on the assigned $\mathbb{Z}_2$ charges of the fermions as shown in Tab. 3.1. We will focus on the Yukawa type II. The remaining terms of the scalar potential involve the singlet field Φ_S and respect a global U(1) symmetry, except for the term proportional to μ_χ^2. This term softly breaks the U(1) symmetry, thus providing a non-zero mass for the pNG DM.

Without loss of generality, the field configuration of the vacuum can be expressed as

$$\langle\Phi_1\rangle = \begin{pmatrix} 0 \\ v_1/\sqrt{2} \end{pmatrix} \ , \quad \langle\Phi_2\rangle = \begin{pmatrix} v_{\mathrm{C}}/\sqrt{2} \\ \left(v_2 + \mathrm{i}v_{\mathrm{CP}}\right)/\sqrt{2} \end{pmatrix} \ , \quad \langle\Phi_S\rangle = \left(v_S + \mathrm{i}v_{\mathrm{DM}}\right)/\sqrt{2} \ , \tag{3.44}$$

where we made use of the fact that redundant degrees of freedom related to the gauge symmetries can be removed via an $\mathrm{SU}(2)_L \times \mathrm{U}(1)_Y$ gauge transformation. We will focus on the case in which the EW symmetry is broken by non-zero values of v_1 and v_2, and a discrete $\mathbb{Z}_2$ symmetry, under which ρ_3 changes the sign, is broken by $v_S \neq 0$. The charge-breaking vev v_{CB}, the CP-breaking vev v_{CP}, and v_{DM} are required to be vanishing at the physical minimum, noting that a non-zero value of v_{DM} would give rise to decays of the DM candidate χ. As for the N2HDM, in order to make a connection to the SM and the 2HDM we define the parameters $v^2 = v_1^2 + v_2^2 \sim (246\ \mathrm{GeV})^2$ and $\tan\beta = v_2/v_1$.

Assuming the EW vacuum configuration as described above, the CP-even fields $\rho_{1,2,3}$ mix with each other, giving rise to the mass eigenstates $h_{1,2,3}$, where throughout this thesis the mass hierarchy $m_{h_1} < m_{h_2} < m_{h_3}$ will be assumed. The mixing in the CP-even sector can be written in terms of an orthogonal transformation given by a matrix R, such that

$$\begin{pmatrix} h_1 \\ h_2 \\ h_3 \end{pmatrix} = R \cdot \begin{pmatrix} \rho_1 \\ \rho_2 \\ \rho_3 \end{pmatrix} , \tag{3.45}$$

where R is identically defined as in Eq. (3.36). The charged scalar sector remains unchanged compared to the 2HDM. It contains two physical charged Higgs bosons $H^\pm$ with mass $m_{H^\pm}$ and the charged Goldstone bosons related to the gauge symmetries. The pseudoscalar components η_1 and η_2 form a neutral Goldstone boson and one physical state A with mass m_A. The pseudoscalar A has effectively the same couplings to the fermions as the one of the 2HDM. Here it is important to note that the remnant $\mathbb{Z}_2$ symmetry that is present when $v_{\mathrm{DM}} = 0$, preventing the DM candidate χ from decaying, also forbids the mixing between χ and h_i. The alignment limit in the S2HDM is defined through $C^2_{h_iVV} = C^2_{h_iuu} = C^2_{h_idd} = 1$, where h_i is identified with the observed scalar at 125 GeV, i.e $h_i \equiv h_{125}$, and the coupling factors to gauge bosons and fermions are defined as in the N2HDM in Eq. (3.40) and Eq. (3.39).

Given the definitions of the parameters as defined above, it is possible to replace most of the parameters of the scalar potential shown in Eq. (3.43) by more physically meaningful parameters,

$$m_{h_{1,2,3}} \ , \quad m_A \ , \quad m_{H^\pm} \ , \quad m_\chi \ , \quad \alpha_{1,2,3} \ , \quad \tan\beta \ , \quad M = \sqrt{\mu_{12}^2/\left(s_\beta c_\beta\right)} \ , \quad v_S \ . \tag{3.46}$$

The relations between the parameters shown in Eq. (3.46) and the Lagrangian parameters of the potential in Eq. (3.43) are given in App. A.

3.2 Theoretical and experimental constraints

We review the most important theoretical and experimental constraints on CP-conserving 2HDMs and their singlet extensions, specifying how they apply to each one of the three models under investigation. Further details on the concrete codes used to implement these constraints will be given in the corresponding chapters describing the analyses.

3.2.1 Theoretical constrains

Tree-level perturbative unitarity

In this section we review the constrains derived from unitarity in order to ensure a well-behaved energy growth of scattering amplitudes involving the scalar states. Any scattering amplitude can be expanded in terms of partial waves as follows [185]:

$$\mathcal{M}(\theta) = 16\pi \sum_{l=0}^{\infty} a_l (2l+1) P_l(\cos\theta), \tag{3.47}$$

where $P_l(\cos\theta)$ is the Legendre polynomial of degree l, θ is the scattering angle, and the coefficients of the expansion a_l can be extracted by using the orthonormality of the Legendre polynomials. The 2 → 2 scattering cross section reads

$$\sigma = \frac{16\pi}{s} \sum_l (2l+1) |a_l|^2, \tag{3.48}$$

where s is the center of mass energy. From the unitarity of the S-matrix, the optical theorem that relates the total cross section of the scattering process with the forward scattering amplitude is derived,

$$\sigma = \frac{1}{s} \text{Im } \mathcal{M}(\theta = 0). \tag{3.49}$$

Even though unitarity requires the optical theorem to hold for the full amplitude $\mathcal{M}$, it does not say anything about the individual partial waves a_l. But if a partial wave on its own were to violate the optical theorem, we would need large cancellations between the different partial waves. Therefore any process is expected to satisfy the optical theorem at the level of partial waves,

$$\frac{16\pi}{s} (2l+1) |a_l|^2 = \frac{1}{s} 16\pi (2l+1) \text{Im } a_l, \tag{3.50}$$

which can be recast into the equation of a circle in the complex plane,

$$(\text{Re } a_l)^2 + \left(\text{Im } a_l - \frac{1}{2} \right)^2 = \frac{1}{4}, \tag{3.51}$$

which results in the bound

$$|a_l| < \frac{1}{2}. \tag{3.52}$$

In the high energy limit, diagrams containing trilinear vertices are suppressed by an energy-squared factor coming from the intermediate propagator. Therefore, the scalar scattering amplitudes of 2 → 2 processes are determined by the contact interactions proportional to quartic couplings. Consequently, only the $l = 0$ partial amplitude a_0 will receive nonzero contributions from the leading order terms in the scattering amplitudes. The partial wave amplitude a_0 can be cast in the form of a scattering matrix as follows

$$(a_0)_{ij} = \frac{1}{16\pi} \left(\mathcal{M}_{2\to 2}\right)_{ij} , \tag{3.53}$$

where $\mathcal{M}_{2\to 2}$ is the scattering matrix of 2 → 2 processes in the high-energy limit with different two-body states as rows and columns. Due to the equivalence theorem [186, 187], unphysical Goldstone bosons can be used instead of the longitudinal components of the gauge bosons to compute $\mathcal{M}_{2\to 2}$. Therefore, unitarity constraints can be implemented by solely considering pure scalar scattering. The bound in Eq. (3.52) can be expressed as

$$|\mathcal{M}^i_{2\to 2}| < 8\pi, \tag{3.54}$$

with $\mathcal{M}^i_{2\to 2}$ being the i-th eigenvalue of $\mathcal{M}_{2\to 2}$. The bounds derived from Eq. (3.54) result in upper limits for the maximum size of certain combinations of the quartic couplings, which facilitate the perturbative treatment of the theory, preventing the Higgs sector from becoming strongly coupled.

An additional *naïve* upper bound can be imposed on the absolute values of the quartic couplings λ_i to ensure that they remain relatively small. Even though the exact upper bound is somewhat arbitrary we choose 4π, since it is a common choice in the literature. Therefore, for any quartic coupling λ_i, the following condition is adopted,

$$|\lambda_i| < 4\pi. \tag{3.55}$$

Since various results discussed in Chapters 5 and 6 involve sizeable quartic scalar couplings, the perturbative unitarity constraints play an important role in our analyses.

Tree-level perturbative unitarity in the 2HDM In the CP-conserving 2HDM with a softly broken $\mathbb{Z}_2$ symmetry, perturbative unitarity leads to the following conditions [188, 189]

$$|\lambda_3 \pm \lambda_4| < 8\pi, \tag{3.56}$$

$$|\lambda_3 \pm \lambda_5| < 8\pi, \tag{3.57}$$

$$|\lambda_3 + 2\lambda_4 \pm 3\lambda_5| < 8\pi, \tag{3.58}$$

$$\left|\frac{1}{2}\left(\lambda_1 + \lambda_2 \pm \sqrt{(\lambda_1 - \lambda_2)^2 + 4\lambda_4^2}\right)\right| < 8\pi, \tag{3.59}$$

$$\left|\frac{1}{2}\left(\lambda_1 + \lambda_2 \pm \sqrt{(\lambda_1 - \lambda_2)^2 + 4\lambda_5^2}\right)\right| < 8\pi, \tag{3.60}$$

$$\left|\frac{1}{2}\left(3\lambda_1 + 3\lambda_2 \pm \sqrt{9(\lambda_1 - \lambda_2)^2 + 4(2\lambda_3 + \lambda_4)^2}\right)\right| < 8\pi. \tag{3.61}$$

Tree-level perturbative unitarity in the N2HDM The conditions (3.56)-(3.60) must also be fulfilled by the N2HDM. Additionally, tree-level perturbative unitarity in the N2HDM demands [176, 190]

$$|\lambda_7|\,, |\lambda_8| < 8\pi, \tag{3.62}$$

$$\frac{1}{2}\,|a_{1,2,3}| < 8\pi, \tag{3.63}$$

where $a_{1,2,3}$ are the real roots of the cubic polynomial

$$\begin{aligned}&4(-27\lambda_1\lambda_2\lambda_6 + 12\lambda_3^2\lambda_6 + 12\lambda_3\lambda_4\lambda_6 + 3\lambda_4^2\lambda_6 + 6\lambda_2\lambda_7^2 - 8\lambda_3\lambda_7\lambda_8 - 4\lambda_4\lambda_7\lambda_8 + 6\lambda_1\lambda_8^2)\\ &+ x(36\lambda_1\lambda_2 - 16\lambda_3^2 - 16\lambda_3\lambda_4 - 4\lambda_4^2 + 18\lambda_1\lambda_6 + 18\lambda_2\lambda_6 - 4\lambda_7^2 - 4\lambda_8^2)\\ &+ x^2(-6(\lambda_1 + \lambda_2) - 3\lambda_6) + x^3\end{aligned} \tag{3.64}$$

Tree-level perturbative unitarity in the S2HDM In the case of the S2HDM, besides the conditions (3.56)-(3.60), shared with the 2HDM and the N2HDM, and the condition (3.62), exclusively shared with the N2HDM, tree-level perturbative unitarity also implies

$$|\lambda_6| < 8\pi, \tag{3.65}$$

$$|b_{1,2,3}| < 8\pi, \tag{3.66}$$

where $b_{1,2,3}$ are the real roots of the cubic polynomial

$$\begin{aligned}&(48\lambda_2\lambda_7^2 + 48\lambda_1\lambda_8^2 + 64\lambda_3^2\lambda_6 + 16\lambda_4^2\lambda_6 - 144\lambda_1\lambda_2\lambda_6 + 64\lambda_3\lambda_4\lambda_6 - 64\lambda_3\lambda_7\lambda_8 - 32\lambda_4\lambda_7\lambda_8)\\ &+ (-16\lambda_3^2 - 16\lambda_4\lambda_3 - 4\lambda_4^2 - 8\lambda_7^2 - 8\lambda_8^2 + 36\lambda_1\lambda_2 + 24\lambda_1\lambda_6 + 24\lambda_2\lambda_6)x\\ &+ (-6\lambda_1 - 6\lambda_2 - 4\lambda_6)x^2 + x^3.\end{aligned} \tag{3.67}$$

Stability of the electroweak vacuum

The existence of a sufficiently stable minimum, around which perturbative calculations can be performed, is a basic requirement of any physical theory. In order to guarantee the stability of the EW vacuum, two essential requirements must be imposed. Firstly, we have to make sure that the potential is bounded from below, i.e. there is no direction in field space along which the potential tends to minus infinity. Secondly, even if boundedness-from-below (BfB) is satisfied, the EW minimum has to be either the global minimum or a local minimum of the potential. In case it is not the global minimum, additional constraints arise from the requirement of having a metastable EW vacuum.

BfB is satisfied at tree-level in the SM by the simple condition $\lambda > 0$. However, in models with extended Higgs sectors, the situation is more complicated since we have to ensure that the quartic terms in the scalar potential never become infinitely negative in any direction in field space. We show below, for each of the three models analysed, the sufficient and necessary conditions [190, 191] to ensure the positivity of the quartic terms along any field direction (stability in the *strong sense* as defined in Ref. [191]).

The second requirement for the stability of the EW vacuum concerns the possibility of vacuum decay [192, 193]. If the EW minimum is not the global minimum of the potential, the vacuum can tunnel into a deeper minimum. Since such a devastating phenomenon has not occurred, the EW vacuum must be either a global minimum (stable vacuum) or a minimum with a sufficiently long lifetime as compared to the age of the Universe (metastable vacuum). A conservative approach would require the ground state to be the global minimum of the potential. However, in our analyses in the 2HDM and the N2HDM, we consider metastable minima also as acceptable, as long as their lifetime is larger than the age of the Universe.

In the following we will evaluate the probability of a transition from a true vacuum (the physical EW-breaking vacuum) $\vec{\Phi}_T$ to a false vacuum $\vec{\Phi}_F$ (any other unphysical vaccum configuration). The tunnelling process between vacua can be described semi-clasically. Perturbation theory describes small oscillations near the equilibrium position, and somewhat larger fluctuations are needed to cause an instability and trigger the transition. Therefore, it is natural to expect that the action corresponding to large field fluctuations will be large and, thus, that the problem can be treated quasiclassically [194, 195]. Given a Lagrangian

$$\mathcal{L} = \frac{1}{2}(\partial_\mu \vec{\Phi})(\partial^\mu \vec{\Phi}) - V(\vec{\Phi}), \tag{3.68}$$

where $\vec{\Phi}$ is a vector of scalar fields, the associated four-dimensional Euclidian action takes the form

$$S_4 = \int d^4x \left[\frac{1}{2}(\partial_\mu \vec{\Phi})^2 + V(\vec{\Phi})\right]. \tag{3.69}$$

Assuming spherical symmetry, which means that the solution must be a function of two angular variables, a radial coordinate r and time t, the classical trajectory $\vec{\Phi}_B$ that describes the tunnelling from a $\vec{\Phi}_F$ false to a $\vec{\Phi}_T$ true vacuum solves the equations of motion [196]

$$\frac{\mathrm{d}^2\vec{\Phi}}{\mathrm{d}\rho^2} + \frac{3}{\rho}\frac{\mathrm{d}\vec{\Phi}}{\mathrm{d}\rho} = \nabla V(\vec{\Phi}), \tag{3.70}$$

where $\rho^2 = r^2 - t^2$. The solution $\vec{\Phi}_B$ is often referred as *bounce* and satisfies the boundary conditions

$$\vec{\Phi}(\infty) = \vec{\Phi}_F, \quad \text{and} \quad \left.\frac{\mathrm{d}\vec{\Phi}}{\mathrm{d}r}\right|_{\rho=0} = 0. \tag{3.71}$$

In the interpretation of the variable ρ as a radial coordinate and $\vec{\Phi}$ as a field describing the type of phase, the bounce solution describes a bubble separating an interior phase of true vacuum, corresponding to the value $\vec{\Phi}_T$ of the field, from an exterior phase of false vacuum corresponding to the value $\vec{\Phi}_F$ of the field. One can define the lifetime of the metastable vacuum as the inverse of the decay rate (in units of the age of the Universe T_U),

$$\tau = \frac{1}{\Gamma T_U}. \tag{3.72}$$

The decay probability for the false vacuum per unit volume is given by

$$\Gamma = A e^{-S_4}, \tag{3.73}$$

where A is a subdominant dimensionful parameter that contains contributions from quantum fluctuations around the bounce solution. It can be estimated on dimensional grounds from a typical mass scale of the theory, $A = \mathcal{M}^4$. In Ref. [197–199], it was shown that the threshold of instability given by $\tau \sim 1$ was highly sensitive to S_4 and only mildly sensitive to A, where the variation of the mass scale $\mathcal{M}$ over a generous range, from 10 GeV to 100 TeV, resulted only in small shifts in the border between metastability and instability by less than 10% in S_4. In Ref. [197–199], a false vacuum is considered to be metastable if with $S_4 > 440$ and unstable if $S_4 < 390$. Intermediate values of S_4 indicate an uncertainty of this approach. In order to avoid the possibility of discarding possibly physical scenarios, we will only consider vacua as unstable for which

$$S_4 < 390. \tag{3.74}$$

As pointed out in Sect. 3.1, the most general vacuum configuration of the three models under investigation allows for charge- and CP-breaking minima. Therefore, to guarantee the stability of the physical minimum we shall not only consider the possibility of tunnelling to vacua with $v_\text{C} = v_\text{CP} = 0$ but also to charge and CP-violating minima.

Vacuum stability in the 2HDM The tree-level conditions for the CP-conserving 2HDM scalar potential to be bounded from below read [188, 189, 200]

$$\lambda_1 \geq 0 \tag{3.75}$$

$$\lambda_2 \geq 0 \tag{3.76}$$

$$\lambda_3 + \sqrt{\lambda_1 \lambda_2} \geq 0 \tag{3.77}$$

$$\lambda_3 + \lambda_4 - |\lambda_3| + \sqrt{\lambda_1 \lambda_2} \geq 0. \tag{3.78}$$

In Ref. [201], it was found that the existence of a *normal* vacuum with $v_\text{C} = v_\text{CP} = 0$ ensures it to lie deeper than any possible charge- or CP-breaking vacua in the 2HDM. However, the tunnelling to other normal vacua would still be possible. To avoid this possibility, we require the EW minimum to be the global minimum of the tree-level potential by imposing the positivity of the discriminant [201]

$$D_1 = m_{12}^2 \left(m_{11}^2 - m_{22}^2 \sqrt{\frac{\lambda_1}{\lambda_2}} \right) \left(\tan\beta - \sqrt[4]{\frac{\lambda_1}{\lambda_2}} \right). \tag{3.79}$$

Therefore, in the investigated scenario, the presence of a metastable EW minimum only arises at the loop level. It will be important to test the metastability of the one-loop scalar potential through the condition in Eq. (3.74) by using the four-dimensional Euclidean action S_4 with the one-loop effective potential inserted, which will be defined later in Eq. (4.42).

Vacuum stability in the N2HDM In the N2HDM, the parameter region allowed by BfB is given by [176, 190]

$$\Omega_1 \cup \Omega_2 \tag{3.80}$$

where

$$\begin{aligned}\Omega_1 = \Big\{ & \lambda_1, \lambda_2, \lambda_6 > 0; \sqrt{\lambda_1 \lambda_6} + \lambda_7 > 0; \sqrt{\lambda_2 \lambda_6} + \lambda_8 > 0; \\ & \sqrt{\lambda_1 \lambda_2} + \lambda_3 + D > 0; \lambda_7 + \sqrt{\lambda_1/\lambda_2}\lambda_8 \geq 0 \Big\}\end{aligned} \tag{3.81}$$

and

$$\begin{aligned}\Omega_2 = \Big\{ & \lambda_1, \lambda_2, \lambda_6 > 0; \sqrt{\lambda_2 \lambda_6} \geq \lambda_8 > -\sqrt{\lambda_2 \lambda_6}; \sqrt{\lambda_1 \lambda_6} > -\lambda_7 \geq \sqrt{\lambda_1/\lambda_8}; \\ & \sqrt{(\lambda_7^2 - \lambda_1 \lambda_6)(\lambda_8^2 - \lambda_2 \lambda_6)} > \lambda_7 \lambda_8 - (D + \lambda_3)\lambda_6 \Big\}\end{aligned} \tag{3.82}$$

with the discriminant $D_2 = \min(\lambda_4 - |\lambda_5|, 0)$.

Even though in the 2HDM the existence of a vacuum with $v_\mathrm{C} = v_\mathrm{CP} = 0$ precludes the existence of a deeper CP- or charge-breaking minima at tree-level [201], this cannot be generalised to the N2HDM. Our analysis followed the procedure in Ref. [199]. We chose the model parameters such that there is an EW minimum with $v_1, v_2, v_S \neq 0$, $v_\mathrm{C} = v_\mathrm{CP} = 0$ and $\sqrt{v_1^2 + v_2^2} = v$. Subsequently, all the stationary points of the tree-level N2HDM scalar potential were found and their depths were compared to the depth of the EW vacuum. Whenever the EW minimum was found to be the deepest, we considered it to be absolutely stable. Otherwise, the tunnelling time to each of these deeper extrema was computed and considered to be unstable if the criterion in Eq. (3.74) was met. As in the 2HDM, the (meta)stability of the EW vacuum at the one-loop level will be also tested in the N2HDM by using the same approach.

Vacuum stability in the S2HDM Due to the fact that the quartic part of the potential V is unchanged compared to the N2HDM, we can apply the same conditions that were found for the N2HDM. We exclude all parameter points from our analyses that do not feature a scalar potential that is BfB.

In the S2HDM, we required the EW minimum to be the global minimum of the scalar potential to avoid potentially short-lived vacua as compared to the age of the Universe. We verified for each selected parameter point that exists a global minimum of the potential with $v_1, v_2, v_S > 0$ and $v_C, v_{CP}, v_{DM} = 0$. As opposed to the approach followed in the analyses of the 2HDM and the N2HDM, we did not consider metastable vacua in the S2HDM. Allowing for a richer vacuum structure is not as important in the S2HDM analysis as in the 2HDM and the N2HDM analyses. This is due to the fact that the latter are dedicated studies to the precise thermal evolution of the vacuum configuration in the early Universe, whereas the main focus of the former is on the interplay between collider and DM phenomenology. As explained in the next subsection, we will impose further requirements to avoid loop effects from changing the stability of the tree-level global EW minimum in the S2HDM.

Energy scale dependence of the theoretical constraints

Both the perturbative unitarity constraints and the BfB conditions in many analyses of the 2HDM or its extensions are applied exclusively at a certain energy scale. However, it is known that the model parameters obtain an intrinsic energy scale dependence due to radiative corrections, which is governed by their evolution under the renormalisation group equations (RGE). It is therefore possible that even though at the initial scale, assumed to be $\mu = v$ throughout this dissertation, a parameter point passes the theoretical constraints, the point becomes unphysical at larger energy scales $\mu > v$.

At the loop-level, the common way of achieving BfB and perturbative unitarity is to check the tree-level conditions with running couplings inserted. Due to the fact that the perturbativity conditions allow for values of $|\lambda_i| > 1$, the energy range in which the theoretical constraints are fulfilled could very well lie within the energy scales that are probed at the LHC. One should bear in mind that as long as we are within a perturbative regime, we can to a first approximation neglect the one-loop contribution to the effective potential and simply insert the running couplings into the tree-level conditions. However, it might happen that beyond a certain energy scale, the perturbative expansion breaks down and those conditions are no longer valid. In fact, it was shown in Ref. [202] that large loop corrections can transform a bounded tree-level 2HDM potential into an unbounded one, potentially destabilizing the EW vacuum. This effect is expected to be also present in the N2HDM and the S2HDM, such that our tree-level analysis of the boundedness could permit potentially unphysical parameter points. The possibility of loop corrections changing the boundedness of the potential was shown to be present only in regions of the parameter space with splittings between m_A, m_H and $m_{H^\pm}$ that are larger than ~ 250 GeV, where consequently large quartic couplings are present [202], which then give rise to the corrections.

Since our analyses in the 2HDM and the N2HDM explore large splittings among the scalar masses, we will perform additional checks to the the one-loop effective scalar potential in these two models to ensure the stability of the EW minimum (see Sects. 5.3.1 and 6.2). We will carry out a finite-temperature analysis of these two models, so we will also require the condition(3.55) to hold for the running quartic couplings, extracted from the two-loop β-functions, evaluated at the energy scale $\mu = T$ for the whole range of temperatures analysed.

For the S2HDM, we simply demand an upper limit of 200 GeV on the splitting of the heavy Higgs-boson masses compared to the mass scale M defined in Eq. (3.46), such that the boundedness of the potential, and therefore the stability of the EW vacuum, are not expected to be severely affected by the loop corrections. We apply the previously described tree-level theoretical constraints taking into account the energy-scale dependence of the parameters, utilizing the two-loop β-functions of the S2HDM and demanding that the theoretical constraints are respected up to a certain energy scale.

3.2.2 Experimental constraints

Electroweak precision observables

EW precision observables (EWPO) provide constraints on loop effects arising from the states of extended Higgs sectors. The EWPO are quantities which are very well known experimentally, at the percent level or better (see e.g. Ref. [203] for more details). In the SM at tree-level, they just depend on the parameters of the EW sector –the fine structure constant α_{em} and/or the Fermi constant G_F –but the other model parameters can enter via loop corrections. This is also the case for many extensions of the SM and, in particular, for extensions consisting of Higgs doublets or singlets. If we compute radiative corrections to the predictions for the EWPO and perform a global fit of the floating parameters to the EW data, we can constrain new physics contributions that enter the calculations via those quantum corrections. In extended Higgs sectors, deviations in the EWPO from the SM can at the one-loop level conveniently be expressed in terms of the oblique parameters S, T and U [204, 205]. This approach assumes that the dominant new physics effects reside in the self-energies of the gauge bosons. Since most of the calculations for the EWPO involve the gauge boson propagators, the oblique parameters account for a whole class of corrections which appear in the predictions for the W boson mass and the Z boson observables. Denoting the contributions of the new physics to the various one-loop self-energies by Π_{ij}^{new}, the S, T and U parameters are defined as

$$\hat{\alpha} T \equiv \frac{\Pi_{WW}^{\text{new}}(0)}{M_W^2} - \frac{\Pi_{ZZ}^{\text{new}}(0)}{M_Z^2}, \tag{3.83}$$

$$\frac{\hat{\alpha}}{4\hat{s_Z}^2\hat{c}_Z^2} S \equiv \frac{\Pi_{ZZ}^{\text{new}}(M_Z^2) - \Pi_{ZZ}^{\text{new}}(0)}{M_Z^2} - \frac{\hat{c}_Z^2 - \hat{s}_Z^2}{\hat{c}_Z \hat{s}_Z} \frac{\Pi_{Z\gamma}^{\text{new}}(M_Z^2)}{M_Z^2} - \frac{\Pi_{\gamma\gamma}^{\text{new}}(M_Z^2)}{M_Z^2}, \tag{3.84}$$

$$\frac{\hat{\alpha}}{4\hat{s_Z}^2}(S+T) \equiv \frac{\Pi_{WW}^{\text{new}}(M_W^2) - \Pi_{WW}^{\text{new}}(0)}{M_W^2} - \frac{\hat{c}_Z}{\hat{s}_Z} \frac{\Pi_{Z\gamma}^{\text{new}}(M_Z^2)}{M_Z^2} - \frac{\Pi_{\gamma\gamma}^{\text{new}}(M_Z^2)}{M_Z^2}, \tag{3.85}$$

where $\hat{s}_Z \equiv \sin\theta_W(M_Z)$, $\hat{c}_Z \equiv \cos\theta_W(M_Z)$, and $\hat{\alpha} \equiv \hat{g}^2 \hat{s}_Z^2/(4\pi)$ are defined in the $\overline{\text{MS}}$ scheme and evaluated at M_Z. Notice that the S, T, U parameters are defined such that they vanish for the SM. The BSM contributions to the predictions for the W boson mass and the Z boson observables can be conveniently expressed in terms of these three parameters, such that a global fit to the EW precision data yields [10]

$$T = 0.03 \pm 0.12, \tag{3.86}$$

$$S = -0.02 \pm 0.10, \tag{3.87}$$

$$U = 0.01 \pm 0.11. \tag{3.88}$$

Following Refs. [206, 207], where the S, T, U parameters are computed generically for models exclusively containing gauge-singlet and $\text{SU}(2)_L$-doublet scalar fields, we were able to constrain all the models discussed here by comparing the predictions for the oblique parameters with the values in Eqs. (3.86)-(3.88).[2]

Flavour observables

As discussed in Sect. 3.1, the softly broken $\mathbb{Z}_2$ symmetry defined in Eq. (3.3), extended to the Yukawa sector, forbids FCNCs at tree-level in the three models under investigation. Accordingly, loop contributions play an important role for the predictions of low-energy flavour-physics observables, such as rare B-meson decays and B-meson mixing parameters, and their comparison with the experimental results. In the 2HDM, the dominant deviations from the SM predictions have their origin in the presence of the charged scalars $H^{\pm}$. Most of flavour constraints are expected to be relatively insensitive to the presence of additional singlet fields. In particular, for the Yukawa types II and IV, experimental limits on $\mathrm{BR}(B \to X_s\gamma)$ yield a roughly t_β-independent limit on the charged Higgs boson mass[209, 210]

$$m_{H^\pm} \gtrsim 600 \text{ GeV}, \tag{3.89}$$

whose dependence on the details of the neutral scalar sector is only subleading [211]. On the contrary, constraints derived from rare B_d and B_s decays based on the $b \to s$ flavour changing neutral-current transition such as $B_s \to \mu^+\mu^-$ can get contributions from the neutral scalars and, therefore, differ for each of the models of interest here. However, as we concentrate on the Yukawa type II for all the studies presented here, the flavour constraints for t_β values $1.5 \leq t_\beta \leq 10$ –which is the regime of interest– are mainly derived from experimental data from $B_s \to X_s\gamma$ [210]. Since the additional gauge singlet scalars of the N2HDM and the S2HDM do not couple directly to the SM fermions, the relevant range of $\tan\beta$ is not expected to be substantially modified compared to the 2HDM. In our analyses, we will use parameter points with $\tan\beta \approx 2$ or below, such that the constraints from the $B_{s,d} \to \mu^+\mu^-$ decays are of minor importance. Therefore, we can safely adopt the flavour constraints of the 2HDM in Ref. [210] for our analyses in the N2HDM and the S2HDM. For the 2HDM and the N2HDM, allowed parameter points are required to be located within the 2σ region of the $m_{H^\pm} - t_\beta$ plane as identified via a global fit to experimental data in Ref. [210]. For the S2HDM type II, we applied hard cuts on the values of $m_{H^\pm}$ and $\tan\beta$ corresponding to $m_{H^\pm} > 600$ GeV and $\tan\beta > 1.5$ in order to not be in conflict with constraints from radiative and (semi-)leptonic B meson decays and from their mixing frequencies [210].

Direct searches for additional Higgs bosons

Experimental upper limits on the production of BSM-type Higgs bosons provide important constraints on the parameter space of models with extended Higgs sectors. For each of the scenarios analysed, we list below the most constraining searches which obviously depend on

---

[2] The results given in Eqs. (3.86)-(3.88) do not take into account the new measurement of the W-boson mass reported recently by the CDF collaboration [208].

m_{h_a}	m_{h_b}	m_{h_c}	m_A	$m_{H^\pm}$	tanβ	$C^2_{h_a t\bar{t}}$	$C^2_{h_a VV}$	sgn(R_{a3})	R_{b3}	m^2_{12}	v_S
125.09	$[30, 1000]$	400	650	650	2	1	1	$-1, 1$	$[-1, 1]$	65000	$[1, 1000]$
125.09	400	160	650	650	2	$[0.8, 1.2]$	$[0.7, 1.0]$	1	0	65000	300
125.09	400	105	650	650	2	$[0.8, 1.2]$	$[0.7, 1.0]$	$-1, 1$	0	68500	300

Table 3.4: Set of input parameters for the three different scenarios explored in our analysis. Here the three CP-even scalars (not necessarily ordered in mass) are denoted as $h_{a,b,c}$. The first row corresponds to a case in which the SM-like Higgs boson h_a does not have a singlet component and the two heavier CP-even scalars, h_b and h_c mix with each other. The second and third rows describe scenarios where the SM-like Higgs boson h_a mixes with a heavier and lighter singlet-like scalar h_c, respectively.

the particular parameter space region under investigation. Those searches were identified and applied by means of the public code `HiggsBounds`. Further details on the code and the specific versions that were utilised for each analysis are given in Sects. 5.1.1, 6.1 and 8.1.2.

2HDM For the following ranges of the input parameters

$$\tan\beta = 3 \ , \quad m_h = 125.09 \text{ GeV} \ , \quad 200 \text{ GeV} \leq m_H \leq 1 \text{ TeV} \ ,$$
$$500 \text{ GeV} \leq m_A = m_{H^\pm} \leq 1.2 \text{ TeV} \ , \quad \cos(\beta - \alpha) = 0, \quad M^2 = \frac{m_{12}^2}{s_\beta c_\beta} = m_H^2 \ ,$$

the searches that led to the exclusion of parameters points are:

- ATLAS [174]: $gg \to H \to (h)Z \to (b\bar{b})l^+l^-$ at $\sqrt{s} = 13$ TeV, 139 fb^{-1}
- ATLAS [212]: $pp \to (A)\gamma \to (jj)\gamma$ at $\sqrt{s} = 13$ TeV, 79.8 fb^{-1}

N2HDM In the N2HDM, we focus on three different parameter space regions depending on the mixing patterns between the CP-even neutral scalars. In the first case, for a scenario where the SM-like Higgs boson ($h_1 \equiv h_{125}$) does not have a singlet component and the two heavier CP-even scalars, h_2 and h_3, mix with each other (see first row of Tab. 3.4), the following searches are found to be the most relevant:

- CMS [213]: $gg \to A \to t\bar{t}$ at $\sqrt{s} = 13$ TeV, 35.9 fb^{-1} and including width effects
- CMS [213]: $gg \to h_3 \to t\bar{t}$ at $\sqrt{s} = 13$ TeV, 35.9 fb^{-1} and including width effects

In the case of a SM-like Higgs boson ($h_1 \equiv h_{125}$) that mixes with a heavier singlet-like scalar h_2 (see second row of Tab. 3.4), the searches that led to the exclusion of parameter points are:

- CMS [214]: $pp \to h_3 \to ZZ$ at $\sqrt{s} = 13$ TeV, 35.9 fb^{-1} and including width effects
- CMS [215]: $pp \to (h_2) \to (WW)X$ at $\sqrt{s} = 7 + 8$ TeV, 4.6 fb^{-1}

For the scenario where a SM-like Higgs boson ($h_2 \equiv h_{125}$) mixes with a lighter singlet-like scalar h_1 (see third row of Tab. 3.4), the most constraining direct searches are:

- CMS [214]: $pp \to h_3 \to ZZ$ at $\sqrt{s} = 13$ TeV, 35.9 fb^{-1} and including width effects
- LEP [216]: $ee \to (h_1)Z \to (b\bar{b})Z$ at $\sqrt{s} = 189 - 209$ GeV with combined data

S2HDM For the broader scan performed in the S2HDM over the following ranges of input parameters

$$\begin{gathered}1.5 \leq \tan\beta \leq 10\ , \quad m_{h_1} = 125.09\ \text{GeV}\ , \quad 140\ \text{GeV} \leq m_{h_{2,3}} \leq 1\ \text{TeV}\ , \\ 40\ \text{GeV} \leq m_\chi \leq 80\ \text{GeV}\ , \quad 40\ \text{GeV} \leq v_S \leq 1\ \text{TeV}\ , \quad -\pi/2 \leq \alpha_{1,2,3} \leq \pi/2\ , \\ 400\ \text{GeV} \leq M \leq 1\ \text{TeV}\ , \quad 600\ \text{GeV} \leq m_{H^\pm} \leq 1\ \text{TeV}\ , \quad m_A \leq 1\ \text{TeV}\ , \\ \Delta M_{\text{max}} = \max\left(|m_H - M|, |m_A - M|, |m_{H^\pm} - M|\right) < 200\ \text{GeV}\ , \end{gathered} \tag{3.90}$$

the direct searches that excluded parameter points are:

- ATLAS [174]: $gg \to A \to (h_2)Z \to (b\bar{b})l^+l^-$ at $\sqrt{s} = 13$ TeV, 139 fb^{-1}
- ATLAS/CMS [217, 218]: $pp \to h_2, h_3 \to VV$ at $\sqrt{s} = 13$ TeV/7+8 TeV, 36 fb^{-1}/5.1 fb^{-1}
- CMS/ATLAS [214, 219]: $pp \to h_2 \to ZZ$ at $\sqrt{s} = 13$ TeV, 36 fb^{-1}, 36.1 fb^{-1} and including width effects
- ATLAS [220]: $pp \to h_2, h_3, A \to \tau^+\tau^-$ at $\sqrt{s} = 13$ TeV, 139 fb^{-1}
- ATLAS [221]: $pp \to h_2, h_3 \to h_1 h_1 \to b\bar{b}b\bar{b}$ at $\sqrt{s} = 13$ TeV, 36.1 fb^{-1}
- CMS [222]: $gg \to A \to (h_1)Z \to (b\bar{b})l^+l^-$ at $\sqrt{s} = 13$ TeV, 35.9 fb^{-1} assuming $h_1 = h_{125}$
- ATLAS [223]: $pp \to (H^\pm)tb \to (tb)tb$ at $\sqrt{s} = 13$ TeV, 139 fb^{-1}
- ATLAS [224]: $pp \to h_2, h_3 \to h_1 h_1$ at $\sqrt{s} = 13$ TeV, 36.1 fb^{-1} assuming $h_1 = h_{125}$
- CMS [213]: $gg \to h_2, h_3 \to t\bar{t}$ at $\sqrt{s} = 13$ TeV, 35.9 fb^{-1} and including width effects

Properties of the 125 GeV Higgs boson

The discovery of a Higgs boson with a mass of approximately 125 GeV at the LHC by the ATLAS [225] and the CMS [226] collaborations puts strong constraints on models with extended Higgs sectors. Purely CP-odd fermionic and bosonic couplings to the 125 GeV Higgs boson are excluded, but admixtures are compatible with experimental results[227]. In a CP-conserving 2HDM, the pseudoescalar state A cannot play the role of the discovered Higgs boson and, thus, the only possibility to account for the CP properties of the 125 GeV Higgs boson is to identify one of the CP-even scalars with the discovered particle h_{125}. Furthermore, as the signal-rate measurements of the 125 GeV Higgs boson agree with the predictions of the SM at the 10% level [133, 228], the compatibility with those measurements requires that the couplings of h_{125} should, within the current experimental uncertainties, resemble the couplings of a SM Higgs boson. As discussed above, in the alignment limit in 2HDMs, the properties of the SM-like Higgs boson are recovered. The alignment limit can occur with or without the decoupling of the non-SM-like scalars. In general, the masses of the heavier Higgs bosons take the form

$$m_\phi^2 = M^2 + f(\lambda_i)v^2 + \mathcal{O}(v^4/M^2), \tag{3.91}$$

with $\phi \equiv H, A, H^\pm$, and $f(\lambda_i)$ is a linear combination of the quartic couplings. If $M^2 \gg f(\lambda_i)v^2$, the mass of ϕ is dominated by the soft-breaking scale of the $\mathbb{Z}_2$ symmetry $\sim m_{12}^2$. This is the so-called *decoupling limit*, where the effective theory below M consists of only one doublet, and all the tree-level couplings of $h \equiv h_{125}$ approach those of the SM Higgs. However, a non-decoupling effect can still occur even though the non-SM-like scalars are heavy. If $M^2 \leq f(\lambda_i)v^2$, a large value of m_ϕ arises if $f(\lambda_i)$ is large, which corresponds to the strong coupling regime. Here radiative corrections can appreciably change the low-energy physics. In conclusion, the decoupling effect leads to the alignment limit but this is only a sufficient condition and not necessary. The alignment limit in the 2HDM can also occur within a non-decoupling regime as long as $\cos(\alpha - \beta) = 0$. These arguments can be extended to the N2HDM and the S2HDM, where the alignment limit is defined as in the 2HDM plus a vanishing singlet component for the SM-like Higgs boson. The alignment limit facilitates the agreement between the measured signal rates of the observed Higgs boson and the predicted ones. In the 2HDM and partially in the N2HDM, we will focus on the alignment limit within a non-decoupling regime of the heavy scalars (see Sect. 5.3 and Sect. 6.5.1, respectively). In the N2HDM and the S2HDM, we will be also interested in departures from the alignment limit (see Sect. 6.5.2 and Sect. 8.2.1, respectively). In general, the predicted signal rates for h_{125} in models with extended Higgs sectors deviate from the SM predictions. We have to ensure that these deviations lie within the experimental uncertainties. For the case of the S2HDM, in addition to the global constraints on the measured signal rates of h_{125}, its parameter space can also be probed via possible decays of h_{125} into a pair of DM particles χ with a mass of $m_\chi < 125/2$ GeV. At leading order, the partial decay width of such an invisible decay is given by

$$\Gamma_{\text{inv}}(h_i \to \chi\chi) = \frac{1}{32\pi m_{h_i}}\sqrt{1 - \frac{4m_\chi^2}{m_{h_i}^2}}\left(R_{i1}\lambda_7 v_1 + R_{i2}\lambda_8 v_2 + R_{i3}\lambda_6 v_S\right)^2 \ , \ m_{h_i} > 2m_\chi^2 \ . \tag{3.92}$$

The most recent upper limit on the branching ratio of the invisible decay BR_{inv} of h_{125} has been reported by ATLAS and is given by $\text{BR}_{\text{inv}} < 0.11$ at the 95% confidence level [229]. This additional decay mode also suppresses the ordinary decays of h_{125} into SM final states, whom may lead to the incompatibility with the global constraints on the measured signal rates.

The compatibility with the experimentally measured signal rates of the Higgs boson at about 125 GeV was done by utilising the public code `HiggsSignals`. Further details on the code and the specific versions that were utilised for each analysis are given in Sects. 5.1.1, 6.1 and 8.1.2.

Part II

The EW symmetry in the early Universe

Chapter 4

Extended scalar sectors at finite-temperature

The ΛCDM model offers comprehensive explanations for a broad range of observed phenomena such as the abundances of the light elements, the existence and structure of the CMB, the accelerating expansion of the Universe and the large-scale structure in the distribution of galaxies (see e.g. [10] for a review). The measured abundances of the light elements are the experimental evidence from the earliest stages of the Universe probed up to date, which date back to roughly 180 s after the Big Bang. The detection of GWs in 2016 [230–232] inaugurated the GW astronomy as a promising window into earlier cosmological epochs, unreachable by other means. In particular, the characteristic frequency of the GW signal generated during a FOEWPT overlaps with the sensitivity of the next generation of GW experiments. The detection of such a GW signal would carry invaluable knowledge of the early stages of our Universe, dating back to roughly 10^{-10} s after the Big Bang, when the primordial plasma had a temperature of the order of the EW scale. The discovered Higgs boson confirms the paradigm of a scalar field-driven symmetry breaking in the early Universe, and the study of the EW epoch could shed light on the content of the scalar sector, possibly containing additional scalar states. Extensions of the scalar sector may have been responsible for a variety of phenomena impossible within the SM, such as a FOEWPT or EW SnR at higher temperatures. Since the equilibrium description of the Universe is a good approximation at the EW scale, the primordial plasma can be described by a finite-temperature equilibrium field theory [233]. To see why this approximation holds, we consider the measure of deviation from thermal equilibrium as the ratio of two time scales, of which the first one is the rate of the Universe expansion, given by the Hubble parameter $H(T)$. The second one is a typical reaction time. At the EW scale when $T_{\rm ew} \sim m_W$, the slowest reactions, those involving chirality flips for the lightest fermions (e.g. $e_R h_{125} \to \nu W$), occur at a rate $\Gamma \sim y_e^2 (g/4\pi)^2 T_{\rm ew}$. The ratio $H(T_{\rm ew})/\Gamma \sim 10^{-2} \ll 1$ implies that to a very good approximation the primordial plasma was in thermal equilibrium when its temperature was roughly $T_{\rm ew} \sim m_W$.

Here we present the background material needed for the later discussions in Chapters 5 and 6. In particular, we derive the finite-temperature effective potential (Sect. 4.1). We also discuss the EWPT and other possible effects in the thermal evolution of the EW vacuum configuration, such as EW SnR and vacuum trapping (Sect. 4.2). Finally, we review the production of GWs during a FOEWPT (Sect. 4.3).

4.1 The finite-temperature scalar potential

Generating functionals In quantum field theory (QFT), the n-point correlation functions are the basic objects that allow us to make predictions through the computation of scattering amplitudes and making use of the Lehmann-Symanzik-Zimmermann (LSZ) [234] reduction formula.[1] The correlation or Green's functions are defined as

$$G_n(x_1, ..., x_n) \equiv \langle \omega | \mathcal{T} \boldsymbol{\phi}(x_1) ... \boldsymbol{\phi}(x_n) | \omega \rangle = \lim_{\substack{t_1 \to +\infty \\ t_2 \to -\infty}} \frac{\langle 0 | \mathcal{T} \phi(x_1) ... \phi(x_n) U(t_1, t_2) | 0 \rangle}{\langle 0 | U(t_1, t_2) | 0 \rangle}, \tag{4.1}$$

where $|\omega\rangle$ and $|0\rangle$ denote the respective ground states of the interacting and free theory, described by the full $\mathcal{H}$ and the free $\mathcal{H}_0$ Hamiltonian, respectively. Here ϕ are the fields in the interaction picture, whose evolution is controlled by $\mathcal{H}_0$, whereas $\boldsymbol{\phi}$ are the fields in the Heisenberg picture, which are evolved utilizing the full interacting Hamiltonian $\mathcal{H}$. Both representations are related via a time-dependent unitary transformation

$$\boldsymbol{\phi} = U^\dagger(0, t) \phi U(t, 0), \tag{4.2}$$

where $U(t_1, t_2)$ is the time-evolution operator given by

$$U(t_1, t_2) = e^{i\mathcal{H}_0 t_1} e^{-i\mathcal{H}(t_1 - t_2)} e^{-i\mathcal{H}_0 t_2}. \tag{4.3}$$

The operation $\mathcal{T}$ denotes the time-ordered product. The Eq. (4.1) provides a basis for perturbative calculations in QFT. It expresses the Green's functions, which are expectation values over the physical vacuum of the time-ordered product of Heisenberg field operators, in terms of fields in the interacting picture and expectation values over the vacuum of the free theory. The scattering matrix operator is defined as

$$\mathcal{S} = \lim_{\substack{t_1 \to +\infty \\ t_2 \to -\infty}} U(t_1, t_2) = \lim_{\substack{t_1 \to +\infty \\ t_2 \to -\infty}} \mathcal{T} e^{-i \int_{t_2}^{t_1} dt V(t)} = \mathcal{T} e^{i S_{\text{int}}}, \tag{4.4}$$

where $S_{\text{int}} = -\int_{t_2}^{t_1} dt V(t)$ and is $V(t) = \int d\vec{x} V$ with V given by $\mathcal{H} = \mathcal{H}_0 + V$. The generating functional of the full n-point Green's functions (including vacuum bubbles) is the partition function,

$$\mathcal{Z}[J] = \langle 0 | \mathcal{T} e^{i S_{\text{int}} + i \int dx J(x) \phi(x)} | 0 \rangle, \tag{4.5}$$

from which one can compute the n-point correlation functions by taking derivatives of the partition function with respect to the auxiliary function $J(x)$ as follows

$$G_n(x_1, ..., x_n) = (-i)^2 \frac{1}{\mathcal{Z}[0]} \left. \frac{\mathcal{Z}[J]}{\delta J(x_1) ... \delta J(x_n)} \right|_{J=0}. \tag{4.6}$$

Therefore, all transition amplitudes are encapsulated in the partition function, which –in most cases– cannot be derived in a closed form but can be computed to some order of a perturbative expansion in powers of a coupling constant. The generating functional $\mathcal{Z}$ can

---

[1] In this subsection, we followed the lecture notes in Ref. [235].

be computed as a functional integral over all the possible paths for the field variable ϕ weighted by a phase involving the classical action with boundary conditions $\phi_1 = \phi(t_1, \vec{x})$ and $\phi_2 = \phi(t_2, \vec{x})$ in the limit $t_1 \to +\infty$ and $t_2 \to -\infty$,

$$\mathcal{Z}[J] = \lim_{\substack{t_1 \to +\infty \\ t_2 \to -\infty}} \int [\mathcal{D}\phi(x)] e^{iS + i\int dx J\phi}, \tag{4.7}$$

with

$$S = \int_{t_1}^{t_2} dt \int d^3x \mathcal{L}(\phi(x)) = \int_{t_1}^{t_2} dt \int d^3x \left[\frac{1}{2}(\partial_\mu \phi)(\partial^\mu \phi) - V_{\text{tree}}(\phi) \right], \tag{4.8}$$

where $V_{\text{tree}}(\phi)$ is the tree-level potential. The vacuum-to-vacuum transition amplitude $\mathcal{Z}[J]$ generates all correlation functions by means of Eq. (4.6). We can also define the generating functional for connected correlation functions as the phase of the partition function

$$\mathcal{W}[J] = -i \log \mathcal{Z}[J]. \tag{4.9}$$

From the first functional derivative of $\mathcal{W}[J]$ we obtain the classical expectation value of the field $\phi(x)$ in the presence of the source J as

$$\frac{\delta \mathcal{W}[J]}{\delta J(x)} = \langle \phi_{\text{cl}} \rangle_J = \phi_{\text{cl}}(x). \tag{4.10}$$

Setting $J = 0$, one obtains the 1-point function or the vacuum expectation value of $\phi(x)$

$$\left. \frac{\delta \mathcal{W}[J]}{\delta J(x)} \right|_{J=0} = \langle \phi(x) \rangle. \tag{4.11}$$

Furthermore, the Legendre transform of $\mathcal{W}[J]$ as a function of $J(x)$ defines the effective action

$$\Gamma[\phi_{\text{cl}}] = \mathcal{W}[J] - \int d^4x J(x) \phi_{\text{cl}}(x), \tag{4.12}$$

which is the generating functional for one-particle-irreducible (1PI) correlation functions, $\Gamma^{(n)}(x_1, ..., x_n)$. The expectation value $\langle \phi \rangle$ satisfies Euler-Lagrange equations derived by finding the extrema of the effective action,

$$\left. \frac{\delta \Gamma[\phi_{\text{cl}}]}{\delta \phi_{\text{cl}}(x)} \right|_{\phi_{\text{cl}} = \langle \phi \rangle} = 0. \tag{4.13}$$

Considering quantum fluctuations around the classical vacuum $\phi(x) = \phi_{\text{cl}}(x) + \eta(x)$, the saddle point evaluation of the effective action is given by the sum of the tree-level classical action, a one-loop correction piece written in closed form, plus an infinite series of higher-loop corrections originating from the fluctuations $\eta(x)$ which can only be computed diagrammatically,

$$\Gamma[\phi_{\text{cl}}] = S_r[\phi_{\text{cl}}] \pm \frac{i}{2} \text{Tr} \log \left(-\frac{\delta^2 S_r}{\delta \phi^2}[\phi_{\text{cl}}] \right) - i \left(\begin{array}{c} \text{sum of} \\ \text{higher-loop diag.} \end{array} \right) + \Delta S[\phi_{\text{cl}}]. \tag{4.14}$$

Here S_r corresponds to the renormalised classical action and ΔS to the set of counterterms. The one loop contribution can be understood as the sum of all one-loop 1PI diagrams with any number of external scalar fields legs. The ± sign in front of the 1-loop contribution depends on whether the loops originate from bosonic (+) or fermionic (−) fields. For a translationally invariant theory we have

$$\phi_{\text{cl}}(x) = \phi_{\text{cl}}, \tag{4.15}$$

i.e. ϕ_{cl} is independent of x. Therefore, we define the effective potential as

$$\Gamma[\phi_{\text{cl}}] = -\int d^4x V_{\text{eff}}(\phi_{\text{cl}}). \tag{4.16}$$

Thermal field theory The partition function has the interpretation of a statistical field theory with the temperature identified as the inverse of imaginary time.[2] To get an intuitive idea on this, we consider the transition amplitude between an initial state $\phi(t_a, \vec{x}) = \phi_a$ and final state $\phi(t_b, \vec{x}) = \phi_b$ given in terms of the path integral representation

$$\langle \phi_a | e^{-i\mathcal{H}(t_b - t_a)} | \phi_b \rangle = \int [\mathcal{D}\phi] e^{i \int_{t_a}^{t_b} dt \int d^3x \mathcal{L}}. \tag{4.17}$$

A system in thermal equilibrium with temperature T, described by the hamiltonian $\mathcal{H}$ and with several conserved charges Q_i ($[Q_i, \mathcal{H}] = 0$), is defined by its density matrix ρ,

$$\rho = \frac{1}{\mathscr{Z}} e^{-\frac{1}{T}\left(\mathcal{H} + \sum\limits_i \mu_i Q_i\right)}, \tag{4.18}$$

where μ_i is a set of chemical potentials. The grand canonical partition function $\mathscr{Z}$ is the statistical sum of the system,

$$\mathscr{Z} = \text{Tr} e^{-\frac{1}{T}\left(\mathcal{H} + \sum\limits_i \mu_i Q_i\right)} = \text{Tr} e^{-\beta\left(\mathcal{H} + \sum\limits_i \mu_i Q_i\right)}, \tag{4.19}$$

where we have made the identification $\frac{1}{T} \equiv \beta$. In the following, we will assume the approximation of vanishing chemical potentials, as suggested by the observed BAU. Taking the trace amounts to compute the integral

$$\mathscr{Z} = \int d\phi_a \langle \phi_a | e^{-\beta \mathcal{H}} | \phi_a \rangle, \tag{4.20}$$

where ϕ_a are the set of eigenstates of the full interacting hamiltonian. We observe that the computation of $\mathscr{Z}$ reduces to the computation of a path integral similar to Eq. (4.17) after performing a Wick rotation

$$t \to -i\tau. \tag{4.21}$$

As a consequence of taking the trace, we require periodic boundary conditions for bosonic fields

$$\phi_a(0, \vec{x}) = \phi_a(\beta, \vec{x}), \tag{4.22}$$

---

[2] In this subsection, Refs. [233, 236–239] were followed.

and anti-periodic boundary conditions for fermionic fields,

$$\psi_a(0,\vec{x}) = -\psi_a(\beta,\vec{x}). \tag{4.23}$$

After the Wick rotation, the Lagrangian density for the real scalar field in Euclidean space $(\tau,\vec{x})$ reads

$$\mathcal{L} \to \mathcal{L}_E = \frac{1}{2}\left(\frac{\partial\phi}{\partial\tau}\right)^2 + \frac{1}{2}\sum_{i=1}^{3}\left(\frac{\partial\phi}{\partial x_i}\right) + V_{\text{tree}}(\phi). \tag{4.24}$$

The path integral representation of the statistical sum $\mathscr{X}$ (Eq. (4.19)) in the presence of external sources is given by

$$\mathscr{X}[J] = \int[\mathcal{D}\phi(x)]e^{-S_E+\int d\tau\int d^3xJ\phi}, \tag{4.25}$$

with the Euclidean action defined on a finite τ-interval $0<\tau<\beta$,

$$S_E = \int_0^\beta d\tau\int d^3x\mathcal{L}_E. \tag{4.26}$$

The (anti-)periodicity on the boundary conditions allows the expansion of the fields in Fourier modes

$$\begin{aligned}\text{Bosons:}\quad \phi(\tau,\vec{x}) &= \frac{1}{\sqrt{\beta}}\sum_{n=-\infty}^{\infty}\phi_n(\tau,\vec{x})e^{-i\omega_n\tau},\\ \text{Fermions:}\quad \psi(\tau,\vec{x}) &= \frac{1}{\sqrt{\beta}}\sum_{n=-\infty}^{\infty}\psi_n(\tau,\vec{x})e^{-i\omega_n\tau},\end{aligned} \tag{4.27}$$

where the Matsubara frequencies $\omega_n = 2n\pi\beta^{-1}$ and $\omega_n = (2n+1)\pi\beta^{-1}$ lead to the discretization of the energy of the bosonic and fermionic modes, respectively.

Given the equivalence between a finite-temperature equilibrium field theory and an Euclidean field theory defined on a finite "time" interval, many methods developed for the zero-temperature QFT are inherited by the finite-T case. In particular, perturbation theory at finite temperature looks precisely like perturbation theory at zero-temperature with a substitution of quantities associated with the zero component of the 4-momentum. For instance,

$$\begin{aligned}\text{Boson propagator}\ &:\ \frac{i}{p^2-m^2};\ p^\mu = [2ni\pi\beta^{-1},\vec{p}]\\ \text{Fermion propagator}\ &:\ \frac{i}{\gamma\cdot p-m};\ p^\mu = [(2n+1)i\pi\beta^{-1},\vec{p}]\\ \text{Loop integral}\ &:\ \frac{i}{\beta}\sum_{n=-\infty}^{\infty}\int\frac{d^3p}{(2\pi)^3}\\ \text{Vertex function}\ &:\ -i\beta(2\pi)^3\delta_{\sum\omega_i}\delta^{(3)}\left(\sum_i\vec{p}_i\right).\end{aligned} \tag{4.28}$$

There is a standard trick to perform the infinite sums that appear in loop integrals [236]. For a particular choice of contour C, we have

$$\frac{1}{\beta}\sum_{n=-\infty}^{\infty} f(p^0 = i\omega_n) = \int_{-i\infty}^{+i\infty} \frac{dz}{4\pi i}[f(z) + f(-z)] + \eta \int_C \frac{dz}{2\pi i} n(z)[f(z) + f(-z)], \quad (4.29)$$

where $\eta = \pm 1$ for bosons/fermions. Here $n(\omega)$ are the Bose-Einstein and Fermi-Dirac distribution functions for bosons and fermions, respectively

$$n(\omega) = \frac{1}{e^{\omega/T} - \eta}, \quad (4.30)$$

with the Matsubara frequencies

$$\omega^2(\vec{p}, \phi_{\rm cl}) = |\vec{p}|^2 + m^2(\phi_{\rm cl}). \quad (4.31)$$

Here $m^2(\phi_{\rm cl})$ is the background-field-dependent mass of $\phi(\tau, x)$ computed as

$$m^2(\phi_{\rm cl}) = \left.\frac{\partial^2 V_{\rm tree}(\phi)}{\partial \phi^2}\right|_{\phi=\phi_{\rm cl}}, \quad (4.32)$$

for the Lagrangian in Eq. (4.24).

One-loop effective potential at finite T For a generic interacting theory, the generating functional of Green's functions $\mathcal{Z}[J]$ in Euclidean space with periodic boundary conditions over the interval $\tau \in [0, \beta]$ corresponds to the grand canonical partition function $\mathscr{Z}[\beta, J]$ in the presence of an external source J coupling to the field variables. The generating functional $\mathcal{W}[J]$ of connected Green's functions is interpreted as the Helmholtz free energy functional $F[\beta, J] = -1/\beta \log \mathscr{Z}[\beta, J]$, whereas the effective action corresponds to the Gibbs free energy functional

$$G[\beta, \phi_{\rm cl}] = F[\beta, J] + \int J\phi_{\rm cl}. \quad (4.33)$$

Since we can extend the definition of the effective action to finite-temperature field theory, we can use the computational machinery seen in the first part of Sect. 4.1 to obtain the one-loop effective potential $V_{\rm eff}^1$ at finite-temperature. The effective scalar potential can be diagrammatically understood as the sum of all 1PI diagrams with any number of external legs

$$V_{\rm eff} = -\sum_{n=0}^{\infty} \frac{\phi_{\rm cl}^n}{n!} \Gamma^{(n)}(p = 0). \quad (4.34)$$

Here $\Gamma^{(n)}(p = 0)$ is the n-point vertex function that contains all possible interactions at any loop order for vanishing external momenta. In particular, the diagrammatic expansion of the one-loop contributions to $V_{\rm eff}^1$ from scalars, fermions and gauge bosons can be seen in Fig. 4.1.

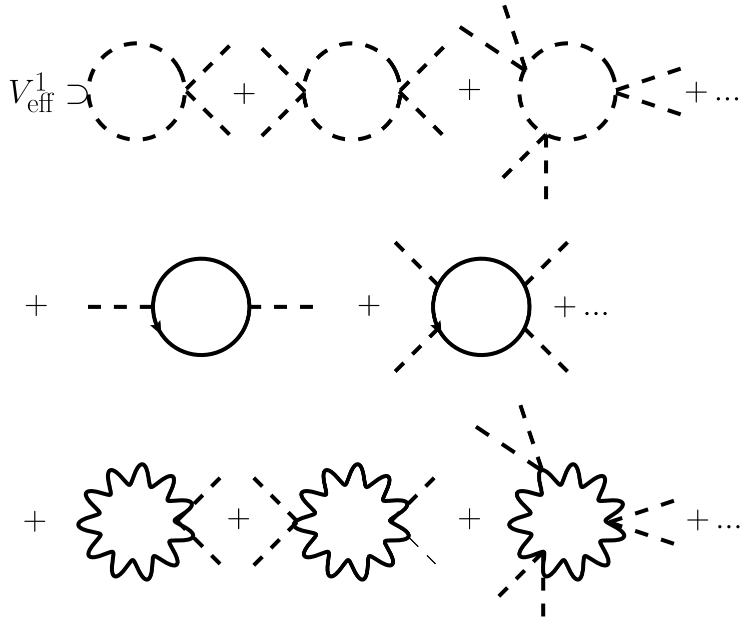

Figure 4.1: Illustrative example of the type of one-loop diagrams included in the 1-loop effective potential.

To explicitly compute the closed form of the one-loop effective potential for a single real scalar field, we consider the one-loop contribution to the effective action in Eq. (4.14) (second term in the sum). Together with the definition of the effective potential in Eq. (4.16), $V^1_{\rm eff}$ reads

$$V^1_{\rm eff} = \frac{1}{2}{\rm Tr}\,\log\left(-\partial^2_\tau - \vec{\nabla}^2 + m^2(\phi_{\rm cl})\right) = \frac{T}{2}\sum_n \int \frac{d^3\vec{p}}{(2\pi)^3}\log\left(\omega_n^2 + \omega^2(\vec{p},\phi_{\rm cl})\right), \qquad (4.35)$$

with $\omega(\vec{p},\phi_{\rm cl})$ defined in Eq. (4.31). In the second step in Eq. (4.35) we evaluated the trace in the Fourier mode expansion in Eq. (4.27). This can be rewritten in the form

$$V^1_{\rm eff} = \int \frac{d^3\vec{p}}{(2\pi)^3} I(\omega(\vec{p})), \qquad (4.36)$$

in terms of the function

$$I(\omega) = \frac{T}{2}\sum_n \log\left(\omega_n^2 + \omega^2(\vec{p},\phi_{\rm cl})\right). \qquad (4.37)$$

Since we are only interested in the field-dependent part $\omega \equiv \omega(\vec{p},\phi_{\rm cl})$, we can take the derivative of $I(\omega)$ with respect to ω, and subsequently integrate the result. This yields

$$I(\omega) = \frac{\omega}{2} + \frac{1}{\beta}\log\left[1 - e^{-\frac{\omega}{T}}\right]. \qquad (4.38)$$

Inserting this result into Eq. (4.36), we obtain the one-loop radiative corrections to the scalar potential at zero-temperature ($V_{\text{eff}}^{1(0)}$) and at finite temperature ($V_{\text{eff}}^{1(T)}$),

$$\begin{aligned} V_{\text{eff}}^{1(0)}(\phi_{\text{cl}}) &= \int \frac{d^3\vec{p}}{(2\pi)^3}\frac{\omega}{2}, \\ V_{\text{eff}}^{1(T)}(\phi_{\text{cl}}) &= \frac{T^4}{2\pi^4}\int_0^{+\infty} dx x^2 \log\left[1 - e^{-\sqrt{x^2+(\frac{m}{T})^2}}\right]. \end{aligned} \tag{4.39}$$

The generalisation to higher-spin fields coupling to several scalar fields ϕ_i yields

$$\begin{aligned} V_{\text{eff}}^{1}(\phi_{\text{cl},i}) &= \sum_j \frac{n_j T}{2}\sum_{n=-\infty}^{+\infty}\int \frac{d^3\vec{p}}{(2\pi)^3}\log\left(\omega_n + \vec{p}^2 + m_j^2((\phi_{\text{cl},i}))\right) \\ &= V_{\text{eff}}^{1(0)}(\phi_{\text{cl},i}) + V_{\text{eff}}^{1(T)}(\phi_{\text{cl},i}) \\ &= \sum_j \frac{n_j}{2}\left(\int \frac{d^3\vec{p}}{(2\pi)^3}\sqrt{|\vec{p}|^2 + m_j^2(\phi_{\text{cl},i})}\right. \\ &\left. + \frac{T^4}{\pi^4}\int_0^{+\infty} dx x^2 \log\left[1 - e^{-\sqrt{x^2+(\frac{m_j}{T})^2}}\right]\right), \end{aligned} \tag{4.40}$$

where $m_j(\phi_i)$ is the background-field-dependent tree-level mass of the particle species j, and n_j its corresponding number of degrees of freedom.

The temperature-independent contribution $V_{\text{eff}}^{1(0)}$ is UV-divergent, so the divergences must be isolated through regularisation and subsequently absorbed by an appropriate set of counterterms. After renormalising $V_{\text{eff}}^{1(0)}$ in the $\overline{\text{MS}}$ renormalisation scheme, we obtain the well-known Coleman-Weinberg (CW) potential V_{CW} [240]. For brevity, we will drop the index of ϕ_{cl} keeping in mind the background-field approach that disregards excitations.

Let us now expand on the above considerations. The full effective potential computed at the one-loop order is given by

$$V_{\text{eff}} = V_{\text{tree}} + V_{\text{CW}} + V_{\text{T}} + V_{\text{CT}}, \tag{4.41}$$

where V_{tree} is the tree-level potential, and V_{CW} denotes the CW potential. V_{CT} includes a finite set of counterterms and will be discussed below. At zero-temperature, the contribution from V_T vanishes,

$$V_{\text{eff}} = V_{\text{tree}} + V_{\text{CW}} + V_{\text{CT}}. \tag{4.42}$$

The CW potential is given in the $\overline{\text{MS}}$ renormalisation scheme by

$$V_{\text{CW}}(\phi_i) = \sum_j \frac{n_j}{64\pi^2}(-1)^{2s_j}\, m_j^4(\phi_i)\left[\ln\left(\frac{|m_j(\phi_i)^2|}{\mu^2}\right) - c_j\right], \tag{4.43}$$

where s_j is the particle spin. Here we set the renormalisation scale μ to be equal to the SM EW vev, $\mu = v$. In the $\overline{\text{MS}}$ renormalisation scheme, the constants c_j are $c_j = 3/2$ for scalars and fermions, and $c_j = 5/6$ for gauge bosons. In the three models analysed, the sum in Eq. (4.43) runs over the various neutral scalars, the charged scalars, the SM quarks q and leptons ℓ, the longitudinal and transversal gauge bosons. The CW potential has been evaluated in the Landau gauge as this allows the omission of ghost contributions to $V_{\rm CW}$. The effective potential is well-known to be gauge-dependent, and the extraction of physical information from $V_{\rm eff}$ has to be done with care.[3]

In scalar extensions of the SM, the tree-level scalar masses and mixing angles in general differ from those extracted from the one-loop effective potential. To perform an efficient scan through the parameter space of these models, we shift from the $\overline{\rm MS}$ scheme to an "on-shell" (OS) renormalisation scheme. To this purpose, we have followed Refs. [244, 245]. We required that the zero-temperature loop-corrected scalar masses and mixing angles be equal to their tree-level values. We achieve this by adding to the effective potential an UV-finite counterterm contribution $V_{\rm CT}$, given by

$$V_{\rm CT} = \sum_i \frac{\partial V_0}{\partial p_i}\delta p_i + \sum_k (\phi_k + v_k)\delta T_k \ , \tag{4.44}$$

where p_i stands for the parameters of the tree-level potential. A tadpole counterterm δT_k is introduced for each field ϕ_k which is allowed to develop a vev. To maintain the tree-level values of the scalar masses and their mixing angles at the loop level, we have imposed the following renormalisation conditions

$$\partial_{\phi_i} V_{\rm CT}(\phi)\Big|_{\langle\phi\rangle_{T=0}} = -\partial_{\phi_i} V_{\rm CW}(\phi)\Big|_{\langle\phi\rangle_{T=0}} \ , \tag{4.45}$$

$$\partial_{\phi_i}\partial_{\phi_j} V_{\rm CT}(\phi)\Big|_{\langle\phi\rangle_{T=0}} = -\partial_{\phi_i}\partial_{\phi_j} V_{\rm CW}(\phi)\Big|_{\langle\phi\rangle_{T=0}} \ , \tag{4.46}$$

where $\langle\phi\rangle_{T=0}$ corresponds to the tree-level vev at zero temperature. The derivatives of the CW potential have been computed following Ref. [246]. The contribution V_T is the one-loop thermal potential [236, 247] given in Eq. (4.40), which can be more conveniently expressed in terms of the functions $J_\pm$,

$$V_T(\phi_i, T) = \sum_j \frac{n_j\, T^4}{2\pi^2}\, J_\pm\left(\frac{m_j^2(\phi_i)}{T^2}\right) . \tag{4.47}$$

The thermal integrals for fermionic (J_+) and bosonic (J_-) particle species are defined by

$$J_\pm\left(\frac{m_j^2(\phi_i)}{T^2}\right) = \mp \int_0^\infty dx\, x^2 \,\log\left[1 \pm \exp\left(-\sqrt{x^2 + \frac{m_j^2(\phi_i)}{T^2}}\right)\right] \ , \tag{4.48}$$

which vanish as $T \to 0$ assuming that m_j^2 is positive. In addition to the degrees of freedom considered in Eq. (4.43), the sum in Eq. (4.47) includes the photon, due to the non-zero effective thermal mass of its longitudinal polarisation.

---

[3] Often the Nielsen identities [241, 242] are employed in this context; see e.g. [243] for a discussion of this issue.

In certain situations (e.g. when studying EW SnR at high T) it is convenient to expand the thermal functions $J_\pm$ in the high temperature limit [236]

$$\begin{aligned} J_-(y) &\approx -\frac{\pi^4}{45} + \frac{\pi^2}{12} y - \frac{\pi}{6} y^{\frac{3}{2}} - \frac{1}{32}\, y^2 \log\left(\frac{|y|}{a_b}\right) + \mathcal{O}(y^3)\,, \\ J_+(y) &\approx -\frac{7\pi^4}{360} + \frac{\pi^2}{24} y + \frac{1}{32}\, y^2 \log\left(\frac{|y|}{a_f}\right) + \mathcal{O}(y^3) \qquad \text{for } |y| \ll 1\,, \end{aligned} \tag{4.49}$$

with $a_b = \pi^2 \exp(3/2 - 2\gamma_E)$ and $a_f = 16\pi^2 \exp(3/2 - 2\gamma_E)$, $\gamma_E = 0.57721\ldots$ being the Euler-Mascheroni constant.

Breakdown of perturbation theory The fact that thermal-loop effects overpower a temperature-independent tree-level potential hints at the breakdown of perturbation theory. This effect is what permits the high-temperature restoration of the EW symmetry in the SM. Otherwise radiative corrections should be unable to restore the symmetry, since they would be subleading with respect to the tree-level piece.

The perturbative expansion breaks down at high temperature due to zero-Matsubara-modes that behave as massless degrees of freedom and generate divergences via an infrared(IR)-mass pole in the propagator. Only bosons can have a vanishing Matsubara frequency (see Eq. (4.27)), and therefore fermions do not cause IR-divergences.[4] It is clear that this problem will be accentuated in the high temperature regime, where the particles can be approximated as nearly massless.

The breakdown of perturbation theory in finite-temperature field theory has a deep physical reason [233]. At zero temperature, we consider processes where only a small number of particles participate. However, at high temperature a very dense environment favour the interaction among a large number of particles. For bosons, the number density is proportional to the Bose-Einstein distribution function $n(\omega)$ (Eq. (4.30)). The number density becomes large for zero-modes in the IR. Therefore, since the distribution function enters the computation of loop integrals (see Eq. (4.28)), there will be certain diagrams for which this feature becomes an IR-divergence. For fermions the situation is different, given that the Pauli exclusion principle forbids the occupation of a single mode by more than two particles.

Therefore, we cannot trust the completeness of the one-loop result due to the existence of some higher-loop corrections of the same order. Furthermore, the leading part of these multi-loop corrections that need to be resummed in the IR-limit is all contained in the set of diagrams called *daisy diagrams* [249–251], shown in Fig. 4.2.

The first method to perform the resummation, introduced by Parwani [250], consists in shifting the masses of all the Matsubara modes for the bosonic fields. In this way, the IR-divergences are avoided by giving the bosons a finite mass,

$$m_j^2(\phi_i) \to m_j^2(\phi_i) + \Pi_j(T). \tag{4.50}$$

---

[4] In the gauge sector, only longitudinal polarisations lead to the breakdown of the perturbative expansion [248].

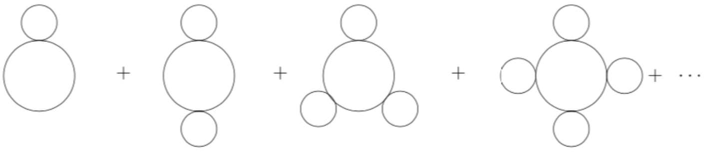

Figure 4.2: Sum of daisy diagrams. Image taken from [239]

This temperature-dependent shift is the thermal mass, which is an effective mass that particles acquire through their continuous interaction with the heat bath. The thermal masses can be computed as the leading order contributions to the masses in the high-temperature expansion of the one-loop thermal potential (Eq. (4.47)). Using the prescription in Eq. (4.50), the one-loop effective potential is given by

$$V_{\text{eff}}^{1+\text{Parwani}} = \sum_j \frac{n_j T}{2} \sum_{n=-\infty}^{+\infty} \int \frac{d^3\vec{p}}{(2\pi)^3} \log\left(\omega_n + \vec{p}^2 + m_j^2(\phi_i) + \Pi_j(T)\right). \tag{4.51}$$

With this replacement, each bosonic propagator is substituted by its "dressed" version, and we implicitly account for the daisy diagram contributions and remove their divergences. The main problem arising in this approach is that, after renormalising the UV-divergent part of the potential (4.51), the UV-behavior of the theory depends on the IR-dynamics. Instead, we prefer the other frequently used approach that consists in "dressing" only the zero-modes propagators. This is the so-called Arnold-Espinosa (AE)[5] approach [251]

$$\begin{aligned} V_{\text{eff}}^{1+\text{AE}} = \sum_j \frac{n_j T}{2} \Bigg\{ &\sum_{n=-\infty\setminus\{0\}}^{+\infty} \int \frac{d^3\vec{p}}{(2\pi)^3} \log\left(\omega_n + \vec{p}^2 + m_j^2(\phi_i)\right) \\ &+ \int \frac{d^3\vec{p}}{(2\pi)^3} \log\left(\vec{p}^2 + m_j^2(\phi_i) + \Pi_j(T)\right) \Bigg\} \equiv V_{\text{eff}}^1 + V_{\text{daisy}}. \end{aligned} \tag{4.52}$$

The part containing the resummation of the daisy diagrams reads

$$V_{\text{daisy}}(\phi_i, T) = -\sum_i \frac{T}{12\pi} \text{Tr}\left[\left(m_i^2(\phi_i) + \Pi_i^2\right)^{\frac{3}{2}} - \left(m_i^2(\phi_i)\right)^{\frac{3}{2}}\right]. \tag{4.53}$$

Since V_{daisy} effectively generates a cubic term which may affect the energy barrier between degenerate minima in a FOEWPT, this contribution is crucial to correctly asses its strength. The inclusion of the daisy resummation diminishes the strength of the FOEWPT due to the screening caused by the thermal mass Π_i for the field-dependent terms in $m_i^2(\phi_i)$.

In conclusion, we will use in the following the full effective potential including the resummation of daisy diagrams, which is given by

$$V(\phi_i, T) = V_{\text{tree}} + V_{\text{CW}} + V_{\text{T}} + V_{\text{CT}} + V_{\text{daisy}}. \tag{4.54}$$

---

[5] See Chapter 6 for a comparison between the AE and the Parwani resummation methods.

Scale dependence and perturbativity The renormalization group evolution of the quartic scalar couplings λ_i can provide meaningful constraints on the viable region of the parameter space of the models analisyed. Even if $\lambda_i(\mu)$ are perturbative at an energy scale $\mu = v$, the running of the parameters may drive the scalar quartic couplings into a non-perturbative regime. Depending on the values of $\lambda_i(v)$ this can happen already at relatively low energy scales (i.e. not far from the EW scale). Hence, as a key ingredient in our analysis, we solve the renormalization group equations (RGEs) for each model parameter point discussed, and require that $|\lambda_i(\mu)| < 4\,\pi$ for $v < \mu < T_{\mathrm{max}}$, where T_{max} is the maximum temperature analysed in each case. Due to the renormalisation prescription showed in Eqs. (4.45) and (4.46), it is necessary to transform the OS values of the model parameters p^{OS} at $\mu = \mu_0$ into the corresponding $\overline{\mathrm{MS}}$ values $p^{\overline{\mathrm{MS}}}$, such that the running of the parameters can be applied by numerically solving the RGEs, given in terms of the β functions in the $\overline{\mathrm{MS}}$ scheme. The transformation between the two schemes is given by the finite parameter counterterms δp_i introduced in Eq. (4.44), using

$$p^{\mathrm{OS}}(\mu_0) + \delta p^{\mathrm{OS}}(\mu_0) = p^{\overline{\mathrm{MS}}}(\mu_0) + \delta p^{\overline{\mathrm{MS}}}(\mu_0) \tag{4.55}$$

$$\Rightarrow\; p^{\overline{\mathrm{MS}}}(\mu_0) = p^{\mathrm{OS}}(\mu_0) + \delta p^{\mathrm{OS}}_{\mathrm{fin.}}(\mu_0)\ , \tag{4.56}$$

where the second equality follows from the fact that by definition the counterms $\delta p^{\overline{\mathrm{MS}}}$ do not contain finite pieces. Accordingly, the counterterms $\delta p^{\mathrm{OS}}_{\mathrm{fin.}}(\mu_0)$ for the different parameters p_i correspond to the finite counterterms δp_i in Eq. (4.44).

In the perturbative regime, the evolution of the parameters under a variation of μ is logarithmic. Therefore, the scale dependence gives rise to only a relatively small uncertainty in the context of FOEWPTs, which naturally take place at $T \lesssim v$. On the other hand, for the study of the scalar potential at temperatures beyond the EW scale, e.g. for the purpose of investigating EW SnR, the variation of the quartic couplings λ_i with the energy scale within the whole temperature region can be numerically important. Methods to improve the theoretical uncertainties are discussed e.g. in Refs. [252, 253]. In order to limit the impact of a potentially large scale dependence, we restrict our analysis to parameter points with values of the renormalised couplings in the $\overline{\mathrm{MS}}$ renormalisation scheme, $|\lambda_i^{\overline{\mathrm{MS}}}(\mu_0)|$, considerably below the perturbativity bound 4π.

4.2 Thermal evolution

In this section, we describe the relevant phenomena that may have occurred to the cosmological history of the Universe around the EW scale. In particular, we focus on the EWPT (Sect. 4.2.1), vacuum trapping (Sect. 4.2.2) and EW SnR (Sect. 4.2.3).

4.2.1 The EWPT

The effective potential $V(\phi_i, T)$ (see Eq. (4.54)) can be interpreted as the free energy density of a medium at a temperature T with the (homogeneous) background scalar fields equal to ϕ_i. In thermal equilibrium, the free energy density is minimised with respect to all the macroscopic parameters and, in particular, with respect to the fields ϕ_i, as we also deduce from its connection to the effective action (Eq. (4.33)). At zero temperature, the ground state is not invariant under the EW gauge group $\mathrm{SU}(2)_L \times \mathrm{U}(1)_Y$: the symmetry is spontaneously broken down to the gauge group $\mathrm{U}(1)_{\mathrm{em}}$ due to the non-zero EW vev, which in the three models explored is given by $v = \sqrt{v_1^2 + v_2^2} \approx 246$ GeV (see Sect. 3.1).

As we have seen in the previous section, the effective potential at finite-temperature acquires additional contributions, resulting in the temperature dependence of the EW vev, $v(T) = \sqrt{v_1^2(T) + v_2^2(T)}$. As predicted by standard comoslogy,[6], the EW symmetry is unbroken at very early times, so $v(T)$ vanishes at sufficiently high temperatures, i.e. $v(T \gtrsim v) = 0$. This means that, as the Universe cooled down, there must have been a transition between the unbroken phase of the EW symmetry (in which $v = 0$) and the broken phase (where $v \neq 0$).

Essentially there are two different types of phase transitions: these are first and second-order phase transitions. A FOEWPT is associated to a jump in the vev as a function of temperature, while a second-order transition is characterised by a continuous change. This can be observed in Fig. 4.3, where the families of curves represent the effective potential for different temperatures in a particular field direction. Upper curves represent the potential at higher temperatures. The left plot illustrates a FOEWPT. As temperature decreases, we see how the minimum at the origin (false minimum) gets separated by an energy barrier from the minimum where the EW symmetry is broken (true minimum). The true minimum is the minimum that evolves towards the zero-temperature physical situation of an unbroken EW symmetry with $v = 246$ GeV. It must have been adopted by Universe at some point of its thermal evolution. The vacuum state associated to the true minimum is called "true vacuum". A false minimum is any other minimum that does not converge to a physically allowed minimum as the temperature approaches zero, and the vacuum state associated to that minimum is called "false vacuum". At the critical temperature, T_c, both the true and the false minima are degenerate, and, eventually, the false minimum becomes unstable. At the nucleation temperature T_n, the transition occurs via the nucleation of bubbles of the true vacuum phase, their subsequent expansion and mergers, culminating in an abrupt

---

[6] We will also consider the less conventional scenario in which the EW symmetry can be broken already at temperatures much larger than the EW scale (see Sect. 4.2.3).

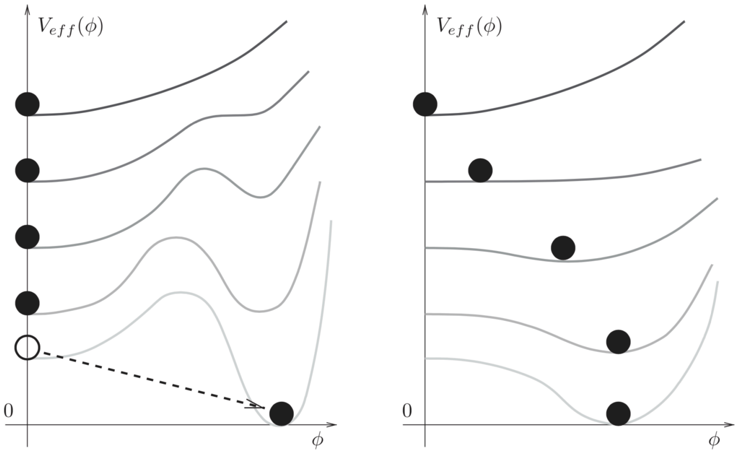

Figure 4.3: Shape of the effective potential at various temperatures: upper darker curves correspond to higher temperatures. The left and right panels describe first and second order phase transitions, respectively. Black circles show the expectation value $\langle\phi\rangle$. Image taken from [254].

change of the vev (see Fig. 4.4). When the unbroken phase percolates, the Universe returns to an spatially homogeneous state of thermal equilibrium with $v \neq 0$. The turbulent expansion and collision of the bubbles generates GWs (see Sect. 4.3).

The right plot in Fig. 4.3 exemplifies a second-order phase transition, which proceeds by a slow and homogeneous change of the medium properties over the entire space. At every moment of time, the medium is in a state close to thermal equilibrium and the vev changes continuously with temperature. Here we remark that the background-field method utilised to derive the effective potential in Eq. (4.54) is a good approximation for the study of a strong FOEWPT, but breaks down for weakly first-order and second-order phase transitions close to the critical temperature. We define a strong FOEWPT as a transition for which the following condition is satisfied

$$\frac{v_n}{T_n} \gtrsim 1, \tag{4.57}$$

where $v_n \equiv v(T_n)$. During a strong FOEWPT, a large barrier between the two phases suppresses large amplitude thermal fluctuations around the false minimum. Therefore, an initial false vacuum state is well-defined, as no sizeable fraction of volume is in the new phase before the transition occurs [255]. In this situation, neglecting the fluctuations around the background field in Eq. (4.14) is a good approximation to study the transition. For weaker first-order and second-order phase transitions, at the critical temperature the curvature at both degenerate minima is close to or exactly zero, and large-amplitude fluctuations are expected to cause a substantial mixing between the two phases. In this situation an initial vacuum state located at the origin of field space is ill-defined. Therefore, the method based on the analysis of the effective potential in Eq. (4.54) is appropriate to study

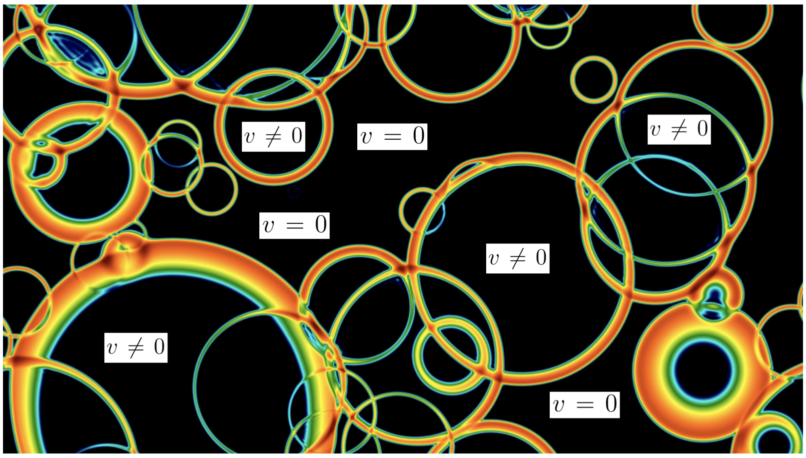

Figure 4.4: Three-dimensional simulation of a FOEWPT, which proceeds via the nucleation of growing bubbles of a broken phase with $v \neq 0$ in a background unbroken phase with $v = 0$. The image shows a moment where a substantial fraction of the bubbles have collided. Image by David Weir [256, 257].

strong FOEWPTs, but the calculation of the critical temperature for weakly first-order and second-order EWPTs should be regarded as a mere illustrative quantity.

The occurrence of a strongly FOEWPT depends on the transition rate per unit time and unit volume from the false vacuum into the true (EW) vacuum [192, 193, 258, 259]

$$\Gamma(T) = A(T)\, e^{-S_3(T)/T}, \tag{4.58}$$

with S_3 being the three-dimensional action for the "bounce" (multi-)field configuration $\vec{\phi}_{\mathrm{B}}$ that interpolates between the false and the true (EW) vacua for $T < T_c$,

$$S_3(T) = 4\pi \int r^2 dr \left[\frac{1}{2} \left(\frac{d\vec{\phi}_{\mathrm{B}}}{dr} \right)^2 + V\left(\vec{\phi}_{\mathrm{B}}, T\right) \right] . \tag{4.59}$$

Specifically, the bounce $\vec{\phi}_{\mathrm{B}}$ is the configuration of scalar fields ϕ that solves the equations of motion derived from the action Eq. (4.59) with boundary conditions $d\phi/dr|_{r=0} = 0$ and approaching the false vacuum at $r \to \infty$. Physically, $\vec{\phi}_{\mathrm{B}}$ describes a bubble of the true vacuum phase nucleating in the false vacuum background. The prefactor $A(T)$ is a functional determinant [193] given approximately by $A(T) \sim T^4\,(S_3/2\pi T)^{3/2}$ [258]. The onset of the FOEWPT occurs when the time integral of the transition rate,Eq. (4.58), within a Hubble volume H becomes of order one. This defines the nucleation temperature T_n (see e.g. [260]) as

$$\int_{T_n}^{T_c} \frac{T^4}{H^4} \frac{A(T)}{T}\, e^{-S_3(T)/T}\, dT \sim 1 \ , \tag{4.60}$$

where we have used that the time-temperature relation in an expanding Universe is assumed to be dominated by radiation. The Hubble parameter H is given by

$$H^2(T) = (8\,\pi^3 g_{\mathrm{eff}}(T)\, T^4)/(90\, \mathrm{M}_{\mathrm{Pl}}^2), \tag{4.61}$$

where $g_{\rm eff}(T)$ denotes the effective number of relativistic degrees of freedom at a temperature T, and $\mathrm{M_{Pl}} = 1.22 \times 10^{19}$ GeV is the Planck mass. Eq. (4.60) roughly yields [27]

$$S_3(T_n)/T_n \sim 140 \tag{4.62}$$

as the requirement for the occurrence of a FOEWPT. The possibility that the condition (4.60) is not satisfied for any temperature below the critical temperature T_c will be discussed in section Sect. 4.2.2.

On general grounds, a cosmological first-order phase transition can be characterised by four macroscopic parameters which we specify in the following. These quantities are obtained from the microscopic properties of the underlying particle physics model. As will be discussed in more detail in Sect. 4.3, these parameters also determine the predictions of the amplitude and the spectral shape of the stochastic GW background that is generated during the first-order phase transition. The first key parameter is the temperature T_* at which the phase transition takes place. The second parameter, α, measures the strength of the phase transition. Following Refs. [26, 27], we define α as the difference of the trace of the energy-momentum tensor between the two (false and true vacua) phases, normalised to the radiation background energy density, i.e.

$$\alpha = \frac{1}{\rho_R}\left(\Delta V(T_*) - \left(\frac{T}{4}\frac{\partial \Delta V(T)}{\partial T}\right)\bigg|_{T_*}\right) . \tag{4.63}$$

Here $\Delta V(T) = V_f - V_t$, with $V_f \equiv V(\phi_f)$ and $V_t \equiv V(\phi_t)$ being the values of the potential in the false and the true vacuum, respectively.[7] ρ_R is the background energy density assuming a radiation dominated Universe, i.e. $\rho_R = \pi^2 g_{\rm eff}(T_*) T_*^4/30$. We also note that for cosmological phase transitions in which $\alpha \ll 1$, the transition temperature T_* can be identified with the nucleation temperature T_n defined by Eq. (4.60) [26], since the temperature at the onset of the transition is approximately equal to the temperature for which true vacuum bubbles collide and the phase transition completes. The third quantity is the inverse duration of the phase transition in Hubble units, β/H. It can generally be expressed (see [263] for a discussion) in terms of the derivative of the action S_3 with respect to the temperature evaluated at the time of the phase transition,

$$\frac{\beta}{H} = T_* \left(\frac{d}{dT}\frac{S_3(T)}{T}\right)\bigg|_{T_*} . \tag{4.64}$$

The fourth quantity that characterises a cosmological first-order phase transition is the bubble wall velocity $v_{\rm w}$ in the rest frame of the fluid and far away from the bubble. So far, except for the case of ultrarelativistic bubbles [264–266], the computation of $v_{\rm w}$ is

---

[7] In some studies (see, for instance, Refs. [145, 261] for 2HDM analyses) the parameter α has been defined instead as the latent heat released during the transition divided by ρ_R, in which case the factor 1/4 in the second term in Eq. (4.63) is absent. However, recent studies have shown that the definition used here yields a better description of the energy budget available for the production of GW waves compared to a definition of α by means of the pressure difference or the energy difference [262].

generally a very complicated task that requires solving a coupled system of Boltzmann and scalar field equations in a fairly model-dependent approach (see Refs. [267–276], as well as [26, 27] for a general discussion). There is no precise prediction for v_w in the 2HDM (or related extensions of the SM) available in the literature.[8] Hence, we will treat v_w as a free parameter in our analysis in the 2HDM Chapter 5.

EW baryogenesis EW baryogenesis is an interesting scenario to explain the BAU that predicts new phenomena at the EW scale potentially accessible at present and near-future colliders, precision experiments and GW interferometers. The generation of the observed BAU requires out-of-equilibrium dynamics [24] to avoid the wash-out of the baryon number. Such a prerequisite can be fulfilled by the EWPT, but only if it is first order [52]. The SM predicts that EWSB happened in the early Universe via a smooth crossover [40–44], where all the medium properties changed continuously with temperature. A crossover is not considered to be a proper phase transition even though there are similarities between its features and those of a second-order phase transition, i.e. the continuous temperature evolution of $v(T)$. In contrast, a second-order phase transition shows a discontinuity in the temperature evolution of the second derivative of the free energy density, whereas for a crossover there are no discontinuities at any order in the derivatives of the free energy density. The fact that the SM predicts a smooth crossover instead of a FOEWPT has been often used as a motivation for BSM physics (see e.g. the review [277]).

The role of the FOEWPT is fundamental for EW baryogenesis [52], which essentially proceeds in three steps. Firstly, provided the existence of baryon number and C- and CP-violating processes, when the nucleated bubbles expand, particles in the plasma can scatter with the phase interface and generate CP and C asymmetries in the particle number densities in front of the bubble wall. Secondly, these asymmetries diffuse into the symmetric phase ahead of the bubble wall, where they bias EW sphaleron transitions to produce more baryons than antibaryons [277]. Finally, some of the net baryon charge created outside the bubble wall is swept up by the expanding wall into the broken phase, where sphaleron processes must be sufficiently suppressed in order to avoid the wash-out of the generated baryon asymmetry. This prerequisite leads to the condition in Eq. (4.57), which arises from requiring the rate of sphaleron processes inside the bubble to be smaller than the Hubble expansion rate [277]. One should note that the ratio v_n/T_n is not a well-defined physical quantity, since it is gauge-dependent. In addition, the frequently used criterion in Eq. (4.57) implicitly assumes specific choices for various parameters such as the duration of the transition or the factor accounting for fluctuations that are not sphaleron zero-modes [277]. Given that the goal of this dissertation is the study of the EWPT independently of baryogenesis, the precise criterion to avoid the baryon asymmetry washout is not of prime importance. Nevertheless, the intrinsic gauge dependence of the

---

[8] See Ref. [39] for estimates of v_w in the 2HDM for some specific parameter configurations. A simple analytical formula to predict v_w has been obtained in Ref. [275]. However, this formula has not yet been applied to models with a second Higgs doublet, and it is unclear how accurate the prediction for v_w would be for the 2HDM.

scalar field vacuum expectation values at any temperature, the critical and the nucleation temperatures is indeed a source of uncertainty that does affect our analysis. In Ref. [278] it was noted that, in most models, the uncertainty arising from the quantitative dependence on the gauge-fixing parameter should be rather small as compared to the uncertainty of neglecting two-loop contributions to the effective potential.

4.2.2 Vacuum trapping

The Universe must evolve to the EW minimum at $T = 0$. This condition has a highly non-trivial impact on the physically allowed parameter space of BSM models. It implies that a zero-temperature analysis does not suffice to determine the viable parameter space region. A scalar potential that is bounded from below and has the EW vacuum as the global minimum at $T = 0$ could still correspond to a scenario that is not physically acceptable. It is possible that the scalar potential at $T = 0$ has more than one local minimum: the EW vacuum as global minimum and, for instance, a false vacuum with $\langle \Phi_{1,2} \rangle = 0$ (using the notation of Sect. 3.1). If at some temperature $T > 0$ only the $\langle \Phi_{1,2} \rangle = 0$ vacuum is present, the Universe can only evolve to the EW minimum by tunnelling from the false one. Then, if the conditions for the on-set of the first-order phase transition were never fulfilled (Eq. (4.60)), the Universe would be trapped in a false vacuum at $T = 0$.

This phenomenon is dubbed *vacuum trapping*. In particular, when aiming to identify the parameter space regions of a BSM model where a FOEWPT occurs, the possibility of vacuum trapping indicates that an approach based solely on the critical temperature T_c is not sufficient and may yield misleading results. Vacuum trapping will be discussed in the context of the 2HDM and of the N2HDM in Chapters 5 and 6, respectively. It has been recently discussed in the NMSSM [279] and also previously in the context of colour-breaking minima within the MSSM [280]. In the 2HDM, vacuum trapping has been also recently explored in Ref. [145], emphasising that this phenomenon may take place in particular if the barrier between the false and the true vacua is driven almost exclusively by the radiative corrections, rather than by the thermal contributions to the effective potential.

4.2.3 EW symmetry non-restoration

It is known that in certain extensions of the SM the EW symmetry can be broken already at temperatures much larger than the EW scale, resulting in EW SnR [46–51, 281]. The effect of SnR can exist up to possibly very high temperatures, and it is also possible to find no restoration at all within the energy range in which the model under consideration is theoretically well-defined. As we will discuss in Chapter 5 for the 2HDM and in Chapter 6 for the N2HDM, in doublet extensions of the SM the presence of EW SnR is related to the existence of sizeable quartic scalar couplings and the impact of the resummation of infrared divergent modes in the scalar potential. In that scenario, the maximum temperature up to which the analysis of SnR is valid corresponds to the upper cut-off $\Lambda_{4\pi}$ defined as the energy scale μ at which one of the quartic couplings reaches the naive perturbative bound

4π (see the end of Sect. 4.1 for a related discussion). $\Lambda_{4\pi}$ is representative of the energy scale μ at which the theory enters a non-perturbative regime.

The occurrence of EW SnR in the early Universe has a number of cosmological consequences [47]. For instance, in the absence of a FOEWPT, there will be no GW signal. Even though the absence of GW signals is also a prediction of the SM, scenarios with EW SnR could be distinguished through deviations from the SM that are potentially measurable at colliders. Furthermore, an unrestored EW symmetry at high temperature maintained down to the EW scale allows the possibility of high-scale or GUT baryogenesis [282–286]. Through the suppression of EW sphalerons, any possible baryon asymmetry generated at high energy scales could be preserved as the Universe cools down. This situation would allow for sources of CP-violation that are only manifest at those possibly very high energy scales, ensuring the compatibility with the required amount of CP-violation to generate the baryon asymmetry and bounds from electric dipole moments. In general, EW SnR can cause changes in the thermal evolution of the Universe as compared to the symmetry-restored "vanilla" cosmology. In particular, it can alter the evolution of the relativistic degrees of freedom g_{eff}, add contributions to the Hubble rate, induce changes in the decoupling/recoupling to the thermal bath of particles that obtain mass through the Higgs sector, modify their equations of state, trigger a period of early matter domination (possibly influencing structure formation), and modify freeze-in and freeze-out calculations with potential effects on the abundance of DM and SM particles.

4.3 Cosmological gravitational wave backgrounds

We review the framework that underlies the analysis about GWs in the 2HDM in Chapter 5.[9] In Sect. 4.3.1, we define the GWs. We describe the basic formalism that connects first principles from GR to the actual measurable quantity in GWs observatories, the GW power spectrum Ω_{GW}. In Sect. 4.3.2, we estimate the dependencies of Ω_{GW} with some of the relevant quantities in the FOEWPT. Towards the end of the section, we give the formulas for the different contributions to Ω_{GW} depending on the specific source in a FOEWPT.

4.3.1 Characterisation of a stochastic GW background

The Friedmann–Lemaître–Robertson–Walker (FLRW) metric is the background metric that describes our expanding Universe under the assumptions of spatial isotropy and homogeneity. GWs are represented by transverse and traceless tensor spatial perturbations h_{ij} $(i, j = 1, 2, 3)$ of the FLRW metric

$$ds^2 = -dt^2 + a^2(t)(\delta_{ij} + h_{ij})dx^i dx^j, \tag{4.65}$$

where t, x^i are the comoving coordinates and $a(t)$ is the scale factor. Due to general covariance, the perturbation h_{ij} is imposed to satisfy the transverse-traceless gauge conditions

$$h_{ii} = 0 \quad \text{and} \quad \partial_i h_i j = 0, \tag{4.66}$$

---

[9] This section is partly based in Ref. [287], which offers a very comprehensive review on GWs.

which yield a total of two propagating degrees of freedom.

The GW equation of motion is given by Einstein equations linearised to first order in h_{ij} over a FLRW background

$$\ddot{h}_{ij}(t,\mathbf{x}) + 3H\dot{h}_{ij}(t,\mathbf{x}) - \frac{\nabla^2}{a^2}h_{ij}(t,\mathbf{x}) = 16\pi G\ \Pi^{TT}_{ij}(t,\mathbf{x}), \tag{4.67}$$

where ∇^2 is the Laplacian in comoving coordinates, a dot denotes the derivative with respect to the comoving time t, $H = \dot{a}/a$ is the Hubble rate and Π^{TT}_{ij} is given by the traceless and transverse part of the anisotropic stress,

$$a^2\Pi_{ij} = T_{ij} - pa^2(\delta_{ij} + h_{ij}), \tag{4.68}$$

where p is the background pressure and T_{ij} are the spatial components of the energy-momentum tensor of the source. $\Pi^{TT}_{ij}(t,\mathbf{x})$ contains the information relative to the source of the perturbation h_{ij} and depends on the specific scenario. In general, the solutions to Eq. (4.67) can be decomposed into the two polarisation states $r = +, \times$ as

$$h_{ij}(t,\mathbf{x}) = \sum_{r=+,\times} \int \frac{d^3k}{(2\pi)^3} h_r(t,\mathbf{k}) e^{-i\mathbf{k}\cdot\mathbf{x}} e^r_{ij}(\hat{k}), \tag{4.69}$$

where $\hat{k} = \mathbf{k}/k$ is the unit vector in the $\mathbf{k}$ direction and the two polarisations satisfy $e^r_{ij}(-\hat{k}) = e^r_{ij}(\hat{k})$. The polarisation vectors can be written as

$$e^+_{ij}(\hat{k}) = \hat{m}_i\hat{m}_j - \hat{n}_i\hat{n}_j \tag{4.70}$$

$$e^\times_{ij}(\hat{k}) = \hat{m}_i\hat{n}_j - \hat{n}_i\hat{m}_j, \tag{4.71}$$

with $\hat{n}$, $\hat{m}$ and $\hat{k}$ orthogonal among them. With these definitions we have $e^r_{ij}(\hat{k})e^{r'}_{ij}(\hat{k}) = 2\delta_{rr'}$.

While performing GW experiments, the variation of the cosmological expansion can be neglected during the duration of the signal. Under this assumption, we can rewrite the expansion in Eq. (4.69) in terms of the frequency f and the unit wave vector $\hat{k}$

$$h_{ij}(t,\mathbf{x}) = \sum_{r=+,\times} \int_{-\infty}^{+\infty} df \int d^2\hat{k}\bar{h}_r(f,\hat{k}) e^{i2\pi f(t-\hat{\mathbf{k}}\cdot\mathbf{x})} e^r_{ij}(\hat{k}). \tag{4.72}$$

In the following, we would like to relate the Fourier amplitude modes $\bar{h}_r(f,\hat{k})$ to the energy density of GWs ρ_{GW}, which is ultimately related to the measurable GW spectrum.

To obtain the energy density of GWs, we need to compute the effective stress-energy tensor, by firstly noting the need to distinguish a GW originated by metric fluctuations over those caused by the curved background metric. The differentiation is usually done by exploiting a separation of scales/frequencies. If the background metric varies over a typical length scale given by the current value of the Hubble parameter H_0, $L_B \sim 1/H_0$, and the fluctuation is characterised by a typical wave length λ, then they are distinguishable provided that $\lambda \ll L_B$. On practical grounds, this requires performing averages of physical quantities over length-scales l such that $\lambda \ll l \ll L_B$. Einstein equations at second order in the metric perturbation yield

$$T_{\mu\nu}^{\mathrm{GW}} = \frac{\langle \nabla_\mu h_{\alpha\beta} \nabla_\nu h^{\alpha\beta} \rangle}{32\pi G}, \tag{4.73}$$

where ∇ denotes the covariant derivative with respect to the background metric, G is the gravitational constant and $\langle \ldots \rangle$ is an average over a length or time scale. The energy density of GWs is the 00 component of the stress energy tensor which, for the FLRW metric, can be expressed as

$$\rho_{\mathrm{GW}} = T_{\mathrm{GW}}^{00} = \frac{\langle \dot{h}_{ij} \dot{h}^{ij} \rangle}{32\pi G}. \tag{4.74}$$

The GW background originated from cosmological sources is an stochastic background, i.e. the amplitude of the tensor perturbation h_{ij} is understood as a random variable which can be characterised only statistically. The resulting GW signal is the outcome of the superposition of a large number of independent sources distributed uniformly across the Universe. The stochastic GW background is assumed to be statistically **homogeneous** and **isotropic**, **unpolarised** and **Gaussian**. Homogeneity and isotropy are inherited properties of the FLRW metric. As a consequence of the lack of significant sources of parity violation in the early Universe, the GW background is also considered unpolarised. Finally, by the central limit theorem, the superposition of many independent signals is expected to follow a Gaussian distribution. According to these four properties, the power spectrum of the Fourier amplitude modes $\bar{h}_r(f, \hat{k})$ can be written as

$$\langle \bar{h}_r(f, \hat{k}) \bar{h}_p^*(g, \hat{q}) \rangle = \frac{1}{8\pi} \delta(f - g) \delta^{(2)}(\hat{k} - \hat{q}) \delta_{rp} S_h(f), \tag{4.75}$$

where $S_h(f)$ is the spectral density which satisfies $S_h(-f) = S_h(f)$ and has frequency dimensions.

Using Eq. (4.72) and Eq. (4.75), one is able to compute the energy density of GWs ρ_{GW} (4.74). Finally, the intensity of a stochastic background of GWs can be characterised by the GW power spectrum

$$\Omega_{\mathrm{GW}}(f) = \frac{1}{\rho_c} \frac{d\rho_{\mathrm{GW}}}{d \log f}, \tag{4.76}$$

where ρ_c is the value of the critical energy density for closing the Universe

$$\rho_c = \frac{3H^2}{8\pi G}. \tag{4.77}$$

Ω_{GW} and ρ_c are normally computed at the moment of the detection or at the moment of the GWs production. In the following subsection, we explain how both relate.

4.3.2 Stochastic GW background from FOEWPTs

Cosmological GWs arriving at the Earth are redshifted as compared to the originally emitted waves. This is a consequence of their propagation across the expanding Universe. After the production of the GWs, they travel unperturbed due to the fact that they are decoupled from the rest of the Universe. The GW energy density is diluted as radiation with the expansion of the Universe $\rho_{\rm GW} \propto a^{-4}$, whereas the frequency and the wave vector of GWs redshifts as $\propto a^{-1}$. Considering that the Universe expands adiabatically. The conservation of the entropy per comoving volume $S \propto a^3 g_{\rm eff}(T) T^3$ yields the ratio of the scale factor at the transition (dubbed with $*$) to the scale factor today (dubbed with 0) [288]

$$\frac{a_*}{a_0} = 8.0 \times 10^{-14} \left(\frac{100}{g_*}\right)^{1/3} \left(\frac{1 \text{ GeV}}{T_*}\right), \tag{4.78}$$

where $g_* \equiv g_{\rm eff}(T_*)$ is the effective number of relativistic degrees of freedom at the temperature of the phase transition. Now we can relate the GW amplitude $\Omega_{\rm GW,*}$ and the characteristic frequency f_* at the moment of the transition with the amplitude $\Omega_{\rm GW}$ and the frequency f_0 measured today, respectively.

$$f_0 = f_* \left(\frac{a_*}{a_0}\right) = 1.65 \times 10^{-7} \text{ Hz} \left(\frac{f_*}{H_*}\right) \left(\frac{T_*}{1 \text{ GeV}}\right) \left(\frac{g_*}{100}\right)^{1/6} \tag{4.79}$$

$$\Omega_{\rm GW} = \Omega_{\rm GW,*} \left(\frac{a_*}{a_0}\right)^4 \left(\frac{H_*}{H_0}\right)^2 = 1.67 \times 10^{-5} h^{-2} \left(\frac{100}{g_*}\right)^{1/3} \Omega_{\rm GW,*}. \tag{4.80}$$

We can easily estimate how the GW amplitude at the moment of the production $\Omega_{\rm GW,*}$ scales with the duration of the phase transition $1/\beta$ and the tensor anisotropic stress of the GW source Π^{TT} (see Eq. (4.68)). In the following we drop the indices for simplicity. Assuming that the processes associated to Π have a typical duration $1/\beta$ with $\beta/H_* > 1$, $H_* = H(T_*)$ and

$$\dot{h} \simeq \Delta h / \Delta t, \quad \Delta h \sim h \quad \Delta t = 1/\beta, \tag{4.81}$$

the Eq. (4.67) implies

$$\beta^2 h \sim 16\pi G \Pi, \tag{4.82}$$

which suggests that

$$\dot{h} \sim 16\pi G \Pi. \tag{4.83}$$

The energy density of GWs (4.74) at the time of the production is therefore estimated as

$$\rho^*_{\rm GW} \sim \frac{\dot{h}^2}{32\pi G} \sim \frac{8\pi G \Pi^2}{\beta^2}. \tag{4.84}$$

Dividing by the total energy density at the time of the GW production we have

$$\frac{\rho^*_{\rm GW}}{\rho^*_{\rm tot}} \sim \left(\frac{H_*}{\beta}\right)^2 \left(\frac{\Pi}{\rho_{\rm tot}}\right)^2. \tag{4.85}$$

Using Eq. (4.80), we arrive at

$$h^2 \Omega_{\rm GW} \sim 1.67 \times 10^{-5} h^{-2} \left(\frac{100}{g_*}\right)^{1/3} \left(\frac{H_*}{\beta}\right)^2 \left(\frac{\kappa\alpha}{1+\alpha}\right)^2, \tag{4.86}$$

where Π/ρ_{tot} has been rewritten by using

$$\rho^*_{\text{tot}} = \rho^*_R + \rho_{\text{vac}}. \tag{4.87}$$

ρ_{vac} is the vacuum energy released in the transition. We have used the approximation $\alpha \approx \rho_{\text{vac}}/\rho_R$. We have also set $\kappa \sim \Pi/\rho_{\text{vac}}$, where κ is an efficiency factor that can be either

$$\kappa_\phi = \rho_\phi/\rho_{\text{vac}} \text{ or } \kappa_v = \rho_v/\rho_{\text{vac}}., \tag{4.88}$$

depending on the source. ρ_ϕ and ρ_v are the vacuum energy released during the transition that is converted into gradient energy of the scalar fields driving the transition and into bulk motion of the plasma, respectively.

From Eq. (4.86) we see that processes that minimise β/H_*, i.e. slow processes, favour a detectable GW signal. At the same time, very energetic transitions, where a large amount of vacuum energy is released, also favour the detection. Considering the typical time scale of the transition given by $1/\beta$, we get from Eq. (4.79) the GWs characteristic frequency today

$$f \sim 1.65 \times 10^{-5}\ \text{Hz} \left(\frac{f_*}{H_*}\right) \left(\frac{T_*}{100\ \text{GeV}}\right) \left(\frac{g_*}{100}\right)^{1/6}. \tag{4.89}$$

From here we estimate that the characteristic frequency of the GW spectrum associated to a FOEWPT ($T_* \sim 100$ GeV) falls in the frequency range of LISA for values $1 \lesssim \beta/H_* \lesssim 10^5$.

Sources of GWs in a FOEWPT Beyond the rough estimates that Eqs. (4.86) and (4.89) provide, there are three specially compelling sources of GW in FOEWPTs whose precise contributions to the spectrum have to be modelled by means of numerical simulations. The collisions of the expanding bubbles, the resulting motion of the ambient cosmic fluid and magnetohydrodynamic turbulence in the plasma source a stochastic GW background that could be observable at future GW interferometers (see e.g. [26, 27, 289] for a discussion). For FOEWPTs in the 2HDM, where the expanding bubbles do not run-away [39], the contribution from the bubble collisions themselves can be safely neglected. Then, GWs are generated from the sound waves and turbulence generated in the plasma following the bubble collisions [26]. As introduced in Sect. 4.2.1 the GW spectrum produced in a FOEWPT is characterised by four essential quantities [26, 27]: the transition temperature T_*, the strength α, the inverse duration of the phase transition β/H, and the bubble wall velocity v_{w}, i.e. the speed of the bubble wall after nucleation in the rest frame of the plasma far away from the phase-transition interface. The GW power spectrum as a function of frequency $h^2\Omega_{\text{GW}}(f)$ is given by

$$h^2\Omega_{\text{GW}}(f) = h^2\Omega_{\text{sw}}(f) + h^2\Omega_{\text{turb}}(f)\ , \tag{4.90}$$

where $h^2\Omega_{\text{sw}}$ and $h^2\Omega_{\text{turb}}$ are respectively the contributions from sound waves and turbulence. The contribution from sound waves propagating in the plasma was originally obtained with the help of large-scale lattice simulations of bubble collisions inducing bulk fluid motion [256, 290]. It can be written as [26] (see also [291, 292])

$$\Omega_{\rm sw}\,(f) = 0.687\,F_{\rm gw,0}\,\Gamma^2\,\bar{U}_f^4\left(\frac{H_* R_*}{c_s}\right)\tilde{\Omega}_{\rm gw}\left(\frac{H_*\tau_{\rm sw}}{c_s}\right)C\,(f/f_{\rm sw,p})\ , \tag{4.91}$$

with

$$F_{\rm gw,0} = 3.57\cdot 10^{-5}\left(\frac{100}{g_*}\right)^{1/3}\ ,\quad \tilde{\Omega}_{\rm gw} = 0.012\ . \tag{4.92}$$

We have also introduced the speed of sound of a relativistic plasma $c_s = 1/\sqrt{3}$ and the adiabatic index $\Gamma = 4/3$. $\bar{U}_f$ is the the root-mean-square four-velocity of the plasma given by

$$\bar{U}_f^2 = \frac{\kappa\alpha}{\Gamma(1+\alpha)}\ , \tag{4.93}$$

where κ denotes the efficiency factor taking into account the relevant energy fraction for sound waves introduced in Eq. (4.88), which is a function of α and $v_{\rm w}$ that also depends on the steady-state bubble expansion regime (deflagrations, detonations or hybrids, see e.g. [293]), which we obtain following Ref. [293]. The mean bubble separation R_* entering (4.91) is defined by

$$H_* R_* = (8\pi)^{1/3}\left(\frac{\beta}{H}\right)^{-1}\max(v_{\rm w}, c_s)\ . \tag{4.94}$$

The factor $H_*\tau_{\rm sw}$ in Eq. (4.91) is introduced in order to account for a timescale $\tau_{\rm sh}$ for the formation of shocks in the plasma (leading to the damping of the sound waves) that may be shorter than one Hubble time [294]

$$H_*\tau_{\rm sw} = \min(1, H_*\tau_{\rm sh}) \quad \text{with} \quad H_*\tau_{\rm sh} \simeq \frac{H_* R_*}{\bar{U}_f}\ . \tag{4.95}$$

Finally, the spectral shape of the sound-wave signal is approximated by the function

$$C(s) = s^3\left(\frac{7}{4+3s^2}\right)^{7/2}\ , \tag{4.96}$$

and the associated peak frequency is given by

$$f_{\rm sw,p} = 26\left(\frac{1}{H_* R_*}\right)\left(\frac{T_*}{100\ \text{GeV}}\right)\left(\frac{g_*}{100}\right)^{1/6}\mu\text{Hz}\ . \tag{4.97}$$

As indicated above, if the sound-wave period is much shorter than a Hubble time ($H_*\tau_{\rm sw} \ll 1$), a large fraction of the energy stored in the bulk motion of the plasma does not get to produce GW from sound waves. Yet, when the fluid flow becomes nonlinear (giving rise to shock formation), it can lead to the appearance of turbulence in the plasma, which in turn can also generate GWs. Following Ref. [294], we have modelled $h^2\Omega_{\rm turb}$ under the most optimistic assumption that all the energy remaining in the plasma when the sound waves are damped gets transformed into turbulence. In this case, the spectrum of GWs from turbulence may be written as [295]

$$\Omega_{\mathrm{turb}} = 7.23 \cdot 10^{-4} \left(\frac{100}{g_*}\right)^{1/3} v_{\mathrm{w}} \left(\frac{\beta}{H}\right)^{-1} (1 - H_* \tau_{\mathrm{sw}})\, \Gamma^{3/2}\, \bar{U}_f^3\, D(f, f_{\mathrm{turb},p}) \;, \tag{4.98}$$

with peak frequency

$$\frac{f_{\mathrm{turb},p}}{H_*} = 1.75 \left(\frac{\beta}{H}\right) \left(\frac{1}{\max(v_{\mathrm{w}}, c_s)}\right) \mu\mathrm{Hz} \;, \quad \text{with} \quad H_* = 1.65{\cdot}10^{-5} \left(\frac{T_*}{100\ \mathrm{GeV}}\right) \left(\frac{g_*}{100}\right)^{1/6} , \tag{4.99}$$

and the spectral shape approximated by

$$D(f, f_p) = \left(\frac{f}{f_p}\right)^3 \left(1 + \frac{f}{f_p}\right)^{-11/3} \left(1 + 8\pi \frac{f}{H_*}\right)^{-1} \;. \tag{4.100}$$

We note in any case that the details of the GW spectrum produced from turbulence constitute a subject of ongoing debate (see e.g. Refs. [296–298]). At the same time, we have assumed for simplicity in this work that all the energy remaining in the plasma after the sound waves are switched-off leads to turbulence. This gives rise to the factor $(1 - H_* \tau_{\mathrm{sw}})$ in Eq. (4.98), to be compared with the factor $H_* \tau_{\mathrm{sw}}$ in Eq. (4.91). We also stress that the efficiency of turbulence generation as a result of nonlinearities in the plasma is currently under investigation [299]. Nevertheless, we here find that Ω_{turb} plays only a minor role in our estimate of the GW spectrum, since it has a substantially smaller peak amplitude compared to Ω_{sw}.[10]

The value of the EW scale is such that the GW signal from a FOEWPT would lie within the frequency sensitivity band of the future space-based LISA GW interferometer. In order to assess the detectability of a GW signal from a FOEWPT by LISA one has to evaluate the Signal-to-Noise Ratio (SNR) of the GWs. The SNR can be computed according to [26]

$$\mathrm{SNR} = \sqrt{\mathcal{T} \int_{-\infty}^{+\infty} \mathrm{d}f \left[\frac{h^2 \Omega_{\mathrm{GW}}(f)}{h^2 \Omega_{\mathrm{Sens}}(f)}\right]^2} \;, \tag{4.101}$$

where $\mathcal{T}$ is the duration of the mission times its duty cycle. We have used values for $\mathcal{T} = 3\,\mathrm{y}$ and $7\,\mathrm{y}$. $\Omega_{\mathrm{Sens}}(f)$ is the nominal sensitivity of a given LISA configuration to stochastic sources[11], obtained from the power spectral density $S_h(f)$

$$h^2 \Omega_{\mathrm{Sens}}(f) = \frac{2\pi^2}{3H_0^2} f^3 S_h(f), \tag{4.102}$$

---

[10] In particular, we find that including Ω_{turb} does not affect the SNR at LISA at the level of turning an undetectable GW signal into a detectable one. Still, for strong GW signals Ω_{turb} affects the overall GW spectral shape: as will be discussed in more detail in section 5.3.2, Ω_{turb} enhances the signal at the high-frequency tail, which leads to a slight increase in SNR (compared to the GW signal originated by Ω_{sw} alone) when the peak frequency of the sound wave contribution Ω_{sw} is lower than the frequency-range for which LISA has the best sensitivity.

[11] Then, When showing the LISA sensitivity curve in this work (e.g. in Fig. 5.4), it corresponds to the nominal LISA sensitivity $h^2\Omega_{\mathrm{Sens}}(f)$ rather than to the so-called power-law sensitivity of LISA [300] to cosmological sources.

with $S_h(f)$ taken from the LISA mission requirements [142]. In order to be considered detectable, a GW signal should give rise to roughly SNR $\gtrsim 10$ [26]. It should be noted, however, that our model predictions for SNR suffer from sizable theoretical uncertainties. In particular, both the peak frequency and the maximum amplitude of the power spectrum Ω_{sw} depend on the bubble wall velocity v_{w}, for which no well-established model prediction is available even though there are promising recent proposals such as in Refs. [275, 276]. For most parts of our analysis, we will choose $v_{\mathrm{w}} \simeq 0.6$, for which the best prospects regarding GW detection at LISA are obtained in the 2HDM (see section 5.3.3 for details).[12] We nevertheless note that values of v_{w} largely different from 0.6 may give rise to substantially smaller SNR values at LISA. Thus, the predictions for the SNRs in our numerical discussion should be regarded as rough estimates.

---

[12] Remarkably, in Ref. [276] it has been found that for the values of α generically realised in the 2HDM, deflagration bubbles with $v_w \sim c_s$ (thus fairly close to our choice $v_w = 0.6$) are a relatively common feature of FOEWPTs, independently of the precise microscopic properties of the BSM model under consideration.

Chapter 5

Interplay between gravitational waves and LHC physics in the 2HDM

In this Chapter we analyse in detail the thermal history of the Universe in the 2HDM, discussing the occurrence of a FOEWPT as needed for EW baryogenesis, as well as the production of GWs potentially observable by LISA. We show the important impact that SnR and vacuum-trapping phenomena (which can appear in the 2HDM despite its relatively simple structure) have in shaping the 2HDM regions of parameter space where baryogenesis and/or GW production are possible. In particular, we demonstrate that vacuum-trapping reduces the 2HDM parameter range for which a GW signal from a FOEWPT would be observable by LISA to a very fine-tuned parameter-space region. In addition, focusing on the type II 2HDM, we investigate the connection between the thermal history of the early Universe, particularly regarding a possible FOEWPT, and phenomenological signatures at colliders (see Refs. [145, 172, 244, 301–303] for earlier analyses of this connection in the 2HDM): we study the new BSM Higgs boson signatures that are favored by scenarios with a FOEWPT. We demonstrate that ongoing and future LHC searches in final states with top-quarks will probe the vast majority of the 2HDM parameter-space region yielding a strongly FOEWPT, already covering the entire region accessible via GW observations by LISA. We also analyse the connection between a FOEWPT and a large enhancement of the 125 GeV Higgs-boson self-coupling with respect to its SM value [304, 305]. We show that probes of the Higgs boson self-coupling at the HL-LHC and particularly at the International Linear Collider (ILC) yield a very promising probe of FOEWPT scenarios in the 2HDM (and more broadly, in extended Higgs sectors).

This Chapter is organised as follows. In Sect. 5.1 we briefly discuss the finite temperature effective potential of the 2HDM, focusing on the implementation of the various constraints applied to the zero-temperature scalar potential. Our analysis of the cosmological evolution of the scalar vacuum in different regions of the 2HDM parameter space is then presented in section 8.2, and the connection with both GW production and collider phenomenology is discussed, providing a critical view on the interplay between these two.

This chapter is based on ref. [4].

5.1 The 2HDM: an overview

In this section we discuss several aspects of the 2HDM in connection with the material presented in the Chapters 3 and 4. Here we will mainly focus on the numerical tools utilised in the different steps of the analysis.

5.1.1 The zero-temperature 2HDM effective potential

Tree-level scalar potential In order to specify our notation and conventions we refer to Sect. 3.1.1, where the CP-conserving 2HDM tree-level scalar potential V_{tree} was given in (3.2).

Theoretical and experimental constraints The set of 8 independent input parameters,

$$t_\beta(:= \tan\beta) \ , \ m_{12}^2 \ , \ v \ , \ \cos(\beta-\alpha) \ , \ m_h \ , \ m_H \ , \ m_A \ , \ m_{H^\pm} \ , \tag{5.1}$$

is restricted by various experimental and theoretical constraints. To implement these in our analysis, we make use of several public codes. We scan the 2HDM parameter space with the code `ScannerS` [306, 307] in terms of the set of parameters shown in Eq. (5.1). `ScannerS` checks whether the parameter point under investigation is in agreement with perturbative unitarity, boundedness from below and vacuum stability at zero temperature. Concerning the experimental constraints, `ScannerS` also ensures that a parameter point is in agreement with bounds coming from flavour-physics observables [210] and electroweak precision observables (EWPO) [206, 207, 210].[1] In addition, we make use of `HiggsSignals` [308–311] and `HiggsBounds` [312–316] to incorporate bounds from measurements of the properties of the experimentally detected 125 GeV Higgs boson and searches for additional scalar states, respectively. The required cross sections and branching ratios of the scalars have been obtained with the help of `SusHi` [317] and `N2HDECAY` [318], respectively.

One-loop effective potential and renormalisation conditions At one-loop, the effective potential V_{eff} for the 2HDM is given by

$$V_{\text{eff}} = V_{\text{tree}} + V_{\text{CW}} + V_{\text{CT}} \,, \tag{5.2}$$

where V_{tree} is the 2HDM tree-level potential given in Eq. (3.2), V_{CW} represents the CW potential in the $\overline{\text{MS}}$ renormalisation prescription given in Eq. (4.43). V_{CT} contains the UV-finite counterterm contributions that were shown in Eq. (4.44), and that were defined by imposing the OS renormalisation conditions given in Eqs. (4.45) and (4.46). To compute the finite set of counterterms, we made use of the public code `BSMPT` [319, 320]. In the 2HDM, the sum in the CW potential runs over the neutral scalars $\Phi^0 = \{h, \, H, \, A, \, G^0\}$, the charged scalars $\Phi^\pm = \{H^\pm, \, G^\pm\}$, the longitudinal and transversal gauge bosons, $V_L =$

---

[1] The check for the agreement with the EWPO (carried out on the basis of the oblique parameters) does not take into account the new measurement of the W-boson mass reported recently by the CDF collaboration [208], which is in significant tension with the SM predictions.

$\{Z_L,\, W_L^+,\, W_L^-\}$ and $V_T = \{Z_T,\, W_T^+,\, W_T^-\}$ and the SM quarks q and leptons ℓ. The degrees of freedom n_j for the species of each type are

$$n_{\Phi^0} = 1\,, \quad n_{\Phi^\pm} = 2\,, \quad n_{V_T} = 2\,, \quad n_{V_L} = 1\,, \quad n_q = 12\,, \quad n_\ell = 4\,.$$

The omission of ghost contributions is achieved by evaluating the Coleman-Weinberg potential in the Landau gauge.[2]

5.1.2 Scale dependence and perturbativity of scalar couplings

The renormalisation group evolution of the quartic scalar couplings λ_i can provide meaningful constraints on the viable region of the 2HDM parameter space, as emphasised in Sect. 4.1. We require that the $\lambda_i(\mu)$ remain below the perturbativity bound 4π for any value of the energy scale μ up to the physical scalar masses of the theory m_j, i.e. $\lambda_i(\mu) < 4\pi$ for $\mu \leq m_j$ $(\forall j)$. This provides a (minimal) theoretical consistency condition on the 2HDM parameter space in relation to renormalisation group evolution.

We have solved numerically the RGEs taking into account the one-loop and two-loop contributions to the β-functions of the model parameters computed with the help of the public code `2HDME` [322]. In order to obtain $\overline{\text{MS}}$ parameters $p^{\overline{\text{MS}}}$ (as required by `2HDME`) from our OS parameters p^{OS}, we refer to the transformation displayed in Eq. (4.56). We also stress that thermal effects, to be discussed in the next section, introduce the temperature of the system T as a relevant energy scale. Then, for the study of the scalar potential at temperatures substantially larger than the EW scale, $T \gg v$ (targeted towards the determination of whether the EW symmetry is restored in this limit, see section 4.2.3), we must also require $\lambda_i(\mu = T)$ to be perturbative.

5.2 The finite-temperature 2HDM effective potential

We now briefly comment on the addition of thermal corrections to the effective potential V_{eff}, which was discussed in detail in Sect. 4.1. The several phenomena which may occur in the thermal evolution of the vacuum configuration of a (multi-) Higgs potential were reviewed in Chapter 4: a FOEWPT (see Sect. 4.2.1), possibly with an accompanying stochastic signal of GW (see Sect. 4.3); the non-restoration of EW symmetry at high temperatures (see Sect. 4.2.3); and the trapping of the vacuum in an unbroken EW configuration (see Sect. 4.2.2).[3]

With the inclusion of thermal corrections, the 2HDM (finite-temperature) one-loop effective potential with daisy-resummation reads

$$V_{\text{eff}} = V_{\text{tree}} + V_{\text{CW}} + V_{\text{CT}} + V_{\text{T}} + V_{\text{daisy}}\ . \tag{5.3}$$

---

[2] Discussions on the gauge dependence of the effective potential in the context of the electroweak phase transition can be found in Refs. [243, 247, 278, 321].

[3] We refer to Chapter 6 and to Refs. [279]–[281] for other analyses on vacuum trapping and EW SnR in 2HDMs.

with V_{tree}, V_{CW} and V_{CT} specified in Sec. 5.1, and V_T and V_{daisy} given in Eqs. 4.47 and 4.53, respectively. Besides the degrees of freedom considered in the CW potential and specified in Sec. 5.1, the sum in V_T includes the photon, which acquires an effective thermal mass at finite temperature (and therefore must be included in the sum in spite of being massless at $T = 0$). In V_{daisy}, the sum in Eq. (4.53) runs over all the fields $\phi \in \{\Phi^0, \Phi^\pm, V_L, \gamma_L\}$, where γ_L is the longitudinal polarisation of the photon, which acquires a mass at finite temperature. The thermal squared masses Π_i^2 have been obtained as in Ref. [244]. We used the public code `CosmoTransitions` [196]) to analyse the thermal evolution of the effective potential V_{eff}.

5.3 2HDM thermal history and phenomenological implications

In this section we study the thermal history of the 2HDM regarding a FOEWPT and the associated production of GWs, as well as the occurrence of vacuum trapping and/or EW SnR. We analyse how these can yield meaningful constraints on the parameter space of the 2HDM, and we discuss the potential complementarity between colliders searches and GW probes with LISA.

The FOEWPT in the CP-conserving 2HDM has been extensively studied (see Refs. [39, 145, 146] for analyses that include a calculation of the nucleation temperature). The usual scenario that features such a first-order transition requires relatively large quartic couplings, which subsequently implies sizeable splittings among the scalar masses and/or between these masses and the overall (squared) mass scale of the second doublet, $M^2 = m_{12}^2/s_\beta c_\beta$ [39, 172]. In this work we focus on the 2HDM with type II Yukawas, for which stringent limits arising from flavour observables constrain the mass of the charged states to be $m_{H^\pm} \gtrsim 600$ GeV [210]. This requirement in conjunction with the constraints from electroweak precision observables favors the degeneracy of the masses of the heavy pseudoscalar and the charged scalar, $m_A \sim m_{H^\pm}$. In order to explore the parameter space of the 2HDM taking into account these considerations, we have scanned the parameter space of the CP-conserving type II 2HDM over the following ranges of the input parameters,

$$\begin{gathered} t_\beta = 3 \ , \quad m_{h_1} = 125.09 \text{ GeV} \ , \quad 200 \text{ GeV} \leq m_H \leq 1 \text{ TeV} \ , \\ 600 \text{ GeV} \leq m_A = m_{H^\pm} \leq 1.2 \text{ TeV} \ , \quad \cos(\beta - \alpha) = 0, \quad M^2 = \frac{m_{12}^2}{s_\beta c_\beta} = m_H^2 \ . \end{gathered} \tag{5.4}$$

Using `ScannerS`, we have generated 10k 2HDM parameter points within the above ranges, passing all the theoretical and experimental constraints discussed in section 5.1.1. In a second step, we have analysed the thermal history of each of these 10k benchmark points with `cosmoTransitions` [196], exploring the temperature range $[0, 700 \text{ GeV}]$. We have studied the temperature dependence of the minima of the one-loop effective potential V_{eff} from Eq. (5.3) in terms of the two CP-even neutral fields $(\rho_1(T), \rho_2(T))$. We then have computed the tunneling rate defined in Eq. (4.58) between coexisting minima at finite temperature, evaluating whether the criterion from Eq. (4.60) is met and a FOEWPT takes place.[4]

In section 5.3.1, we explore the different thermal histories that the CP-conserving 2HDM features within our parameter scan, which targets the regions where a FOEWPT is realised, as well as the vicinity of such regions. As mentioned before, a FOEWPT in the 2HDM strongly favours sizeable values of the quartic couplings, and we complement this analysis with a study of the energy scale dependence of the quartic couplings. We stress the rich variety of phenomena that arise within this parameter space region, and investigate in particular the effects of vacuum trapping and EW SnR. The analysis of the 2HDM thermal history will allow us to determine the regions of the parameter space in which the strongest FOEWPT can be realised in the type II 2HDM, and to assess how strong such transitions are. In section 5.3.2 we analyse the GW signals that are produced during the phase transitions. We will compare the predicted GW signals to the expected LISA sensitivity in order to assess whether such signals could be detectable at LISA. Finally, in section 5.3.3 we compare the prospects of a GW detection at LISA with the collider phenomenology of the corresponding 2HDM parameter regions in order to address the question whether those regions could also be probed in a complementary way by (HL-)LHC searches.

5.3.1 The cosmological evolution of the vacuum in the 2HDM

In this section we will investigate possible realisations of non-standard cosmological histories in the 2HDM. Even though the motivation for the analysed parameter plane was its suitability for the occurrence of FOEWPTs, as described above, we point out that the considered parameter space also features a rich variety of thermal histories in terms of the patterns of symmetry breaking and symmetry restoration.

Before we start the discussion of the 2HDM cosmological history, we briefly inspect the additional constraints from the RGE running of the parameters, that we have applied in order to restrict the analysis to parameter benchmarks for which our perturbative analysis is applicable. Since we are interested in FOEWPTs, we explore a parameter space region where relatively large quartic couplings are present. A key check on the validity of our perturbative calculation of the quantities that characterise the FOEWPT is to make sure that at the energy scales relevant for our analyses the values of the couplings remain in the perturbative range $|\lambda_i| < 4\pi$ (see section 5.1.2 for details). In Fig. 5.1 we show the analysed parameter space in the (m_H, m_A) plane of the 2HDM of type II as specified in Eq. (5.4). For each point we indicate the energy scale $\Lambda_{4\pi}$ at which one of the 2HDM quartic couplings reaches the naive perturbative bound 4π. The lower-right corner in which no points are shown is excluded from the requirement on the tree-level potential to be bounded from below, imposed via `ScannerS`.[5] In the lower right strip we find points

---

[4] We do not take into account the possibility of CP-breaking or charge-breaking minima at finite temperature.

[5] Such parameter points could still feature a bounded potential upon inclusion of loop corrections [202]. We did not include this possibility in our analysis because we focus here on the thermal evolution of the

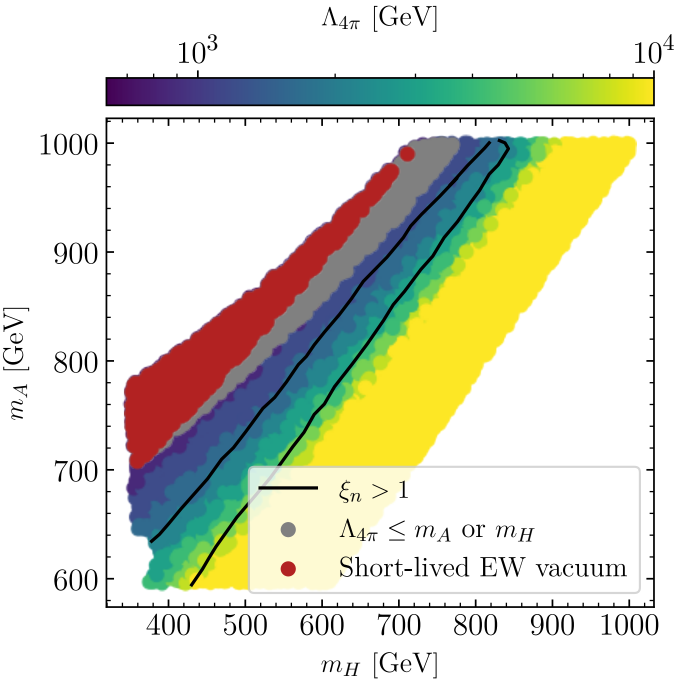

Figure 5.1: Constraints from perturbativity and vacuum stability, and region featuring a strong FOEWPT in the plane of the mass of the heavy CP-even scalar m_H and the masses of the CP-odd scalar and the charged scalars $m_A = m_{H^\pm}$ in the type II 2HDM, with the other parameters specified in Eq. (5.4). The displayed points pass all the theoretical and experimental constraints discussed in section 5.1.1. The colour bar indicates the energy scale $\Lambda_{4\pi}$ at which one of the quartic couplings of the parameter point reaches the naive perturbative bound 4π (for points with $\Lambda_{4\pi} < 10$ TeV). Points with $\Lambda_{4\pi} < m_A$ or m_H are indicated in gray, and points with a short-lived EW vacuum are shown in red. Yellow points feature $\Lambda_{4\pi} \geq 10$ TeV. The black line circumscribes all the points that feature a strong FOEWPT (see text for details).

with $\Lambda_{4\pi} \geq 10$ TeV, which are indicated in yellow. On the other hand, we find that a large part of the parameter space that is allowed by the constraints discussed in section 5.1.1 features relatively low values for $\Lambda_{4\pi}$, smaller than 10 TeV. This feature arises as a consequence of the sizeable values of the quartic couplings λ_i at the initial scale $\mu_0 = v$ that are required to achieve large splittings among the scalar masses, as described in section 5.3. In particular, our scan contains points for which $\Lambda_{4\pi} < m_A = m_{H^\pm}$ or $\Lambda_{4\pi} < m_H$, which are shown in gray in Fig. 5.1. Since for these points the perturbativity bound is reached for an energy scale that is lower than one of the involved masses, we regard such a situation as unphysical. Accordingly, we consider this parameter region as excluded and will not analyse it further. As will be discussed below, this region exclusively features scenarios where the global minimum of the potential at $T = 0$ is the origin of field space. Consequently, this

---

potential. Including the boundedness check for the loop-corrected scalar potential at zero temperature is computationally much more expensive compared to the application of the tree-level conditions which were determined in compact analytical form [201].

additional constraint does not exclude parameter points that otherwise would predict a FOEWPT. Furthermore, we verified that a subset of points with $\Lambda_{4\pi} < m_A = m_{H^\pm}$ or $\Lambda_{4\pi} < m_H$ features a short-lived EW minimum, i.e. the probability for quantum tunnelling from the EW minimum into the deeper minimum (the origin of field space) in this case is such that it gives rise to a lifetime of the EW vacuum that is substantially smaller than the age of the universe.[6] The points with a short-lived EW vacuum are shown in red in Fig. 5.1. Finally, all the points that feature a strong FOEWPT in Fig. 5.1 are circumscribed by a solid-black line. The strong FOEWPT region is characterised by

$$\xi_n = \frac{v_n}{T_n} > 1, \tag{5.5}$$

where v_n is the vev in the minimum adopted by the universe at the nucleation temperature T_n. We stress that for values of ξ_n substantially smaller than 1 it becomes numerically impossible to distinguish between a first- and a second-order phase transition in a perturbative analysis, and such a distinction would then require to take into account non-perturbative effects [40, 323].

We now discuss the different kinds of symmetry-breaking patterns that occur in the analysed parameter space. In the upper plot of Fig. 5.2, we indicate six qualitatively distinct zones of the (m_H, m_A) plane of the 2HDM of type II shown in Fig. 5.1, labelled by A, B, C, D, E and F (as discussed above, in our analysis we regard the gray/red points as excluded). Each of the six zones features a different temperature evolution of the vacuum configuration of the 2HDM Higgs potential. The red line divides the mass plane into two regions. The points above and to the left of the red line feature at $T = 0$ a global minimum at the origin of field space, whereas those below and to the right of the red line have the EW minimum as global minimum at $T = 0$. The different zones in the upper plot of Fig. 5.2 are analysed individually in the six plots shown in the lower part. These plots indicate the typical temperature dependence of the minima of the potential for each of the six labelled regions (where the specific point is taken where the label is located). The six benchmark points have been analysed with `cosmoTransitions` up to a temperature $T_{\text{max}} = 550$ GeV. The blue lines indicate the temperature evolution of $v_{\text{min}} \equiv \sqrt{v_1^2 + v_2^2}|_{\text{min}}$ evaluated at the minimum where the electroweak symmetry is broken. The absence of a blue line for a given temperature indicates that no EW symmetry breaking minimum exists at this temperature. The orange line shows the temperature dependence of the minimum located at the origin of field space. The absence of this line for a given temperature shows that there is no (local or global) minimum at the origin of field space. The vertical dashed-red lines show the temperature at which the two minima involved in the transition are degenerate, i.e. the critical temperature. The label "origin" corresponds to a range of temperatures where

---

[6] The calculation of the lifetime of the EW vacuum relies on the computation of the four-dimensional euclidean bounce action instead of the three-dimensional bounce action that determines the decay rate of the false vacuum at finite temperature. It should also be noted that in the scenario investigated here the presence of the global minimum in the origin only arises at the loop level, such that a tree-level analysis of the EW vacuum stability would not be sufficient here.

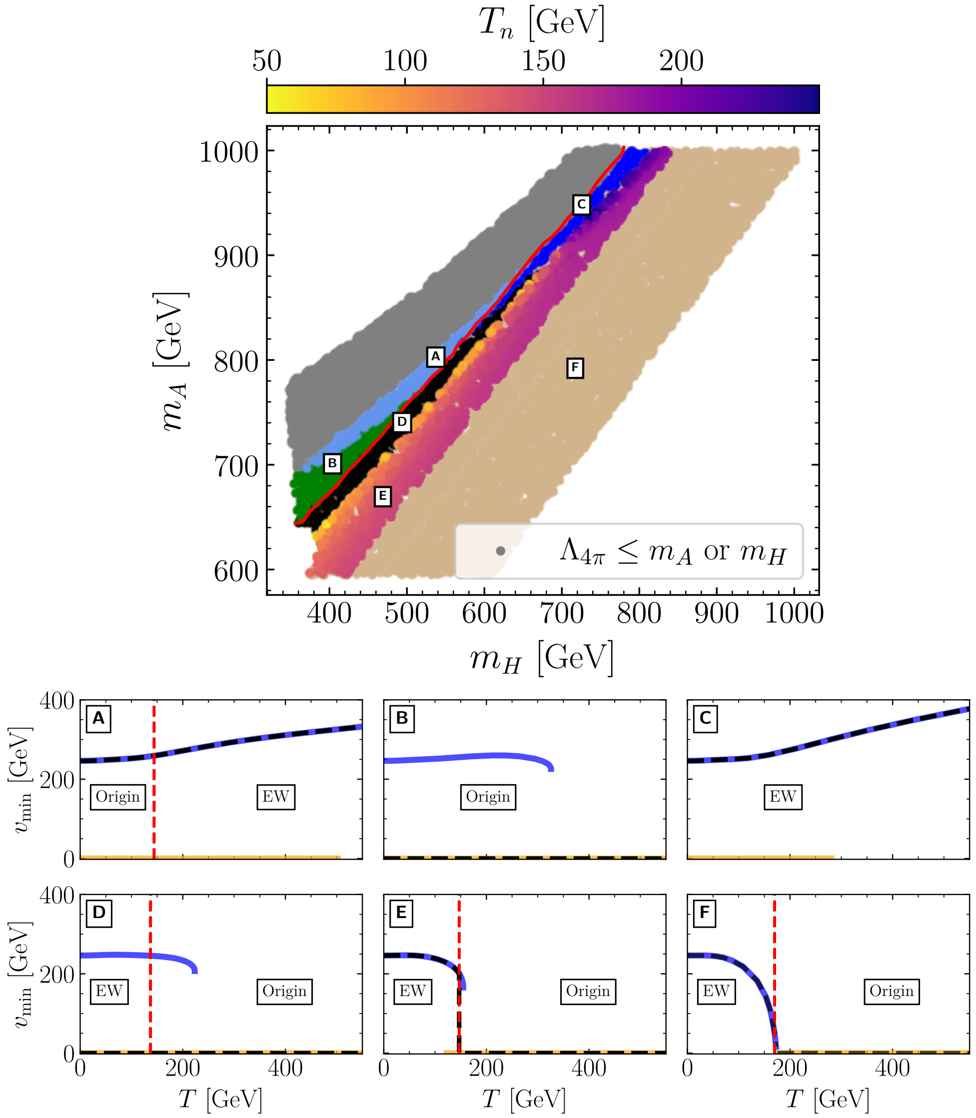

Figure 5.2: Top: The parameter plane as shown in Fig. 5.1, with zones featuring qualitatively different thermal histories of their vacuum structure labelled as A, B, C, D, E and F. The red line separates the region with a zero-temperature global minimum at the origin of field space (left) from the region with a zero-temperature electroweak global minimum (right). Bottom: characteristic temperature dependence of v_{min} for the local minima of the potential for each of the six labelled regions. The blue lines indicate the temperature evolution of v_{min} evaluated at the minimum where the electroweak symmetry is broken. The orange lines denote how the minimum where the electroweak symmetry is unbroken evolves. The dashed black lines show the vacuum configuration adopted by the universe taking into account phase transitions between co-existing minima. The vertical red lines show the critical temperature, and the labels "origin" and "EW" indicate the global minimum of the potential.

the origin is the global minimum of the potential, and "EW" indicates a global minimum where the EW symmetry is broken. Taking into account the possible transitions between coexisting minima, the dashed-black line indicates the temperature dependence of the vev actually adopted by the universe for each of the benchmark scenarios.

The parameter points with a zero-temperature global minimum at the origin, i.e. the points on the upper left of the red line, are classified into two different zones (A and B). We find that a zero-temperature vacuum stability analysis would allow those points as they all feature meta-stable EW minima whose lifetime is compatible with the age of the universe. The benchmark point belonging to zone A has an EW-broken minimum for the entire temperature range explored, whereas a minimum at the origin only appears for temperatures below $T \sim 500$ GeV. Consequently, the adopted vacuum configuration at high temperature is the one breaking the EW symmetry, and zone A features EW SnR at high temperature. This implies that the breaking of the EW symmetry in the early universe would have taken place at temperatures substantially above the EW scale (in particular $T > T_{\text{max}}$). Such a high value of the transition temperature can have profound consequences in the context of EW baryogenesis and the related phenomenology at colliders or other low-energy experiments searching for CP-violating effects. In view of those features and of the existing limits on BSM physics around the EW scale at the LHC, the proposal of EW *high-scale* baryogenesis has gained attention in recent years [1, 47–50, 281, 324–326]. Based on the perturbative treatment of the effective potential, we find in this work that the 2HDM, or more broadly speaking extensions of the SM containing a second Higgs doublet, could feature EW SnR and possibly allow for EW baryogenesis at energy scales much higher than the EW scale. On the other hand, for the benchmark scenario belonging to zone B, the only existing minimum at T_{max} is the minimum at the origin, i.e. the EW symmetry is restored at the maximum temperature that we have analysed. The broken phase appears for temperatures below $T \sim 325$ GeV, but never becomes deeper than the minimum at the origin, which remains the global minimum for all T. A phase transition into the broken phase is not possible, and the EW symmetry is preserved as the temperature approaches zero. Consequently, this parameter region is regarded as unphysical and therefore excluded.

Now we turn to the analysis of the parameter space region that features a global EW minimum at $T = 0$, located on the lower right side of the red line in the upper plot of Fig. 5.2. Here we identify four qualitatively different zones depending on their thermal histories (C, D, E, F). For the benchmark point of region C, an EW symmetry breaking minimum exists already at T_{max}, whereas no minimum of the potential at the origin exists at this temperature. Consequently, this zone exhibits EW SnR at high temperature. The EW minimum is always deeper than the one at the origin, which for our chosen benchmark within this region appears for temperatures below $T \sim 280$ GeV, such that no transition to the minimum at the origin can occur, and the parameter points in this region are, at least in principle, not excluded (in order to definitely determine whether such points are physically viable, one would require a detailed analysis of the behaviour of the scalar potential at even higher temperatures).

Region D features the phenomenon of vacuum trapping. In the benchmark scenario shown in plot D, the EW symmetry is restored at high temperature, and the EW phase appears for temperatures below $T \sim 225$ GeV. Even though a critical temperature exists in this scenario, the condition Eq. (4.62) is never satisfied, and as a consequence the universe remains trapped in a false vacuum at the origin as $T \to 0$. This parameter region is therefore not phenomenologically viable and has to be excluded. The possibility of vacuum trapping in the thermal history of the universe and its phenomenological implications will be further discussed in section 5.3.2.

All the points in region E feature a strong FOEWPT, where the quantity ξ_n meets the condition (5.5). The plot E exemplifies the typical temperature dependence of the vacuum configuration for one of such parameter points. In this benchmark scenario, the EW symmetry is restored at T_{max}. The EW minimum appears for temperatures below $T \sim 155$ GeV, and a strong FOEWPT takes place at a nucleation temperature $T_n \approx 140$ GeV. The nucleation temperatures for all points in zone E are given by the colour coding in the upper plot of Fig. 5.2. In region E gravitational wave signals that are sufficiently strong to be detected by LISA could potentially be generated. In section 5.3.2, we will discuss zone E regarding the possible detectability of such GW signals by LISA.

Finally, the points in zone F feature either a weak FOEWPT with $\xi_n < 1$ or a second-order EW phase transition.[7] The plot F shows a specific benchmark in this region with a second-order phase transition (or a very weak FOEWPT) taking place at $T \sim 170$ GeV. At low temperature the minimum adopted by the universe breaks the EW symmetry, whereas the minimum adopted at high temperature is located at the origin of field space and therefore the EW symmetry is restored.

To summarise the above discussion, taking into account the requirement that the universe has to reach the correct minimum that breaks the EW symmetry at zero temperature has shown that the regions B and D are unphysical and have to be excluded.

5.3.2 Phenomenological consequences of vacuum trapping

Vacuum trapping, as outlined in section 4.2.2, corresponds to the situation where the universe remains trapped in an EW symmetric phase while it cools down, even though a global EW symmetry breaking minimum of the potential exists at zero temperature. The potential in this case is such that Eq. (4.62) is never fulfilled at any temperature at which the EW symmetry breaking minimum is deeper than the minimum at the origin.[8] Several recent analyses [1, 145, 279] have noted the importance of this phenomenon for the phenomenology of models with extended Higgs sectors, in particular regarding the possibility of a FOEWPT, the realisation of EW baryogenesis, or the production of a

---

[7] The numerical precision of the calculation of ξ_n is not sufficient to distinguish between a very weak FOEWPT, $\xi_n \ll 1$, and a second-order EW phase transition, but for the purpose of our analysis such a distinction is of no phenomenological relevance anyway.

[8] We stress that in the 2HDM analysis presented in this chapter we did not encounter vacuum trapping in any false minimum other than the one located at the origin.

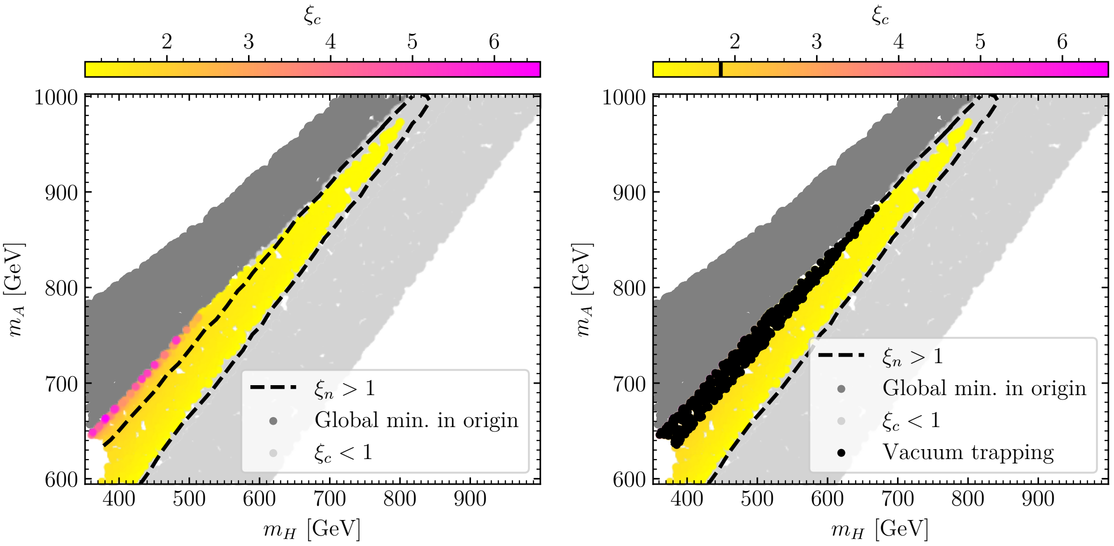

Figure 5.3: The parameter plane as shown in Fig. 5.1, where the points shown in light gray feature a second-order EW phase transition or a FOEWPT with $\xi_c < 1$, whereas for the dark gray points the global minimum is in the origin (corresponding to the area of the gray points and the zones A and B in Fig. 5.2), and accordingly the points do not feature an EW phase transition within the investigated temperature range. The coloured points feature a critical temperature T_c at which the EW minimum becomes the global one, where the colour coding of the points indicates the value of ξ_c. The dashed black line circumscribes all points that feature a FOEWPT with $\xi_n > 1$. In the right plot the black points indicate the parameter region that is excluded as a consequence of vacuum trapping, and the vertical black line in the colour bar indicates the maximum value of ξ_c that is found after the incorporation of the constraint from vacuum trapping.

stochastic GW background. As we will show in the following, taking into account the constraints from vacuum trapping has an important impact on the prospects for probing parameter regions featuring such phenomena at particle colliders. We start with an analysis of the implications of vacuum trapping for parameter regions in which EW baryogenesis could occur. Afterwards we discuss the impact of vacuum trapping on the possibility of generating GW spectra during a FOEWPT in the 2HDM with a sufficient amplitude to be detectable at future GW observatories.

Implications for electroweak baryogenesis

Although the LHC has set important limits on the presence of additional Higgs bosons at the EW scale, the 2HDM remains compatible with those limits as a viable framework for the explanation of the matter–antimatter asymmetry of the universe by means of EW baryogenesis [39]. In addition to new sources of CP-violation that can be present in the 2HDM compared to the SM, another vital ingredient for the realisation of baryogenesis is the presence of a strong FOEWPT. In the following, we will focus on the criterion of a

FOEWPT.[9] As an indicator of the presence of a FOEWPT that is sufficiently strong for allowing the generation of the observed matter–antimatter asymmetry, the criterion

$$\xi_c = \frac{v_c}{T_c} > 1, \tag{5.6}$$

has often been used in the 2HDM and extensions thereof [172, 244, 245, 302, 303, 327–333]. Here v_c is the vev in the EW symmetry breaking minimum at the critical temperature T_c, and ξ_c is denoted as the *strength* of the transition. This so-called baryon number preservation criterion [243] (see also Ref. [236] and references therein) yields a condition for avoiding the wash-out of the baryon asymmetry after the EW phase transition. However, in parts of the literature it is also used as a sufficient requirement for the presence of a FOEWPT via the existence of the critical temperature T_c at which the EW minimum becomes the global minimum. In contrast to this, we will show in this section that the criterion of Eq. (5.6) is not a reliable indicator of the occurrence of a FOEWPT in the 2HDM (see also Ref. [243]). As analysed below, instead the calculation of the nucleation (or transition) temperature with the help of Eq. (4.62) is crucial, not only in order to assess the actual strength of the FOEWPT which happens at temperatures $T_* \sim T_n < T_c$, but more importantly to determine whether the FOEWPT takes place at all. The nucleation criterion shown in Eq. (4.62) should then be used in order to accurately determine the 2HDM parameter space that reaches the EW vacuum configuration at zero temperature as a result of a FOEWPT, whereas a criterion based on the existence of T_c would include also parameter space regions that are unphysical due to the occurrence of vacuum trapping.

In Fig. 5.3 we show the parameter scan points in the (m_H, m_A) plane, where the colour coding indicates (both for left and right plots) the values of ξ_c for parameter points for which $\xi_c > 1$. According to several existing analyses (see the discussion above) these points would be classified as featuring a strong FOEWPT that could generate the observed baryon asymmetry of the universe. The dark gray points in Fig. 5.3 correspond to the region with a zero-temperature global minimum at the origin of field space (corresponding in Fig. 5.2 to the combined area of the gray points and of the zones A and B). These points are thus not relevant for the present analysis (being either unphysical or featuring EW SnR up to the highest temperatures analysed in our scan). The light gray region depicts parameter points that, while featuring a zero-temperature global EW minimum, do not meet the condition imposed on the strength of the transition based on T_c, see Eq. (5.6). The dashed black line circumscribes the points that meet the more appropriate requirement for a strongly FOEWPT based on T_n, defined in Eq. (5.5) (coinciding with the solid black line in Fig. 5.1 and the zone E in Fig. 5.2). Fig. 5.3 - left shows that the region with highest values of ξ_c (corresponding to the pink points) lies at the border with the dark gray region, and features transition strength values up to $\xi_c \sim 6$, which would be particularly well suited for EW baryogenesis. However, taking into account the constraint from vacuum trapping (zone D in Fig. 5.2), indicated by the black points in Fig. 5.3 - (right), one can see that

---

[9] We assume that the required sources of CP violation do not have an impact on the dynamics of the phase transition and can therefore be neglected in our analysis.

the parameter region featuring the highest ξ_c values is in fact excluded as a consequence of vacuum trapping. After taking into account this constraint, the maximum allowed value for ξ_c is $\xi_c \sim 1.8$ (instead of $\xi_c \sim 6$), indicated by a vertical black line inside the colour bar on the right plot of Fig. 5.3. At the same time, Fig. 5.3 highlights that vacuum trapping not only has a strong impact on the maximum values of ξ_c that can be achieved in the physically viable parameter regions, but it is also crucial for determining the 2HDM parameter region that does feature a FOEWPT: the constraint from vacuum trapping excludes the parameter region in Fig. 5.3 - (left) with the largest values for the mass splitting $m_A - m_H$ for a fixed value of m_H. This has important consequences for the prospects of probing 2HDM scenarios featuring a strong FOEWPT at current and future colliders. For instance, the cross section for the LHC signature $pp \to A \to ZH$ (which would indicate the existence of such a strong FOEWPT in the 2HDM [39, 172, 302]) depends on the mass splitting between A and H, since the branching ratio for the decay $A \to ZH$ grows with increasing mass splitting. The constraint from vacuum trapping can then place an upper limit on the cross section for such $A \to ZH$ signature within the 2HDM (see e.g. [145]). A more detailed discussion on the collider phenomenology of the parameter region with a FOEWPT will be given in section 5.3.3.

Finally, we point out that the black-dashed line in Fig. 5.3, defined by the criterion $\xi_n > 1$, circumscribes also light-gray points at the upper end of the m_A, m_H mass ranges considered here. Thus, in this mass region we find parameter points that feature strongly FOEWPTs based on the transition strength evaluated at T_n, but would not satisfy the corresponding criterion for avoiding the wash-out of the baryon asymmetry evaluated at T_c. As a consequence, the criterion based on T_n allows for larger values of m_A and m_H compared to the (potentially misleading) criterion based on T_c.

Gravitational waves

As discussed in section 4.3, a cosmological FOEWPT can produce a stochastic GW background that could be observable by the future LISA GW interferometer. We now analyse the production of GWs from a FOEWPT in the 2HDM, discussing the quantities T_*, α, β/H and v_w and studying the prospects for the detection of the GW signals at LISA. We will specifically show how the phenomenon of vacuum trapping puts severe limitations on the GW SNR achievable at LISA in the 2HDM.

We first discuss briefly the dependence on the bubble wall velocity v_w. In Fig. 5.4 we show, for different values of v_w, the predictions for the GW spectrum of a specific 2HDM benchmark point with BSM scalar masses $m_H = 419.33$ GeV and $m_A = m_{H^\pm} = 663.05$ GeV, yielding a FOEWPT at a temperature of $T_n = 52.43$ GeV with $\alpha = 0.172$ and $\beta/H = 26.2$. The solid lines correspond to the predictions for $h^2\Omega_\mathrm{GW}$ omitting the contribution from turbulence in the plasma, whereas the dashed lines include such contribution. Fig. 5.4 also shows the LISA nominal sensitivity obtained from its noise curve (see section 4.3 for details). The bubble wall velocity has a strong impact on the GW spectrum, shifting the position of the peak of the GW signal and significantly modifying its amplitude. These translate

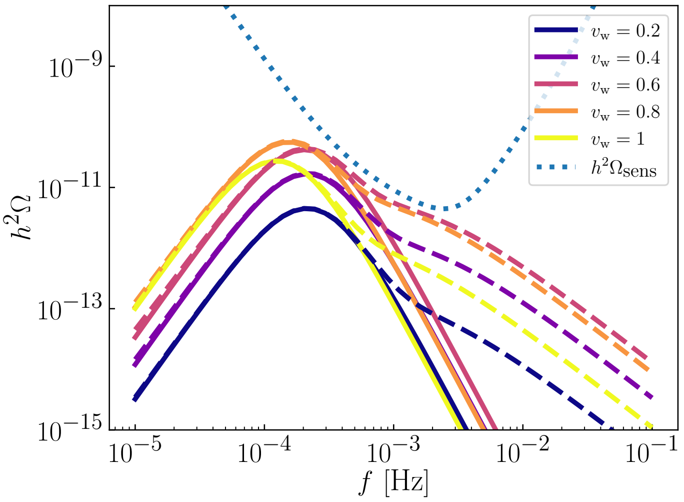

Figure 5.4: GW spectrum for a 2HDM benchmark point with BSM scalar masses $m_H = 419.33$ GeV and $m_A = m_{H^\pm} = 663.05$ GeV, yielding a FOEWPT with $T_n = 52.43$ GeV, $\alpha = 0.172$ and $\beta/H = 26.2$. $h^2\Omega_{\rm GW}$ predictions for different bubble wall velocity values ($v_{\rm w} = 0.2, 0.4, 0.6, 0.8, 1$) are shown in different colours for the concave curves. The dotted curve indicates the nominal sensitivity of LISA to stochastic sources, $h^2\Omega_{\rm sens}$. Solid lines omit the turbulence contribution to $h^2\Omega_{\rm GW}$, included in the dashed lines.

$v_{\rm w}$	turb.	no turb.
0.2	23	18
0.4	149	67
0.6	522	153
0.8	431	101
1	70	28

Table 5.1: LISA SNR of the GWs for the 2HDM benchmark scenario shown in Fig. 5.4 for different values of the bubble wall velocity $v_{\rm w}$ taking into account the effect of turbulence as a source of GWs ("turb.") and neglecting it ("no turb.").

into a large variation of the SNR at LISA (assuming a duration of the LISA mission $\mathcal{T} = 7$ years) for different values of $v_{\rm w}$, as shown in Table 5.1. Both with and without the inclusion of turbulence, the highest SNR occurs for $v_{\rm w} \sim 0.6$. This is fairly generic in the 2HDM (not particular to the benchmark chosen for illustration), and we thus use $v_w = 0.6$ for the predictions of the GW signals in the rest of this work.

In Fig. 5.5 we show the values of the inverse duration of the phase transition β/H in dependence of the strength α for all the points in our random scan satisfying $\xi_n > 1$ (region E in Fig. 5.2). The colour code indicates the value of the SNR at LISA (for $v_w = 0.6$ and a LISA mission duration $\mathcal{T} = 7$ years). As expected, the points with the largest values of α

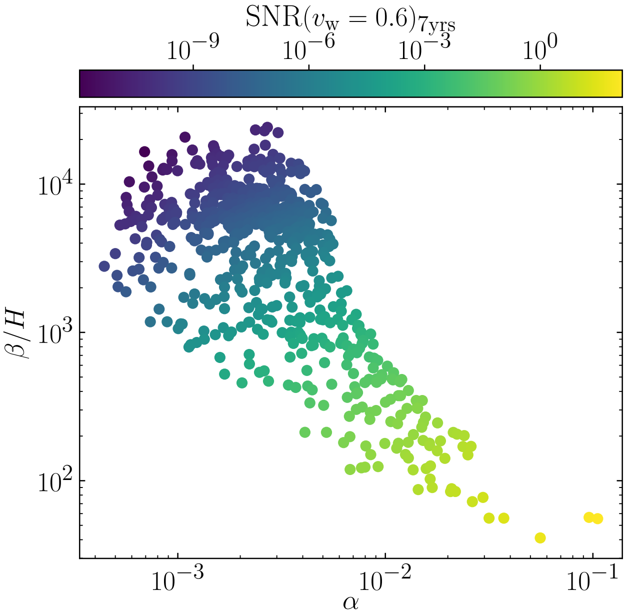

Figure 5.5: Parameter points of the scan shown in Fig. 5.1 in the (α, β/H) plane, with the colour-code indicating the SNR at LISA (assuming $v_\mathrm{w} = 0.6$ and $\mathcal{T} = 7$ years).

and the smallest values of β/H feature the largest SNRs for LISA. The SNR values range over several orders of magnitude for relatively small changes in the values of the masses m_H and m_A, as will be shown below. This is a consequence of the strong sensitivity of the predicted GW spectra to the underlying 2HDM model parameters (specifically, the BSM scalar masses).[10] We also note that the strongest GW signals are concentrated in a very narrow region of the (m_H, m_A) mass plane adjacent to the parameter space featuring vacuum trapping, and thus only a very small fraction of the 2HDM neutral BSM mass plane could be probed by LISA.

To explore in detail the region of parameter space where the strongest GW signals are present, we have performed a linear regression of the points featuring SNR $\gtrsim 0.5$, which are effectively found along a line given by $m_A = a\, m_H + b$, with $a = 0.87$ and $b = 295$ GeV. We have then performed a finer scan of the regions adjacent to this line along parallel lines in the m_H-m_A plane by shifting the value of b in steps of 1 GeV, i.e. for $b \in \{291, 292, 293, 294, 295, 296, 297\}$ GeV. The results of this dedicated, finer scan can be seen in Fig. 5.6, where we show the GW SNR at LISA in dependence of the mass difference $\Delta m \equiv m_A - m_H$ (we recall that we set $m_A = m_{H^\pm}$ and $M = m_H$ throughout this work). The colour code indicates the value of m_H. Bearing in mind the large uncertainties of the predictions for the GW signal from a FOEWPT, as discussed in section 4.3, we consider as potentially detectable by LISA any SNR of $\mathcal{O}(1)$, and mark the corresponding (indicative) threshold SNR = 1 in Fig. 5.6 as a horizontal dashed-red line. The largest SNR values that

---

[10] Such strong sensitivity has already been observed in Ref. [39] (see, for instance, Fig. 3 therein). Similar observations have been made in the triplet extension of the SM [334].

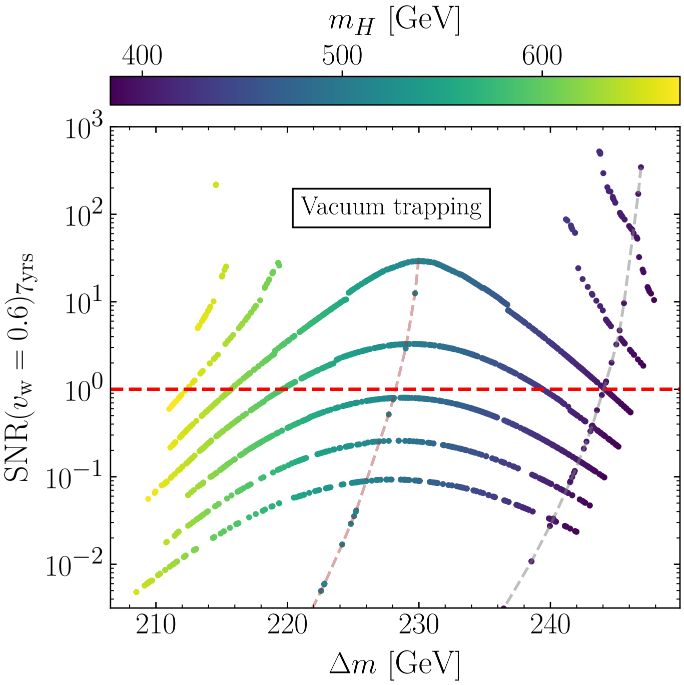

Figure 5.6: SNR at LISA (for $v_w = 0.6$ and $\mathcal{T} = 7$ years) against $\Delta m = m_A - m_H$ for the parameter points of the dedicated finer scan (see text) with $m_A = a\, m_H + b$, $a = 0.87$ and $b = \{291, 292, 293, 294, 295, 296, 297\}$. The colour coding of the points indicates the values of m_H.

we find in our finer scan are $\mathcal{O}(100)$ to $\mathcal{O}(1000)$ (such points could therefore be detected by LISA for $\mathcal{T} < 7$ years and/or with a substantially different assumption on v_w). For $b = 296$, 297 GeV, Fig. 5.6 shows a region ranging from $\Delta m \sim 215$ GeV to $\Delta m \sim 240$ GeV where the would-be points yielding the largest SNR values are found to be unphysical due to vacuum trapping (the corresponding lines of benchmarks in Fig. 5.6 are thus interrupted in this region). Large values of SNR are only found at the lower and the upper end of the Δm scan range, where the parameter points barely avoid vacuum trapping. In fact, a further would-be line of parameter points in Fig. 5.6 with $b = 298$ GeV is entirely excluded as a result of vacuum trapping.

In addition to the finer scan discussed above, we show in Fig. 5.6 the SNR resulting from scans with fixed value of m_H and increasing Δm, specifically, for $m_H = 400$ GeV (grey-dashed line in Fig. 5.6) and $m_H = 511$ GeV (brown-dashed line in Fig. 5.6). Both show the same features regarding vacuum trapping as discussed above. This whole analysis then demonstrates that the phenomenon of vacuum trapping severely limits the possibility of achieving large values of SNR at LISA from GW production in the 2HDM.

The strong dependence of the SNR on the 2HDM model parameters, pointed out at the beginning of this section and shown explicitly in Fig. 5.6, is related to the fact that the largest GW signals occur just at the border of the parameter space region in which the universe remains trapped in the false vacuum. To investigate this in more detail,

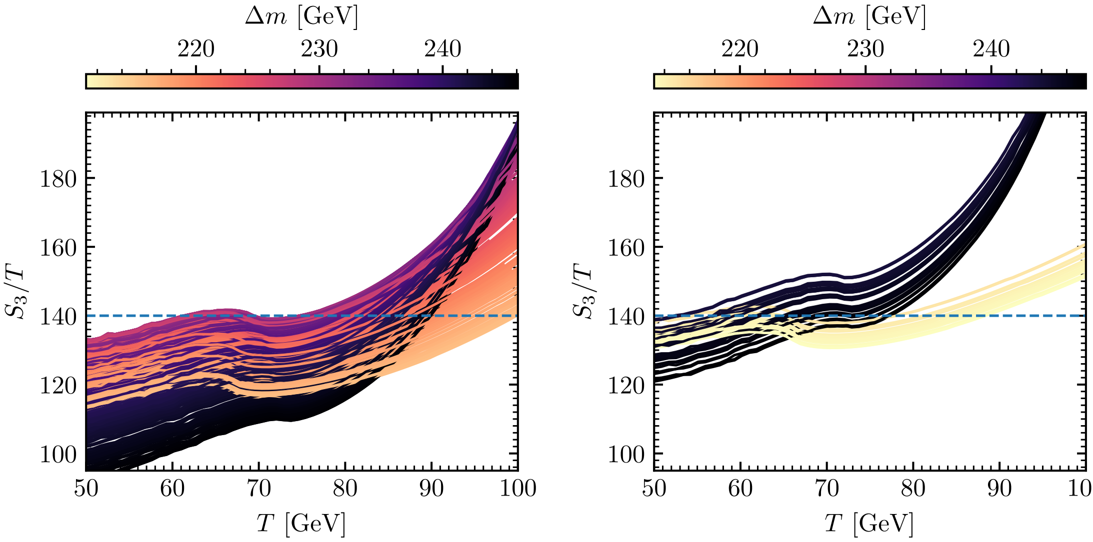

Figure 5.7: $S_3(T)/T$ as a function of T with the colour coding indicating the value of $\Delta m = m_A - m_H$. In the left plot, we show the results for scan points corresponding to $b = 295$ GeV in the dedicated scan of Fig. 5.6, whereas in the right plot we show the results for the $b = 297$ GeV line of points (which is interrupted at intermediate values of Δm due to the presence of vacuum trapping). The dashed blue horizontal line indicates $S_3(T)/T = 140$. The crossing of the lines for $S_3(T)/T$ with the dashed-blue line for decreasing T signals the onset of the phase transition at the respective temperature (see the nucleation criterion in Eq. (4.62)).

we depict in Fig. 5.7 the values of the bounce action over the temperature, $S_3(T)/T$ for temperatures lower than T_c, such that a FOEWPT can occur. In the left panel of Fig. 5.7 we show $S_3(T)/T$ for $b = 295$ GeV in our detailed scan from Fig. 5.6 (corresponding to the benchmark line in Fig. 5.6 with the largest values of SNR without featuring a gap as a consequence of vacuum trapping): bearing in mind that we assume the onset of the FOEWPT occurs for $S_3(T)/T \sim 140$ (recall the discussion in section 4.2.1), we see that the benchmarks in Fig. 5.7 - (left) with $\Delta m \sim 230$ GeV barely reach $S_3(T)/T \sim 140$, and are thus on the verge of being vacuum-trapped. In the right panel of Fig. 5.7, we show the corresponding values of $S_3(T)/T$ for the $b = 297$ GeV benchmark set, which features vacuum trapping for Δm in the approximate range [215, 240] GeV (as seen in Fig. 5.6). As a result, the lines in Fig. 5.7 - (right) are separated into two different bundles. The would-be lines in between these two bundles remain above $S_3(T)/T = 140$ (depicted as as dashed-blue line) over the whole temperature interval $0 < T < T_c$, reflecting vacuum trapping. In addition, many $S_3(T)/T$ lines have their minima just below the dashed-blue line. Since they are on the verge of vacuum-trapping, these lines become rather flat as they approach $S_3(T)/T = 140$, leading to a large variation of T_n (i.e. the temperature at which $S_3(T)/T \simeq 140$ is achieved) within a very small Δm range. As an example, for the black bundle of lines in Fig. 5.7 - (right) we have 243 GeV $< \Delta m <$ 247 GeV (only four GeV!), yet T_n varies in the range 52 GeV $< T_n <$ 77 GeV. At the same time, by comparing the two panels of Fig. 5.7 we observe that a very small change in b from our detailed scan, leads to

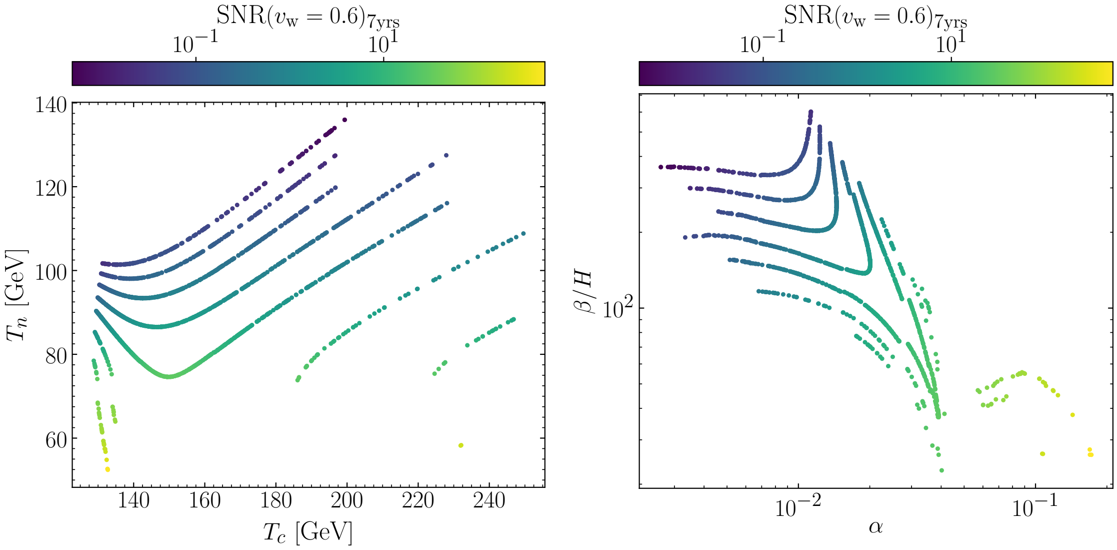

Figure 5.8: Parameter points of the dedicated finer scan of Fig. 5.6, in the (T_c, T_n) plane (left-panel) and in the $(\alpha,\ \beta/H)$ plane (right-panel), with the colour coding of the points indicating the SNR at LISA.

large variations of the T_n behaviour as a function of Δm. The very strong dependence[11] of T_n on subtle changes of the 2HDM masses then feeds into the GW spectra (e.g. $\alpha \sim 1/T_n^4$) and ultimately into the SNRs at LISA. As a result, values of SNR > 1 are found only in a very restricted region of the 2HDM parameter space, in the vicinity of the vacuum-trapping (unphysical) parameter region.

In Fig. 5.8 we explicitly show, for the detailed scan introduced in Fig. 5.6, the dependence of the LISA SNR on the quantities T_n, α and β/H. In Fig. 5.8 - (left), we show the relation between the nucleation temperature T_n and the critical temperature T_c for this scan (with colour-code indicating the SNR at LISA). The large difference between both temperatures for all the points in this scan reaffirms the necessity of computing the nucleation temperature to make reliable predictions concerning the FOEWPT properties in the 2HDM, since not even a qualitative description of the strength of the phase transition is possible based on the knowledge of the critical temperature. On the right panel of Fig. 5.8 we show the corresponding detailed scan points in the $(\alpha,\ \beta/H)$ plane, from which an intricate dependence of both parameters on the 2HDM masses can be inferred by correlating with

---

[11] We stress that the FOEWPT nucleation criterion used here, $S_3(T)/T = 140$, is only an approximation [26], and also the computation of the tunneling rate given by Eq. (4.58) suffers from sizable theoretical uncertainties from missing higher-order contributions (both in the prefactor $A(T)$, and in the perturbative formulation of V_{eff}, affecting S_3) as well as from the issue of gauge dependence [243]. Yet, such uncertainties only have a sizable impact on parameter points close to the vacuum-trapping region, whereas regions leading to weaker GW signals (i.e. not in the vicinity of the vacuum-trapping region) do not feature such large uncertainties in the SNR prediction. Thus, our conclusion that most of the parameter points with a FOEWPT do not give rise to a GW signal that could be observed at LISA is therefore robust even in view of these issues.

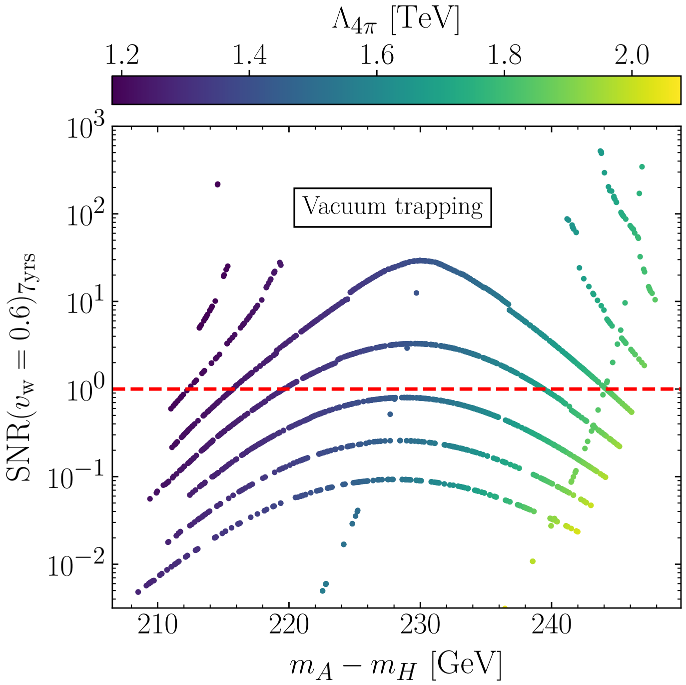

Figure 5.9: Parameter points of the dedicated finer scan of Fig. 5.6, in the $(\Delta m = m_A - m_H, \mathrm{SNR})$ plane, with the colour coding indicating the energy scale $\Lambda_{4\pi}$ at which one of the quartic couplings reaches the naive perturbative bound 4π.

the information on Fig. 5.6. Compared to the broader scan shown in Fig. 5.5, we find here a substantially smaller range of β/H (down to $\beta/H \sim 23$) and overall larger values of α (up to $\alpha \sim 0.17$). We stress here that values of $\beta/H \ll 100$ are an indicator of being close to featuring vacuum trapping (see e.g. the discussion in [263]).

Finally, we re-stress that a FOEWPT in the 2HDM requires sizable quartic scalar couplings λ_i for a potential barrier between the two minima involved in the transition to be generated via radiative and/or thermal loop corrections. The RGE evolution of such sizable quartic couplings can drive the theory into a non-perturbative regime already at energies not far from the TeV scale, as discussed in detail in section 5.1.2 (see also Ref. [335] for a one-loop analysis). This issue is most severe for the strongest phase transitions, such as the ones that produce GW signals with sizable SNR values at LISA. We then need to investigate the energy range in which the theory is well-defined for the type II 2HDM parameter regions that could yield an observable GW signal at LISA. In Fig. 5.9 we show the 2HDM parameter points of our detailed scan in the $(\Delta m = m_A - m_H$, SNR) plane, as in Fig. 5.6, but now with the colour-code indicating the energy scale $\Lambda_{4\pi}$ at which one of the quartic scalar couplings λ_i reaches the naive perturbative bound 4π (see section 5.1.2 for details). The value of $\Lambda_{4\pi}$ signals the energy scale μ at (or below) which new BSM physics should be present in order to avoid a Landau pole and render the theory well-behaved above that energy scale. We observe that the lowest values of $\Lambda_{4\pi}$ in our detailed scan are $\Lambda_{4\pi} \sim 1.2$ TeV, whereas the largest values are found slightly above $\Lambda_{4\pi} = 2$ TeV. By comparing with Fig. 5.6, we also observe that the smallest values of $\Lambda_{4\pi}$ correlate with the largest values of m_H in the scan, which can have important phenomenological implications (as we discuss in the next section). Altogether, Fig. 5.9 shows that parameter regions that feature a potentially detectable (SNR > 1) GW signal at LISA would require new-physics effects (e.g. new strongly coupled states) at energy scales that are well within the reach of the LHC, which calls for a critical assessment of the complementarity between LHC (and future collider) searches and GW probes with LISA in these theories.

5.3.3 Interplay between the LHC and LISA

As already outlined above, the 2HDM parameter regions featuring a GW signal potentially observable at LISA generally predict signatures of BSM physics within reach of the LHC, both from the presence of the 2HDM scalars themselves and from further new (strongly coupled) states that would be needed to prevent the appearance of a Landau pole close to the TeV scale. In this section, we focus on the collider signals of the 2HDM scalars, taking a critical view on the interplay between the possible observation of a stochastic GW signal from the 2HDM at LISA and LHC (and future collider) probes of the 2HDM states.

GWs at LISA vs. direct BSM searches at LHC

Given the projected HL-LHC and LISA timelines, the HL-LHC would scrutinise the 2HDM parameter space of relevance for GW searches before the LISA observatory will start taking data. We show that, within the type II 2HDM, the hypothetical absence of direct BSM signatures at the high-luminosity phase of the LHC would already exclude (to a very large extent) the prospects of observing a GW signal at LISA.

Among the possible collider signatures of the heavy 2HDM scalars, the most promising ones to probe the 2HDM parameter with a FOEWPT consist of Higgs cascade decays, due to the sizable mass splittings between the BSM Higgs bosons. Specifically, the production of the pseudoscalar A that then decays into a Z-boson and the heavy CP-even scalar H is a *smoking-gun* collider signature of FOEWPT scenarios in the 2HDM [172]. This signature has been searched for at the LHC with $\sqrt{s} = 8$ TeV and 13 TeV assuming that A is produced via gluon-fusion or in association with a pair of bottom quarks, and utilizing the leptonic decay modes of the Z-boson. The scalar H was required to decay either to a pair of bottom quarks or to a pair of tau leptons [173, 175, 336]. However, as already pointed out in Ref. [1], the combination of theoretical and experimental constraints in the type II 2HDM currently pushes m_H to be above the di-top threshold in almost the entire parameter region featuring a FOEWPT. Then, the branching fractions for $H \to b\bar{b}$ and $H \to \tau^+\tau^-$ become very small (except for large values of t_β), and searches via these final states do not yield relevant constraints on FOEWPT scenarios. It is instead much more promising to search for $A \to ZH$ signatures with H decaying into a pair of top quarks, and preliminary studies of this final state exist already in the literature [337, 338]. While this channel has not yet been probed experimentally at the LHC, efforts to analyse the $Z\,t\bar{t}$ final

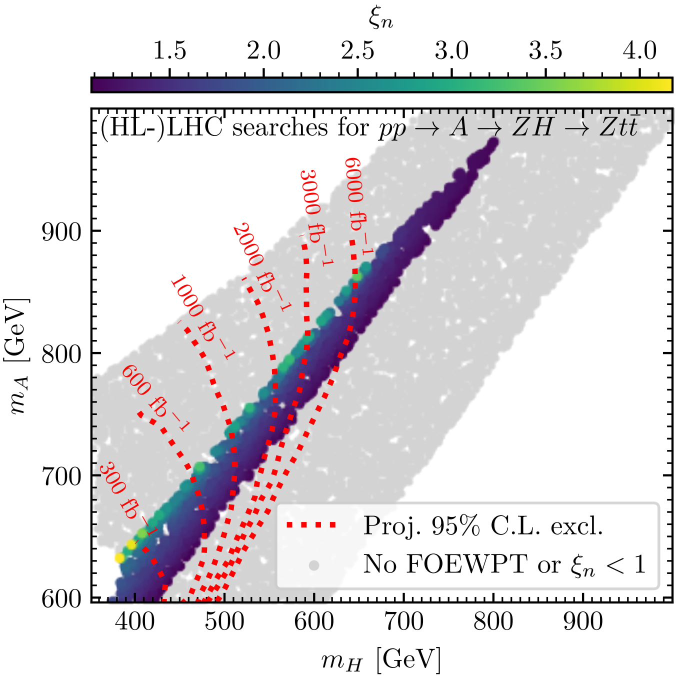

Figure 5.10: Parameter points of the parameter scan discussed in section 5.3.1 in the (m_H, m_A) plane, with the colour coding indicating the value of ξ_n for the points that feature a strong FOEWPT, i.e. $\xi_n > 1$. The remaining points are shown in gray. The red dashed lines indicate the projected 95% C.L. exclusion regions resulting from the (HL-)LHC searches for the process $pp \to A \to ZH$ with H decaying into a pair top quarks (see text for details).

state are ongoing by both the ATLAS [339] and CMS [340, 341] collaborations. We here use the public preliminary CMS results on this channel (using only the $Z \to \mu^+\mu^-$ decay mode) for an integrated luminosity of $41\,\mathrm{fb}^{-1}$ at 13 TeV [340] to estimate the projected (HL-)LHC sensitivity to the process $A \to ZH$ in the $Z\,t\bar{t}$ final state, for several integrated luminosities: $\mathcal{L} = 300\,\mathrm{fb}^{-1}$, $600\,\mathrm{fb}^{-1}$, $1000\,\mathrm{fb}^{-1}$, $2000\,\mathrm{fb}^{-1}$, $3000\,\mathrm{fb}^{-1}$ and $6000\,\mathrm{fb}^{-1}$ (the latter corresponds to the total integrated luminosity collected by ATLAS and CMS combined at the HL-LHC). We obtain the predicted 2HDM production cross sections (at NNLO) times branching ratios for the $pp \to A \to ZH \to \mu^+\mu^-\,t\bar{t}$ signature as a function of m_A and m_H (with the rest of parameters fixed as in Eq. (5.4)) using `SusHi` [317] and `N2HDECAY` [318], and show in Fig. 5.10 the expected 95% C.L. exclusion sensitivity for different values of $\mathcal{L}$ from a naive rescaling of the CMS expected limits by a factor $\sqrt{(41\,\mathrm{fb}^{-1})/\mathcal{L}}$ (which assumes that the present CMS sensitivity is limited by statistics rather than systematics). We emphasise that taking into account also other (leptonic) decay modes of the Z-boson yields even stronger projected limits [341], and the exclusion regions shown in Fig. 5.10 should be regarded as rough conservative estimates of the reach of BSM Higgs searches in the $Z\,t\bar{t}$ final state at the (HL-)LHC.

In Fig. 5.10 we also show the points of the 2HDM parameter scan discussed in section 5.3.1, with the parameter points featuring a strong FOEWPT shown in colour (colour-code indicates the value of ξ_n) and the remaining points depicted in gray. Already at the end of LHC Run 3 with $300\,\mathrm{fb}^{-1}$ ($600\,\mathrm{fb}^{-1}$ assuming a potential combination of ATLAS and CMS data), a substantial part of the interesting parameter space will be explored, with values $m_H \lesssim 470$ GeV being probed. In particular, the 2HDM region yielding observable GW signals at LISA with values of $\Lambda_{4\pi} > 2$ TeV (see Fig. 5.6 and Fig. 5.9) will be completely covered by this LHC search during Run 3, and so will be the parameter points with the strongest phase transitions, corresponding to values of $\xi_n \sim 4$. The HL-LHC, with ten times more data, will be able to probe masses up to $m_H \sim 650$ GeV via the $A \to ZH$ ($H \to t\bar{t}$) search, covering almost the entire 2HDM region that features a GW signal potentially detectable with LISA (see Fig. 5.6). This analysis highlights the importance of putting the expectations for GW signals from FOEWPTs that could be detectable by LISA into the context of the projected (HL-)LHC results.

GWs at LISA vs. Higgs boson self-coupling measurements at LHC and ILC

A well-known avenue to probe the thermal history of the EW symmetry, particularly in connection with a possible FOEWPT, is the measurement of the trilinear self-coupling of the 125 GeV Higgs boson. FOEWPTs are generically associated with a sizable enhancements of the trilinear coupling λ_{hhh} as compared to the SM prediction [304, 305].[12] In the following, we determine the values of λ_{hhh} predicted in the 2HDM parameter space regions which feature a FOEWPT, including the regions that would yield a GW signal potentially observable at LISA. According to our definition of the zero-temperature effective potential from Eq. (5.2), λ_{hhh} is here calculated at the one-loop level, and to align our analysis with the experimental interpretations of the Higgs trilinear self-coupling measurements performed by the ATLAS and CMS collaborations within the κ-framework, we here define $\kappa_\lambda = \lambda_{hhh}/\lambda_{hhh}^{\mathrm{SM}}$, where $\lambda_{hhh}^{\mathrm{SM}}$ is the tree-level Higgs self-coupling prediction of the SM. In Fig. 5.11 we show the values of κ_λ in dependence of the mass splitting $m_A - m_H$ for the parameter scan from Eq. (5.4). In the left panel, the various colours indicate the different types of thermal histories (the letter in each region specifies the corresponding thermal evolution of the vacuum according to the description of Fig. 5.2). As expected, large values of $m_A - m_H$ are correlated with large values of κ_λ. In particular, parameter points featuring a strong FOEWPT (region E) predict values of up to $\kappa_\lambda \sim 2$, and vacuum trapping (region D) excludes part of the parameter space with even larger values of κ_λ. There are still physically viable parameter points predicting values of $\kappa_\lambda > 2$ (regions A and C; we remind the reader that region B is unphysical, see section 5.3.1), associated with the phenomenon of EW SnR. Finally, the largest values of κ_λ occur for 2HDM parameter regions that are not phenomenologically viable (dark-grey points), as these regions feature an energy cutoff $\Lambda_{4\pi}$ smaller than the masses of the BSM scalar states, i.e. $\Lambda_{4\pi} < m_A = m_{H^\pm}$ or $\Lambda_{4\pi} < m_H$; a large fraction of these points also features a short-lived EW vacuum (see Fig. 5.1).

---

[12] This is specially the case for FOEWPTs which are not *singlet-driven* (caused by a singlet scalar field coupling to the SM Higgs doublet). For a singlet-driven FOEWPT, it is possible to avoid such large enhancements [342].

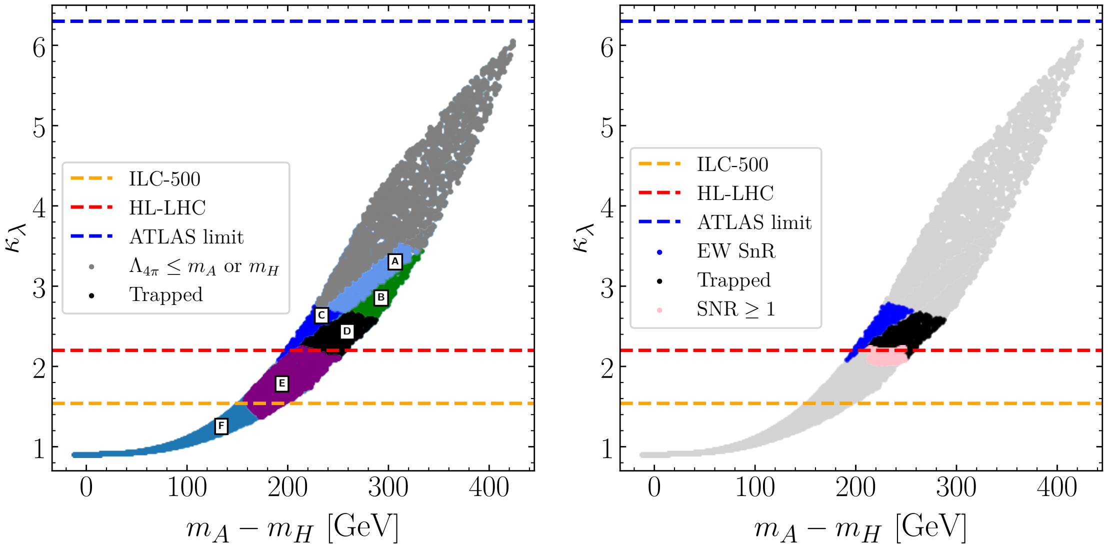

Figure 5.11: Parameter points from the scan as defined in Eq. (5.4) with the mass difference $m_A - m_H$ on the horizontal axis and κ_λ on the vertical axis. In the left panel, the colour of the points indicates the different kinds of thermal histories: the letter specifies each region according to Fig. 5.2, and dark-grey points feature $\Lambda_{4\pi} \leq m_A$ or m_H, and/or a short-lived EW vacuum. In the right panel, blue points feature EW SnR, black points feature vacuum trapping (and are therefore unphysical), and pink points predict a FOEWPT with an associated GW signal that could be detectable at LISA (SNR ≥ 1, see text for details). The characteristics of the light-grey points can be inferred from the left panel.

The value of κ_λ can be constrained via the measurements of single and double Higgs boson production at colliders. In order to compare the 2HDM predictions for κ_λ with present and future experimental constraints, we show in Fig. 5.11 the currently strongest 95% C.L. experimental limit on κ_λ, corresponding to $\kappa_\lambda < 6.3$ as reported by ATLAS[13] using the full Run II dataset and combining measurements of single Higgs boson and (nonresonant) Higgs boson pair production [133]. We also show the projected 95% C.L. sensitivity of the HL-LHC (dashed-red line), given by $\kappa_\lambda < 2.2$ [134], and the projected 95% C.L. sensitivity of the future International Linear Collider (ILC) with $\sqrt{s} = 500$ GeV and an integrated luminosity of $4000\,\text{fb}^{-1}$ (dashed-yellow line), given by $\kappa_\lambda < 1.54$ [343]. We stress that these experimental limits on κ_λ hold under the assumption that the couplings of h to other SM particles are those of the SM, which is the case in the alignment limit of the 2HDM (at leading order) used in this work. In addition, the projected limits shown for HL-LHC and ILC assume that $\kappa_\lambda = 1$ will be measured experimentally (we discuss below the impact of a different assumption).[14] While the current LHC experimental sensitivity is not sufficient to probe the viable parameter space analysed here, HL-LHC would be capable

---

[13] CMS has reported a comparable upper limit of $\kappa_\lambda < 6.49$ [228].

[14] Note that, with our definition of κ_λ (which matches that of the ATLAS and CMS experimental collaborations), $\kappa_\lambda = 1$ corresponds to the SM prediction only when one-loop corrections to λ_{hhh} in the SM (which amount to -9% of the tree-level value [302]) are neglected.

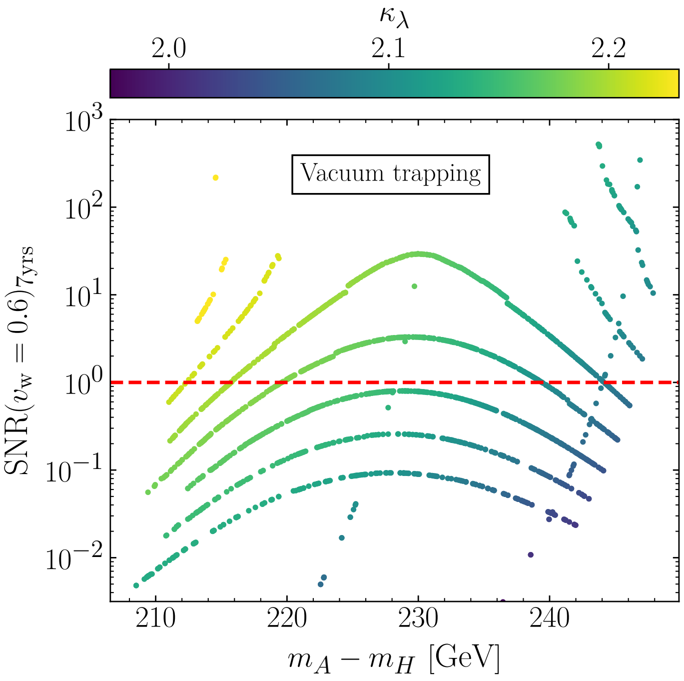

Figure 5.12: Parameter points of the detailed finer scan discussed in section 5.3.2 (already shown in Fig. 5.6 and Fig. 5.9), in the ($\Delta m = m_A - m_H$, SNR) plane. The colour-code here indicates the prediction for κ_λ.

of virtually probing the entire parameter space featuring EW SnR, while ILC-500 would further probe most of the region featuring a strong FOEWPT.

In order to estimate the values of κ_λ for parameter points with detectable GW signals at LISA, we show in the right panel of Fig. 5.11 the same parameter plane as in the left panel, but with the strong FOEWPT parameter points predicting SNR ≥ 1 at LISA highlighted in light-pink. These points have values of $\kappa_\lambda \sim 2$, and thus lie in the ballpark of the expected HL-LHC upper limit on κ_λ. To further scrutinise this parameter region, focusing on the interplay between measurements of the Higgs boson self-coupling at colliders and potential observations of GWs at LISA, we show in Fig. 5.12 the same plane as depicted in Fig. 5.6 and Fig. 5.9, with the colour-code now indicating the values of κ_λ (points above the dashed-red line in Fig. 5.12 then correspond to the pink area in Fig. 5.11 - (right)). Values of κ_λ in this plot range from $\kappa_\lambda \sim 2$ up to $\kappa_\lambda \sim 2.2$, possibly within reach of HL-LHC. The plot further illustrates that a strong FOEWPT that gives rise to a potentially detectable GW signal is associated with a significant deviation from $\kappa_\lambda = 1$ (see also Ref. [145]). Conversely, if no deviations of κ_λ from the SM prediction are observed at the HL-LHC, no GW signal at LISA would be expected.

We also stress that future measurements of κ_λ at the HL-LHC and ILC will be a very important probe of the EW phase transition, independently of the associated GW production (as shown in Fig. 5.11, a large fraction of the parameter space featuring a strong FOEWPT does not yield an observable GW signal at LISA). In this sense, we note that

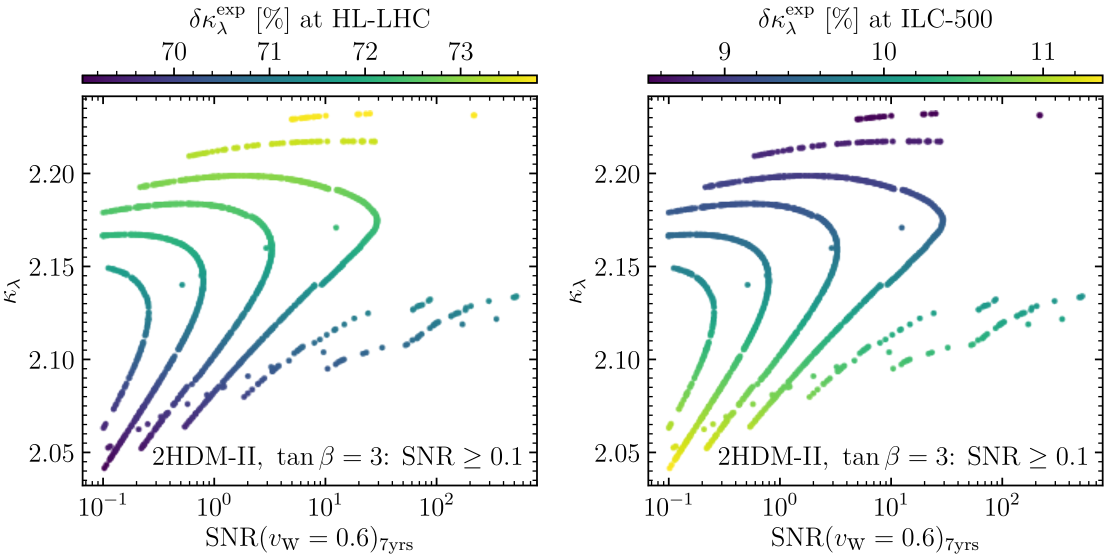

Figure 5.13: Parameter points from Fig. 5.12 with SNR ≥ 0.1 in the (SNR, κ_λ) plane. The colour coding of the points indicates the projected experimental precision of the measurement of κ_λ at the HL-LHC (left) and the ILC-500 (right), see text for details.

the leading two-loop corrections to the self-coupling of the SM-like Higgs boson can yield a sizable enhancement of κ_λ [344] with respect to the one-loop result. Thus, an analysis of κ_λ at the two-loop level may result in even better prospects for a measurement of a modification of the Higgs boson self-coupling with respect to the SM value, a study we leave for the future.[15]

In all the above discussion, we have focused on the potential of HL-LHC and ILC measurements of κ_λ to exclude the presence of sizable BSM contributions to λ_{hhh}, by assuming $\kappa_\lambda = 1$ will be measured. However, the expected HL-LHC and ILC precision of the κ_λ measurement, $\delta\kappa_\lambda^{\rm exp}$, would significantly change in the event of a $\kappa_\lambda > 1$ measurement (for $\kappa_\lambda = 1$ the HL-LHC and ILC-500 precision are respectively given by $\delta\kappa_\lambda^{\rm exp} = 60\%$ [134] and $\delta\kappa_\lambda^{\rm exp} = 27\%$ [343]). In order to analyse how precisely the HL-LHC and ILC would measure a value of κ_λ in the 2HDM parameter space region yielding an observable GW signal at LISA, we show in Fig. 5.13 the parameter points of Fig. 5.12 with SNR ≥ 0.1 in the (SNR, κ_λ) plane, with the colour-code indicating the experimental precision with which κ_λ could be measured at the HL-LHC (left panel) and ILC-500 (right panel). At the HL-LHC, the experimental precision of a $\kappa_\lambda \sim 2$ measurement ($\delta\kappa_\lambda^{\rm exp} \gtrsim 70\%$) worsens compared to that of $\kappa_\lambda = 1$. This is due to the enhanced negative interference between signal and background diagrams, leading to a reduced cross section at the HL-LHC (see, for instance, Fig. 3 of Ref. [345] for the cross-section predictions). On the other hand, the situation would be much more favorable at the ILC with $\sqrt{s} = 500$ GeV in the process $e^+e^- \to Zhh$,

---

[15] For a complete analysis of the possible impact of these two-loop effects on the interplay between LISA and the (HL-)LHC, two-loop corrections would have to be taken into account also for the prediction of the FOEWPTs, which however lies beyond the scope of this analysis.

for which a precision $\delta\kappa_\lambda^{\mathrm{exp}} \sim 10\%$ could be expected for a $\kappa_\lambda \sim 2$ measurement with an integrated luminosity of $4000\,\mathrm{fb}^{-1}$ [343]. The Higgs boson self-coupling measurement at the ILC-500 relies mainly on the Higgs-strahlung channel, which exhibits a positive interference between signal and background diagrams and thus an enhanced di-Higgs production cross section for $\kappa_\lambda > 1$ (see Fig. 8 of Ref. [346]).

Finally, regarding the interpretation of Fig. 5.13 we remind the reader that the current theoretical uncertainties on the prediction for the GW spectra from a FOEWPT, as well as the lack of knowledge of the value of v_{w} (see section 4.3 for details), translate into an uncertainty on the SNR (not shown in the plots), much larger than that stemming from a $\delta\kappa_\lambda^{\mathrm{exp}} \sim 10\%$ uncertainty in the measurement of κ_λ, reachable at the ILC-500. This should be taken into account when trying to investigate the complementarity between colliders and GW detectors within the 2HDM. Still, we can robustly conclude that the type II 2HDM parameter space that features GW signals potentially detectable at LISA predicts values of $\kappa_\lambda \sim 2$, which would be measured only poorly at the HL-LHC, but with a much better precision at the ILC-500 or other e^+e^- colliders with sufficient center-of-mass energy to produce pairs of Higgs bosons.

Chapter 6

EW symmetry non-restoration and trapped vacua in the N2HDM

Extensions of the Higgs sector of the Standard Model allow for a rich cosmological history around the EW scale. In this chapter, we show that besides the possibility of strong first-order phase transitions (Sect. 4.2.1), which have been thoroughly studied in the literature, also other important phenomena can occur, like the non-restoration of the EW symmetry (Sect. 4.2.3) or the existence of vacua in which the Universe becomes trapped (Sect. 4.2.2), preventing a transition to the EW minimum. Focusing on the N2HDM of type II and taking into account the existing theoretical and experimental constraints (Sect. 3.2), we identify the scenarios of EW SnR, vacuum trapping and first-order phase transition in the thermal history of the Universe. We analyse these phenomena and in particular their relation to each other, and discuss their connection to the predicted phenomenology of the N2HDM at the LHC. Our analysis demonstrates that the presence of a global EW minimum of the scalar potential at zero temperature does not guarantee that the corresponding N2HDM parameter space will be physically viable: the existence of a critical temperature at which the EW phase becomes the deepest minimum is not sufficient for a transition to take place, necessitating an analysis of the tunnelling probability to the EW minimum for a reliable prediction of the thermal history of the Universe.

This chapter is organised as follows: In Sect. 6.1 we introduce the N2HDM, in connection to the content of Sect. 3.1.2. In Sect. 6.2, we describe the numerical implementation of the theoretical and experimental constraints discussed in Chapter 3 (Sect. 3.2) for the (zero-temperature) analysis of the N2HDM parameter space. Then, in Sect. 6.3 we present the finite-temperature scalar potential of the N2HDM. We study the phenomenon of EW SnR in Sect. 6.4, both via an analytical and a numerical approach, and analyse its interplay with the occurrence of a FOEWPT in the N2HDM. In Sect. 6.5 we investigate the possible occurrence of vacuum trapping, together with the connection between the thermal history of the N2HDM and its LHC phenomenology.

This chapter is based on ref. [1].

6.1 The N2HDM at zero-temperature

Tree-level scalar potential The N2HDM is the extension of the CP-conserving (real) 2HDM with a softly broken $\mathbb{Z}_2$ symmetry by a real scalar field. In order to specify our notation and conventions we refer to Sect. 3.1.2, where the N2HDM tree-level scalar potential V_{tree} was given in (3.27).

One-loop effective potential and renormalisation At the one-loop order, the effective scalar potential at zero temperature V_{eff} is given by

$$V_{\text{eff}} = V_{\text{tree}} + V_{\text{CW}} + V_{\text{CT}}, \tag{6.1}$$

where V_{CW} denotes the Coleman-Weinberg potential given in the $\overline{\text{MS}}$ renormalisation prescription (see Eq. (4.43)). For the N2HDM, the sum in V_{CW} runs over the neutral scalars $\Phi^0 = \{h_a,\, h_b,\, h_c,\, A,\, G^0\}$, the charged scalars $\Phi^{\pm} = \{H^{\pm},\, G^{\pm}\}$, the SM quarks q and leptons ℓ, the longitudinal and transversal gauge bosons $V_L = \{Z_L,\, W_L^+,\, W_L^-\}$ and $V_T = \{Z_T,\, W_T^+,\, W_T^-\}$. The respective degrees of freedom n_j for the species in each category are

$$n_{\Phi^0} = 1\,, \quad n_{\Phi^{\pm}} = 2\,, \quad n_{V_T} = 2\,, \quad n_{V_L} = 1\,, \quad n_q = 12\,, \quad n_\ell = 4\,. \tag{6.2}$$

The Coleman-Weinberg potential has been evaluated in the Landau gauge. The effective potential is well-known to be gauge dependent, and the extraction of physical information from V_{eff} has to appropriately handle this problem. Here we note that in the present case the EW symmetry breaking dynamics will be dominantly dictated by quartic scalar interactions that are not gauge dependent, or explored at high T retaining only gauge-invariant contributions. Thus, the gauge dependence of V_{eff} is of minor concern for our analysis. For the N2HDM, the sum in Eq. (4.43) includes the scalars $h_{1,2,3}$, A, $H^{\pm}$, the Goldstone bosons $G^{\pm}$, G^0, the massive EW gauge bosons and the SM fermions (where the main contribution arises from the top quark).

Furthermore, to perform an efficient scan through the parameter space of the N2HDM, we required the zero-temperature loop-corrected scalar masses and mixing angles to be equal to their tree-level values by adding to V_{eff} the UV-finite counterterm contribution V_{CT} given by Eq. (4.44), and imposing the conditions in Eq. (4.46). In the case of the CP-conserving N2HDM, the tadpole counterterms are δT_1, δT_2, δT_S. They vanish since no additional symmetry is broken by the radiative corrections at the one-loop level. Accordingly, in the following we apply Eq. (4.44) with $\delta T_k = 0$. We have found perfect agreement with the implementation of the N2HDM renormalised zero-temperature effective potential of the public code `BSMPT` [319].

Scale dependence and perturbativity As discussed in Sect. 4.1, including radiative corrections induces a dependence of the model parameters on the unphysical energy scale μ, which is controlled by the RGEs. In our finite-temperature analysis, we verified that the absolute values of the quartic couplings $|\lambda_i|$ remain substantially smaller than the perturbativity bound 4π over the range $\mu = [\mu_0, T_{\max}]$, where $T_{\max}$ is the maximum temperature analysed in each case.

We have numerically solved the RGEs, given in terms of their β functions, in the $\overline{\text{MS}}$ scheme. We took into account the one- and two-loop contributions to the β functions, which we obtained with the help of the public code `SARAH v.4.14.3` [347, 348], solving the general expressions published in Refs. [349–351]. We have checked the expressions for the β functions using the public code `PyR@TE v.3.0` [352] and found exact agreement. For the dominant one-loop terms we analytically checked that, in the limit $\lambda_{6,7,8} \to 0$, the terms reduce to the ones of the 2HDM, which are well-known in the literature (see e.g. [335, 353]). Due to the renormalisation prescription specified in Eq. (4.46), which we call "on-shell" (OS) in the following, it is necessary to transform the OS values of the model parameters p^{OS} at $\mu = \mu_0$ into the corresponding $\overline{\text{MS}}$ values $p^{\overline{\text{MS}}}$, such that the running of the parameters can be applied as described above. The transformation between the two schemes is given by the finite parameter counterterms δp_i introduced in Eq. (4.44), using

$$p^{\text{OS}}(\mu_0) + \delta p^{\text{OS}}(\mu_0) = p^{\overline{\text{MS}}}(\mu_0) + \delta p^{\overline{\text{MS}}}(\mu_0) \tag{6.3}$$

$$\Rightarrow \; p^{\overline{\text{MS}}}(\mu_0) = p^{\text{OS}}(\mu_0) + \delta p^{\text{OS}}_{\text{fin.}}(\mu_0) \;, \tag{6.4}$$

where the second equality follows from the fact that by definition the counterms $\delta p^{\overline{\text{MS}}}$ do not contain finite pieces. Accordingly, the counterterms $\delta p^{\text{OS}}_{\text{fin.}}(\mu_0)$ for the different parameters p_i correspond to the finite counterterms δp_i in Eq. (4.44).

In order to limit the impact of a potentially large scale dependence, we restrict our analysis to parameter points with values of $|\lambda_i^{\overline{\text{MS}}}(\mu_0)|$ considerably below the perturbativity bound 4π in these cases. To be more precise, for the benchmark scenarios discussed in sections 6.4.1 and 6.4.2 related to SnR we only take into account points with $|\lambda_i^{\overline{\text{MS}}}(\mu_0 = v)| < 3$. In Sec. 6.4.3 we discuss the interplay between EW SnR at high-T and the occurrence of a FOEWPT at intermediate temperatures. Here, somewhat larger values are required in order to give rise to a potential barrier between true and false vacuum. However, the values of $|\lambda_i^{\overline{\text{MS}}}(\mu_0)|$ are still substantially smaller than 4π, and we additionally checked that the values of $|\lambda_i^{\overline{\text{MS}}}(\mu)|$ remain below the bound within the relevant temperature region that has been analysed. Moreover, the conditions for perturbative unitarity were applied (see Sec. 6.2), yielding further limitations on $|\lambda_i^{\overline{\text{MS}}}|$.

6.2 Constraints

The N2HDM has 12 real independent parameters. It is convenient to choose the particle masses of the Higgs sector as input parameters since they have a direct physical meaning. In this section we outline the various theoretical and experimental constraints that we have imposed. We discuss their impact on the parameter space of the N2HDM. We have made use of the public code `ScannerS` [306, 307]. The input parameters that we supply to `ScannerS` are

$$C^2_{h_a tt} \;,\; C^2_{h_a VV} \;,\; \text{sgn}(R_{a3}) \;,\; R_{b3} \;,\; t_\beta \;,\; v_S \;,\; m_{h_a} \;,\; m_{h_b} \;,\; m_{h_c} \;,\; m_A \;,\; m_{H^\pm} \;,\; m^2_{12} \;, \tag{6.5}$$

where the three CP-even scalar mass eigenstates (not necessarily ordered in mass) are denoted as $h_{a,b,c}$. We identify these masses with the physical (OS) values; accordingly, the λ_i that are obtained from those input values (see (3.27)) correspond to on-shell quantities, λ_i^{OS} (these on-shell parameters are converted to their $\lambda_i^{\overline{\text{MS}}}$ counterparts where running parameters are required). Under the assumption $C_{h_a VV} \cdot C_{h_a tt} > 0$, the above parameters determine the mixing angles $\alpha_{1,2,3}$ [307]. In the following we conveniently choose a parameterization where h_a is identified with the Higgs boson at about 125 GeV, i.e. $h_a \equiv h_{125}$ and $m_{h_a} \approx 125$ GeV. With an appropriate choice of the masses $m_{h_{b,c}}$, the states $h_{a,b,c}$ can then be identified with the mass-ordered eigenstates $h_{1,2,3}$. For further details on the experimental and theoretical constraints we refer to Sect. 3.2.1 and Sect. 3.2.2, respectively. In the following, we will mainly focus on the methods and codes involved in their application to the N2HDM.

Theoretical constraints: Vacuum stability and unitarity `ScannerS` discards points in which the tree-level N2HDM scalar potential is not bounded from below, making use of the conditions from Refs. [176, 190]. Apart from global EW minima, we also consider in our analysis metastable EW minima (at $T = 0$). In the latter case, we evaluate the probability for the quantum tunnelling from the EW minimum into the deeper minima and, subsequently, determine whether the lifetime of the EW minimum is sufficiently long compared to the age of the Universe. This investigation is carried out with the linked public code `EVADE` [198, 354]. Parameter points are regarded as allowed if the EW minimum is the global minimum or if it is sufficiently long-lived (metastable). In addition, BfB and the stability of the EW vacuum were also checked at the one-loop level. We implemented the one-loop effective potential in `cosmoTransitions`, which found the minima of the potential at zero-temperature and computed the tunnelling rate among them. The code was also able to identify any unbounded direction of the one-loop potential.

In addition, we require that each parameter point fulfils perturbative unitarity constraints, formulated in terms of $2 \to 2$ scalar scattering processes. We use the approach implemented by default into `ScannerS` for the N2HDM, demanding that the eigenvalues of the scattering matrix should be smaller than 8π. The relevant expressions can be found in Ref. [176]. Since various results discussed in sections 6.4 and 6.5 involve sizeable quartic scalar couplings, the perturbative unitarity constraints play an important role in our study.

Flavor-physics observables As discussed in Sect. 3.2.2, we can safely adopt the flavour constraints of the 2HDM for our N2HDM analysis. We have followed the approach implemented in `ScannerS`, where allowed parameter points are required to be located within the $2\,\sigma$ region of the $m_{H^\pm}$–t_β plane as identified via a global fit to experimental data in Ref. [210]. In our analysis the flavour-physics observables exclude values of $t_\beta \lesssim 0.8$ in all four N2HDM types from Table 3.2. In addition, a roughly t_β-independent limit on the charged scalar mass $m_{H^\pm} \gtrsim 600$ GeV is obtained for type II and IV of the N2HDM.

Properties of the observed Higgs boson at 125 GeV The compatibility with the signal-rate measurements of the Higgs boson at about 125 GeV requires that the couplings of $h_a = h_{125}$ should, within the current theoretical and experimental uncertainties, resemble the couplings of a SM Higgs boson. In the N2HDM, the effective Higgs couplings (defined as the coupling strength normalised to the SM prediction for a Higgs boson with the same mass) are determined by the mixing angles α_i and t_β. Accordingly, those mixing angles are constrained by the LHC Higgs signal-rate measurements. In order to check the compatibility of the N2HDM parameter space points with the experimentally measured signal rates of the Higgs boson at about 125 GeV, we use the public code `HiggsSignals v.2.6.0` [308–311], conveniently linked to `ScannerS` by default for the N2HDM. In the scenario of an almost decoupled singlet-like Higgs boson, the N2HDM can reproduce the alignment and decoupling limits of the usual 2HDM. In these limits the couplings of h_a are equal to the SM couplings. Since `ScannerS` allows one to use C_{h_aVV} and C_{h_att} as input parameters, choosing $C_{h_aVV} \approx 1$, $C_{h_att} \approx 1$ yields parameter points that generally pass the `HiggsSignals` test. A parameter point is regarded to be excluded if

$$\Delta\chi^2_{\text{HiggsSignals}} = \chi^2_{\text{N2HDM}} - \chi^2_{\text{SM}} \geq 6.18 \ , \tag{6.6}$$

where χ^2_{N2HDM} and χ^2_{SM} are calculated via a fit to all currently available signal-rate measurements of the Higgs boson at about 125 GeV from the Tevatron and the LHC. The SM result for a mass of 125 GeV is $\chi^2_{\text{SM}} = 84.4$ for 107 considered measurements.

Direct searches for additional Higgs bosons Experimental upper limits on the production of the BSM-type Higgs bosons h_b, h_c, A and $H^\pm$ provide important constraints on the parameter space of the N2HDM. We take into account the limits from Higgs-boson searches at LEP, the Tevatron and the LHC for each parameter point by employing the public code `HiggsBounds v.5.9.0` [312–315]. For the N2HDM, the `HiggsBounds` code is linked to `ScannerS` by default, where the so-called effective-coupling input is used for the cross sections, while the branching ratios are calculated internally using the code `N2HDECAY` [176, 318] and given as input directly to `HiggsBounds`. The code then determines for the considered parameter point the channel with the most sensitive expected limit for each Higgs boson and tests whether the parameter point is allowed at the 95% confidence level by comparing for the selected channels the prediction for the production cross section times branching ratio with the observed upper limit.

EW precision observables In the N2HDM, deviations in the EWPO from the SM can conveniently be expressed in terms of the oblique parameters S, T and U [204, 205]. They are determined via the gauge-boson self energies, and we define them relative to the SM with a Higgs-boson mass of ≈ 125 GeV. The parameter T provides the strongest constraints on the N2HDM parameter space. Since it accounts for the breaking of custodial symmetry, the contributions of the BSM-type Higgs bosons to T approximately vanish when either the CP-odd scalar A or the doublet-like CP-even scalar (h_b or h_c) are close in mass to the charged scalar $H^\pm$, i.e. $m_A^2 \approx m_{H^\pm}^2$ or $m_{h_{b,c}}^2 \approx m_{H^\pm}^2$. We make use of the implementation in `ScannerS` of the S, T and U computation for models exclusively containing gauge-singlet and $SU(2)_L$-doublet scalar fields [206, 207]. A point is considered to be excluded if the prediction for the S, T and U parameters yields a $\Delta\chi^2$ of more than $2\,\sigma$ relative to the best-fit point from a global fit to the EWPO [210].

6.3 The N2HDM at finite-temperature

The discussion of the N2HDM in Sect. 6.1, followed by the introduction of the relevant constrains in Sect. 6.2, was limited to the zero-temperature case. In this section, we will introduce the necessary ingredients to study the N2HDM at finite temperature and analyse the thermal history of the Universe in this scenario. Further details on the derivation and the structure of the finite-temperature scalar potential are given in Sect. 4.1.

Finite-T effective potential The one-loop effective potential at finite temperature is given by

$$V \equiv V_{\text{tree}} + V_{\text{CW}} + V_{\text{CT}} + V_T\,, \tag{6.7}$$

where V_T is the one-loop thermal potential given in Eq. (4.47). In addition to the degrees of freedom considered in Eq. (6.2), the sum in (4.47) includes the photon.

As discussed in Sect. 4.1, the breakdown of the conventional perturbative expansion results in the need to resum a certain set of higher-loop diagrams, the daisy contributions. We follow here the AE method, which amounts to add another piece, V_{daisy} (given by Eq. (4.53)), to the one-loop effective potential at finite temperature. In the N2HDM, the sum in V_{daisy} runs over W_L, Z_L, γ_L, and the field-dependent masses $M_{\text{C}}^2(\phi)$, $M_\eta^2(\phi)$ and $M_\rho^2(\phi)$. Π_k^2 denotes their corresponding squared thermal mass matrices [248]. Considering the resummation of daisy diagrams as part of the effective potential yields

$$V \equiv V_{\text{tree}} + V_{\text{CW}} + V_{\text{CT}} + V_T + V_{\text{daisy}}\,. \tag{6.8}$$

Using the AE resummation method, the effective potential can be treated analytically in the high-temperature regime using the expansions of Eqs. Eq. (4.49). In this limit, the resummation simply amounts to performing the substitution $m^2(\phi) \to m^2(\phi) + \Pi^2$ inside the $y^{3/2}$ term in Eq. (4.49). We have compared our resummation prescription with the Parwani resummation method, frequently used in the literature.

The two methods are commonly assumed to be equivalent in the $m^2(\phi)/T^2 \to 0$ limit, since the field-dependent contributions from the logarithmic terms in Eq. (4.43) and Eq. (4.49) cancel each other. However, it should be noted that the expansion of Eq. (4.49) is no longer justified when using the Parwani resummation prescription, since $\Pi^2 \sim T^2$ at leading order, and thus $y = (m^2(\phi) + \Pi^2)/T^2$ does not necessarily go to zero in the high-T limit. For $m^2(\phi) \ll \Pi^2$, we can use the expansion for $J_\pm(y)$ from Refs. [36, 244, 251], which includes contributions of $\mathcal{O}(y^3)$ and higher, to obtain the leading difference between the two methods in the high-T limit, given by

$$\begin{aligned}
\Delta V_{m^2/T^2\to 0} \quad \simeq \quad & \sum_{j\in b} \frac{n_j\, m_j^2(\phi) T^2}{2} \left[\sum_{\ell=2}^{\infty} \left(\frac{-\Pi_j^2}{4\,\pi^2 T^2} \right)^{\ell} \frac{(2\ell-3)!!\,\zeta(2\ell-1)}{(2\ell)!!} \right] \\
- \quad & \sum_{j\in f} \frac{n_j\, m_j^2(\phi) T^2}{2} \left[\sum_{\ell=2}^{\infty} \left(\frac{-\Pi_j^2}{4\,\pi^2 T^2} \right)^{\ell} \frac{(2\ell-3)!!\,\zeta(2\ell-1)}{(2\ell)!!} (2^{2\ell-1}-1) \right] \qquad (6.9)
\end{aligned}$$

where $\zeta(x)$ is the Riemman ζ-function, and $(x)!!$ denotes the double factorial. The respective sums are carried out for bosons b and fermions f. This difference can qualitatively modify the high-T behavior of V in specific regions of parameter space, and even yield a different answer about the fate of the EW symmetry in such regions, as we will discuss in more detail in Sect. 6.4.

The leading ($\sim T^2$) contributions to the thermal masses for the scalars in the N2HDM are given by (in the interaction basis)

$$\Pi_{\rho_1\rho_1} = \Pi_{\eta_1\eta_1} = \Pi_{\phi_1^+\phi_1^+} = T^2 \left(c_1 + \begin{cases} 0\,, & \text{Type I/III} \\ \frac{1}{4} y_b^2\,, & \text{Type II/IV} \end{cases} \right), \qquad (6.10)$$

$$\Pi_{\rho_2\rho_2} = \Pi_{\eta_2\eta_2} = \Pi_{\phi_2^+\phi_2^+} = T^2 \left(c_2 + \begin{cases} \frac{1}{4} y_b^2\,, & \text{Type I/III} \\ 0\,, & \text{Type II/IV} \end{cases} \right), \qquad (6.11)$$

$$\Pi_{\rho_3\rho_3} = c_3 T^2, \qquad (6.12)$$

with

$$c_1 = \frac{1}{16}(g'^2 + 3g^2) + \frac{\lambda_1}{4} + \frac{\lambda_3}{6} + \frac{\lambda_4}{12} + \frac{\lambda_7}{24}\,, \qquad (6.13)$$

$$c_2 = \frac{1}{16}(g'^2 + 3g^2) + \frac{\lambda_2}{4} + \frac{\lambda_3}{6} + \frac{\lambda_4}{12} + \frac{\lambda_8}{24} + \frac{1}{4} y_t^2\,, \qquad (6.14)$$

$$c_3 = \frac{1}{6}(\lambda_7 + \lambda_8) + \frac{1}{8}\lambda_6\,. \qquad (6.15)$$

In Eq. (6.10) and Eq. (6.11) the only considered fermionic contributions are the ones from the top and bottom quarks through their respective Yukawa couplings y_t and y_b. Upon diagonalization of the $M_k^2(\phi) + \Pi_k^2$ matrices, one can obtain the effective masses including thermal effects for the N2HDM scalars. The thermal masses of the longitudinal parts of the SM gauge bosons can be found in Ref. [244].

N2HDM thermal history In the following we analyse the thermal history of the N2HDM scalar potential for the regions of parameter space that satisfy the constraints discussed in Sec. 6.2.

We use the public code `CosmoTransitions` [196] to study the scalar potential evolution with temperature, and the phenomenon of vacuum trapping (see Sect. 4.2.2). Previous studies of the N2HDM in the early Universe [245, 319] have relied on identifying the critical temperature T_c at which the EW minimum would have been degenerate in energy with other potential vacua. Therein, it was furthermore assumed that the phase transition to the EW vacuum always takes place if the EW vacuum is the global minimum of the potential at $T = 0$. However, as argued above, this is by no means guaranteed, but depends on the false vacuum tunnelling rate per unit time and volume given by Eq. (4.58).

As will be discussed below, we find that such a situation is quite common in the N2HDM, with the metastable vacuum corresponding to a minimum in which only $\langle \Phi_S \rangle$ is non-zero.[1] In particular, when aiming to identify the regions of the N2HDM parameter space where a FOEWPT is possible, the approach based just on T_c [245, 319] (but not T_n) is not sufficient and can result in rather misleading specifications of the parameter space. In Sec. 6.5 we will discuss these "trapped-vacuum" scenarios in detail.

In addition, our study of the thermal history of the N2HDM reveals the possibility that the EW symmetry is not restored at high T, as well as the possible non-restoration of the discrete $\mathbb{Z}_2'$ symmetry of the singlet sector, see Eq. (3.28). The occurrence of $\mathbb{Z}_2'$ SnR at high temperature has also been explored for a singlet extension of the SM [355]. We will discuss the details of EW SnR within the N2HDM in the next section.

6.4 Symmetry non-restoration at high T

We now investigate whether the EW symmetry remains un-restored at high T within the N2HDM. In a first step we do this analytically by studying the curvature of the effective potential around $\langle \Phi_1 \rangle = 0$, $\langle \Phi_2 \rangle = 0$ in the high-temperature limit. We find that, under certain assumptions (see below), the fate of the EW symmetry at high temperatures (restoration *vs.* non-restoration) can be reliably determined from our analysis, while this is not necessarily true for the restoration or non-restoration of the $\mathbb{Z}_2'$ symmetry of the singlet field. We then compare our analytical results with our numerical study of the effective potential evolution with temperature in Sec. 6.4.2, and discuss the implications of our results for the EW phase transition in Sec. 6.4.3.

6.4.1 Analytical considerations

In order to analytically study the behavior of the effective potential at high T, we use Eq. (4.49) for the thermal functions $J_\pm$ and compute V_{daisy}, given by Eq. (4.53), in the limit $m^2(\phi)/T^2 \ll 1$. In addition, since the leading ($\sim T^2$) contributions to the squared thermal masses Π^2 enter only into the diagonal elements of the scalar mass matrices, as shown in Eqs. (6.10)–(6.12), the off-diagonal terms can be neglected in the high-T limit.

The restoration of *both* the EW symmetry and the discrete $\mathbb{Z}_2'$ symmetry of the singlet field requires the origin of field space $\langle \Phi_1 \rangle = 0$, $\langle \Phi_2 \rangle = 0$, $\langle \Phi_S \rangle = 0$ to be a minimum at high temperature. In order to assess whether this is the case we compute the principal minors of the Hessian matrix $H^0_{ij} = \partial^2 V / \partial\rho_i \partial\rho_j \big|_{(0,0,0)}$ as a function of the parameters of

---

[1] A corresponding observation of such a situation has recently been made for the NMSSM [279].

the theory. The conditions for the origin to be a minimum of the N2HDM potential at large T (large in comparison to the bilinear terms of the theory) are

$$H_{11}^0 > 0 \ , \tag{6.16}$$

$$H_{11}^0 H_{22}^0 - \left(H_{12}^0\right)^2 > 0 \ , \tag{6.17}$$

$$H_{33}^0 > 0 \ , \tag{6.18}$$

where we made use of the fact that $H_{13}^0 = H_{23}^0 = 0$. Since the cross derivative $H_{12}^0 = -m_{12}^2$ does not depend on T, the above conditions can be simply cast as $c_{ii} \equiv \lim\limits_{T\to\infty} H_{ii}^0/T^2 > 0$ with $i = 1, 2, 3$. The coefficients c_{ii} are given by

$$c_{11} \simeq -0.025 + c_1 - \frac{1}{2\pi}\left(\frac{3}{2}\lambda_1\sqrt{c_1} + \lambda_3\sqrt{c_2} + \frac{1}{2}\lambda_4\sqrt{c_2} + \frac{1}{4}\lambda_7\sqrt{c_3}\right) \ , \tag{6.19}$$

$$c_{22} \simeq -0.025 + c_2 - \frac{1}{2\pi}\left(\frac{3}{2}\lambda_2\sqrt{c_2} + \lambda_3\sqrt{c_1} + \frac{1}{2}\lambda_4\sqrt{c_1} + \frac{1}{4}\lambda_8\sqrt{c_3}\right) \ , \tag{6.20}$$

$$c_{33} = c_3 - \frac{1}{2\pi}\left(\lambda_7\sqrt{c_1} + \lambda_8\sqrt{c_2} + \frac{3}{4}\lambda_6\sqrt{c_3}\right) \ , \tag{6.21}$$

with $\lambda_i \equiv \lambda_i^{\mathrm{OS}}$. Here, the contribution of the SM gauge couplings g and g' to (6.19) and (6.20) arising from the resummation of daisy diagrams is given numerically (≈ -0.025) for reasons of compactness. Even though our analysis focuses in the N2HDM type II, these coefficients are valid for all Yukawa types up to subleading corrections proportional to the tau lepton and the bottom quark Yukawa couplings. The quantity c_2 receives a large positive contribution from the top Yukawa coupling (see Eq. (6.14)). Thus, for the moderate values of λ_i used in our analysis one finds $c_{22} > c_{11}$, and accordingly the simultaneous restoration of both the EW and $\mathbb{Z}_2'$ symmetries at high temperature occurs for positive c_{11} and c_{33}. In contrast, for positive c_{33} but negative c_{11} the EW symmetry is not restored at high temperatures.[2]

For $c_{33} < 0$, the origin of field space is unstable along the singlet field direction ρ_3. The analysis of EW symmetry restoration in this case requires the investigation of the curvature of the effective potential at high temperature around $\langle\Phi_1\rangle = 0$, $\langle\Phi_2\rangle = 0$, $\langle\Phi_S\rangle = v_S(T)$, where $v_S(T)$ denotes the (nonzero) minimum of the potential along the ρ_3 field direction. The curvature around $(0,\,0,\,v_S(T))$ in the direction of ρ_1 is given by

$$c_{11}^S = \lim_{T\to\infty} \frac{H_{11}^S(v_S(T),T)}{T^2} \ , \quad \text{with} \quad H_{11}^S(\rho_3,T) = \left.\frac{\partial^2 V}{\partial\rho_1^2}\right|_{(0,0,\rho_3)} \ . \tag{6.22}$$

Then, $c_{11}^S < 0$ is a sufficient condition for EW SnR when $c_{33} < 0$. As discussed above, from the large positive contribution of the top Yukawa coupling to the curvature in the direction of ρ_2, we generally expect this to be larger than the curvature in the direction of ρ_1. So, for

---

[2] We note that in this case, determining whether the $\mathbb{Z}_2'$ symmetry is restored or non-restored at high T would require the exploration of the N2HDM scalar potential away from the origin of field space, along the EW field directions (for $\langle\Phi_1\rangle \neq 0$, $\langle\Phi_2\rangle \neq 0$), corresponding to a much more involved analysis.

$c_{11}^S > 0$ (when $c_{33} < 0$) the EW symmetry is generally restored at high T. The coefficient c_{11}^S takes the form

$$\begin{aligned} c_{11}^S = \lim_{T\to\infty} \Bigg\{ &- 0.025 + c_1 + \frac{\lambda_7}{2}\frac{v_S^2(T)}{T^2} - \frac{1}{2\pi}\Bigg(\frac{3}{2}\lambda_1\sqrt{c_1 + \frac{\lambda_7}{2}\frac{v_S^2(T)}{T^2}} \\ &+ \lambda_3\sqrt{c_2 + \frac{\lambda_8}{2}\frac{v_S^2(T)}{T^2}} + \frac{\lambda_4}{2}\sqrt{c_2 + \frac{\lambda_8}{2}\frac{v_S^2(T)}{T^2}} + \frac{\lambda_7}{4}\sqrt{c_3 + \frac{\lambda_3}{2}\lambda_6\frac{v_S^2(T)}{T^2}}\Bigg)\Bigg\} \\ &= c_{11} + \mathcal{O}\left(\frac{v_S(T)^2}{T^2}\right) . \end{aligned} \tag{6.23}$$

From a computational perspective, calculating c_{11}^S is slightly more involved than obtaining c_{11} since one has to identify the extrema of the scalar potential in the plane $(0, 0, \rho_3)$ as a function of temperature to obtain $v_S(T)$. We also remark that the analysis of EW SnR based on the sign of c_{11}^S relies on the validity of the high-T expansion: the N2HDM scalar masses evaluated at $(0,\, 0,\, v_S(T))$ receive contributions (dependent on λ_6, λ_7 and λ_8) proportional to the singlet vev $v_S(T)$, and $|v_S(T)|$ will be a monotonically increasing function of temperature. In order to guarantee that these contributions do not render the scalar masses at $(0,\, 0,\, v_S(T))$ comparable to the temperature, thus invalidating the high-T expansion, we require $|\lambda_6|, |\lambda_7|, |\lambda_8| < 1$ at the initial scale $\mu_0 = v$.[3]

From Eq. (6.23), if the corrections proportional to $v_S(T)^2/T^2$ are subleading compared to the coefficient c_{11}, i.e. $|c_{11}| \gg |v_S(T)^2/T^2|$, this coefficient c_{11} defined at the origin in field space also controls the stability of the field space point $(0, 0, v_S(T))$ in the direction of ρ_1 in the high-temperature limit. Then, the sign of c_{11} determines the high-T restoration/non-restoration of the EW symmetry for both $c_{33} > 0$ and $c_{33} < 0$. On the other hand, if the $\mathcal{O}\left(v_S(T)^2/T^2\right)$ term in Eq. (6.23) is comparable in size to c_{11}, then the full calculation of c_{11}^S is needed to assess the fate of the EW symmetry at high T (when $c_{33} < 0$). The coupling λ_7 plays an important role in this respect: the only $\mathcal{O}(v_S(T)^2/T^2)$ term in Eq. Eq. (6.23) proportional to a single power of λ_i, and not suppressed by an additional $(2\pi)^{-1}$ factor, depends precisely on λ_7. This is then the most important parameter for the $\mathcal{O}(v_S(T)^2/T^2)$ corrections in c_{11}^S.

In order to illustrate this analytic assessment of the EW SnR behavior at high temperature, we now discuss several benchmark scenarios ($A_{1,2}$, $B_{1,2}$, $C_{1,2}$, D), defined in Table 6.1 in terms of their `ScannerS` input parameters, which are in agreement with all constraints discussed in Sec. 6.2. We have required $|\lambda_{6,7,8}| < 1$ for all benchmarks to ensure the validity of the high-T expansion, and imposed $|\lambda_{1,\ldots,5}(\mu = v)| < 3$ for the other quartic couplings to guarantee that they remain perturbative much above the TeV scale, as discussed in Sec. 6.1. The bounds on $|\lambda_i|$ lead to a common feature for all benchmarks: the pseudoscalar A, the charged Higgs bosons $H^\pm$ and the heavy doublet-like scalar are close to each other in mass,

---

[3] The dependence of $\lambda_{6,7,8}$ on μ is very mild for $|\lambda_{6,7,8}(\mu_0)| < 1$ due to the singlet nature of ρ_3. In the following, all quoted values of $\lambda_{6,7,8}$ (e.g. in Table 6.2) are understood to be given at $\mu_0 = v$, having in mind that they are not substantially different at $\mu > v$ within the perturbative regime.

	m_{h_1}	m_{h_2}	m_{h_3}	m_A	$m_{H^\pm}$	t_β	C_{h_1tt}	C_{h_1VV}	$\mathrm{sgn}\,(R_{13})$	R_{23}	m_{12}^2	v_S
A_1	125.09	934	1263	1008	958	1.72	0.94	0.94	-1	-0.22	604^2	2637
A_2	125.09	840	1355	904	828	1.73	0.99	0.96	-1	-0.104	557^2	2298
B_1	125.09	589	760	739	748	1.51	0.99	0.99	$+1$	-0.96	495^2	2500
B_2	125.09	685	700	680	678	2	0.97	0.97	$+1$	-0.46	436^2	1100
C_1	125.09	835	1370	897	834	1.1	0.97	0.96	$+1$	0.04	559^2	2707
C_2	125.09	792	850	835	814	1.02	0.99	0.99	-1	0.51	510^2	2565
D	125.09	408	717	731	707	2	0.99	0.99	$+1$	0.86	380^2	1487

Table 6.1: Illustrative type II N2HDM benchmarks for high-T EW symmetry restoration/non-restoration, in terms of `ScannerS` input parameters. The parameters m_{h_i}, m_A, $m_{H^\pm}$, m_{12} and v_S are given in GeV.

with their mass scale roughly given by $M \equiv \sqrt{m_{12}^2/(s_\beta c_\beta)}$.[4] Also, the values $t_\beta \gtrsim 1$ that have been chosen for all displayed benchmarks correspond to the parameter region for which the various theoretical and experimental constraints are most easily accommodated [176]. In Table 6.2 we show the values of c_{11} and c_{33} for each of the benchmarks (we have verified that $c_{22} > 0$ for all of them). For benchmarks $\mathrm{C}_{1,2}$ we find $c_{33} > 0$, and accordingly the sign of c_{11} fully determines the fate of EW symmetry at high temperature. In both cases $c_{11} < 0$ holds, and thus the EW symmetry is un-restored at high T. For benchmarks $\mathrm{A}_{1,2}$, $\mathrm{B}_{1,2}$ and D we have $c_{33} < 0$, and thus the origin of field space is unstable along the singlet field direction. The possible restoration of the EW symmetry in this case is controlled by the sign of c_{11}^S, also shown in Table 6.2. For $\mathrm{B}_{1,2}$ and D we find $c_{11}^S > 0$, and thus the EW symmetry is restored at high T, while the singlet $\mathbb{Z}_2'$ symmetry remains broken at high T. In contrast, for $\mathrm{A}_{1,2}$ the EW symmetry is not restored at high temperature since $c_{11}^S < 0$.

The scenarios $\mathrm{A}_{1,2}$ and $\mathrm{B}_{1,2}$ are benchmarks for which $|c_{11}| \gg |v_S(T)^2/T^2|$ at high temperature, such that c_{11} determines the fate of the EW symmetry in this limit. The signs of c_{11} and c_{11}^S are the same for such a case, as shown explicitly in Table 6.2. In contrast, for benchmark D we have $c_{11}^S > 0$ despite the negative value of c_{11}. This behavior is caused by the small value of $|c_{11}|$ (the smallest among all benchmarks) together with a sizeable value of λ_7 (the largest among all benchmarks, also shown in Table 6.2). This renders the contribution given by $\lambda_7/2\ v_S^2(T)/T^2$ in (6.23) large in comparison to c_{11}, leading to the restoration of the EW symmetry at high T even for $c_{11} < 0$.

The different types of scenarios regarding EW symmetry restoration or non-restoration at high temperature discussed above are illustrated in Figure 6.1, where each plot corresponds to a different type of benchmark (A, B, C, D). Figure 6.1 shows the behavior of the effective potential (in the high T approximation) along the $(0,\, 0,\, \rho_3)$ field space direction and in dependence of T. The region for which $H_{11}^S(\rho_3, T) < 0$ is depicted in light blue, and the

---

[4] This is h_2 for benchmarks $\mathrm{A}_{1,2}$, C_1 and h_3 for benchmarks B_1, D. For benchmarks B_2, C_2 the doublet–singlet mixing is sizeable, such that $m_{h_{2,3}} \approx M$.

	A_1	A_2	B_1	B_2	C_1	C_2	D
c_{11}	-0.092	-0.06	0.182	0.10	-0.104	-0.04	-0.006
c_{33}	-0.011	-0.02	-0.002	-0.002	0.058	0.005	-0.010
$\text{sgn}(c_{11}^S)$	-	-	+	+	-	-	+
λ_6	0.211	0.329	0.058	0.382	0.246	0.104	0.115
λ_7	0.154	0.400	-0.199	-0.440	-0.465	0.218	0.760
λ_8	0.703	0.986	0.007	-0.362	-0.613	0.087	0.271

Table 6.2: The values of c_{11}, c_{33} and $\text{sgn}(c_{11}^S)$ for each of the benchmarks defined in Table 6.1. For all displayed benchmark scenarios $c_{22} > 0$ holds. Also shown are the values of the singlet field quartic couplings $\lambda_{6,7,8} = \lambda_{6,7,8}^{\text{OS}}$.

dark blue lines show the stationary points along the singlet field direction,[5] i.e. the solutions to

$$N_S(\rho_3, T) = \left.\frac{\partial V(T)}{\partial \rho_3}\right|_{(0,0,\rho_3)} = 0\,. \tag{6.24}$$

Given the symmetry of the potential, these solutions correspond to $\rho_3 = 0$ and $\rho_3 = \pm v_S(T)$, the latter only appearing as solutions (in this case, yielding two identical stationary points) when the field space point (0, 0, 0) is either a maximum or a saddle point of the effective potential. When a dark blue line in Figure 6.1 lies within the light blue region, the corresponding extremum along the singlet direction ρ_3 is unstable along the ρ_1 field direction, and the EW symmetry will not be restored there. For benchmark A_1 in the upper-left plot of Figure 6.1, none of the $N_S(\rho_3, T)$ stationary points is stable in the direction of ρ_1 for $T \gtrsim 2$ TeV. Therefore, the EW symmetry is inevitably un-restored at high temperature. In contrast, for benchmark B_1 in the upper-right plot of Figure 6.1, the extrema $(0, 0, \pm v_S(T))$ are stable along the ρ_1 field direction and correspond to global minima of the N2HDM potential at high temperature, leading to EW symmetry restoration. For benchmark C_1 in the lower-left plot of Figure 6.1, the only extremum along the singlet direction at high T (in this case, for $T \gtrsim 3.5$ TeV) is $\rho_3 = 0$, since $c_{33} > 0$. Yet, the origin of field space is unstable in the direction of ρ_1 at high T, as a result of $H_{11}^S(0, T \gtrsim 3\,\text{TeV}) < 0$, and the EW symmetry is therefore not restored in this case. Finally, for benchmark D in the lower-right plot of Figure 6.1, we observe that for the extremum $\rho_3 = 0$ (a maximum along the singlet direction), we have $H_{11}^S(0, T) < 0$ as a consequence of $c_{11} < 0$. However, for the other two extrema $\rho_3 = \pm v_S(T)$, which correspond to minima along the singlet direction, we have $H_{11}^S(\pm v_S(T), T) > 0$. This leads to EW symmetry restoration at high temperature in the field space points $(0, 0, \pm v_S(T))$.

To summarise, our analytical approach based on the high-T expansion of the effective potential allows one to determine the restoration or non-restoration of the EW symmetry

---

[5] Note that along the ρ_1 and ρ_2 field directions the derivatives are 0 automatically for $(0, 0, \rho_3)$ due to $SU(2)_L$ gauge invariance.

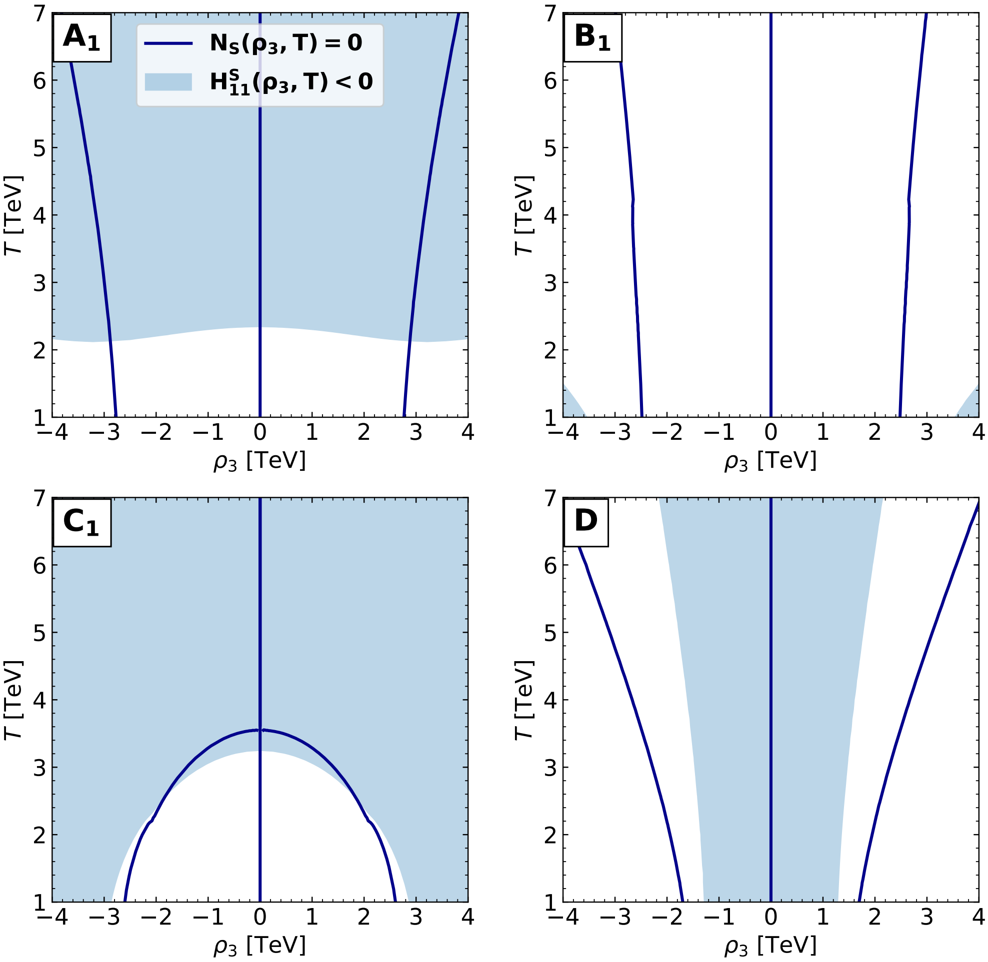

Figure 6.1: (ρ_3–T) plane for four qualitatively different benchmark scenarios (depending on the sign of the coefficients c_{11}, c_{33} and c^S_{11}, see text for details) from Table 6.1, A$_1$ (top-left), B$_1$ (top-right), C$_1$ (bottom-left) and D (bottom-right). The region for which $H^S_{11}(\rho_3, T) < 0$ is depicted in light blue. The dark blue lines indicate the stationary points with $N_S(\rho_3, T) = 0$ of the high temperature approximation of the potential.

above the TeV scale in the N2HDM (our approach could be easily applied also to other multi-scalar BSM scenarios), in a fast and computationally inexpensive way.[6] We find that in this scenario a part of the parameter space leads to EW SnR at high temperatures. It is also interesting to note that in previous studies of EW SnR (see e.g. [47, 48]), the daisy resummation terms tend to restore the EW symmetry at high T, partially counterbalancing the SnR effect of $c_h < 0$ (where c_h denotes the corresponding coefficient c_i for the case of the SM-like Higgs boson). In our study of the N2HDM we observe the opposite behavior, as the SnR at high temperature is driven by contributions from the resummation of daisy

---

[6] It is certainly much less expensive than a fully-fledged numerical minimization of the 1-loop finite temperature potential in the three-dimensional field space $(\rho_1(T), \rho_2(T), \rho_3(T))$.

diagrams[7] that enter the computation of the curvature with an overall minus sign. They can prevent the restoration of the EW symmetry without the occurrence of negative values of the quartic couplings, which are often in contradiction with bounded-from-below constraints. Since the daisy contributions to Eqs. (6.19)–(6.21) depend on a higher power of the scalar quartic couplings λ_j than the coefficients c_i, the potential non-restoration behavior for the N2HDM arises for the case where (some of) the scalar couplings λ_j are of $\mathcal{O}(1)$. Accordingly, for all benchmark points discussed in this section we have checked the RGE running (as discussed in Sec. 6.1), ensuring that the quartic couplings satisfy the general perturbativity condition $\left|\lambda_i^{\overline{\mathrm{MS}}}(\mu)\right| < 4\pi$ for energy scales into the tens of TeV. A detailed discussion on this issue is deferred to the following section.

Finally, we bear in mind that the study in this section has been based on the high-T expansion,[8] and as such the T dependence in Figure 6.1 is expected to be fully controlled only in the high-T limit. A more detailed analysis of the intermediate T regime should be based on the full one-loop finite-T effective potential, which can only be computed numerically. This issue is addressed in the next section.

6.4.2 Numerical Analysis

As discussed above, while the analytical approach developed in the previous section allows the determination of the fate of the EW symmetry at temperatures far above the TeV scale, the details of the temperature evolution from the vicinity of the EW scale upwards need to be explored numerically. For the numerical computations, we have implemented the full one-loop effective potential given in Eq. (6.7), together with the resummed daisy contributions following the AE method, given by Eq. (4.53), using `CosmoTransitions` [196] to analyse its phase/vacuum structure as a function of T. The thermal functions have been calculated using a cubic spline approximation to the exact functions given in Eq. (4.48).

In order to ensure the validity of our numerical analysis, we first have to verify that the values of the quartic couplings $\lambda_i^{\overline{\mathrm{MS}}}$ are well within the perturbative regime over the whole temperature range that has been investigated. As explained in Sec. 6.1, we perform the RGE evolution of the model parameters at the two-loop level, and the energy scale μ has been varied far beyond the maximum temperature that is relevant to our analysis. To illustrate this we show in Figure 6.2 the $\overline{\mathrm{MS}}$ values of the quartic couplings, $\lambda_i^{\overline{\mathrm{MS}}}$, as a function of the scale μ for benchmarks A_2 (left), B_2 (middle) and C_2 (right) from Table 6.1. For all three benchmarks, the various $\lambda_i^{\overline{\mathrm{MS}}}$ remain perturbative up to at least $\mu = 50$ TeV, and the overall change of the couplings with the energy scale is mild below 10 TeV due to the small coupling values at the initial scale $\mu_0 = v$. Similar results are obtained for all our benchmarks from Table 6.1.

We present a first comparison between our analytical and numerical analyses in Figure 6.3, which shows (as Figure 6.1) the behavior of the effective potential along the $(0,\, 0,\, \rho_3)$ field space direction and in dependence of T, here for the benchmarks A_2 (top), B_2 (middle) and

---

[7] The same behaviour has been reported very recently in Ref. [356].

[8] The use of only the leading T^2 terms guarantees here the gauge independence of the effective potential.

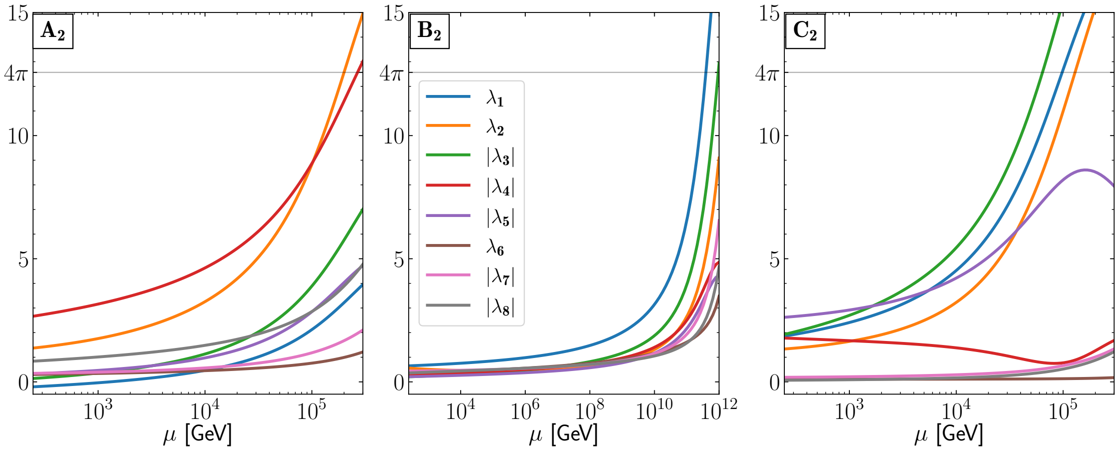

Figure 6.2: Dependence of the quartic couplings $\lambda_i^{\overline{\rm MS}}$ on the energy scale μ for the benchmark points A$_2$ (left), B$_2$ (center) and C$_2$ (right). The gray line indicates the perturbativity bound of 4π.

C$_2$ (bottom). The predictions based on the high-T approximation used in our analytical approach are shown on the left-hand side, whereas the numerical results based on the full one-loop potential are shown on the right-hand side. As in Figure 6.1, the dark-blue lines correspond to $N_S(\rho_3, T) = 0$, and the region in which $H^S_{11}(\rho_3, T) < 0$ is shown in light-blue. In the case of benchmark A$_2$ (upper row of Figure 6.3), while both the numerical and analytical approaches show the non-restoration of the EW symmetry at high T, the shape of the $H^S_{11}(\rho_3, T) < 0$ region differs between the two approaches. This difference is due to the inaccuracy of the analytical treatment in field space points in which the field values are comparable in size to the temperature. Since $c_{33} < 0$ (see Table 6.1), $|v_S(T)|$ grows with temperature at high T, and the scalars whose masses receive a large contribution from the singlet vev (note that $\lambda_{6,7,8}$ are sizeable for this benchmark) can therefore affect the convergence of the high-T expansion. Here it should also be noted that the derivatives of the $J^\pm$ functions have a slower convergence towards the corresponding high-T expansions than the functions themselves [357]. At the same time, the numerical implementation of the thermal functions $J^\pm$ via a cubic spline introduces a small source of uncertainty when computing numerical derivatives,[9] which can also impede a better agreement between the two methods (see also discussion below). For benchmarks B$_2$ and C$_2$ only minor differences arise from the uncertainties discussed above, and a good agreement between the analytical and numerical approaches is found.

In order to better understand the differences between the analytical and the numerical approach, in Figure 6.4 we show for the three benchmark points used above the curvatures at the origin of field space, H^0_{ii}, as a function of temperature. In the numerical analysis, we compare the AE (solid-red lines) and Parwani (dotted-green lines) approaches. The values of H^0_{ii} computed analytically using the high-T expansion (according to the AE approach,

---

[9] See [357] for a detailed discussion of the numerical issues related to the precise form of the implementation of the thermal functions $J^\pm$ and their derivatives.

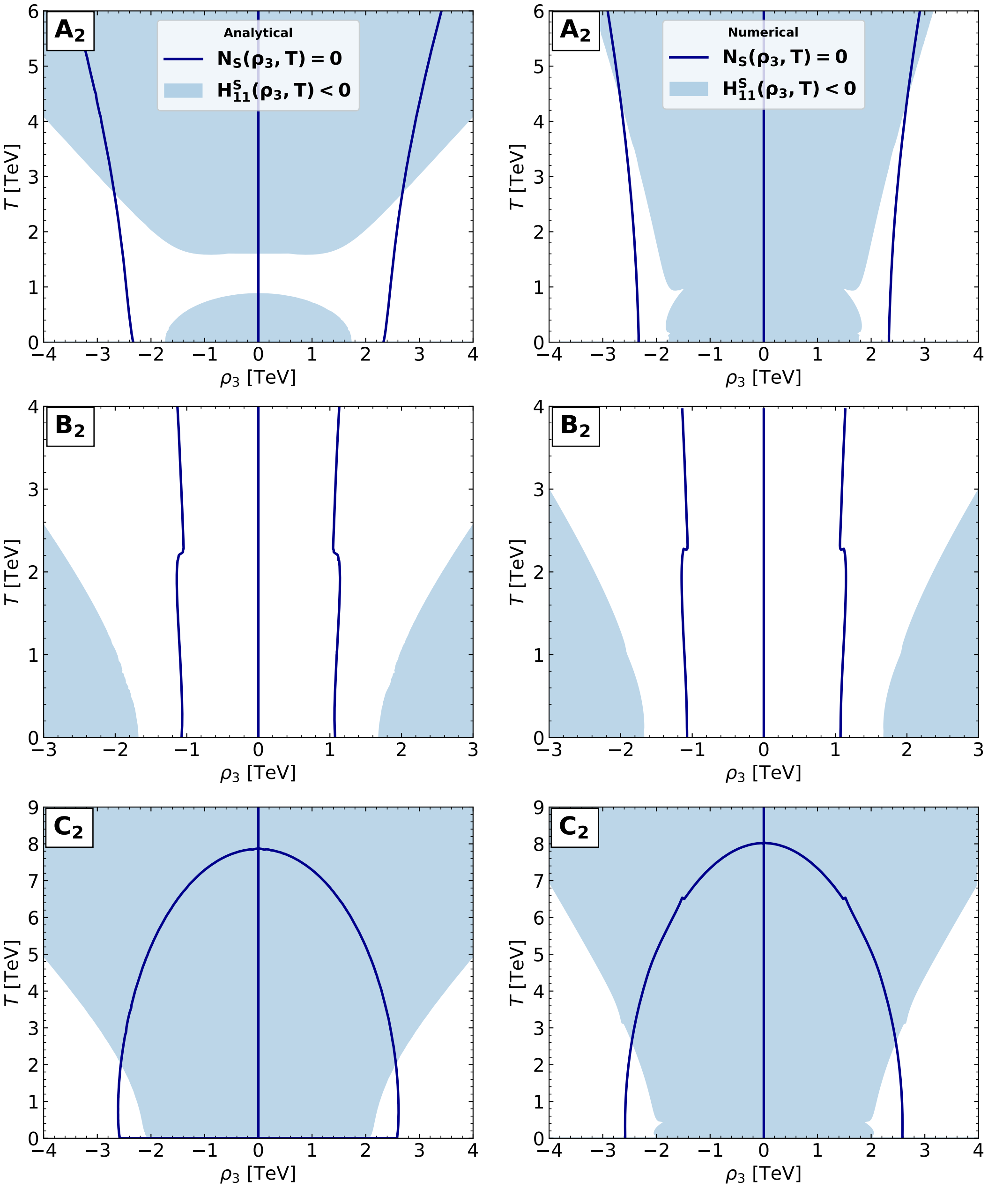

Figure 6.3: Comparison of the (ρ_3–T) plane obtained analytically (left) and numerically (right) for the benchmark scenarios A_2 (top), B_2 (middle) and C_2 (bottom) from Table 6.1. The colour code is the same as in Figure 6.1.

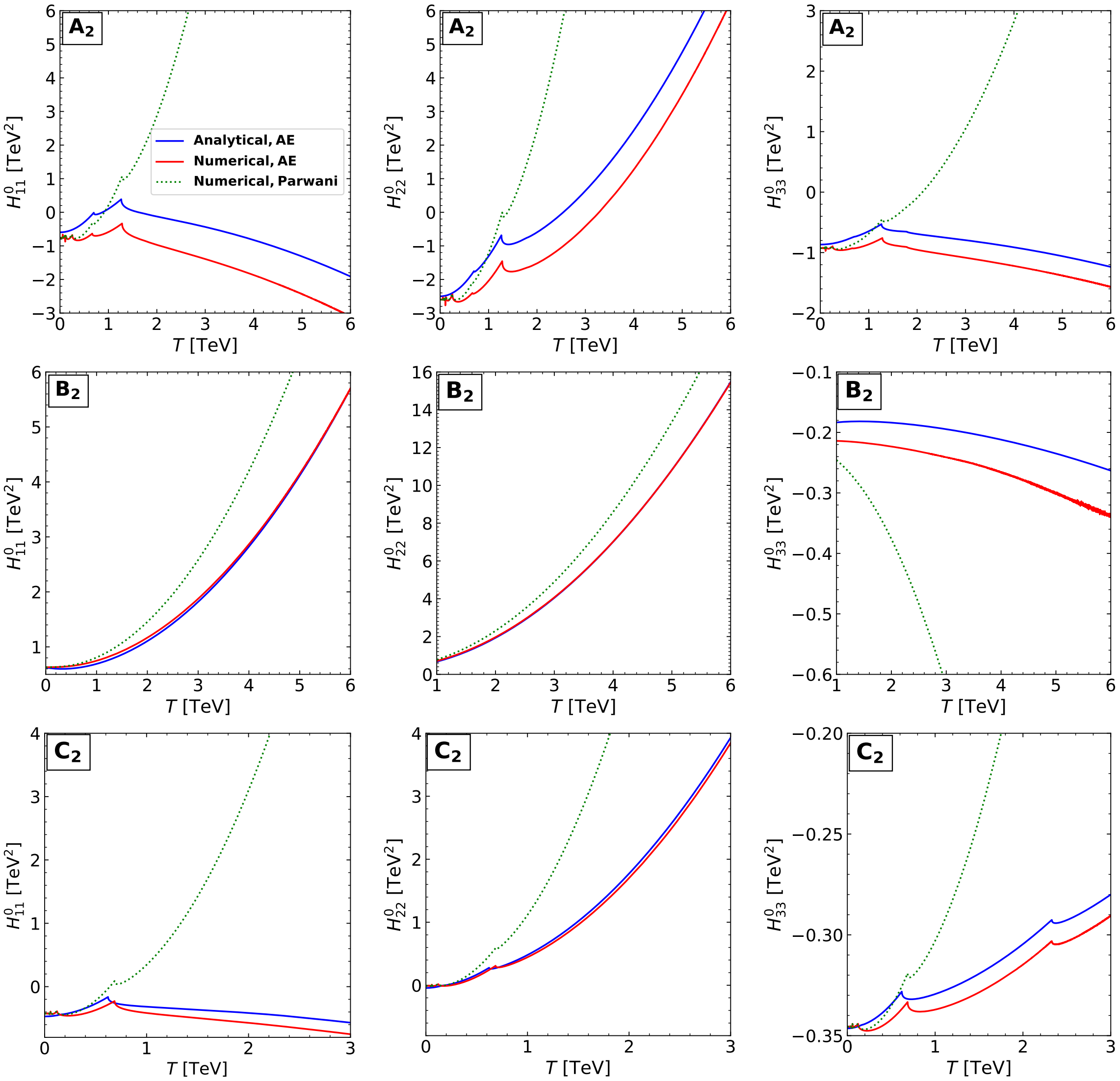

Figure 6.4: Second derivatives of the effective potential at the origin of field space, H^0_{ii}, as a function of temperature for the benchmarks A_2 (upper row), B_2 (middle row) and C_2 (lower row) using the analytical (within the AE – AE – approach) high-T approximation (blue) and evaluated numerically using the AE approach (red) and the Parwani approach (dashed green).

see the discussion in Sec. 6.4.1) are also depicted (solid-blue lines). One can observe that the Parwani method agrees with the AE numerical result only for very small T and thus can lead to a different prediction for the restoration of both the EW and the $\mathbb{Z}_2'$ symmetries.[10] This is indicated by the fact that in several cases the result for H_{ii}^0 grows with temperature using the Parwani implementation, while the result for H_{ii}^0 obtained with the AE method decreases with temperature (see, for instance, the upper left and upper right plot of Fig. 6.4). Thus, these two methods employed in the literature to resum the contributions from daisy diagrams may yield qualitatively different behaviors at high temperature, as was already pointed out in Sec. 6.3 (see also Eq. (6.9)).

We also see from Figure 6.4 that our H_{ii}^0 analytical computation agrees well with the AE numerical result. Only a minor difference is present between the numerical result and the analytical one (both rely on the AE method). This difference is mainly driven by the fact that the $\mathcal{O}(y^3)$ and, in particular, the logarithmic pieces of the expansions of the $J^{\pm}$ functions are not taken into account in the analytical treatment, whereas they are implicitly contained in the numerical result, for which the thermal functions are implemented as an interpolation to the exact form of the integrals. As a result of this interpolation, also the numerical predictions for the second derivatives suffer from an uncertainty at large temperatures, due to the fact that the tiny variations of the functional argument y cannot be resolved.[11] In combination, the uncertainties of both methods give rise to the small offsets between the blue and the red curves that are visible in Fig. 6.4. These differences however do not affect our results for the EW symmetry restoration behavior, for which the predictions obtained using the numerical and the analytical method within the AE approach are very similar In view of the discussion in the previous section, this adds support to the reliability of our analytical analysis for predicting the fate of the EW symmetry at high temperature in the N2HDM [359]. In particular, if $c_{33} > 0$ or if $c_{33} < 0$ and $v_S(T)^2/T^2$ is sufficiently small at high T (see Eq. (6.23)), the coefficient c_{11} controls the stability of the effective potential along the doublet field directions at high T.

An analogous approach can be applied to the study of the fate of the discrete $\mathbb{Z}_2'$ symmetry as a function of temperature. In this case, however, we can only make definite analytical statements regarding the restoration of the $\mathbb{Z}_2'$ symmetry in a handful of scenarios: if both c_{11} and c_{33} are positive, the $\mathbb{Z}_2'$ symmetry is restored at high T, while if $c_{33} < 0$ and $c_{11}^S > 0$ then the $\mathbb{Z}_2'$ symmetry is broken at high T. The investigation of other scenarios would require a numerical analysis of the finite temperature effective potential for $\langle \Phi_1 \rangle \neq 0$, $\langle \Phi_2 \rangle \neq 0$, which can be in principle performed with `CosmoTransitions`, but which we do not pursue further in this work.

The cosmological consequences of the possible non-restoration of EW and/or $\mathbb{Z}_2'$ symmetries are several: domain wall problems in cosmology are associated with the existence

---

[10] The Parwani method inconsistently mixes loop contributions of different orders in the couplings and the temperature (see e.g. [358, 359]), such that thermal effects are enhanced as compared to the AE approach. Using the latter, the cancellation between logarithmic contributions between V_{CW} and V_T are ensured in the high-T limit.

[11] We used a step size of $y_{\text{step}} = 0.01$ for the cubic spline interpolation of $J^{\pm}(y)$.

m_{h_a}	m_{h_b}	m_{h_c}	m_A	$m_{H^\pm}$	$\tan\beta$	$C^2_{h_a t\bar{t}}$	$C^2_{h_a VV}$	R_{b3}	m^2_{12}	v_S
125.09	$[30, 1000]$	400	650	650	2	1	1	$[-1, 1]$	65000	$[1, 1000]$

Table 6.3: Set of input parameters for our `ScannerS` scan. All the input parameters remain fixed except for the mass of one of the CP-even Higgs bosons m_{h_b}, its singlet component R_{b3} (with $\Sigma_{h_b} = |R_{b3}|^2$) and the singlet vev at $T = 0$, v_S.

of multiple vacua in theories with spontaneous breaking of discrete symmetries. However, N2HDM scenarios in which the $\mathbb{Z}'_2$ symmetry is never restored would trivially avoid the formation of domain walls, i.e. eliminating the domain-wall problem. On the other hand, an un-restored EW symmetry at high temperatures would lead to a very strong suppression of the baryon-number-violating sphaleron transitions at those temperatures, possibly hindering baryogenesis/leptogenesis mechanisms relying on sphalerons. Yet, we stress that high-T EW SnR is not incompatible with having $H^0_{11} > 0$ at intermediate temperatures, as shown e.g. in Figure 6.4, top-left (see also Figure 6.3, top-left). This means that the EW phase transition could take place also in such scenarios. We will explore this possibility in more detail in the next section.

6.4.3 The EW phase transition and SnR

In this section we explore the possibility of a FOEWPT in the N2HDM and discuss its connection to the possible non-restoration of the EW symmetry at high T. The simultaneous occurrence of both phenomena requires a temporary restoration of the EW symmetry, together with its breaking at higher temperatures.

In order to investigate the parameter region of the N2HDM possibly realising a FOEWPT, we start by discussing the region of the 2HDM featuring a FOEWPT, and analyse in the next step how the presence of the singlet field Φ_S in the N2HDM affects this picture. In the type II 2HDM the region of parameter space giving rise to a FOEWPT is quite constrained: it generally correlates with the existence of sizeable quartic couplings among $\lambda_{3,4,5}$ in the 2HDM scalar potential. Since the mass splittings between the 2HDM scalars are also controlled by such couplings, at least one of the additional 2HDM scalars (apart from the SM-like Higgs boson at about 125 GeV) must be significantly lighter or heavier than the overall mass scale $M = \sqrt{m^2_{12}/(\sin\beta\cos\beta)}$ of the second Higgs doublet [302]. Therefore, in general a FOEWPT in the 2HDM relies on a hierarchical spectrum with a considerable mass splitting between the pseudoscalar A and the heaviest CP-even Higgs boson H [39, 172, 301]. In the type II 2HDM B-physics observables push the mass of the charged scalar to $m_{H^\pm} > 590$ GeV [210]. In combination with EWPO constraints, this results in a most obvious possibility for the realization of a FOEWPT in a type II 2HDM consisting on a hierarchical spectrum with $m_A \approx m_{H^\pm} \gtrsim 600$ GeV and a substantially lighter scalar state H.[12]

---

[12] The opposite case with $m_H \approx m_{H^\pm} \gg m_A$ is much less favorable for FOEWPTs, as it requires almost exact alignment in order to decouple the heavy H from the phase transition dynamics [39, 172, 301].

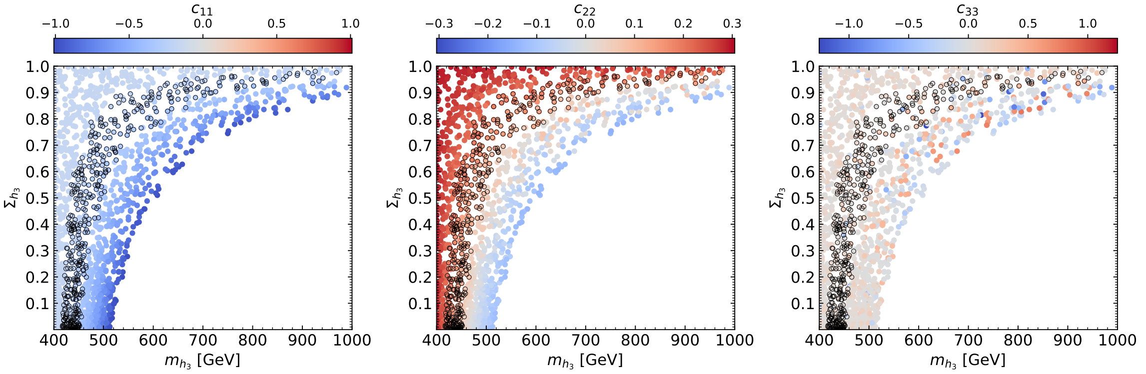

Figure 6.5: Singlet component Σ_{h_3} of the third CP-even Higgs boson in dependence of its mass m_{h_3}. The colour code indicates the value of the coefficients c_{11} (left), c_{22} (middle) and c_{33} (right). Points with a black circular edge feature a FOEWPT.

Based on the above considerations for the 2HDM, we generated a total of 2000 N2HDM benchmark points with `ScannerS` using values for the free parameters as shown in Table 6.3, with a flat prior for the parameters m_{h_b}, R_{b3} and v_S that have been varied. All the benchmarks fulfil the theoretical and experimental constraints described in Sec. 6.2. The chosen mass gap between m_{h_c} and m_A increases the possibility of a FOEWPT in analogy to the 2HDM case. We also focused on the alignment limit with $C^2_{h_a tt} = C^2_{h_a VV} = 1$, such that only h_b and h_c can have a non-zero singlet admixture (hence $R_{a3} = 0$). The parameters varied in our scan correspond to those related to the presence of the singlet in the N2HDM Higgs sector, i.e. the mass of a third CP-even Higgs boson m_{h_b}, its singlet component R_{b3} and the value of the singlet vev v_S.

Using `CosmoTransitions`, we have numerically analysed the thermal history of each scan point within the temperature regime $T = [0, 600\text{ GeV}]$, which covers the region relevant for the possible presence of a FOEWPT. At $T = 0$, we observe that each point has a global EW minimum of the kind (v_1, v_2, v_S) and a false minimum of the kind $(0, 0, \tilde{v}_S)$, separated by a potential barrier generated already at $T = 0$ by V_{CW}. We find that 542 points out of the 2000 initial `ScannerS` benchmarks feature a FOEWPT. Most of the scan points satisfy the general perturbativity conditions $|\lambda_i^{\overline{\text{MS}}}| < 4\pi$ up to energy scales larger than $\mu = 2$ TeV. At the same time, we find that our analytical analysis to ascertain the fate of the EW symmetry at high temperature is, for a large set of the scan sample, already applicable for $T \lesssim 1$ TeV, given that the mass scale of the doublet field bilinears is close to the EW scale for most of the benchmarks (e.g. the mass scale of the non-SM Higgs doublet is $M \approx 400$ GeV).

In Figure 6.5 we show the results of our `ScannerS` parameter scan in the $(m_{h_3}$–$\Sigma_{h_3})$ plane, i.e. the heaviest CP-even scalar mass vs. its singlet component, with the colour code indicating the value of the coefficients c_{11} (left), c_{22} (center) and c_{33} (right). The absence of points in the lower right region is due to the perturbative unitarity constraints. The points that feature a FOEWPT are highlighted with a black circular edge. We see that none of the points of our scan features the restoration of both the EW and $\mathbb{Z}_2'$ symmetries

	m_{h_1}	m_{h_2}	m_{h_3}	$m_{A,H^\pm}$	t_β	$C_{h_1tt/VV}$	sgn (R_{13})	R_{23}	m_{12}^2	v_S	c_{11}	c_{33}
E_1	125.09	400	517.29	650	2	1	-1	0.98	255^2	746.79	-0.99	0.007
E_2	125.09	400	487.29	650	2	1	-1	0.64	255^2	559.31	-0.24	0.03
E_3	125.09	400	550.25	650	2	1	-1	0.48	255^2	544.63	-0.25	0.03

Table 6.4: Type II N2HDM benchmarks corresponding to the scan described by the input parameters in Table 6.3. Point E_1 is a benchmark point for which the EW symmetry is never restored up to the maximum temperature analysed, $T_{\max}$, E_2 features a FOEWPT, and E_3 features a Universe trapped in a false vacuum at zero temperature. Also shown are the values of c_{11} and c_{33} for the three benchmark points. c_{22} is positive for the three scenarios. The parameters m_{h_i}, m_A, $m_{H^\pm}$, m_{12} and v_S are given in GeV.

at high temperature, given that $c_{11} < 0$ for all points. The coefficient c_{22}, even though positive for most benchmarks in the scan, reaches negative values for a fraction of the points. However, there is no point with $c_{22} < 0$ and $c_{11} > 0$ due to the positive Y_t contribution to c_{22}, which confirms our expectation that c_{22} provides no relevant information for the fate of the EW symmetry at high T (see the discussion in Sec. 6.4.1). The coefficient c_{33}, which is related to the possible restoration of the $\mathbb{Z}_2'$ symmetry, obtains values in our scan that range from ≈ -1.25 to ≈ 0.8. Figure 6.5 highlights that it is perfectly possible to have a FOEWPT together with an unrestored EW symmetry at higher temperatures within the N2HDM. Actually, all the scan points featuring a FOEWPT have $c_{11} < 0$ (note however that as discussed above $c_{11} < 0$ is only a sufficient condition for EW SnR at high T if $c_{33} > 0$). The connection between both phenomena lies in the fact that the sizeable scalar quartic couplings which contribute to making the EW phase transition strongly first-order in the (N)2HDM may also contribute to rendering the coefficients c_{ii} negative, see Eqs. (6.19)–(6.21).

In the following we choose three benchmark points from our parameter scan to illustrate different EW thermal histories (we give further details on the rationale behind this choice in the next section). The `ScannerS` input parameters of the three benchmarks $E_{1,2,3}$ are given in Table 6.4, in which we also show the values for their coefficients c_{11} and c_{33}. For these three benchmarks, we also use `CosmoTransitions` to numerically track the evolution of the vacuum of the system[13] ($v(T)$, $v_S(T)$) from a temperature $T_{\max} = 1$ TeV down to $T = 0$. We show in Figure 6.6 the temperature evolution of the EW vev $v(T)$ (left) and the singlet vev $v_S(T)$ (right) for each of the three benchmarks. For scenario E_1 the EW symmetry is never restored up to $T_{\max}$, and no EW phase transition occurs in this temperature range, in agreement with the expectation from the values of c_{11} and c_{33} for this benchmark (see Table 6.4). In contrast, scenario E_2 shows a FOEWPT with a nucleation temperature $T_n = 138$ GeV, and the EW symmetry is restored in the temperature range $T \in [T_n, 620 \text{ GeV}]$. For temperatures larger than ≈ 620 GeV the vacuum with $v(T) = 0$ is unstable, and the EW symmetry is thus un-restored at high T. The singlet vev $v_S(T)$

---

[13] We take into account all possible local minima at each temperature in the three-dimensional field space.

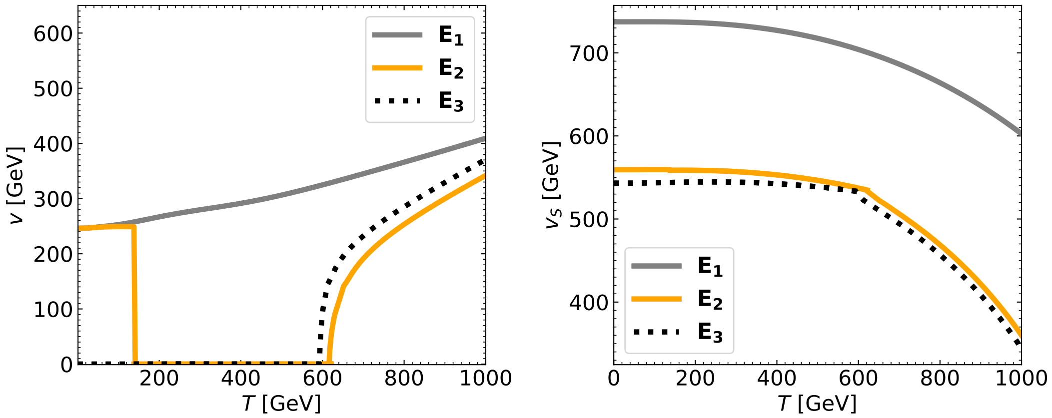

Figure 6.6: EW vev v (left) and singlet vev v_S (right) in dependence of the temperature for the benchmarks E_1 (solid gray), E_2 (orange) and E_3 (dashed black). These curves were computed using our numerical implementation of the full 1-loop potential in `CosmoTransitions`.

starts to decrease for $T \gtrsim 600$ GeV, which suggests that at very high temperatures the Universe would have been in an EW-breaking but $\mathbb{Z}_2'$-conserving vacuum configuration (this is in agreement with the values of c_{11} and c_{33} found for this scenario). Finally, for benchmark scenario E_3 the EW symmetry is broken at high temperatures and becomes unbroken when the Universe reaches a temperature $T \approx 600$ GeV. However, for lower temperatures the Universe does not undergo another transition to the EW vacuum,[14] but rather it is trapped in an EW symmetric phase down to $T = 0$, which makes this scenario unphysical. The existence of these *trapped-vacuum* scenarios in the N2HDM has already been briefly discussed in Sec. 6.3, and we will explore it in more detail in Sec. 6.5.

Before moving on to the next section, we note that for all three benchmarks $\mathrm{E}_{1,2,3}$ the value of the singlet vev $v_S(T)$ shows a decreasing trend for increasing temperature, as shown in Figure 6.6. Yet, the $\mathbb{Z}_2'$ symmetry is not restored at $T_{\max}$ and one would have to go to larger temperatures to observe its restoration (as expected from the value of c_{33} for all three benchmarks, see Table 6.4). However, the values of the quartic couplings λ_i for these benchmarks are relatively large, and we find that the RGE evolution of λ_i cannot be neglected for energies above 1 TeV. We therefore did not investigate here the behavior of the effective potential beyond $T_{\max} = 1$ TeV, which would require including the effect of this RGE evolution.

6.5 Trapped metastable singlet vacua

In Sec. 4.2.2 we pointed out the phenomenon of *vacuum trapping*: in the N2HDM a scenario with a global EW minimum at $T = 0$ could be unphysical due to the Universe being trapped in a false (singlet) vacuum. Vacuum trapping is expected to be particularly relevant in

---

[14] The point E_3 shows the peculiar phenomenon that the EW symmetry is broken at high T but unbroken at $T = 0$, the opposite of the commonly expected behavior.

parameter regions in which FOEWPTs can occur, as for such regions several minima that are simultaneously present in the early Universe (one of them being the EW-broken phase) can co-exist down to $T = 0$ (see also the analysis of the vacuum structure of the N2HDM at $T = 0$ that was performed in Ref. [199]). In this section we explore in more detail the occurrence of (singlet) vacuum trapping, and discuss its relation to the N2HDM parameter space region featuring a FOEWPT. Our analysis is divided into two different parts, which concentrate on two regions of the N2HDM parameter space with different phenomenological features: in Sec. 6.5.1 we analyse scenarios with a SM-like Higgs boson at about 125 GeV, h_{125}, where the singlet field mixes with the 2HDM-like heavy CP-even scalar H; in Sec. 6.5.2 we then analyse scenarios in which h_{125} contains a singlet admixture, while the singlet field does not mix with H. In both cases we study the interplay between scenarios with trapped singlet vacua and with a FOEWPT, as well as the connection of such early Universe phenomena to the phenomenology of the N2HDM.

In the following we also emphasise the conceptual differences between the N2HDM and the (extensively studied) 2HDM regarding the EW phase transition. In the N2HDM, due to the presence of the singlet field and its associated $\mathbb{Z}_2'$ symmetry, there can be several phase transitions during the thermal history of a specific N2HDM scenario. Yet, since the singlet field does not couple directly to the massive degrees of freedom of the SM (besides the Higgs sector), the breaking of the $\mathbb{Z}_2'$ symmetry usually takes place at higher temperatures than the EW phase transition.[15] Thus, the FOEWPTs that we analyse in the following are of the type $(0, 0, \tilde{v}_S(T)) \rightarrow (v_1(T), v_2(T), v_S(T))$, where $\tilde{v}_S(T)$ and $v_S(T)$ are the vevs of the singlet field in the EW-conserving *false* minimum and the EW-breaking *true* minimum, respectively. This type of transitions obviously does not exist in the case of the 2HDM.

6.5.1 Case 1: Singlet admixture in H

We focus here on scenarios where the singlet scalar field mixes only with the heavy CP-even 2HDM state H, while the SM-like Higgs boson at about 125 GeV is unaffected by the mixing with the singlet state. We use again the N2HDM parameter scan discussed in Sec. 6.4.3 in connection to EW SnR, as defined in Table 6.3. We note that the scan parameter values, and in particular the hierarchy between m_{h_c} and $m_A = m_{H^\pm}$, have been chosen so as to explore in detail the impact of the presence of the singlet field within the N2HDM, relative to scenarios that would feature a FOEWPT in the 2HDM [172, 244, 301, 303].

In Figure 6.7 we show the scan results for the critical and nucleation temperatures T_c (left) and T_n (right) of a FOEWPT, in the plane of the heaviest CP-even scalar mass m_{h_3} vs. its singlet component $\Sigma_{h_3} = |R_{33}|^2$. The lower-right region of the plots is excluded due to the perturbative unitarity constraints (as discussed in Sec. 6.4.3). For the gray points, the EW symmetry is not restored up to the maximum temperature used for this numerical analysis (recall the discussion in Sec. 6.4.3), $T_{\max} = 600$ GeV, and no FOEWPT takes place

---

[15] Only for very small values of $v_S \ll v$ a simultaneous breaking (in a single transition) of the EW and $\mathbb{Z}_2'$ symmetries can be realised. A discussion of this scenario is left for future work.

(T_c and T_n are thus not defined).[16] For the coloured points in the left plot of Figure 6.7 there exists a critical temperature T_c at which there are two degenerate minima, of the form $(0, 0, \tilde{v}_S(T))$ and $(v_1(T), v_2(T), v_S(T))$, and one could naively be led to conclude that these points also feature a FOEWPT. However, looking at the right plot of Figure 6.7, one can see that only a fraction of these points yield a FOEWPT occuring at $T = T_n$. The black points in the right plot have T_c defined, but there is no temperature $T < T_c$ for which the nucleation criterion of Eq. (4.60) is fulfilled. As a consequence, the Universe stays trapped in the false vacuum $(0, 0, \tilde{v}_S(T))$, and the EW phase transition does not occur.

In agreement with the results from Ref. [245], we observe from Figure 6.7 that for large values of the mass m_{h_3} a FOEWPT is associated with a very singlet-like state h_3. This is also reflected in the fact that for a fixed value of m_{h_3} both T_c and T_n decrease with increasing Σ_{h_3}. On the other hand, for smaller values of m_{h_3} a FOEWPT is possible for a sizeable doublet component in h_3. Moreover, for a fixed value of Σ_{h_3}, T_c and T_n decrease with decreasing m_{h_3}. This may be understood as follows: Higgs bosons that participate in the EW phase transition (by acquiring a vev) should not be too heavy, since large Higgs boson masses require in general large bilinear terms, which hinder a FOEWPT if they enter the transition dynamics [39]. In addition, the trilinear terms generating the potential barrier between true and false vacua are absent at tree-level in the N2HDM, and arise only from the radiative and thermal corrections to the potential, thus depending on the quartic scalar couplings λ_i. The values of λ_i (and therefore the size of the potential barrier) grow with the splitting between the masses of $h_{2,3}$ and A (where m_A has been fixed at 650 GeV in our scan). The strongest FOEWPTs are then expected to occur for low values of $m_{h_3} \approx m_{h_2} \ll m_A$, except when h_3 is almost entirely singlet-like, i.e. $\Sigma_{h_3} \approx 1$.

For a given Σ_{h_3}, there is a critical value of m_{h_3} below which the energy barrier becomes so large that the probability for the tunnelling between vacua is too small to allow for the onset of the phase transition as defined in Eq. (4.60). The corresponding black points in Figure 6.7 thus yield trapped metastable singlet vacua $(0, 0, \tilde{v}_S)$ down to $T \to 0$. This situation yields an inflationary process that suffers from the "graceful-exit" problem [362] and leads to an unphysical scenario. This is the case even though a critical temperature T_c (at which the EW minimum becomes the global minimum of the potential) does exist for such points, as shown in the left plot of Figure 6.7. Furthermore, Figure 6.7 highlights that this trapped-vacua region features the lowest values of T_c. In EW baryogenesis scenarios, the strength of the FOEWPT is precisely quantified as (see e.g. [236]) $\xi = v_c/T_c$ (where $v_c = \sqrt{v_1(T_c)^2 + v_2(T_c)^2}$ is the EW vev at the critical temperature). In an investigation based only on T_c one would then naively – and erroneously – conclude that the strongest FOEWPTs for EW baryogenesis would occur in the region of parameter space corresponding to the black points in Figure 6.7. However, our results show that this region is unphysical.

Overall, the black "vacuum-trapping" region constitutes a sizeable fraction of the pa-

---

[16] One could also argue that the gray points avoid the problem of vacuum trapping, because no FOEWPT has to take place in order to reach the EW minimum at $T = 0$. Similar solutions were proposed in the context of supersymmetric GUT theories [360, 361].

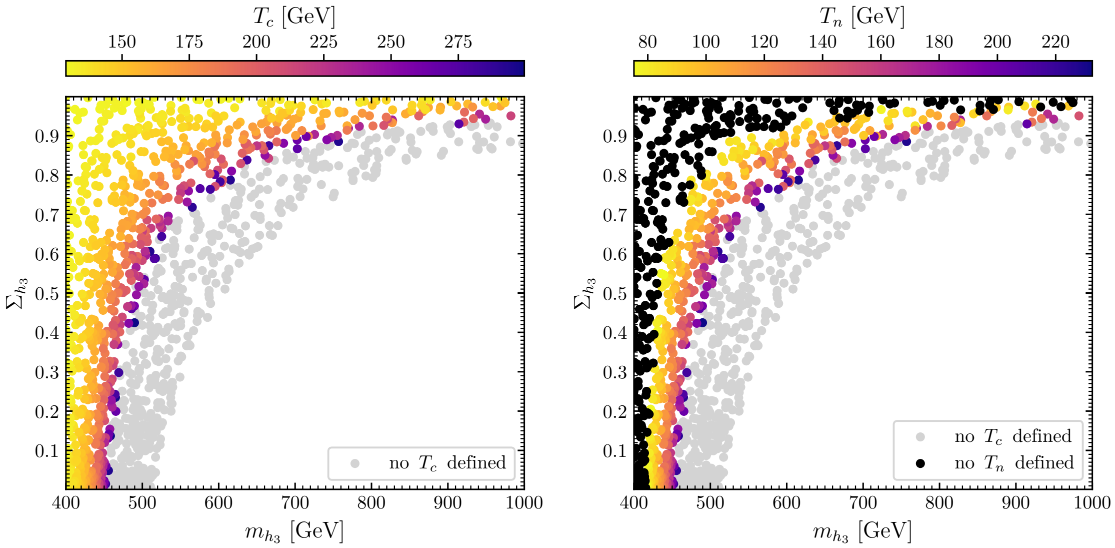

Figure 6.7: Parameter points according to Table 6.3. The singlet component Σ_{h_3} of the third CP-even Higgs boson is shown in dependence of its mass m_{h_3}. The colour code indicates the values for the critical temperature T_c (left) and the nucleation temperature T_n for the points with a FOEWPT (right). Black points do not feature a T_n, and the Universe is trapped in a false minimum. For the gray points, for which T_c cannot be defined, the Universe is in the EW minimum already at $T_{\max} = 600$ GeV, i.e. the EW symmetry is not restored within the investigated temperature range, and no FOEWPT occurs.

rameter space in our scan that based on the thermal history of the Universe is ruled out because the breaking of the EW symmetry does not occur. This result makes manifest an important shortcoming of a zero temperature analysis of the stability of the EW minimum in extended scalar sectors (as implemented e.g. in `ScannerS`, see Sec. 6.2), as we demonstrate that the presence of a global EW minimum at $T = 0$ is not a sufficient criterion for an acceptable vacuum configuration in the N2HDM (this has also been shown recently within the NMSSM [279]). If further local minima besides the EW minimum are present at $T = 0$, an analysis of the thermal history of the Universe including the nucleation probabilities of possible metastable minima is necessary to assess whether an N2HDM scenario is physical. An analysis based only on the critical temperature (as done e.g. in Ref. [245]), is not sufficient and can yield misleading predictions. We also note that an analysis of the N2HDM thermal history based on the Parwani resummation scheme would lead to a larger region of the parameter space experiencing vacuum-trapping: The Parwani method typically predicts smaller values for T_c as compared to the AE method used in this work, since in the former the finite-T contributions tend to restore the EW symmetry at lower temperatures (the same was found in the 2HDM [244]). The tunnelling probability scales with $\exp(-S_3/T)$ (see Eq. (4.60)), and so the onset of the EW phase transition is further suppressed in the Parwani resummation method.[17] While we regard the AE method as

---

[17] We have found that all our 2000 scan points feature trapped-vacua when using the Parwani method,

more appropriate for the analyses in our study (see the discussion above), the comparison with the Parwani resummation method shows that the parameter regions in the N2HDM that we have indicated as unphysical because of vacuum-trapping are robust and conservative, in the sense that those regions would be identified as unphysical based on both methods.

As a further step, we now discuss the interplay between the thermal evolution and the collider phenomenology of the N2HDM. For the case of the 2HDM it has been found that the occurrence of a FOEWPT is favoured by a hierarchical spectrum [244, 301], and the decay $A \to Zh_i$ has emerged as a “smoking-gun” collider signature [172] of a FOEWPT in the 2HDM. Also in the N2HDM such a type of signature is linked with the possible presence of a FOEWPT, but the collider phenomenology related to this class of processes in the N2HDM is much richer than in the 2HDM. In the alignment limit[18] (which is realised in our parameter scan), the AZh_{125} coupling between the pseudoscalar A, the Z boson and the SM-like Higgs boson at about 125 GeV vanishes at tree-level. While in the 2HDM in this limit only the decay $A \to ZH$ is possible if kinematically allowed, in the N2HDM the two decays $A \to Zh_2$ and $A \to Zh_3$ can occur, whose branching ratios depend on both the singlet component and the masses of $h_{2,3}$. As shown in Figure 6.7, these parameters also play an important role for the thermal history of the N2HDM. In our parameter scan we find that both decay channels are generally open in scenarios with a FOEWPT, except when h_3 is very singlet-like (and can thus effectively decouple from the FOEWPT dynamics, $m_{h_3} \gg v$).

In Figure 6.8 we show as result of our parameter scan defined in Table 6.3 the predictions for the signal rates $pp\,(gg) \to A \to Zh_2$ and $pp\,(gg) \to A \to Zh_3$ at the LHC with $\sqrt{s} =$ 13 TeV, where the production cross section has been calculated with `SusHi v.1.6.1` [317, 363], and the branching ratios have been obtained with `N2HDECAY` [176, 318]. Since the production cross section $\sigma(gg \to A)$ is constant in our scan (it only depends on m_A and $\tan\beta$), Figure 6.8 effectively shows the interplay between $\mathrm{BR}(A \to Zh_3)$ and $\mathrm{BR}(A \to Zh_2)$. As a result, we find that (stronger) FOEWPTs with smaller nucleation temperatures are correlated with larger values for these branching fractions. However, the largest values of the signal rates for each of the two processes in our scan correspond to unphysical trapped-vacua scenarios. The detection of the processes $pp \to A \to Zh_2$ and $pp \to A \to Zh_3$ at the LHC would open the possibility to infer details about the thermal history of the Universe that would have occurred in the N2HDM. Regarding the current status of LHC searches of this kind, ATLAS and CMS have searched for the $pp \to A \to Zh_i$ (with $h_i \neq h_{125}$) signature within their 8 TeV [364] and 13 TeV [365, 366] data sets, assuming that the Higgs boson h_i decays into a pair of bottom quarks or a pair of τ-leptons. It should be noted that our scan shows that for scenarios featuring a FOEWPT in the N2HDM the masses of both h_2 and h_3 could easily be above the decay threshold into top-quark pairs. In fact, for the rather small value of $\tan\beta = 2$ in our scan the discovery potential for the “smoking-gun”

---

despite the EW minimum being the global minimum at $T = 0$ for all of them.

[18] We note that this limit is strongly preferred for a FOEWPT in the 2HDM, see e.g. [302].

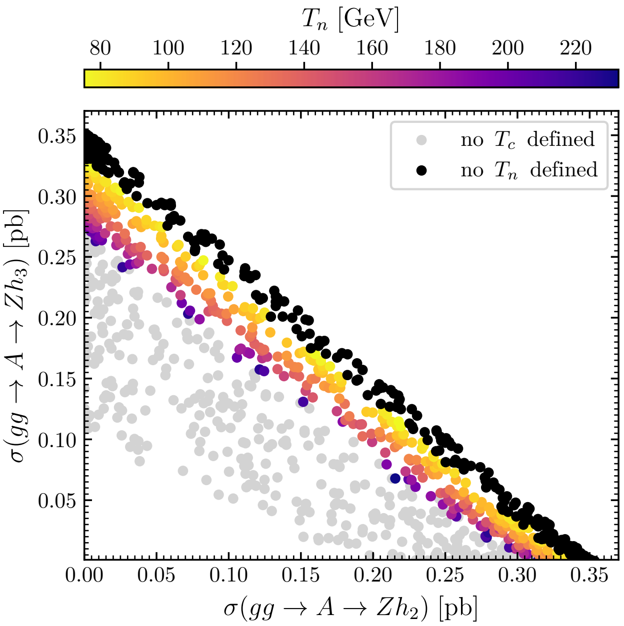

Figure 6.8: Correlation of the cross sections for the processes $A \to Zh_2$ and $A \to Zh_3$ for the N2HDM benchmark scenarios defined in Table 6.3. The colour coding is the same as in Figure 6.7 (right).

signatures in the N2HDM scenarios could be higher for the decay of $h_{2,3} \to \bar{t}t$. Thus, our results motivate to explore the signature $pp \to A \to Z(h_i) \to Z(\bar{t}t)$ within the programme of experimental searches at the LHC (see also [337]).

6.5.2 Case 2: Singlet admixture in h_{125}

In contrast to the scan studied in the previous section, we now explore scenarios where the Higgs boson h_{125} has a singlet admixture (whereas the heavy CP-even state H does not), and study the impact of such an admixture on the N2HDM thermal history. The measurements of the signal rates of the SM-like Higgs boson together with the EWPO set limits on the possible amount of a singlet component that can be acquired by h_{125} [176, 367]. These limits also constrain the possible impact of the singlet-doublet mixing on the FOEWPT in the considered scenario. In order to be able to study the effect of a singlet admixture in h_{125} over a substantial mixing range, here we will fix the mass of the singlet-like scalar in our parameter scan to be relatively close to 125 GeV (the relatively small mass splitting between the Higgses then allows for sizeable mixing). We perform two N2HDM parameter scans with `ScannerS`, defined in Table 6.5, to cover both mass orderings (as they have different phenomenological implications): a singlet-like scalar somewhat heavier than h_{125}, and a singlet-like scalar somewhat lighter than h_{125}. In both scans we keep the hierarchy between the masses of the heavier CP-even doublet-like Higgs boson (h_b in Table 6.5) and the CP-odd state A in order to guarantee the presence of a potential barrier separating the false minimum at $(0, 0, \tilde{v}_S)$ and the true minimum at (v_1, v_2, v_S).

m_{h_a}	m_{h_b}	m_{h_c}	m_A	$m_{H^\pm}$	tanβ	$C^2_{h_a t\bar{t}}$	$C^2_{h_a VV}$	sgn(R_{a3})	R_{b3}	m^2_{12}	v_S
125.09	400	160	650	650	2	$[0.8, 1.2]$	$[0.7, 1.0]$	1	0	65000	300
125.09	400	105	650	650	2	$[0.8, 1.2]$	$[0.7, 1.0]$	$-1, 1$	0	68500	300

Table 6.5: `ScannerS` input parameters used in the study of the impact of a singlet admixture in h_{125} on the N2HDM thermal history. The upper (lower) row corresponds to the scan parameters for $m_{h_c} > (<)\, 125.09$ GeV.

We first analyse the scenario in which h_{125} is the lightest Higgs boson h_1, choosing our `ScannerS` scan parameters as shown in the first row of Table 6.5. We generate 1000 benchmark points fulfilling the theoretical and experimental constraints discussed in Sec. 6.2. The only parameters that are varied in our scan are the scalar mixing angles, under the condition that the singlet component of $h_b = h_3$ vanishes. We choose the mass of the singlet-like Higgs boson $m_{h_2} = 160$ GeV to allow for a sizeable mixing with the SM-like Higgs boson h_1 without being in conflict with the LHC searches for scalar resonances decaying into a pair of Z bosons [368]. In Figure 6.9 we show the set of parameter points in the plane of normalised squared-couplings of the Higgs boson at 125 GeV to EW gauge bosons and SM fermions, $C^2_{h_1 VV}$ and $C^2_{h_1 t\bar{t}}$, respectively. Note that $C^2_{h_1 VV}$ also corresponds to the singlet component of h_2, i.e. $\Sigma_{h_2} = 1 - \Sigma_{h_1} = C^2_{h_1 VV}$ ($\Sigma_{h_3} = 0$ because of $R_{b3} = 0$). The allowed parameter space in Figure 6.9 is defined by three different constraints: boundedness from below of the tree-level potential requires $\lambda_1 > 0$, which excludes the lower-right triangular region of the ($C^2_{h_1 VV}$, $C^2_{h_1 t\bar{t}}$) plane in Figure 6.9; it also requires $\lambda_2 > 0$, which excludes the upper-left triangular region of the ($C^2_{h_1 VV}$, $C^2_{h_1 t\bar{t}}$) plane in Figure 6.9. We then find a diagonal band of allowed parameter space, based only on these theoretical considerations. Finally, the roughly elliptical shape of this allowed band in Figure 6.9 is due to the experimental LHC constraints on the h_{125} signal strengths, which we implement using the χ^2 result of `HiggsSignals` (see Sec. 6.2).

For each of the 1000 scan points, we have performed a finite-T analysis with `CosmoTransitions`, computing the thermal evolution of the effective potential from a maximum temperature $T_{\text{max}} = 300$ GeV[19] down to $T = 0$. In contrast to the scan results discussed in Sec. 6.5.1, here we find that at T_{max} the Universe finds itself in a minimum of the kind $(0, 0, \tilde{v}_S)$ for all N2HDM benchmarks, and so the EW symmetry is always restored (at least in an intermediate temperature regime). As the Universe cools down from T_{max}, all benchmark points feature a critical temperature T_c, shown in Figure 6.9 (left), at which the EW-broken minimum is degenerate with the singlet minimum $(0, 0, \tilde{v}_S)$. For 609 points in our scan the Universe remains trapped in the false (singlet) vacuum, as indicated by the black points in the right plot of Figure 6.9, while for the remaining (391) points a FOEWPT takes place. In the latter case, the nucleation temperature T_n is shown in Figure 6.9 (right). We see

---

[19] The maximum temperature T_{max} that we consider here is substantially lower than in our previous scans, since here we are not interested in the SnR behavior, but rather in the appearance of trapped vacua, for which the temperatures studied need not be much larger than the EW scale.

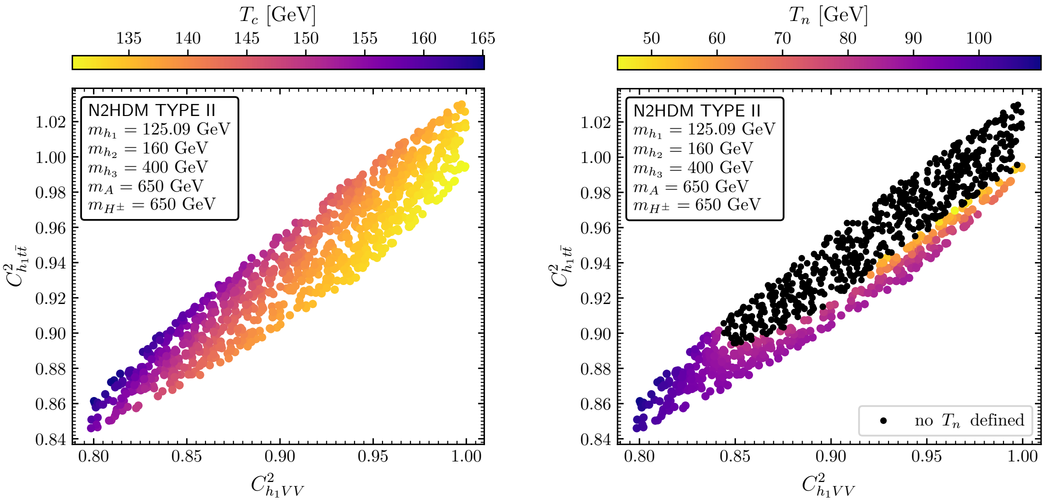

Figure 6.9: Parameter scan according to Table 6.5 (upper row) in the $C^2_{h_1VV}$–$C^2_{h_1t\bar{t}}$ plane. The colour coding indicates the values of the critical temperature T_c (left) and the nucleation temperature T_n for the points with a FOEWPT (right). For the black points the Universe is trapped in a false minimum, such that no nucleation temperature can be defined.

that both T_c and T_n decrease with increasing $C^2_{h_1VV}$, in agreement with results previously obtained in the 2HDM [244, 303]. This suggests (as we have discussed also in the previous sections) that the strength of the transition reaches the largest values in the alignment limit, in which the heavier doublet-like CP-even Higgs boson does not obtain a vev. We note that within the 2HDM this reduces the prospects for detecting deviations from the SM case via signal rate measurements of h_{125} in the parameter space that is relevant for FOEWPTs. Our results show that this is also the case for the N2HDM if h_{125} is the lightest Higgs boson. However, the opposite effect can occur if h_{125} is the second-lightest Higgs boson, as we will show below.

We turn now to the analysis of scenarios where the singlet-like scalar state is lighter than h_{125}, in order to demonstrate the importance of the mass ordering of the singlet- and doublet-like Higgs bosons. Our parameter scan now corresponds to the lower row of Table 6.5, with $m_{h_1} = 105$ GeV. This allows for a sizeable variation of the mixing with $h_{125} = h_2$ without being in conflict with the cross section limits obtained from the LEP Higgs searches [369]. We also slightly increase the value of m^2_{12} compared to the previous analysis (see the upper row of Table 6.5) in order to increase the tunnelling rate between minima in a FOEWPT.[20] We generate 1000 points fulfilling the theoretical and experimental constraints using `ScannerS` and use `CosmoTransitions` to analyse the thermal history of

---

[20] As shown in Ref. [303] for the 2HDM, larger values of m^2_{12} reduce the potential barrier and the distance in field space between false and true minima, thus increasing the tunnelling rate of FOEWPTs. In the present scan, the increased value of m^2_{12} counterbalances the otherwise suppressed tunnelling probability due to the overall reduced mass scale of the CP even Higgs bosons when $m_{h_1} = 105$ GeV and $m_{h_2} = 125$ GeV compared to the previous scan with $m_{h_1} = 125$ GeV and $m_{h_2} = 160$ GeV.

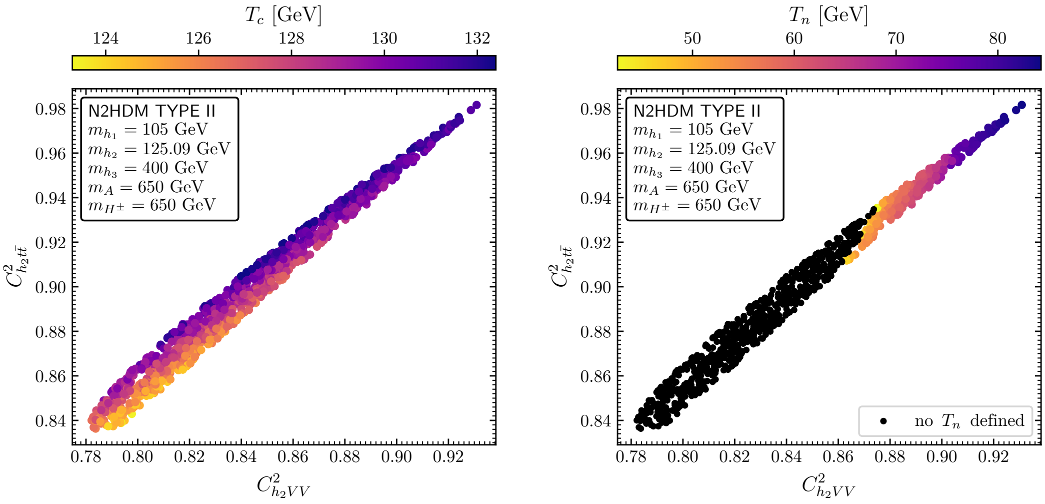

Figure 6.10: Parameter scan according to Table 6.5 (lower row) in the $C^2_{h_2VV}$–$C^2_{h_2t\bar{t}}$ plane. The colour coding indicates the values of the critical temperature T_c (left) and the nucleation temperature T_n for the points with a FOEWPT (right). For the black points the Universe is trapped in a false minimum, such that no nucleation temperature can be defined.

each scan point as described above for the previous scan. In Figure 6.10 we show the resulting points in the plane of the effective couplings $C^2_{h_2VV}$ and $C^2_{h_2t\bar{t}}$. The allowed parameter space is defined as in Figure 6.9 by the bounded-from-below constraints $\lambda_{1,2} > 0$ and by the constraints on the signal rates of h_{125} that are tested with `HiggsSignals`. It is interesting to note that the region with $C_{h_2VV} = C_{h_2t\bar{t}} = C_{h_2b\bar{b}} = 1$, i.e. the alignment limit, cannot be realised with the choice of parameters of this scan, since in this region one finds $\lambda_1 < 0$. For the allowed points, we find $0.5 \lesssim C_{h_2b\bar{b}} \lesssim 0.8$ (not shown in the plots) together with $C_{h_2VV} < 1$ and $C_{h_2t\bar{t}} < 1$ in order to satisfy the constraints on the signal rates of h_{125}.[21]

All 1000 points in our scan feature a critical temperature T_c (at which the true EW minimum is degenerate with the false minimum $(0, 0, \tilde{v}_S)$), shown in the left plot of Figure 6.10. However, the majority of scan points correspond to trapped-vacuum scenarios, shown in the right plot of Figure 6.10 as black points, and excluded since a FOEWPT does not take place (from the 1000 points only 225 yield a FOEWPT). For the points that do feature a FOEWPT, the colour coding in Figure 6.10 (right) indicates the nucleation temperature T_n. As opposed to the scenario with h_{125} as the lightest Higgs boson, here both T_c and T_n are reduced for decreasing values of $C_{h_{125}VV}$. A decrease in $C_{h_{125}VV}$ is linked to an increase in the mixing between the (singlet-like) lightest Higgs boson h_1 and h_{125}, $\Sigma_{h_{125}} \approx 1 - C^2_{h_{125}VV}$, which decreases the mass scale of the particles obtaining a vev during the transition. This in turn increases the strength of the FOEWPT and leads to a lower T_n. As Figure 6.10 highlights, this decrease in T_n eventually results in vacuum-trapping, which in our scan rules out all points with $\Sigma_{h_{125}} \gtrsim 0.15$. The fact that, given the presence

---

[21] For $C^2_{h_{125}VV}, C^2_{h_{125}t\bar{t}} < 1$ and $C^2_{h_{125}b\bar{b}} \approx 1$ the diphoton branching ratio of h_{125} would be too small.

of a singlet-like scalar below 125 GeV, the N2HDM can realise a FOEWPT quite far away from the alignment limit is a very important difference w.r.t. the 2HDM (in which the strength of the FOEWPT is maximised in the alignment limit [244, 302]). In the N2HDM, a mixing of h_{125} with a lighter singlet-like scalar reverses the dependence of the EW phase transition strength on $C_{h_{125}VV}$ compared to the case of the 2HDM. This constitutes a key feature of the N2HDM regarding the interpretation of possible deviations from the SM in the couplings of the Higgs boson at 125 GeV that could be revealed in future measurememts at the LHC and the HL-LHC.

Part III

Dark matter

Chapter 7

Dark matter direct-detection

Dark matter is still today one of the greatest mysteries in physics. Although the first hints of its existence were reported almost 100 years ago, and significant pieces of evidence have been gathered from different sources, we are nevertheless ignorant of its nature. Perhaps the simplest way to be in tune with all experimental results is to consider DM as a particle yet to be discovered. There are many ongoing experiments that can provide further directions in the search for the correct description of the DM field. However, in order to unmistakably observe a DM candidate, one needs direct-detection experiments that probe the mass and couplings of the DM particle with the SM particles via its interactions with known objects such as nuclei. As a DM particle interacts with nuclei, light and electric charge are emitted, providing information about energy and location of the collision.

In this chapter, we illustrate in the context of the S2HDM, the distinct feature of the pNG DM: having a negligible DM DD cross section at LO (see Sect. 7.1). In Sect. 7.2, we describe the basic formalism used in Chapter 9 to predict the one-loop DM-nucleus DD cross section in the S2HDM.

7.1 Pseudo-Nambu Goldstone dark matter

In the S2HDM (see Sect. 3.1.3) at the tree level, the scattering of χ on a quark q is transmitted via the t-channel exchange of the Higgs bosons h_i. The corresponding amplitude $\mathcal{M}$ can be written as

$$\mathcal{M} = -\frac{Y_q}{\sqrt{2}} \sum_{i=1}^{3} \frac{R_{ia} i\Gamma_{h_i\chi\chi}}{m_{h_i}^2 + t} \ , \tag{7.1}$$

where y_q is the Yukawa coupling of the quark $q = \{u, d, c, s, t, b\}$, $\Gamma_{h_i\chi\chi}$ is the tree-level coupling between the DM particle χ and the Higgs bosons h_i given by

$$i\Gamma_{h_i\chi\chi} = \lambda_7 v_d R_{i1} + \lambda_8 v_u R_{i2} + \lambda_6 v_S R_{i3} \ , \tag{7.2}$$

and R_{ia} are the elements of the mixing matrix of the CP-even scalars defined in Eq. (3.45), with $a = 1$ or $a = 2$ depending on whether the quark q is coupled to the doublet field Φ_1 or Φ_2, respectively. Hence, in type I and type LS $a = 2$ for $q = \{u, d, c, s, t, b\}$, whereas in type II and type F $a = 2$ for $q = \{u, c, t\}$ and $a = 1$ for $q = \{d, s, b\}$. Rewriting the amplitude $\mathcal{M}$ in terms of the squared masses, or vice-versa replacing the squared masses in terms of the Lagrangian parameters and the vevs, and by making use of the orthogonality of R, it is easy to show that $\mathcal{M}$ vanishes in the limit of zero-momentum exchange, i.e. $t \to 0$.

7.2 Dark matter direct detection

The DM halo of a galaxy envelops the galactic disc and extends well beyond the visible part of the galaxy. If DM has a WIMP-nature, the Earth would receive a flux of DM particles of the order of $10^5(100\ \text{GeV}/m_\chi)\text{cm}^{-2}\text{s}^{-1}$ [370] as it traverses the Milky way rotating around its center. Even though DM is weakly interacting with ordinary matter (if it interacts at all), this flux is sufficiently large to cause a potentially measurable fraction of nuclear recoils as a result of WIMP elastic scattering off nuclei in dedicated low background detectors. This is the main idea that drives DM DD experiments, whose major role in probing the WIMP region is central to unmistakably confirm the existence of a DM particle candidate. In this section[1], we will review how to derive the physical observable *differential detection rate per recoil energy* in the context of a model providing a scalar DM candidate like the S2HDM.

General considerations The detector material is typically kept at low temperatures, such that the target nuclei can be considered at rest with respect to the laboratory frame prior to the interaction with the DM particle. The DM halo is gravitationally bound, so the typical velocity with which a DM particle incises on the Earth must be smaller than the local escape velocity, which has been measured to be $v_{\text{esc}} = 533\ \text{km/s}^{-1} \approx 2 \cdot 10^{-3}$ at the 90% C.L. [374]. Therefore, the non-relativistic treatment of the kinematics of the DM-nucleus scattering is justified. For a WIMP scattering off a typical nucleus, the maximum momentum transfer q can be estimated to be of the order of $|q| \sim \mathcal{O}(10\ \text{MeV} - 100\ \text{MeV})$ [375]. This sets a characteristic length scale for the process of the order of the radius of the target, i.e. $1/|q| \sim \mathcal{O}(1\ \text{fm} - 10\ \text{fm})$. In the small momentum transfer limit, $1/|q| \ll 10$ fm, the DM interacts with the whole nucleus coherently. In particular, for a Higgs portal to scalar DM, only spin-independent interactions will be relevant to the computation of the DM-nucleus scattering cross section, such that the total nuclear cross section is enhanced by the square of the atomic mass due to the coherent summation over all the scattering centers in the nucleus.

The detection rate The detection rate per recoil energy per total target mass is computed as [372]

$$\frac{d\mathcal{R}}{dE_R} = \frac{\rho_\chi}{m_\mathcal{N} m_\chi} \left\langle v_\chi \frac{d\sigma_\mathcal{N}}{dE_R} \right\rangle , \tag{7.3}$$

where ρ_χ is the local mass density of the DM candidate, $m_\mathcal{N}$ is the mass of the target nucleus, m_χ is the DM mass, $\sigma_\mathcal{N}$ is the the DM scattering cross section off a nucleus, and the brackets indicate the average over the velocity v_χ distribution of the DM in the reference frame of the detector. For spin-independent interactions, the DM scattering cross section $\sigma_\mathcal{N}$ can be written in terms of the scattering amplitudes of the DM particle off the

---

[1] Here the references Refs. [370–373]were followed.

constituent nucleons [373]

$$\sigma_{\mathcal{N}} = \frac{\mu_{\mathcal{N}}^2}{\pi} |Z\mathcal{M}_{\text{proton}} + (A - Z)\mathcal{M}_{\text{neutron}}|^2 |F(q)|^2 \tag{7.4}$$

with $\mu_{\mathcal{N}}$ being the WIMP-nucleus reduced mass, Z is the number of protons of the nucleus and A the total number of nucleons. Here $\mathcal{M}_{\text{proton}}$ and $\mathcal{M}_{\text{neutron}}$ stand for the scattering amplitudes of the DM particle on a proton and a neutron, respectively. The form factor for coherent interactions $F(q)$ can be qualitatively understood as a Fourier transform of the nucleon density. $F(q)$ is normalised to unity at zero momentum transfer [370]. In the approximation $\mathcal{M}_N \equiv \mathcal{M}_{\text{proton}} \approx \mathcal{M}_{\text{neutron}}$ we obtain

$$\sigma_{\mathcal{N}} = \frac{\mu_{\mathcal{N}}^2}{\mu_N^2} A^2 \sigma_N |F(q)|^2, \tag{7.5}$$

where we used the DM-nucleon scattering cross section σ_N expressed as

$$\sigma_N = \frac{\mu_N^2}{\pi} |\mathcal{M}_N|^2. \tag{7.6}$$

Here μ_N stands for the reduced mass of the WIMP-nucleon system. Once stated the connection between the DM-nucleon scattering cross section (7.6) and the detection rate (7.3), for the rest of the discussion we will work at the level of nucleons, yielding results independent of the specific target material. To compute $\mathcal{M}_N$, we consider the effective Lagrangian reproducing the interactions between the DM particles and nucleons

$$\mathcal{L}_{\text{eff}} = \alpha_N \chi\chi \bar{N} N, \tag{7.7}$$

where N is the nucleon spinor field and α_N is the effective coupling. The scattering amplitude of the DM particle and the nucleon is given by

$$i\mathcal{M}_N = i\alpha_N \bar{u}_N u_N = i2m_N \alpha_N, \tag{7.8}$$

where it was used that, in the limit of zero external momentum, the product of the two spinors, u_N and $\bar{u}_N$, can be replaced by their normalisation, $2m_N$, with m_N being the mass of the nucleon. Using Eq. (7.8), the cross section σ_N can be expressed as

$$\sigma_N = \frac{1}{4\pi} \left(\frac{m_N}{m_\chi + m_N} \right)^2 |\mathcal{M}|^2. \tag{7.9}$$

In order to obtain the effective coupling α_N in terms of the parameters of the underlying DM model, we have to match the quark level operators onto the nucleon level operators. The scattering cross sections of the DM particle on a quark q can be effectively described by the effective scalar operator

$$m_q C_q^s \chi\chi \bar{q} q \ , \tag{7.10}$$

where m_q is mass of the quark, and C_q^s is the Wilson coefficient that is determined order by order in perturbation theory from the matching to the full model. The precise form of the radiative corrections that we incorporate into C_q^s will be discussed in Sect. 9. The heavy quark contributions will be included as gluon initiated processes making use of the QCD trace anomaly that relates the heavy quark $Q = b, c, t$ operators with the gluon field strength tensor [376]

$$m_Q \bar{Q} Q \to -\frac{\alpha_s}{12\pi} G_{\mu\nu} G^{\mu\nu} \,. \tag{7.11}$$

Here we should note that the parton operator basis forming the most general spin-independent interactions for scalar DM should also include interactions induced by gluon-DM interactions and twist-2 operators related to additional gluon-induced interactions. However, as it was argued in Ref. [69] for a pNG DM model with one Higgs doublet, their contribution was found to be subleading with respect to the contributions arising from the operator in Eq. (7.10). Therefore, we will consider the operator $m_q C_q^s \chi\chi\bar{q}q$ as the sole contribution to the DM-nucleon scattering cross section in the S2HDM.

The effective Lagrangian for the scattering of the DM particle on a quark q can be expressed as

$$\mathcal{L}_{\text{eff}} = m_q C_q^s \chi\chi\bar{q}q + C_Q^s m_Q \chi\chi\bar{Q}Q, \tag{7.12}$$

with C_Q^s being the Wilson coefficient for the contributions from heavy quarks Q. The effective couplings extracted from the effective Lagrangian to quarks and gluons are $\alpha_q^s = 2m_q C_q^s$ and $\alpha_Q^s = 2m_Q C_Q^s$, respectively. We can compute α_N in Eq. (7.7) as the sum of two contributions:

$$\begin{aligned}\alpha_N &= \sum_{q=u,d,s} \langle n|\bar{q}q|n\rangle \alpha_q^s + \sum_{Q=b,c,t} \langle n|\bar{Q}Q|n\rangle \alpha_Q^s, \\ &= \sum_{q=u,d,s} \langle n|\bar{q}q|n\rangle \alpha_q^s + \sum_{Q=b,c,t} \langle n| -\frac{\alpha_s}{12\pi} G_{\mu\nu} G^{\mu\nu} |n\rangle 2C_Q^s, \end{aligned} \tag{7.13}$$

with the bracket products interpreted as the probability to find a specific quark flavour in the nucleon [373]. The first sum in Eq. (7.13) contains the contributions from the scattering of χ directly on the valence quarks. The second term in Eq. (7.13) contains the contributions from the scattering on the gluons, where we take into account at LO only the quark-mediated contributions. As a consequence of this approximation, this contribution can also be expressed in terms of the effective operator shown in Eq. (7.10). The expectation values of the operators are defined as [376–378]

$$\langle n|m_q \bar{q}q|n\rangle \equiv m_n f_{Tq}^n \,, \tag{7.14a}$$

$$\langle n| -\frac{\alpha_s}{12\pi} G_{\mu\nu} G^{\mu\nu} |n\rangle \equiv \frac{2}{27} m_n f_{Tg}^n. \tag{7.14b}$$

f_{Tq}^N are the contributions of the valence quarks to the nucleon mass. Their numerical values have been extracted from lattice simulations and from data-driven methods to be [378–381]

$$f_{Tu}^p = 0.029 \;,\; f_{Td}^p = 0.027 \;,\; f_{Ts}^p = 0.009 \;, \tag{7.15}$$

$$f_{Tu}^n = 0.013 \;,\; f_{Td}^n = 0.040 \;,\; f_{Ts}^n = 0.009 \;. \tag{7.16}$$

The gluon contribution can at LO be expressed in terms of the contributions of the valence quarks. It is given by [370]

$$f^N_{Tg} = 1 - \sum_{q=u,d,s} f^N_{Tq} \,. \tag{7.17}$$

By plugging Eqs. (7.14) and (7.13) in Eq. (7.9), we find that the scattering cross section for the scattering of χ on nucleons as a function of C^s_q can be expressed as as [370]

$$\sigma_N = \frac{1}{\pi} \frac{m_n^4}{(m_n + m_\chi)^2} \left| \sum_{q=u,d,s} C^s_q f^N_{Tq} + \frac{2}{27} f^N_{Tg} \sum_{q=b,c,t} C^s_q \right|^2 \,. \tag{7.18}$$

Chapter 8

Pseudo-Nambu Goldstone dark matter in the S2HDM

In this chapter, we investigate a possible realization of pNG DM in the framework of the S2HDM, which was introduced in Sect. 3.1.3. pNG DM gained attraction due to the fact that DD constraints can be avoided naturally because of the momentum-suppressed scattering cross sections, whereas the relic abundance of DM can nevertheless be accounted for via the usual thermal freeze-out mechanism. We confront the S2HDM with a multitude of theoretical and experimental constraints, paying special attention to the theoretical limitations on the scalar potential, such as vacuum stability and perturbativity. In addition, we discuss the complementarity between constraints related to the DM sector, on one hand, and to the Higgs sector, on the other hand. In our numerical discussion we explore the Higgs funnel region with DM masses around 60 GeV using a genetic algorithm. We demonstrate that the S2HDM can easily account for the measured relic abundance while being in agreement with all relevant constraints. We also discuss whether the so-called center-of-galaxy excesses can be accommodated, possibly in combination with a Higgs boson at about 96 GeV that can be the origin of the LEP- and the CMS-excess observed at this mass in the $b\bar{b}$-quark and the diphoton final state, respectively.

This chapter is organised as follows. Since the model was already presented in Sect. 3.1.3, we start by describing in Sect. 8.1 the precise implementation of the relevant experimental and theoretical constraints that we applied to the parameter space of the S2HDM. In Sect. 8.2, we describe the genetic algorithm that was used to scan the parameter space and to determine the parameter points that pass the various theoretical and experimental requirements. In Sect. 8.2.1, we explore the Higgs funnel region after imposing the previously described constraints and disregarding the explanation of the excesses at LEP and CMS, whereas in Sect. 8.2.2 we additionally demand that the collider excesses are accommodated.

This chapter is based on ref. [2].

8.1 Constraints

Here we briefly discuss the constraints on the parameter space of the S2HDM that we applied in our analyses, mainly focusing on the methods and codes utilised. For further details on the relevant experimental and theoretical constraints we refer to Sect. 3.2.1 and Sect. 3.2.2, respectively.

8.1.1 Theoretical constraints: vacuum stability and unitarity

Due to the fact that the quartic part of the potential V is unchanged compared to the N2HDM, we can apply the same BfB conditions on the tree-level scalar potential that were found for the N2HDM (see Eq. (3.80)). We excluded all parameter points from our analyses that did not feature a scalar potential that is BfB. As explained in Sect. 3.2.1, to avoid the possibility of loop corrections changing the boundedness of the potential, we also demanded an upper limit of 200 GeV on the splitting of the heavy Higgs-boson masses compared to the mass scale M, defined in Eq. (3.46).

We demanded the EW minimum to be the global minimum of the tree-level potential V (3.43), by solving the stationary conditions $\partial V/\partial(v_1, v_2, v_{\rm C}, v_{\rm CP}, v_S, v_{\rm DM})$, where we used the code `Hom4PS-2` [382] to solve the system of polynomial equations. For each extrema we calculated the value of V in this point of field space. One can conclude that, if for any of the extrema the value of V is smaller than for the field values of the EW vacuum, the EW minimum is not the global minimum of V. In this case, the EW vacuum is potentially short-lived compared to the age of the universe, such that the corresponding parameter point might be unphysical, and we rejected it from the analyses.[1]

The precise form of the conditions to ensure a perturbative treatment of the model for a specific parameter point is given in Sect. 3.2.1. Due to the fact that compared to the N2HDM the only additional degree of freedom is the CP-odd component of the singlet field Φ_S, the perturbativity conditions are in most parts very similar to the N2HDM conditions [176]. However, an important difference is that an additional condition on the singlet self-coupling of the form $|\lambda_6| < 8\pi$ appears. In addition, the constraints related to scattering amplitudes involving the singlet field components and the field components of the doublet fields (see Eq. (3.67)) are modified with respect to the N2HDM.

We applied the previously described theoretical constraints taking into account the energy scale dependence of the parameters, utilizing the two-loop β-functions of the S2HDM and demanding that the theoretical constraints are respected up to a certain energy scale μ_v. The

---

[1] A (zero temperature) calculation of the lifetime of an unstable EW vacuum shows that in some cases the EW vacuum can be considered to be sufficiently long-lived, even though there are deeper minima present, such that a parameter point with a non-global EW minimum could still be viable (see Ref. [199] for an N2HDM analysis). However, in such cases it is still unclear whether the universe would have adopted the (meta-stable) EW vacuum at some point within the thermal history of the universe, or would have rather transitioned into a deeper unphysical minimum. The analysis of the thermal history of the scalar potential of the S2HDM is beyond the scope of this analysis (see Chapter 6 for an N2HDM analysis), such that we demand the most conservative constraint, i.e. excluding all parameter points for which the EW minimum is not the global minimum of the potential.

β-functions for the S2HDM were obtained with the help of the public code `SARAH` [347, 348], solving the general expressions known in the literature [349–351]. We also calculated the β-functions with the code `PyR@TE 3` [352] to be able to cross check the expressions and found exact agreement. We discarded a parameter point when the scale μ_v at which the scalar potential becomes unbounded or at which the perturbative unitarity constraints are violated is below 1 TeV, which was also chosen as the upper limit on the Higgs-boson masses in the numerical discussion (see Sect. 8.2).

8.1.2 Experimental constraints

The S2HDM offers a rich phenomenology that can be probed experimentally by various means. The corresponding experimental (null)-results give rise to numerous constraints that have to be taken into account. We start by discussing the constraints related to the Higgs sector of the model. Subsequently, we describe the manner in which the constraints from measurements from DM experiments were taken into account.

Searches for additional scalars and properties of h_{125}

Regarding the Higgs phenomenology of the model, we used the public code `HiggsBounds v.5.9.0` [312–316, 383] to test the parameter points against a large number of cross-sections limits from direct searches for Higgs bosons at LEP, the Tevatron and the LHC. For each Higgs boson, `HiggsBounds` selects the potentially most sensitive experimental search based on the expected limits. For the selected searches, the code then compares the predicted cross sections against the observed upper limits on the 95% confidence level and excludes a parameter point whenever the theoretical prediction lies above the experimental limit for one of the Higgs bosons.

Regarding the discovered Higgs boson at 125 GeV, we use the public code `HiggsSignals v.2.6.1` [308–311] to verify whether an S2HDM parameter point features a particle h_i that resembles the properties of the discovered particle h_{125} within the experimental uncertainties. `HiggsSignals` performs a χ^2-analysis confronting the predicted signal rates against the experimentally measured signal rates. In our more general parameter scan discussed in Sect. 8.2.1, we applied as constraint that the resulting χ^2 value (called χ^2_{125} in the following) fulfils $\chi^2_{125} \leq \chi^2_{\mathrm{SM},125} + 5.99$, where $\chi^2_{\mathrm{SM},125} = 84.41$ is the fit result assuming a SM Higgs boson at 125 GeV, and where the allowed penalty of 5.99 corresponds to a 95% confidence interval for two-dimensional parameter distributions.[2] In Sect. 8.2.2, in which we aim for accommodating the collider excesses observed at about 96 GeV, we combine the value of χ^2_{125} obtained from `HiggsSignals` with a value χ^2_{96} that quantifies the fit to the excesses. The precise criterion applied will be given in Sect. 8.2.2.

`HiggsBounds` and `HiggsSignals` require as input effective coupling coefficients, which are defined as the couplings of the physical scalars normalised to the coupling of a SM Higgs boson of the same mass. With the help of these coupling coefficients, the codes compute

---

[2] See Ref. [311] for details on the interpretations of the χ^2 analysis of `HiggsSignals`.

the relevant cross sections for the scalars by rescaling the predictions for a hypothetical SM Higgs boson. In the S2HDM, the coupling coefficients can be expressed in terms of $\tan\beta$ and (for the states h_i) in terms of the mixing angles α_i. The precise expressions are identical to the N2HDM expressions and can be found in Ref. [176]. Moreover, the user has to provide the branching ratios of the Higgs bosons. We calculated these in two steps. First, we used the public `Fortran` code `N2HDECAY` [176, 318, 384–386] implemented in the `anyhdecay` `C++` library to calculate the decay widths of h_i, A and $H^\pm$ for decays into SM particles and for cascade decays with one or two Higgs bosons in the final state.[3] In a second step we calculated the decay widths for the invisible decay into a pair of χ as described below (see Eq. (3.92)). We finally divided each partial decay widths by the total widths to obtain the branching ratios for each possible decay mode.

Additionally, we applied the currently strongest upper limit on the branching ratio of the invisible branching ratio $\mathrm{BR}_{\mathrm{inv}}$ from direct searches (see Eq. (3.92)) given by $\mathrm{BR}_{\mathrm{inv}} < 0.11$ at the at the 95% confidence level [229]. However, as will be demonstrated in Sect. 8.2.1, in most cases parameter points with sizable values of the corresponding branching ratios $\mathrm{BR}_{\mathrm{inv}}$ are already excluded by the global constraints on the measured signal rates of h_{125}, since the additional decay mode $h_{125} \to \chi\chi$ suppresses the ordinary decays of h_{125} into SM final states.

Electroweak precision observables

Since the S2HDM extends the SM particle content exclusively by scalar states, one can to a very good approximation apply the formalism of the oblique parameters S, T, U to include the constraints from EWPO. In order to predict the oblique parameters, we applied the general expressions at the one-loop level from Refs. [206, 207] to the S2HDM. Experimentally, S, T and U are constrained via global fits to the EWPO, where we utilise here the results (including their uncertainties) found in Ref. [210]. In 2HDM-like extensions of the SM, the most sensitive parameter is the T parameter, whereas the modifications of the U parameter in practically all cases are orders of magnitude smaller than the experimental sensitivity, and we explicitly checked this to hold in the S2HDM.[4] We therefore performed a two-dimensional χ^2 test regarding S and T, written as χ^2_{ST} in the following, and discarded parameter points for which the predicted values were not in agreement with the experimental fit result [210] at the 95% confidence level. This gives rise to the requirement $\chi^2_{ST} \leq 5.99$. The T parameter is sensitive to the breaking of the custodial symmetry. As a result, one finds strong exclusions when there is a sizable mass splitting between the states A, $H^\pm$ and (depending on the doublet-admixture) one of the *heavy* CP-even state h_2 or h_3.

---

[3] The `anyhdecay` library can be downloaded at `https://gitlab.com/jonaswittbrodt/anyhdecay`.

[4] We found that at the one-loop level the theoretical predictions for S, T and U in the S2HDM and the N2HDM (given the same values of m_{h_i}, m_A and $m_{H^\pm}$) are identical, because they do not depend on the additional state χ of the S2HDM as long as $v_{\mathrm{DM}} = 0$.

Flavour-physics observables

Since there are no public results for the theoretical predictions in singlet extensions of the 2HDM for some of the most relevant flavour observables, we simply applied hard cuts on the ranges of $\tan\beta$ and $m_{H^\pm}$ in our numerical analysis. The cuts were determined by assuming that the exclusion regions known from the 2HDM are not severely modified by the presence of the additional field of the S2HDM, which we expect to be the case due to the singlet nature of this field (see discussion in Sect. 3.2.2). Consequently, working in the type II S2HDM, we set lower limits of $\tan\beta > 1.5$ and of $m_{H^\pm} > 600$ GeV in order to not be in conflict with constraints from radiative and (semi-)leptonic B meson decays and from their mixing frequencies [210].[5]

Dark matter observables

We now turn to the experimental constraints that are related to the presence of the DM candidate χ. The most important limitation arises from the fact that a too large relic abundance of χ after thermal freeze-out would overclose the universe. The currently most precise measurement of today's DM relic abundance Ωh^2 is given by surveying the cosmic microwave background by the Planck satellite, leading to a measurement of $(\Omega h^2)_{\text{Planck}} = (0.119 \pm 0.003)$ [72]. We will use this value as an upper limit on the relic abundance of χ in our analysis, taking into consideration that, in case the relic abundance of χ is smaller than $(\Omega h^2)_{\text{Planck}}$, there is room for additional (particle or astrophysical) contributions to the relic abundance. We focus the analysis on the *Higgs funnel region* with DM masses of $40 \leq m_\chi \leq 80$, where there are good prospects to be able to explain most (or all) of the observed DM relic abundance via the thermal freeze-out of χ [23, 64, 66, 70, 389]. For the theoretical prediction of the relic abundance, we wrote an S2HDM modelfile for the `Mathematica` package `FeynRules v.2` [390–392], which we utilised to obtain a `CalcHEP` [393] input for the public code `MicrOMEGAs v.5` [394] written in `C` and `Fortran`. With this input, `MicrOMEGAs` is capable of calculating the relic abundance and the freeze-out temperature, where for the computation of the annihilation cross section all 2×2 processes and also processes with off-shell vector bosons in the final state are taken into account.

As already pointed out, one of the attractive features of the S2HDM is that due to the pNG nature of the DM particle the cross sections for the scattering of χ on nuclei vanish at leading order in the limit of vanishing momentum transfer [389], such that at this order DD experiments are not sensitive to the presence of χ. In addition, it was shown in models with a single Higgs doublet field and a complex singlet field that the loop contributions to the DD cross sections are small, and the predicted DD scattering cross sections remain far below the current (and near future) sensitivity of DD experiments [62, 63, 69]. We

---

[5] A more recent result suggests a lower limit of $m_{H^\pm} > 800$ GeV in the type II 2HDM from the measurement of the radiative B meson decay [387], whereas Ref. [388] claims that theoretical uncertainties might have been underestimated in the literature, potentially giving rise to a weaker lower limit. We emphasise that the conclusions drawn from our numerical analysis do not depend on the precise value of the lower limit chosen for $m_{H^\pm}$.

assume that these results are not substantially modified by the presence of the second Higgs doublet field in the S2HDM, which is a reasonable assumption in the type II S2HDM in which the additional doublet particle states are substantially heavier than the values of m_χ in our analysis. Consequently, there are no relevant constraints from DD experiments that have to be taken into account in our analysis.

On the other hand, constraints from DM in DD experiments are important, in particular in the Higgs funnel region investigated here, in which χ mainly annihilates into b quark pairs, typically via h_{125} in the s-channel. The most stringent constraints on the annihilation cross sections of DM come from the observation of dwarf spheroidal galaxies (dSph) by the Fermi-LAT space telescope [73]. In order to account for these constraints, we used `FeynRules` to generate UFO [395] model files for the S2HDM, which were then used as input for the public code `MadDM v.3` [396, 397]. `MadDM` is a plugin for `MadGraph5_atMCv.3.1.1` [398] that can be used to compute the relevant velocity-averaged annihilation cross sections $\langle \sigma v_{\mathrm{rel}} \rangle_{b\bar{b}}$, and to subsequently compare the theoretical predictions to the upper limits on the velocity weighted cross section for DM particles annihilating into $b\bar{b}$ final states from the Fermi measurements of gamma rays from dSph at the 95 % CL.[6] The Fermi-LAT collaboration utilises a likelihood analysis to fit the spectral and spatial features of dSphs to obtain upper limits on the annihilation cross section as a function of the DM mass [73]. The analysis accounts for point-like sources from the latest LAT source catalog, models the galactic and isotropic diffuse emission, and incorporates uncertainties in the determination of astrophysical J-factors, which depend on both the DM density profile and the distance. The observed limits are sensitive to the determination method of the J-factors. In Ref. [73] an evaluation of the uncertainties arising from targets lacking measured J-factors was performed. Using only predicted J-factors for the whole sample weakened the observed limits by a factor of about 2 to 3, depending on the choice of J-factor uncertainty, with respect to the limits obtained by using both predicted and measured J-factors. Considering these uncertainties will be important for the discussion of the tension between the constraints coming from dSph and the gamma-ray excesses and anti-protons measured from the galactic center, as will be demonstrated in Sect. 8.2.1.

For the comparison between the predicted annihilation cross section and the Fermi bounds from dSph observations, we rescaled (when not explicitly said otherwise) the cross sections with a factor

$$\xi^2 = \left(\frac{\Omega h^2}{(\Omega h^2)_{\mathrm{Planck}}} \right)^2 , \tag{8.1}$$

in order to account for the suppression of today's annihilation cross section of χ due to the smaller number density when the relic abundance of DM is not made up completely out of χ.[7] We also point out that the velocity-averaged annihilation cross sections can

---

[6] We also computed $\langle \sigma v_{\mathrm{rel}} \rangle$ for other two body final states. However, for the range of m_χ investigated here the b quark final state was always the dominant one. In addition, we applied the so-called fast mode of `MadDM` in order to reduce the duration of the calculation. We checked for several parameter points of our scans that the difference between the values of $\langle \sigma v_{\mathrm{rel}} \rangle$ in the fast and the precise mode are very similar.

[7] For the calculation of ξ we used the value of Ωh^2 as predicted by `MicrOMEGAs`. In principle, also `MadDM` can

be considered here to be velocity-independent in the non-relativistic limit to a very good approximation, since in our scan range of m_χ they are dominantly generated via diagrams with s-channel exchange of either h_1 or h_2 [399]. Nevertheless, we calculated $\langle \sigma v_{\mathrm{rel}} \rangle$ with different relative velocities v_{rel} for the comparison against the Fermi-LAT dSph constraints, on the one hand, and for the comparison against the preferred regions regarding the gamma-ray and the anti-proton excesses, on the other hand. In both cases we used the default values of `MadDM`, which are $v_{\mathrm{rel}} = 2 \cdot 10^{-5}$ for the DM in dSph and $v_{\mathrm{rel}} = 10^{-3}$ for DM in the center-of-galaxy as relevant for the excesses. In agreement with our expectation, the differences of the annihilation cross sections for the two values of v_{rel} stayed below a few percent and are not relevant for our discussion.

8.2 Numerical analysis

We divide our numerical analysis of the type II S2HDM into two parts. In the first part discussed in Sect. 8.2.1, we will demonstrate in a broad parameter scan how the Higgs funnel region with 40 GeV $\leq m_\chi \leq$ 80 GeV is affected by the various theoretical and experimental constraints. Here the DM particle χ is the lightest BSM state, and $h_{125} = h_1$ is the lightest of the three CP-even Higgs bosons h_i. We will describe in detail the predictions for the DM relic density and its interplay with the Higgs sector of the model. In addition, we investigate whether the annihilation of χ in this scenario could give rise to the cosmic-rays anomalies from observations of the spectra of cosmic rays coming from the center of the galaxy. We emphasise at this point that due to the large mass gap between the DM mass m_χ studied here and the masses of the heavy scalar states h_3, A and $H^\pm$ in the type II S2HDM, the predictions for the DM relic abundance and today's DM annihilation cross section mainly depend on the couplings of χ to the SM-like Higgs boson and (when present) the light singlet-like Higgs boson. Accordingly, the properties of the DM sector will be similar compared to the predictions from the pNG DM model with only one Higgs doublet, because additional annihilation processes involving the heavier states do not play a role. However, differences between both models can still arise due to the richer mixing patterns of the states h_i in the S2HDM, where the mixing angles $\alpha_{1,2,3}$ enter the couplings of h_i to χ.

In the second part of our analysis, discussed in Sect. 8.2.2, we focus on the parameter space in which at the same time the collider excesses at about 96 GeV could be accommodated. Consequently, here the presence of a singlet-like Higgs boson $h_{96} = h_1$ with $m_{h_1} = 96$ GeV is enforced as an additional constraint on the parameter space. As a result, the SM-like Higgs boson h_{125} is the second lightest Higgs boson h_2, and its mixing with h_{96} is subject to the constraints from the LHC measurements of the signal rates of h_{125}. Going beyond the discussion of the collider phenomenology and the excesses at 96 GeV, we will illustrate in detail how the presence of h_{96} has also important consequences for the

---

calculate the relic abundance. However, by default `MadDM` does not take into account the contributions to the annihilation cross section with off-shell gauge bosons, which are relevant in our analysis. Moreover, the calculation of the relic abundance is much faster using `MicrOMEGAs`.

DM phenomenology in the Higgs funnel, in particular giving rise to a second s-channel contribution to the thermal freeze-out cross section and today's annihilation cross section relevant for DM in DD experiments.

In both parameter scan presented in the following, we sampled the multi-dimensional parameter space of the model utilizing a genetic algorithm. In contrast to random or uniform (grid)-scans of the model parameters, a genetic algorithm has the advantage that it focuses on the relevant parameter region by minimizing a so-called loss function, which has to be suitably defined in each case. The definition of the loss functions used in both parts of our analysis will be given in Sect. 8.2.1 and Sect. 8.2.2. Apart from the loss function, the properties of the genetic algorithm applied were in large parts identical in both scans. For the interested reader we briefly describe the main design choices here, where we made use of the public `python` package `DEAP` [400] to perform the algorithm.

The algorithm starts by generating an initial sample (also called population) of 50 000 parameter points. Each parameter point (also called individual) is defined by a list of 14 numbers (also called attributes or genes), where each number of this list defines a value of one of the model parameters within a given parameter range. The population is then subject to an evolution including the three steps: selection, mating and mutation. These three steps are performed in a loop for a total number of N cycles (also called generations), such that each cycle gives rise to a new population of parameter points with (desirably) better fitnesses. The fitness of each individual is defined by the corresponding value of the loss function: the smaller the value of the loss function given the parameter values of an individual, the better is the fitness of the individual.

The first step of each cycle, i.e. selection, determines which of the individuals of the population are allowed to take part in the following two steps, i.e. mating and mutation. As a selection function we used the so-called tournament selection with size three. This function selects the individual with the best fitness from three randomly picked individuals of the population. In total 50 000 individuals are selected in this way (where each individual was allowed to be selected more than once) and these then proceed to the mating stage. Since the selection is based on the fitness values, individuals with better fitness have a higher chance of producing new individuals (called offspring).

For the mating process, we divided the selected individuals into two distinct groups, and then we performed a uniform crossover of pairs of individuals from each group. A uniform crossover creates two child individuals from each pair of parent individuals, where the child individuals are defined by swapping the attributes of the two parent individuals, in our case according to a probability of 0.2. Hence, the two parent individuals produce two offspring individuals which have on average 20% of the attributes from one parent and 80% of the attributes from the other parent. In addition, we included a so-called mating probability of 0.8, such that for 20% of the pairs of parent individuals no mating was performed and the parent individuals were just kept in the population without changing their attributes.

Afterwards, the mutation stage is performed, which modifies some of the individuals of the offspring via a randomised function, potentially giving rise to new individuals with good fitness values that belong to so far unexplored parameter regions. As a mutation function we applied the so-called float uniform mutator function with a mutation probability of 0.2. This function multiplies the attributes of an individual with a random number between 0.8 and 1.2 according to a probability of 0.1. As a result, 20% of the individuals of the offspring are mutated, and the mutations modify on average 10% of the attributes of such individual.

At the end of each cycle, we replace the initial population with the offspring and enter a new cycle, until either an individual is found that corresponds to a value of the loss function below a certain threshold, or until the maximum number of cycles is reached. Since it is possible that the individual in the parent population with the best fitness would be lost when the population is replaced, we append this best-fit individual to the offspring population in order to ensure that it always survives the complete cycle. Finally, when the algorithm has completed, we save the parameter point with the best fitness. Accordingly, the above described algorithm is performed as many times as the number of desired parameter points in the final sample.

For the two scans discussed in Sect. 8.2, we compared the performance of the genetic algorithm to the one of a random scan over the free parameters using a flat prior. For a machine-independent estimate of the performances of both algorithms, we chose the number of evaluations of the loss function L (see Eq. (8.3)) that is required until a parameter point featuring a value of L below a certain threshold is found. We found for the first scan discussed in Sect. 8.2.1 that, on average, the genetic algorithm succeeds in finding a value of $L < 90$ with roughly 60% to 70% fewer evaluations of L compared to the random scan, such that the improvment is only moderate. For the second scan discussed in Sect. 8.2.2, in which L receives an additional term, our computations indicate that the genetic algorithms outperforms the random scan drastically. Here we found that using the genetic algorithm the average number of evaluations of L in order to find a parameter point with $L < 150$ was approximately 35 times smaller than using a random scan. Since in this scan the parameter points with the desired features with regards to the collider excesses (see Sect. 8.2.2 for details) require values of L that are even smaller than $L = 150$, we conclude that the usage of the genetic algorithm was a vital piece of our numerical analysis. The reason for the fact that the genetic algorithm performs so much better in the second scan, whereas the improvement was only moderate in the first scan, can be attributed to the fact that the simultaneous minimization of the values of χ_{125} (see Sect. 8.1.2) and the value χ_{96} (defined in Sect. 8.2.2), which quantifies the fit to the collider excesses, requires additional relations between the mixing angles α_i and $\tan\beta$, which the genetic algorithm is able to find more quickly by successively adjusting the parameters of the points with the lowest values of L that have been found in the previous generation.

8.2.1 pNG DM in the Higgs funnel region

In order to explore the Higgs funnel region, we scanned the parameter space of the S2HDM within the parameter ranges

$$1.5 \leq \tan\beta \leq 10 \ , \quad m_{h_1} = 125.09 \text{ GeV} \ , \quad 140 \text{ GeV} \leq m_{h_{2,3}} \leq 1 \text{ TeV} \ ,$$

$$\begin{aligned} 40\text{ GeV} \leq m_\chi \leq 80\text{ GeV} \ , \quad 40\text{ GeV} \leq v_S \leq 1\text{ TeV} \ , \quad -\pi/2 \leq \alpha_{1,2,3} \leq \pi/2 \ , \\ 400\text{ GeV} \leq M \leq 1\text{ TeV} \ , \quad 600\text{ GeV} \leq m_{H^\pm} \leq 1\text{ TeV} \ , \quad m_A \leq 1\text{ TeV} \ , \\ \Delta M_{\max} = \max\left(|m_H - M|, |m_A - M|, |m_{H^\pm} - M|\right) < 200\text{ GeV} \ , \end{aligned} \tag{8.2}$$

where in the last line $m_H = m_{h_2}$ when $\Sigma_{h_2} < \Sigma_{h_3}$ or $m_H = m_{h_3}$ when $\Sigma_{h_2} > \Sigma_{h_3}$. Thus, this condition on $\Delta M_{\max}$ ensures that the masses of the heavy doublet-like states A, $H^\pm$ and $H = h_2$ or $= h_3$ are not further than 200 GeV away from the mass scale M. As explained in Sect. 8.1.1, and as will also be demonstrated in the following, this condition excludes parameter points that have a very small energy range $v \leq \mu \leq \mu_v$ in which the parameter points fulfill the theoretical constraints, with potentially $\mu_v \ll 1$ TeV. The lower limits of $\tan\beta \geq 1.5$ and $m_{H^\pm} \geq 600$ GeV exclude parameter points that are potentially in conflict with constraints from flavour-phyiscs observables. The mass hierarchy of the CP-even Higgs bosons h_i is fixed such that $h_{125} = h_1$ is the lightest one. Their mixing angles α_i are scanned over the theoretically possible range, where it should be noted that their values are strongly constrained by the measurements of the signal rates of h_{125}, as will also be demonstrated below. The vev of the singlet field v_S is allowed to take on values up to 1 TeV, which coincides with the upper value chosen for the masses of the heavier BSM states $H^\pm$, A and $h_{2,3}$. If we would have allowed for larger values of v_S and M, the heavy states could acquire also larger masses and decouple from the lighter states h_1 and χ. However, we wanted to focus on the parameter space region in which the collider constraints from direct searches at the LHC play a role, such that we limited our scan to the case in which all particle states could be produced (and discovered) at the LHC.

The scan points that we will present were obtained in a two step procedure. In the first step we applied the genetic algorithm as described before in order to find parameter points that minimise the loss function

$$L = \chi^2_{125} + \max\left[0, (r^{\text{HB}}_{\text{obs}} - 1) \cdot 100\right] + \begin{cases} C \ , \ \text{when } \chi^2_{ST} > 5.99 \text{ or theo.} \\ \qquad\qquad\qquad \text{constraint violated at } \mu = v \\ 0 \ , \ \text{otherwise} \end{cases} . \tag{8.3}$$

Here χ^2_{125} is the result of the `HiggsSignals` test, and $r^{\text{HB}}_{\text{obs}}$ is provided from the `HiggsBounds` test. $r^{\text{HB}}_{\text{obs}}$ is defined as the ratio of predicted cross section for the most sensitive channel divided by the experimentally observed upper limit (see Sect. 8.1.2 for details). As a result, parameter points featuring a value of $r^{\text{HB}}_{\text{obs}} > 1$ should be rejected, and the second term in the loss function quantifies the penalty of this requirement. The factor 100 is included in order to enhance the importance of this exclusion in terms of the loss function compared to the values of χ^2_{125}, thus making sure that all parameter points with low values of the loss function have $r^{\text{HB}}_{\text{obs}} < 1$ and are consequently not excluded by direct searches. Finally, the third term is a huge constant C that is added when a parameter point does not fulfil the theoretical constraints at the initial energy scale $\mu = v$, or when the constraints from the EWPO are not fulfilled. With this definition of the loss function, the genetic algorithm finds parameter points that pass the theoretical constraints, the constraints from the collider experiments and the EWPO.

In a second step, all the parameter points found with the genetic algorithm were subject to the remaining constraints: according to the discussion in Sect. 8.1.1, we applied the theoretical constraints for scales $\mu > v$ and verified whether they are fulfilled up to at least $\mu = 1$ TeV. In addition, we verified that, regarding the SM-like Higgs boson, we have $\Delta\chi^2_{125} = \chi^2_{125} - \chi^2_{\mathrm{SM},125} \leq 5.99$ and $\mathrm{BR}_{\mathrm{inv}} < 0.11$, and, regarding the DM candidate, that the predicted relic abundance is is not larger than the Planck value, i.e. $\Omega h^2 \leq (\Omega h^2)_{\mathrm{Planck}}$. We also ensured that the constraints from the in DD experiments from the observation of dSph are respected. The DM observables were not taken into account already in the definition of the loss function, because the computation of the relevant theoretical predictions were the most time-consuming part of the analysis, such that it was much more efficient to perform these computations only for the parameter points that otherwise passed all the other theoretical and experimental constraints.

As was already mentioned before, the main purpose of this analysis is to illustrate the combined impact of the various constraints on the model parameters. In particular, we will point out which of the constraints give rise to limitations on which subset of parameters, and whether the constraints cover similar or clearly distinct regions of the S2HDM parameters. In the following, we start the discussion with the theoretical constraints that were applied according to the discussion in Sect. 8.1.1. In the next step, we examine the impact of the collider constraints by taking into account both the constraints from direct searches and from the constraints on the properties of h_{125} (see Sect. 8.1.2). Finally, we consider the physics related to the DM candidate χ, and how its properties are interconnected to the Higgs sector.

In order to analyse the impact of the theoretical constraints, we show in Fig. 8.1 the parameter points with the colour coding indicating the energy scale μ_v until which the theoretical constraints are respected. We remind the reader that all parameter points fulfill the theoretical constraints at the initial scale $\mu = v$. All points for which $\mu_v < 1$ TeV are shown in grey. We performed the RGE running up to $\mu = 100$ TeV, such that points that have $\mu_v = 100$ TeV (yellow points) are potentially valid up to much higher energy scales. In the upper left plot we show the parameter points in the plane $m_{H^\pm} - M$ and $m_A - M$. One can see that only points for which these differences are below roughly 50 GeV are valid at energy scales much beyond 1 TeV. On the other hand, parameter points with values of $|m_{H^\pm} - M| \gtrsim 120$ GeV and/or $|m_A - M| \gtrsim 150$ GeV are always in contradiction with one of the theoretical constraints already at scales $\mu_v < 1$ TeV. The same observation can be made in the upper right plot, in which $|m_H - M|$ is depicted on the vertical axis. Points that feature values of μ_v much larger than about 1 TeV are concentrated at values of $|m_H - M| \lesssim 50$ GeV, whereas points with larger values of $|m_H - M|$ are almost always only well behaved within a small range of energies.

We find that the relevant constraint that give rise to the low values of μ_v are in most cases the tree-level perturbative unitarity constraints. These constraints effectively provide upper limits on the absolute values of the quartic scalar couplings λ_i and combinations thereof (see also Sect. 3.2.1). It is therefore easy to understand why they are more severe

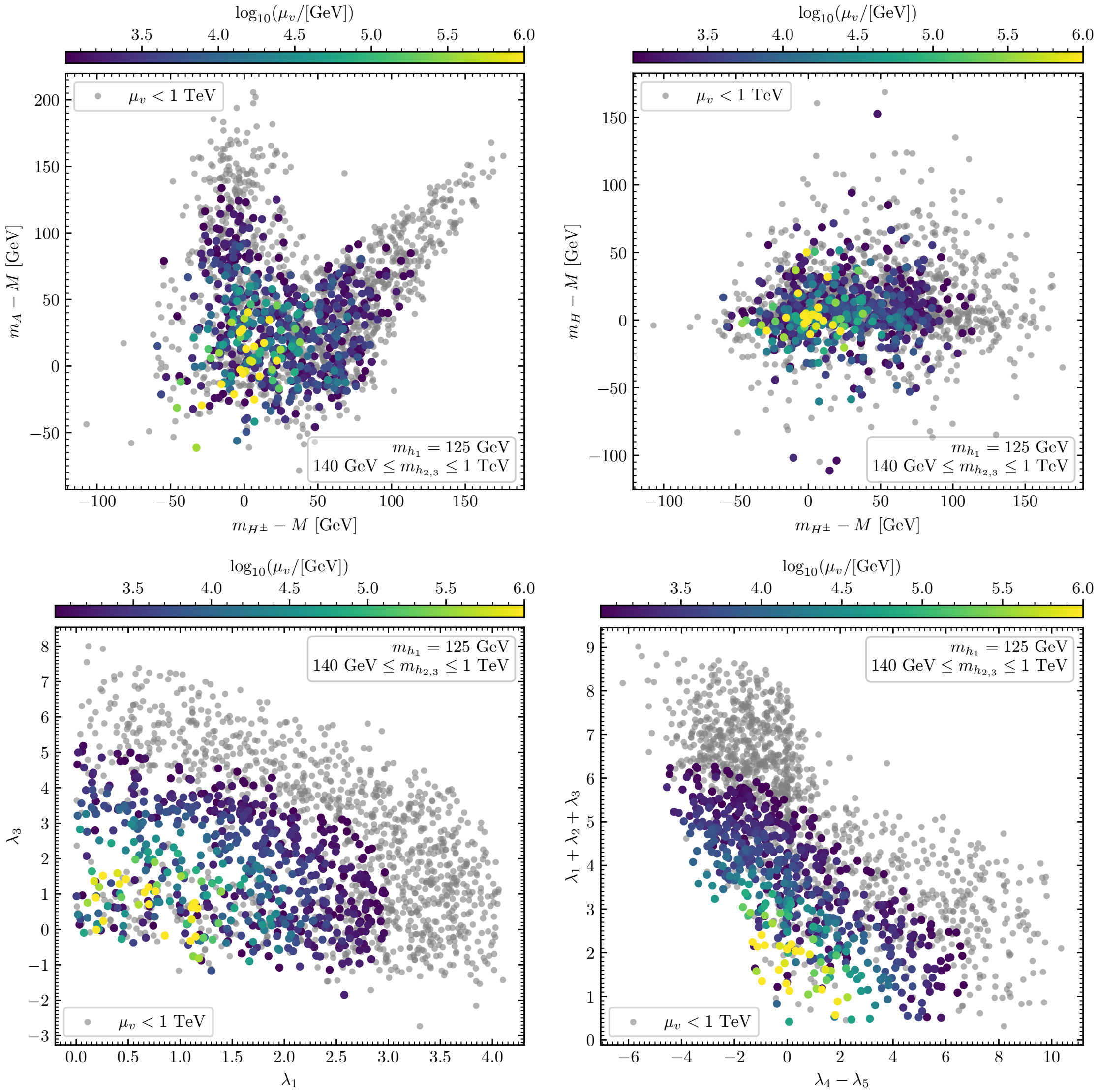

Figure 8.1: Top row: $m_A - M$ (left) and $m_H - M$ (right) in dependence of $m_{H^\pm} - M$, where $m_H = m_{h_2}$ or $m_H = m_{h_2}$ depending on whether $\Sigma_{h_2} < \Sigma_{h_3}$ or vice versa. Bottom row: λ_3 in dependence of λ_1 (left) and $\lambda_1 + \lambda_2 + \lambda_3$ in dependence of $\lambda_4 - \lambda_5$ (right). The colour coding indicates the value of μ_v. Also shown in grey are discarded parameter points with $\mu_v < 1$ TeV.

in region of parameter space with relatively large splittings between the masses of the heavy BSM states and the mass scale M, since such splittings are induced by large absolute values of $\lambda_{1,2,3,4,5}$ (see also App. A). Moreover, for obvious reasons also the energy scale dependence of the quartic couplings is stronger when their absolute values are larger. As a result, points with large mass splittings, which potentially were already on the edge of being excluded via the tree-level perturbative unitarity constraints at the initial energy scale, quickly break one of these constraints once the RGE evolution is considered. This is also reflected in the plots in the lower row of Fig. 8.1, in which we show the points in the planes λ_1-λ_3 on the left and $(\lambda_4 - \lambda_5)$-$(\lambda_1 + \lambda_2 + \lambda_3)$ on the right. In the left plot one can see that verifying the theoretical constraints exclusively at the initial scale $\mu = v$ gives rise to parameter points with values of $\lambda_1 \lesssim 4$ and $-3 \lesssim \lambda_3 \lesssim 8$, whereas demanding that the constraints are respected within a range of energy of at least $v \leq \mu \leq 1$ TeV, the allowed ranges shrink to $\lambda_1 \lesssim 3$ and $-2 \lesssim \lambda_3 \lesssim 5$.[8] A similar observation can be made in the right plot, in which the allowed values change from $\lambda_1 + \lambda_2 + \lambda_3 \lesssim 9$ and $-6 \lesssim \lambda_4 - \lambda_5 \lesssim 10$ to $\lambda_1 + \lambda_2 + \lambda_3 \lesssim 6$ and $-4 \lesssim \lambda_4 - \lambda_5 \lesssim 7$ once the RGE running and the additional constraint $\mu_v > 1$ TeV is taken into account. Note that the limits on the values of the couplings that we found are much below the naive perturbativity criterion $|\lambda_i| < 4\pi$, which is often applied in the analysis of extended Higgs sectors in order to exclude non-perturbative parameter regions.

Consequently, we conclude that regarding the collider phenomenology the main impact of our choice to demand the theoretical constraints to be respected at least until $\mu = 1$ TeV is that the masses of the heavy states are closely related to the overall mass scale M, which, however, does not significantly constrain the values of $\lambda_{6,7,8}$, since they do not depend directly on M (see App. A). Thus, the only exception to the constraints on the mass splittings arises when there is a Higgs boson h_2 or h_3 with almost 100% singlet component present, in which case its mass would be dominantly related to the value of v_S instead of M, and the mass could differ substantially from m_A, $m_{H^\pm}$ and m_H, as will also be further discussed below. Thus, our approach of including the theoretical constraints drives the model predictions towards the decoupling limit of the S2HDM, where the masses of the heavy states m_A, $m_{H^\pm}$ and m_H are approximately determined by the scale M of the soft-breaking of the discrete $\mathbb{Z}_2$. Considering the theoretical constraints described above has in some aspects the same effect as applying the constraints from the EWPO, which are also sensitive to large mass splittings between the scalar states [210]. This fact on its own is not very surprising since also the EWPO observables arise from the radiative corrections. More interesting, however, is that while it is sufficient to have either $m_H \sim m_{H^\pm}$ or $m_A \sim m_{H^\pm}$ in order to be in agreement with the constraints from EWPO (at one-loop level), the inclusion of the RGE running and the requirement $\mu_v > 1$ TeV gives rise to the fact that both conditions should be approximately fulfilled, i.e. $m_H \sim m_A \sim m_{H^\pm}$.

The low values of μ_v that we found for values of $|\lambda_i| \gtrsim 1$ are relevant also for cosmological aspects of the S2HDM, where we stress again that one of the main motivations of the model is the possibility of accommodating a first-order EW phase transition. In order to achieve such a transition, it is required (just as in the 2HDM) to consider parameter space regions where large loop corrections to the scalar potential are present, since at tree level the scalar potential does not allow for an EW phase transition of first order. The required loop corrections have their origin in values of one or more $|\lambda_{1,2,3,4,5}| > 1$ (see Chapter 6). As a result, our analysis indicates that for a perturbative study of the parameter regions of the S2HDM relevant for possible first-order EW phase transitions, it is of crucial importance to take into account constraints in relation to the perturbative unitarity and the RGE running

---

[8] λ_1 has to be positive according to the BfB conditions on the tree-level scalar potential.

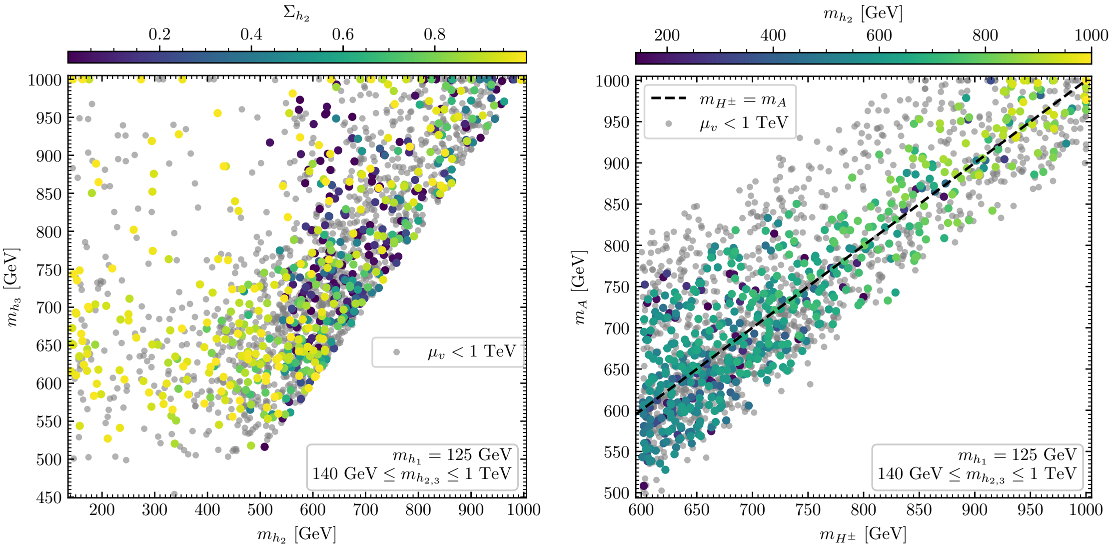

Figure 8.2: Spectrum of the heavy Higgs bosons $h_{2,3}$, A and $H^\pm$ for the parameter points fulfilling the theoretical and experimental constraints. Left: m_{h_3} in dependence of m_{h_2}, with the colours indicating Σ_{h_2}. Right: m_A in dependence of $m_{H^\pm}$, with the colours indicating m_{h_2}. Also shown in grey are excluded parameter points with $\mu_v < 1$ TeV. The dashed line indicates where $m_{H^\pm} = m_A$.

of the quartic couplings.[9] On the other hand, if one restricts an analysis of the S2HDM to regions of the parameter space in which the couplings λ_i have absolute values substantially below one, then the model can be valid to energy scales much beyond the TeV scale. In this case, however, the S2HDM cannot accommodate a first-order EW phase transition and its related phenomenology, and also the heavy BSM states are largely decoupled from the EW scale (as discussed above).

To shed more light on the spectrum of the Higgs bosons, we show in Fig. 8.2 the mass m_{h_3} in dependence of m_{h_2} on the left and m_A in dependence on $m_{H^\pm}$ on the right. In the left plot one can see that it is possible that h_2 is substantially lighter than h_3 when it has a large singlet component of $\Sigma_{h_2} > 90\%$, as indicated by the colours of the points. On the other hand, when h_2 and h_3 are sizably mixed, the masses of both states have to be relatively close to M in order to comply with the theoretical constrains. The same observation can be made in the right plot regarding the masses of A and $H^\pm$. Note here that all the points with $m_A - m_{H^\pm} \gtrsim 150$ GeV are grey, indicating that they feature values of $\mu_v < 1$ TeV. In this plot the colour coding indicates the values of m_{h_2}, and a correlation can be seen between the mass of h_2 and the masses of A and $H^\pm$. The heavier the latter states, the larger also tend to be the values of m_{h_2}. Since by definition $m_{h_2} < m_{h_3}$, one can conclude that in most parameter points all six states $h_{2,3}$, A and $H^\pm$ are relatively close in mass, with the only exception being a very singlet-like state h_2 with $m_{h_2} \ll M$, as

---

[9] For instance, both type II benchmark scenarios in Tab. I of Ref. [70], where first-order phase transitions are discussed in the context of the S2HDM, would be excluded in our analysis due to the large absolute values of $\lambda_4 \sim 5$ and $\lambda_5 \sim -7$.

mentioned earlier already. Hence, our analysis shows a trend towards the decoupling limit of the S2HDM, in which at low energies the model could become practically indistinguishable from the SM. In this case, the only possibility to observe a BSM effect would arise from the DM phenomenology or a possible invisible branching ratio of h_{125} if the decay $h_{125} \to \chi\chi$ is kinematically allowed (see the discussion below). The presence of an invisible branching ratio of h_{125} could also allow for a distinction between the S2HDM and the 2HDM, whereas the S2HDM in the decoupling limit could be practically indistinguishable from the pNG model with one Higgs doublet, in which case only a discovery of one of the additional particles of the S2HDM at a collider could shed light on the model realised in nature.

Going beyond the theoretical limitations, the spectrum of the Higgs bosons is also severely constrained by direct searches at colliders, where due to the fact that we focus here on the mass ordering with $h_1 = h_{125}$ only the LHC results play a role in our discussion.[10] Without going into the details of each of the relevant search channels, the searches that were selected by `HiggsBounds` and which led to exclusions of parameter points in the scenario under investigation were listed in Sect. 3.2.2. In general, the most promising searches at the lower end of the $\tan\beta$ range are the searches for the charged Higgs bosons or the searches for the neutral states h_2, h_3 and A dominantly produced in the gluon fusion channel, where depending on their masses they then mostly decay into pairs of t quarks, pairs of vector bosons or into a lighter Higgs boson and a Z boson. For the upper end of the $\tan\beta$ range, the most promising channel is the resonant search for new Higgs bosons in the invariant mass spectrum of two τ leptons. Here it should be noted that the resulting exclusions in the S2HDM can be substantially different in comparison to the 2HDM, because h_3 and A can have sizable branching ratios for the decays into final states containing a potentially much lighter singlet-like state h_2, in which case the branching ratios in regards to the decays of h_3 and A into a pair of τ-leptons are suppressed. As a result, for a fixed value of $\tan\beta$ both states can be lighter in the S2HDM compared to the 2HDM without being in conflict with the searches for heavy Higgs bosons decaying into two τ leptons [223]. Finally, for parameter points in the intermediate $\tan\beta$ range with $3 \lesssim \tan\beta \lesssim 6$, the bosonic decays of the neutral states are most relevant, such that the searches with two vector bosons in the final state or Higgs cascade decays can probe parts of the parameter space of the S2HDM.

Complementary to the direct searches for the BSM particles, the Higgs sector of the S2HDM can also be probed indirectly via the properties of the Higgs boson $h_1 = h_{125}$ resembling the Higgs boson that was discovered at the LHC. In order to illustrate the impact of such constraints, we show in the left plot of Fig. 8.3 the allowed parameter points, which all fulfil the criterion $\chi^2_{125} \leq \chi^2_{\mathrm{SM},125} + 5.99$ (see Sect. 8.1.2 for details), with $\sin(\alpha - \beta)$ on the horizontal and $\tan\beta$ on the vertical axis. In the case in which one of the heavier states h_2 or h_3 has a singlet component of almost 100%, the S2HDM features an alignment limit similar to the 2HDM. In this limit the couplings of h_1 reduce to the ones of a SM Higgs boson, and the limit is determined by the condition $\sin(\alpha - \beta) = 0$ (see also Ref. [176]). Consequently, departures from this condition are associated with deviations

---

[10] See also Refs. [401, 402] for investigations of the collider phenomenology of a 2HDM extended with a complex singlet scalar, in which no additionally U(1) symmetry is imposed on the singlet.

of the predictions for the signal rates of h_{125} with respect to the SM. As can be seen in the left plot of Fig. 8.3, our analysis indicates that in order to be in agreement with the measured signal rates, one has to fulfil roughly $|\sin(\alpha - \beta)| \lesssim 0.1$. The largest departures from zero are found for the lower end of the $\tan\beta$ range, whereas for larger values of $\tan\beta$ the allowed range of $|\sin(\alpha - \beta)|$ shrinks substantially. The colour coding of the points indicates the singlet component of the SM-like Higgs boson Σ_{h_1}. Notably, we find that the current uncertainties of the signal-rate measurements still allow for a singlet-component of more than 14%.

Precise measurements of the properties of h_{125}, for instance correlated deviations from the SM prediction of the various different couplings coefficients of h_{125} to the up- and down-type fermions $C_{h_{125}u\bar{u}}$ and $C_{h_{125}d\bar{d}}$ and the gauge bosons $C_{h_{125}VV}$, could help to distinguish the type II S2HDM from the usual 2HDM. Here the coupling coefficients $C_{h_{125}u\bar{u},d\bar{d},VV}$ are defined to be the couplings normalised to the ones of a SM Higgs boson. A sizable singlet-component of h_{125}, as found in parts of our parameter points, gives rise to a suppression of $C_{h_{125}VV}$. In the usual 2HDM, a deviation from $|C_{h_{125}VV}| = 1$ is possible via departures from the alignment limit, and thus tightly constrained to values of $C^2_{h_{125}VV} \gtrsim 0.9$ [210]. Since we find parameter points with $\Sigma_{h_{125}} > 0.1$, and since in the S2HDM one has $C^2_{h_{125}VV} \leq 1 - \Sigma_{h_{125}}$, a possible future measurement indicating $C^2_{h_{125}VV} \lesssim 0.9$ at the (HL)-LHC would favor an S2HDM interpretation instead of the 2HDM. It is also interesting to compare the maximum values of $\Sigma_{h_{125}} \sim 14\%$ with the corresponding values found in the pNG DM model with only one Higgs doublet. In Ref. [64] it was shown that in this case the mixing of the SM-like Higgs boson with the singlet state is more constrained, and, except when the singlet scalar and the doublet scalar are degenerate in mass, only values of up to 10% were found to be in agreement with the Higgs-boson measurements. As a result, and under the assumption that a deviation of the properties of h_{125} w.r.t. the SM will be observed, one could potentially distinguish the S2HDM from the simpler model with only one Higgs doublet via the precise measurements of $C_{h_{125}VV}$, $C_{h_{125}u\bar{u}}$ and $C_{h_{125}d\bar{d}}$. Moreover, the model with one Higgs doublet predicts $C_{h_{125}u\bar{u}} = C_{h_{125}d\bar{d}}$, such that experimental indications for $C_{h_{125}u\bar{u}} \neq C_{h_{125}d\bar{d}}$ would clearly favour an S2HDM interpretation. Another obvious possibility to distinguish both models arises from the fact that the S2HDM can predict values of $|C_{h_{125}d\bar{d}}|, |C_{h_{125}u\bar{u}}| > 1$ due to enhancements by factors of $1/c_\beta$ or $1/s_\beta$ (depending on the Yukawa type), while the pNG DM model with one Higgs doublet can only accommodate values equal or smaller than one.

The mixing among the CP-even scalar fields in the S2HDM is identical to the one of the N2HDM, such that it is not surprising that we find similar effects on the allowed parameter ranges of α_i in the S2HDM. However, a crucial difference between both models is the presence of the additional particle χ in the S2HDM. Since we are focusing here on the Higgs funnel region of the model, it is possible that $m_\chi < 125$ GeV/2, giving rise to an additional decay mode of h_{125} into an invisible final state. To illustrate the impact of this additional decay on the allowed parameter regions, we show in the right plot of Fig. 8.3 the branching ratio for the invisible decay of h_{125} in dependence of m_χ for the parameter points with $m_\chi < 125$ GeV/2. Here we show also the parameter points that would be

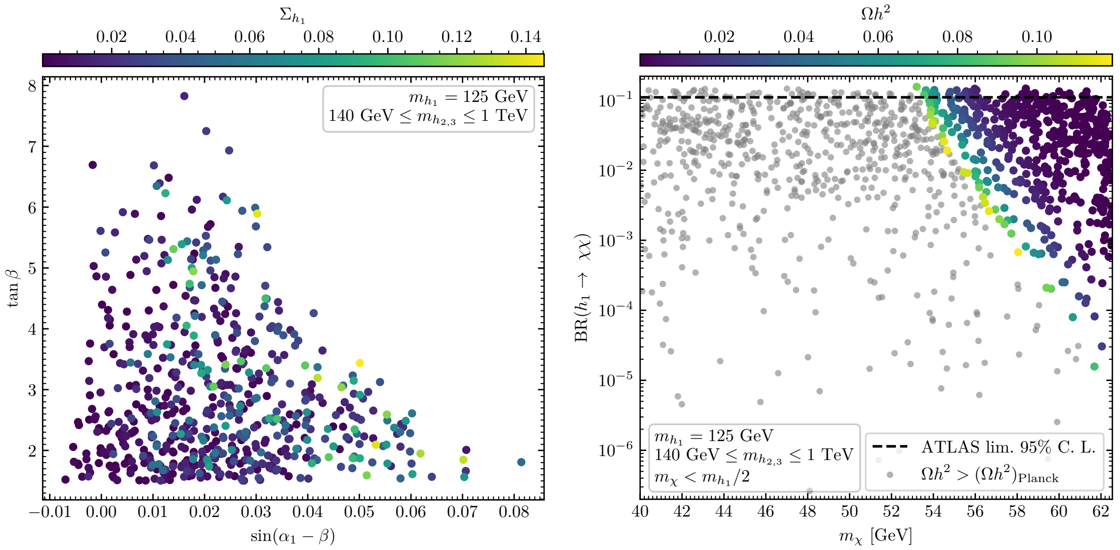

Figure 8.3: Left: $\tan\beta$ in dependence of $\sin(\alpha_1 - \beta)$ for the parameter points that pass all the constraints discussed in Sect. 8.1. Right: Invisible branching ratio $\mathrm{BR}(h_1 \to \chi\chi)$ in dependence of m_χ for the parameter points with $m_\chi < m_{h_1}/2$ that pass the constraints, not taking into account the experimental upper limit on $\mathrm{BR}(h_1 \to \chi\chi)$ as reported by ATLAS [229]. The colour coding indicates Σ_{h_1}.

excluded by the observed upper limit on $\mathrm{BR}(h_1 \to \chi\chi)$ [229] (indicated by the horizontal dashed line). In this way we can demonstrate the interplay between the global constraints from the `HiggsSignals` analysis and the direct limit on the invisible branching ratio. One can see that only a very small fraction of the otherwise allowed parameter points, which in particular have passed the constraint $\chi^2_{125} \leq \chi^2_{\mathrm{SM},125} + 5.99$, lie above the ATLAS limit on the invisible branching ratio. Nevertheless, for some points we find values of $\mathrm{BR}(h_1 \to \chi\chi)$ that are about 50% larger than the upper limit in the whole range of m_χ in which allowed points were found.

The grey points in the right plot of Fig. 8.3 have to be discarded because they feature a too large thermal relic abundance of DM. For the allowed points the DM relic abundance is indicated by the colour coding of the points. One can see that we find a limit of $m_\chi \sim 53.8$ GeV below which no allowed points were found.[11] This limit arises from a combination of the upper limit on $\mathrm{BR}(h_1 \to \chi\chi)$, on the one hand, and the constraint $\Omega h^2 \leq (\Omega h^2)_{\mathrm{Planck}}$, on the other hand. Parameter points with $m_\chi \lesssim 53.8$ GeV feature either a χ that is weakly coupled to h_{125}, in which case $\mathrm{BR}_{\mathrm{inv}}$ can be in agreement with the ATLAS limit but the DM relic abundance is too large because the annihiliation process with h_{125} in the s-channel is not efficient (see also discussion below), or χ is coupled more strongly to h_{125}, in which case the DM relic abundance can be below the upper limit but the invisible branching ratio of h_{125} is unacceptably large. Note here that in the plot almost all parameter points with $m_\chi \lesssim 53.8$ GeV belong to the first option, predicting too large

---

[11] A very similar limit was found in the pNG DM model with one Higgs doublet [64].

values of Ωh^2, while $\mathrm{BR}_{\mathrm{inv}}$ is below the experimental upper limit. On the other hand, there are only three parameter points with $m_\chi \lesssim 53.8$ GeV belonging to the second option, featuring too large values of $\mathrm{BR}_{\mathrm{inv}}$ but with Ωh^2 below the Planck limit. The reason for this lies in our procedure to generate the parameter points using the genetic algorithm. Parameter points with values of $\mathrm{BR}_{\mathrm{inv}} = \mathcal{O}(0.1)$ feature overall larger values of χ^2_{125} and constitute therefore only a very small part of the sample of parameter points, because the genetic algorithm tries to find parameter points that minimise χ^2_{125} (see the definition of the loss function defined in Eq. (8.3)).

The above discussed findings already indicate the strong interplay between the Higgs phenomenology and the DM sector of the S2HDM, in particular in the scenario discussed here that fundamentally relies on the Higgs funnel to predict a DM relic abundance in agreement with experiments. To shed more light on this interplay, we show in Fig. 8.4 the relic abundance as predicted according to the freeze-out mechanism in dependence of the DM mass m_χ. One can see the strong suppression of Ωh^2 for most parameter points at $m_\chi \sim 125/2$ GeV, where the DM annihilation cross sections with h_1 in the s-channel are resonantly enhanced. At this precise resonance region, there are nevertheless also a few parameter points featuring values of Ωh^2 within an order of magnitude below the experimentally measured value $(\Omega h^2)_{\mathrm{Planck}} = 0.119$ (indicated by the grey dashed line in Fig. 8.4). For these parameter points the resonant enhancement of the annihilation cross sections is counteracted by strongly suppressed couplings of χ to h_{125}.[12]

For values of m_χ below $m_{h_{125}}/2$, there is a small band of values 53 GeV $\lesssim m_\chi \lesssim m_{h_{125}}/2$ in which the measured value of the relic abundance can be accommodated, whereas for values below this range the predicted amount of DM density is always too large (grey points). As already mentioned before, the reason for this lies in the constraints on the properties of h_{125}. In order to predict an allowed value for Ωh^2 when $m_\chi \lesssim 53$ GeV it is required that the coupling of χ to h_{125} is large. However, this inevitably results in values of the invisible branching ratio for the decay $h_{125} \to \chi\chi$ above the experimental upper limit. As a result, the lower limit on m_χ found here can be regarded as a robust bound under the assumption that h_{125} corresponds to the lightest scalar h_1. One can compare also to the right plot of Fig. 8.4, where the colour coding indicates the values of the singlet component of the SM-like Higgs boson h_1. A clear distinction is visible between the points below and above the resonance at $m_\chi = 125/2$ GeV. Points with m_χ below the resonance have substantially smaller values of Σ_{h_1}, whereas points with m_χ above the resonance allow for values of $\Sigma_{h_1} \gtrsim 0.1$. Moreover, only points for which m_χ is relatively close to the kinematic threshold of the decay $h_1 \to \chi\chi$, i.e. $m_\chi \sim m_{h_{125}}/2$, feature sizable values of Σ_{h_1} when $m_\chi < m_{h_{125}}/2$. The reason for this is that the couplings λ_7 and λ_8 that couple the singlet field to the doublet fields (see Eq. (3.43)) appear in the partial decay width for the invisible decay as shown in Eq. (3.92). In addition, these couplings are responsible for

---

[12] These parameter points also have highly suppressed DM-SM scattering processes at finite temperatures, such that in some cases χ might be kinematically decoupled already before the freeze-out period. As a result, this effect of *early kinetic decoupling* of DM [403, 404] can give rise to an additional source of uncertainty for the prediction for Ωh^2 for these points.

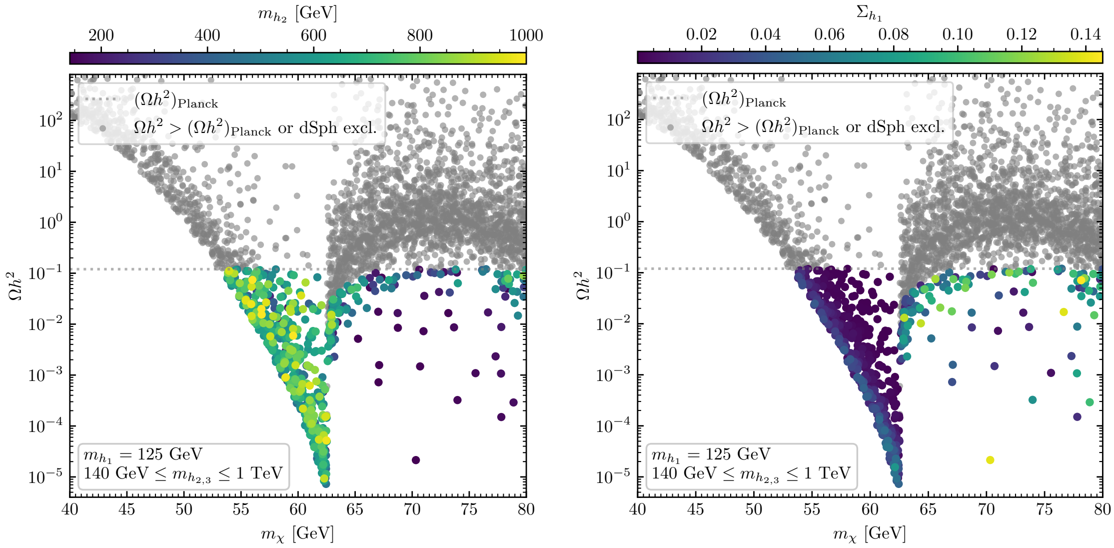

Figure 8.4: Relic abundance Ωh^2 as predicted by thermal freeze-out in dependence of m_χ. The colour coding indicates the values of m_{h_2} (left) and the values of Σ_{h_2} (right). Grey points are excluded by $\Omega h^2 > (\Omega h^2)_{\text{Planck}}$ or Fermi dSph measurements.

the possible singlet admixture of the state h_1. Accordingly, parameter points with sizable values of Σ_{h_1} have sizable values of λ_7 and λ_8, which in turn can give rise to too large values of BR$(h_1 \to \chi\chi)$ whenever this decay is kinematically allowed. In Sect. 8.2.2 we will address the question whether the bound $m_\chi \gtrsim 53$ GeV can be substantially modified in a scenario featuring a scalar h_1 with a mass smaller than 125 GeV, and the second lightest scalar h_2 plays the role of the discovered Higgs boson. In this case χ has two possibilities to annihilate resonantly, either with h_1 or with h_2 in the *s*-channel, and the predictions for the relic abundance can be substantially modified.

For values of $m_\chi > 125/2$ GeV one can see that the prediction for Ωh^2 rises quickly with increasing value of m_χ, because the resonant enhancement of the annihilation cross section is lost. As a result, most parameter points predict a too large DM relic abundance. Taking into account the values of m_{h_2} (indicated by the colour coding of the points in the left plot of Fig. 8.4), one can see that most parameter points with $m_\chi \gtrsim 65$ GeV that are in agreement with the upper limit on Ωh^2 feature a relatively light scalar h_2 with masses at the lower end of the scan range of m_{h_2}. As before, the reason for this is that when h_2 is not much heavier than twice the value of m_χ, the second *s*-channel contribution to the annihilation cross section becomes relevant. This gives rise to a suppression of Ωh^2 such that the prediction can be below the experimental limit even when m_χ is several GeV larger than 125/2 GeV. Again, this hints to the fact that also in the mass range $m_\chi > 125/2$ GeV the prediction for Ωh^2 could be substantially modified using the *inverted* mass hierarchy in which h_{125} is not the lightest scalar, and we investigate this possibility assuming a Higgs boson h_1 at 96 GeV in Sect. 8.2.2.

In both plots in Fig. 8.4 the grey points are characterised by either being excluded

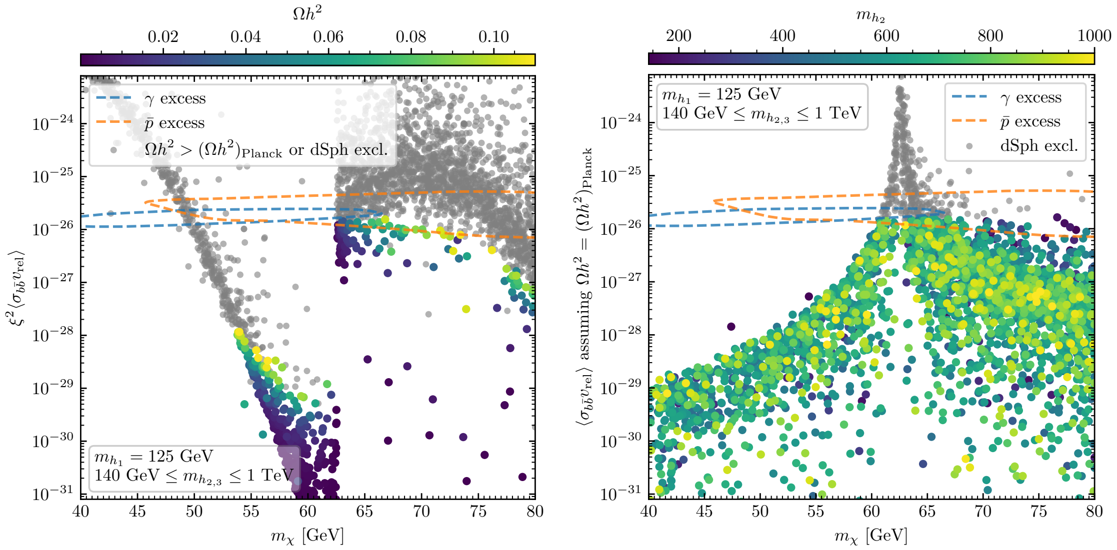

Figure 8.5: Today's velocity averaged annihilation cross section of χ into pairs of b quarks taking into account the number density as predicted by thermal freeze-out (left) and assuming $\Omega h^2 = 0.119$ (right). The colour coding indicates the predicted value of Ωh^2 (left) and the value of m_{h_2} (right). Also indicated are the regions in which the cosmic-rays excesses could be explained within the 2σ confidence level (blue and orange dashed lines) [66, 89]. Grey points are excluded by $\Omega h^2 > (\Omega h^2_{\text{Planck}})$ (left) or Fermi dSph measurements (left and right).

due to $\Omega h^2 > (\Omega h^2)_{\text{Planck}}$, as already mentioned before, or they are excluded due to the constraints from DM in DD experiments. In most parts of the analysed parameter space, the more constraining experimental limit results to be the upper limit on the predicted relic abundance, as indicated by the fact that most of the grey points lie above the horizontal dashed line indicating the Planck measurement. However, there is a small region with 62.5 GeV $\lesssim m_\chi \lesssim$ 67 GeV in which we find grey points below the Planck limit. Consequently, in this mass range of χ the in DD limits from the observation of dSph by the Fermi satellite are more constraining. Note that this is a region in which it appears to be relatively easy to accommodate a value of $\Omega h^2 \sim (\Omega h^2)_{\text{Planck}}$ without being in tension with constraints on h_{125}, since it is just above the resonance of the annihilation cross section, and the decay $h_{125} \to \chi\chi$ is kinematically forbidden. The fact that these parameter points can be probed via in DD experiments is therefore crucial. We remind the reader that the constraints derived from the Fermi measurements are subject to uncertainties, as was also discussed in Sect. 8.1.2, such that the respective limits might change slightly in the future and are currently possibly not as robust as the Planck limit on the relic abundance. Nevertheless, our results indicate that when the DM candidate of the S2HDM in this mass range is responsible for a large fraction of the measured relic abundance, the observation of dSph and the resulting constraints (or signals, more optimistically speaking) will be of great importance for studies in the context of pNG DM.

In this context it is interesting to note that recent in DD experiments found anomalies in the cosmic ray spectra. The first so-called galactic center excess was found by the Fermi satellite, which measured an intensity of gamma-rays coming from the center of the galaxy significantly above the predictions of the standard model of cosmic rays generation and propagation with a peak in the spectrum around a few GeV [74, 75]. Another anomalous cosmic-ray spectra was measured by the Alpha Magnetic Spectrometer (AMS) [85], mounted on the international space station, which reported an excess over the expected flux of cosmic ray antiprotons.[13] While it is still under debate whether the excesses arise from unresolved astrophysical sources [406–408] or the treatment of systematic uncertainties [409, 410], or whether their origin could be the annihilation of DM, we will in the following assume that the latter is the case.[14] In Ref. [89] it was shown that the excesses are compatible with a DM interpretation, where the DM candidate annihilates into pairs of b quarks. For the γ excess the allowed range of the mass of the DM candidate at the 2σ confidence level was found to be 37 GeV $\leq m_{\mathrm{DM}} \leq$ 67 GeV. For the $\bar{p}$ excess the allowed range was found to be 46 GeV $\leq m_{\mathrm{DM}} \leq$ 94 GeV, which partially agrees with the mass range preferred by the γ excess. Consequently, it is an interesting question whether the S2HDM can explain both the excesses simultaneously, while being in agreement with all theoretical and experimental constraints.[15]

In order to answer this question we show in Fig. 8.5 on the vertical axes $\langle \sigma_{b\bar{b}} v_{\mathrm{rel}} \rangle$, being the predicted velocity-averaged annihilation cross sections of χ into pairs of b quarks, in dependence of the DM mass m_χ for the parameter points of our scan. The 2σ confidence level regions of these two parameters required to explain the γ and the $\bar{p}$ excesses are indicated with the blue and orange dashed lines, respectively [66, 89]. We show the parameter points in the two plots of Fig. 8.5 under two different assumptions. In the left plot we assume that the usual thermal freeze-out scenario can be applied, such that we have to take into account the predicted values of the relic abundace for each parameter point. Hence, the values of $\langle \sigma_{b\bar{b}} v_{\mathrm{rel}} \rangle$ on the vertical axis are scaled by the factor ξ^2 as defined in Eq. (8.1). On the other hand, in the right plot we show the parameter points under the assumption that the relic abundance of DM is always accounted for by χ, independently of the prediction from the thermal freeze-out. As a result, they demand a non-standard cosmological history giving rise to the experimentally measured relic abundance, which we will however not specify any further. In the plots the grey points correspond to parameter points that are excluded by a too large predicted relic abundance (left) or by constraints from dSph observations (left and right). In the right plot the dSph constraints are consequently applied also assuming $\Omega h^2 = (\Omega h^2)_{\mathrm{Planck}}$.

Assuming the usual thermal freeze-out scenario (left plot), one can see that the resonant structure of the distribution of the annihilation cross sections gives rise to two distinct regions of m_χ in which points inside the blue and the orange curves can be found. The first region at lower DM masses of $m_\chi \approx 50$ GeV contains parameter points that predict values of $\xi^2 \langle \sigma_{b\bar{b}} v_{\mathrm{rel}} \rangle$ as required for an explanation of the excesses, and where the values of m_χ lie

---

[13] The updated result of the AMS collaboration could neither definitively rule out nor confirm the DM interpretation of the antiproton excess [405].

[14] See also Refs. [411–415] for recent discussions of possible explanations of the center-of-galaxy excesses.

[15] See Ref. [66] for an investigation of the excesses in a singlet-extension of the SM featuring pNG DM.

roughly in the center of the values preferred by the γ excesses and at the lower end of the range preferred by the $\bar{p}$ excess. However, these points are excluded because the predicted values of Ωh^2 are about an order of magnitude larger than the experimentally measured value, as can also be seen in the left plot of Fig. 8.4. Accordingly, the parameter points in this region of m_χ are excluded and the cosmic-ray excesses cannot be realised there. The second region of DM masses in which points within both the blue and the orange curves are found is given by 63 GeV $\lesssim m_\chi \lesssim$ 67 GeV. However, as before, the corresponding points are shown in grey and are consequently excluded. Interestingly, here the responsible experimental constraint do not arise from the Planck measurement of the relic abundance, but from the Fermi-LAT observations of dSph, as was already discussed before. In fact, the predictions for Ωh^2 in this range of m_χ are close or effectively identical to the Planck measurement. Hence, the points in this second region of DM masses possibly predict the correct DM relic abundance and could give rise to both the cosmic γ- and the $\bar{p}$-excesses, but they are in tension with the null-results from the observations of dSph. Here we remind the reader, as was discussed already in Sect. 8.1.2, that the Fermi-LAT dSph constraints are subject to uncertainties in regards to the astrophysical modelling of the spectral curves, and as a result might be slightly weaker as compared to applied here. Nevertheless, with future improvements of the dSph observations, for instance, due to the inclusion of more dSph and the increasing time periods of data taking, a firm exclusion (or confirmation if a DM signal will actually be found) of the parameter space region of the second DM mass range discussed here should be possible [416].

Under the assumption of a non-standard cosmological history that somehow gives rise to a relic abundance of χ in agreement with the Planck measurement (right plot), one can see that this time only one DM mass region with parameter points suitable for a realization of the excesses is present. Naturally, this region lies where the resonant enhancement of $\langle \sigma_{b\bar{b}} v_{\mathrm{rel}} \rangle$ is present, i.e. at 61 GeV $\lesssim m_\chi \lesssim$ 67 GeV, which consequently partially coincides with the second region of DM mass found in the left plot of Fig. 8.5. As before the points that lie within both the blue and the orange curves are in tension with the dSph observations from the Fermi satellite.

We end the discussion of the DM properties in this scan by noting that many of the above mentioned findings crucially depend on the assumed mass ordering of the CP-even Higgs bosons. In particular, the presence of a Higgs boson below 125 GeV can potentially impact the predictions for the relic abundance, as discussed in relation to Fig. 8.4. Moreover, the question whether the cosmic-ray excesses can be accommodated more easily when a second s-channel resonance for the annihilation cross section is available can be addressed. In Sect. 8.2.2 we will investigate these questions following the approach of Ref. [66], in which the presence of a Higgs boson at around 96 GeV was assumed in order to simultaneously explain also two collider excesses found at LEP in the $b\bar{b}$ final state and at the LHC in the diphoton final state.

8.2.2 pNG DM and a Higgs boson at 96 GeV

In Ref. [66] it was used that the hypothetical particle state h_{96} at 96 GeV can be coupled to new relatively light charged states that can give rise to additional contributions to the loop induced coupling of h_{96} to photons in order to account for the diphoton excess found by CMS. In Ref. [367] it was shown that in the N2HDM the presence of the additional doublet Higgs field and the real singlet field are sufficient to accurately describe the collider excesses. Here, the diphoton rate was enhanced not via an enhancement of the coupling coefficient $|C_{h_{96}\gamma\gamma}|$, where the coupling coefficients $C_{h_{96}\dots}$ are defined as the coupplings normalised to the one of a SM Higgs boson of the same mass. Instead, the branching ratio for the diphoton decay of h_{96} was enhanced via a suppression of the couplings of h_{96} to b quarks, which then also gives rise to a suppression of the total width of h_{96}.[16] The required suppression of the coupling coefficient $|C_{h_{96}b\bar{b}}|$ (without suppressing $|C_{h_{96}t\bar{t}}|$ in order to maintain sizable couplings to photons via the t-quark loop) can also be realised in the S2HDM due to the possible mixing patterns in the CP-even sector and the presence of the three mixing angles $\alpha_{1,2,3}$ in total analogy to the N2HDM. In this regard, the only difference in the S2HDM compared to the N2HDM is the possible presence of the additional decay modes $h_{96}/h_{125} \to \chi\chi$, potentially giving rise to a small suppression of the decay modes $h_{96} \to \gamma\gamma$ relevant for the CMS excess and $h_{96} \to b\bar{b}$ relevant for the LEP excess, or to stronger constrains on the properties of h_{125}. In the following we will discuss a scan to illustrate the impact of the presence of h_{96} on the phenomenology of the DM candidate χ, and whether the collider excesses can be realised in combination with the cosmic-ray excesses.

Before going into the description of the parameter scan that we performed, we briefly introduce the relevant details of the collider excesses. At LEP searches for Higgs bosons were performed utilizing the $b\bar{b}$ final state [92], which can be exploited at a lepton collider in contrast to the LHC due to the much smaller SM background. Theoretically, the Higgs boson that is searched for is assumed to be produced via the Higgsstrahlung pocess and subsequently decays into a pair of b quarks. A local excess of about 2σ confidence level was observed at a mass of roughly 96 GeV, where the mass resolution is rather poor due to the hadronic final state. In Ref. [417] it was shown that the excess is consistent with a signal interpretation corresponding to a signal strength of

$$\mu_{\mathrm{LEP}}^{\mathrm{exp}} = 0.117 \pm 0.057 \ . \tag{8.4}$$

Low-mass Higgs-boson searches have also been performed at the LHC in various final states. CMS searched for light Higgs bosons in the diphoton final state utilizing the 8 TeV and parts of the 13 TeV datasets [93]. A local excess of roughly 3σ confidence level was observed at a mass of 96 GeV, hence in agreement with the mass range compatible with the LEP excess. In this case the excess is consistent with a signal interpretation corresponding to a

---

[16] The presence of a second doublet field gives rise to the presence of the states $H^{\pm}$, such that also in the S2HDM (compared to the SM) new charged states are present. However, the loop contributions of $H^{\pm}$ to $|C_{h_{96}\gamma\gamma}|$ are not relevant for the explanation of the CMS excess, such that one can have $m_{H^{\pm}} \gg 96$ GeV.

signal strength of

$$\mu_{\mathrm{CMS}}^{\mathrm{exp}} = 0.6 \pm 0.2 \; . \tag{8.5}$$

In our scan, in which h_1 will play the role of the state h_{96}, we compare the theoretical predictions for the signal strengths to the experimental values given above. The predictions were calculated by

$$\mu_{\mathrm{LEP}} \approx \frac{C^2_{h_{96}VV} \cdot \mathrm{BR}\left(h_{96} \to b\bar{b}\right)}{\mathrm{BR}^{\mathrm{SM}}\left(H \to b\bar{b}\right)} \; , \quad \mu_{\mathrm{CMS}} \approx \frac{C^2_{h_{96}t\bar{t}} \cdot \mathrm{BR}\left(h_{96} \to \gamma\gamma\right)}{\mathrm{BR}^{\mathrm{SM}}\left(H \to \gamma\gamma\right)} \; . \tag{8.6}$$

Hence, in both cases the cross section ratios that enter the definitions of the signal strengths are expressed to a very good approximation in terms of the effective coupling coefficients $C_{h_{96}VV} = c_{\alpha_2} c_{\beta-\alpha_1}$ and $C_{h_{96}t\bar{t}} = s_{\alpha_1} c_{\alpha_2} / s_\beta$, which, as mentioned already, are defined as the couplings of h_{96} normalised to the respective couplings of a SM Higgs boson with the same mass. The values for the SM branching ratios in the denominator, again assuming a SM Higgs boson at 96 GeV, can be found in the literature [418]. From the theoretical predicted values $\mu_{\mathrm{LEP,CMS}}$ and the experimentally determined values $\mu^{\mathrm{exp}}_{\mathrm{LEP,CMS}}$ and their uncertainties we construct a χ^2 function

$$\chi^2_{96} = \frac{\left(\mu_{\mathrm{LEP}} - 0.117\right)^2}{0.057^2} + \frac{\left(\mu_{\mathrm{CMS}} - 0.6\right)^2}{0.2^2} \; , \tag{8.7}$$

in order to quantify the goodness of the fits to the excesses. In this definition we assumed that there is no correlation between both measurements.

Technically, the details of the scan that we discuss here are very similar to the ones of the scan discussed in Sect. 8.2.1. The scan ranges were set as given in Eq. (8.2), except for the masses of the scalars, which were chosen to be

$$m_{h_1} = 96 \text{ GeV} \; , \quad m_{h_2} = 125.09 \text{ GeV} \; , \quad m_{h_3} = m_H \leq 1 \text{ TeV} \; , \tag{8.8}$$

such that $m_{h_3} = m_H$ is further constrained by the condition $\Delta M_{\mathrm{max}} < 200$ GeV, as defined in Eq. (8.2) and substantially heavier than h_1 and h_2 due to the lower limit on $m_{H^\pm}$. We again followed the two-step procedure. In the first step, we used the genetic algorithm to obtain parameter points in agreement with the theoretical constraints and the experimental constraints from the Higgs phenomenology. To the loss function defined in Eq. (8.3) we added a term $10\chi^2_{96}$ in order to obtain parameter points that potentially feature both a good fit to the signal rates of the SM-like Higgs boson $h_2 = h_{125}$ and to the signal rates μ_{LEP} and μ_{CMS}. All parameter points obtained by the help of the genetic algorithm were subject to the constraint

$$\chi^2_{125} + \chi^2_{96} \leq \chi^2_{\mathrm{SM},125} + \chi^2_{\mathrm{SM},96} \; , \quad \chi^2_{\mathrm{SM},125} = 84.41 \; , \quad \chi^2_{\mathrm{SM},96} = 13.99 \; , \tag{8.9}$$

where the value of $\chi^2_{\mathrm{SM},96}$ is obtained from Eq. (8.7) assuming zero values for both μ_{LEP} and μ_{CMS} as predicted by the SM, in which no particle is present at a mass of 96 GeV. As a result, in comparison to the analysis discussed in Sect. 8.2.1 in which the requirement $\chi^2_{125} \leq \chi^2_{\mathrm{SM},125}$ was used, the requirement shown in Eq. (8.9) allows for larger values of

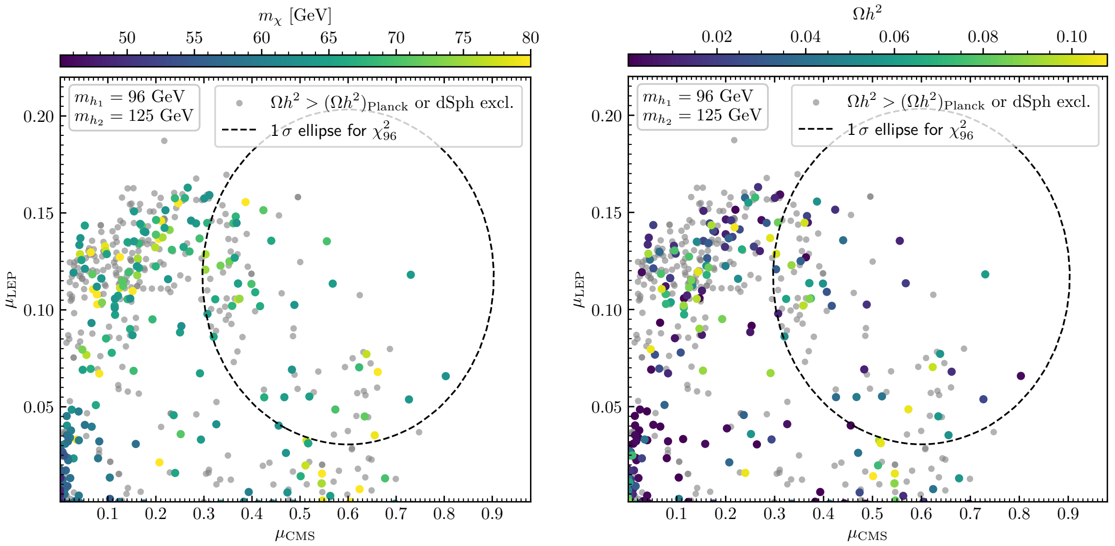

Figure 8.6: μ_{LEP} in dependence of μ_{CMS}, with the colour coding indicating the values of m_χ (left) and Ωh^2 (right). Grey points are excluded by $\Omega h^2 > (\Omega h^2)_{\text{Planck}}$ or Fermi dSph measurements. The dashed ellipse indicates the experimentally preferred region of the collider excesses at the 1σ confidence level.

χ^2_{125} as long as the S2HDM parameter point provides a good fit to the collider excesses, i.e. it features values of $\chi^2_{96} \ll \chi^2_{\text{SM},96}$. Here it should be noted that even in the most extreme case with $\chi^2_{96} = 0$ the allowed maximum value of χ^2_{125} still does not indicate severe modifications of the signal rates of h_{125}, taking into account that the `HiggsSignals` fit result applies a total amount of 107 observables, such that the reduced χ^2 value remains substantially smaller than one even in this case. The second step is totally analogue to the scan discussed in Sect. 8.2.1. All parameter points that pass the constraint shown in Eq. (8.9) were confronted with the theoretical constraints including now the RGE evolution of the parameters. As before, we required the scalar potential to be well behaved up to energy scale of at least $\mu_v = 1$ TeV, such that in particular the values of the quartic couplings λ_i allow for a perturbative treatment at the range of energy at which there are also particle masses in our scan. Finally, the remaining experimental constraints regarding the DM phenomenology were applied.

We show the resulting parameter points in Fig. 8.6, where we display the signal rate μ_{LEP} in dependence of μ_{CMS}. We indicate with the colour coding of the points the value of the DM mass m_χ (left) and the DM relic abundance Ωh^2 as predicted by the usual thermal freeze-out scenario (right). Also shown as grey points are parameter points that are excluded by a too large prediction of the relic abundance or by limits coming from observations of dSph. The ellipse in both plots indicates the region in agreement with the collider excesses at the 1σ confidence level, i.e. $\chi^2_{96} = 2.3$. One can see that we find parameter points within the ellipses. Consequently, both excesses can be explained simultaneously while taking into account the constraints described in Sect. 8.1. In the left

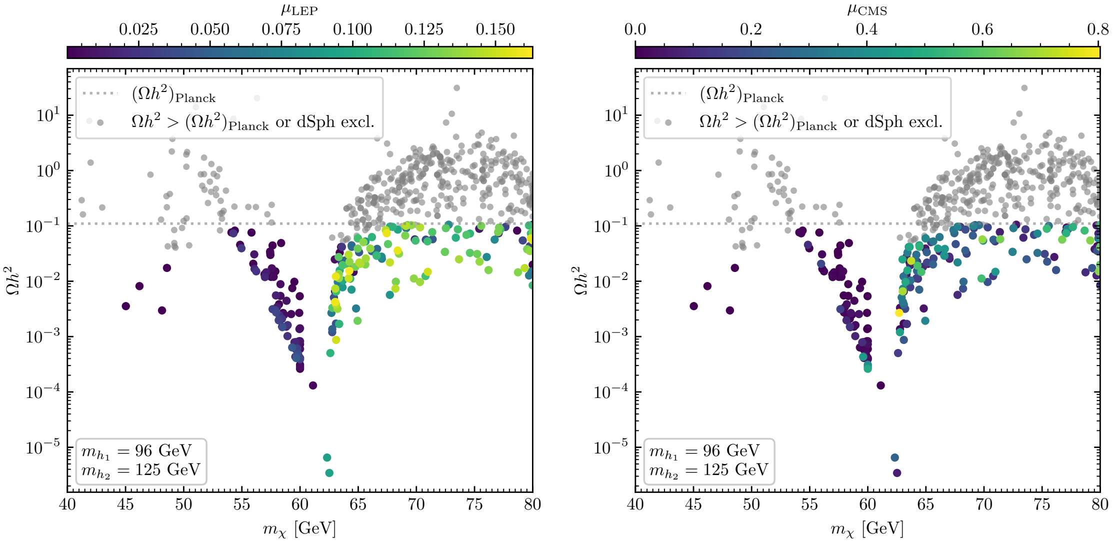

Figure 8.7: Ωh^2 in dependence of m_χ, with the colour coding indicating the values of μ_{LEP} (left) and μ_{CMS} (right). Grey points are excluded by $\Omega h^2 > (\Omega h^2)_{\text{Planck}}$ or Fermi dSph measurements.

plot, we observe that parameter points with sizable values of μ_{LEP} and μ_{CMS} feature DM mass values close to or larger than $m_{h_{125}}/2$. On the other hand, parameter points with $m_\chi < m_{h_{125}}/2$ only predict substantially smaller signal strengths, and the collider excesses cannot be accounted for. The reason for this is, as was also discussed in Sect. 8.2.1, that in this case the decay $h_{125} \to \chi\chi$ is kinematically open. As a result, the possible mixing of the singlet field $h_1 = h_{96}$ with the SM-like Higgs boson $h_2 = h_{125}$ is much more constrained. However, a sizable mixing of h_{96} and h_{125} is necessary to obtain values of μ_{LEP} and μ_{CMS} of the order of the experimentally measured values. We therefore can conclude that a realization of the collider excesses demands DM masses of $m_\chi > m_{h_{125}}/2$. In the right plot of Fig. 8.6 we find that several of the parameter points that are able to explain both excesses also predict sizable values for the relic abundance, with some parameter points saturating the value measured by the Planck collaboration. Accordingly, we come to the conclusion that the S2HDM can accommodate the collider excesses at 96 GeV while at the same time accommodating a large fraction or all of the measured DM relic abundance.

In Fig. 8.7 the predicted relic abundance is shown in dependence of the DM mass. The values of the signal rates measured by LEP (left) and CMS (right) are also indicated by the colour coding of the points. We note a new prominent feature in the distribution of the parameter points with respect to Fig. 8.4. Due to the opening of a new resonant s-channel mediated by the h_{96}, parameter points featuring DM masses smaller than about 53 GeV can now be in agreement with the upper limit imposed by the observed DM relic abundance. Moreover, the presence of h_{96} also gives rise to the fact that a large fraction of parameter points with $m_\chi > m_{h_{125}}/2$ lie below the Planck limit, whereas we found in Sect. 8.2.1 (compare to Fig. 8.4) that in this DM mass region most points predict $\Omega h^2 > (\Omega h^2)_{\text{Planck}}$. Grey points that lay below the experimental upper limit are excluded by dSph observations.

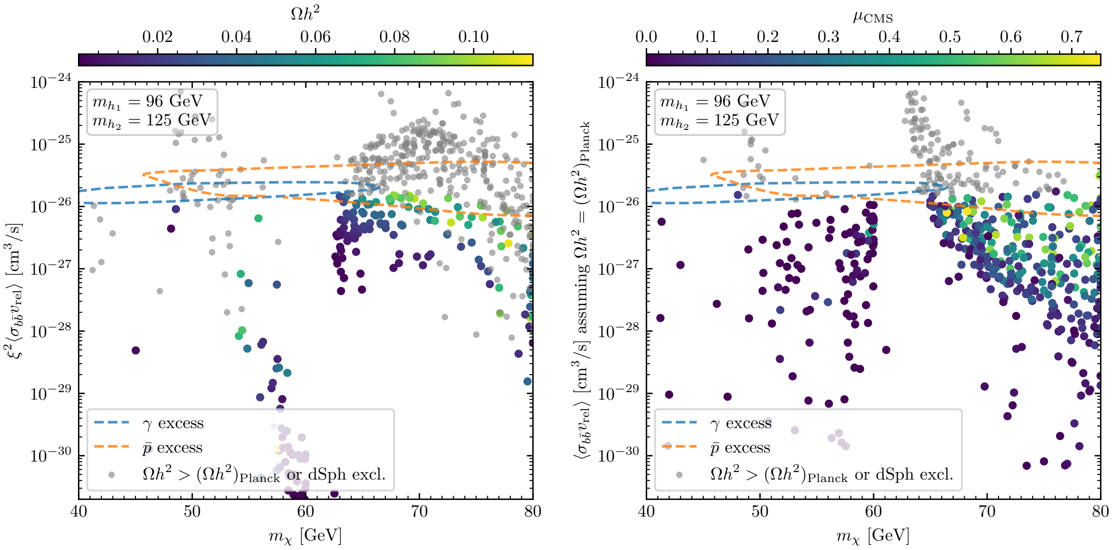

Figure 8.8: Today's velocity averaged annihilation cross section of χ into pairs of b quarks taking into account the number density as predicted by thermal freeze-out (left) and assuming $\Omega h^2 = 0.119$ (right). The colour coding indicates the predicted value of Ωh^2 (left) and the value of m_{h_2} (right). Also indicated are the regions in which the cosmic-rays excesses could be explained (blue and orange dashed lines) [80, 89]. Grey points are excluded by $\Omega h^2 > (\Omega h^2_{\rm Planck})$ (left) or Fermi dSph measurements (left and right).

Here it is interesting to note that we find, in addition to the region around $m_\chi \sim 63$ GeV already present in Fig. 8.4, a second region at 48 GeV $\lesssim m_\chi \lesssim$ 58 GeV in which the dSph constraints discard points that would be in agreement with the Planck measurement of the DM relic abundance. In the left plot of Fig. 8.7 we find that for the points at the right side of the resonance the predicted values of $\mu_{\rm LEP}$ can be close to the measured central value $\mu_{\rm LEP}^{\rm exp} = 0.117$ independently of the precise value of m_χ. On the contrary, as can be seen in the right plot of Fig. 8.7, values of $\mu_{\rm CMS} \sim \mu_{\rm CMS}^{\rm exp} = 0.6$ that are in agreement with the constraints are mostly found in the interval 62 GeV $\lesssim m_\chi \lesssim$ 65 GeV. For larger values of m_χ one can still find parameter points that fit the CMS excess at the level of 1σ. However, they often predict too large values of $\Omega h^2 > (\Omega h^2)_{\rm Planck}$ and are therefore shown mostly as grey points. The reason for this is that, as discussed before, fitting the diphoton excess requires a suppression of the couplings of h_{96} to b quarks. However, this then yields also a suppression of the annihilation cross section via the process $\chi\chi \to h_{96} \to b\bar{b}$.

In order to discuss the gamma-ray and the antiproton excesses, we show in Fig. 8.8 today's velocity-averaged annihilation cross section of χ into pairs of b quarks taking into account the number density as predicted by thermal freeze-out (left) and assuming $\Omega h^2 = 0.12$ (right), as explained in Sect. 8.2.1. In comparison to Fig. 8.5, here we observe that there are more regions of m_χ in which points are found inside the preferred region to explain both cosmic-ray excesses simultaneously. These points remain in tension with present limits imposed by the observation of dSph. We remind the reader about the uncertainties in determining those limits (see Sect. 8.1.2 for more details). Regarding the agreement with the signal rate μ_{CMS}, only the parameter points situated towards the right end of the blue curve could simultaneously explain the two cosmic ray and the CMS excesses. These points are again in tension with in DD limits from dSph observations. Regardless of whether the collider excesses are accommodated or not, we see that the presence of h_{96} gives rise to more points at the lower end of m_χ that lie within the blue and the orange curves. Thus, the new light scalar state gives rise to new interesting regions of parameter space with $m_\chi < 60$ GeV in the context of the cosmic-ray anomalies. However, as was already mentioned, the collider excesses, which were the main motivation to investigate a scenario with $m_{h_1} = 96$ GeV in the first place, cannot be realised here.

Chapter 9

Direct detection of pNG DM in the S2HDM

In the S2HDM, the cross section for the scattering of the DM on nuclei vanishes at tree-level in the limit of zero momentum-transfer due to a U(1) symmetry. However, this symmetry is softly broken in order to give a mass to the DM particle. As a consequence, non-vanishing scattering cross sections arise at the loop level. In Chapter 8, we carried out a detailed investigation of all the relevant constraints that specify the physically allowed parameter space of the S2HDM for DM masses in the range $40 \leq m_\chi \leq 80$. However, DD constraints were not included in this analysis. This was justified due to the fact that, for BSM scalar masses substantially heavier than the DM masses considered, we could safely assume that the relevant loop corrections to the DM-nuclei scattering cross sections were captured by the pNG DM model with only one Higgs doublet, and found to be negligible.

In this chapter, we carry out a follow-up study of the aforementioned analysis, and we calculate the leading radiative corrections to the DM-nucleon scattering for a wide sample of parameter points in the S2HDM. We compare our results with the current limits set by XENON1T [95] PandaX-4T [94] and LUX-ZEPLIN (LZ) [97], and, in addition, with future limits projected for DARWIN [419][1]. We find that the current cross-section limits from DM DD experiments can hardly constrain the parameter space of the S2HDM. However, the loop-corrected predictions for the scattering cross sections can be well within the reach of future DD experiments. As a consequence, future phenomenological analyses of the S2HDM should take into account cross-section predictions beyond tree-level and the experimental constraints from DM DD experiments.

The outline of the chapter is as follows. Since the model was introduced in Sect. 3.1.3, and the implementation of the various constraints matches[2] the methods described in Sect. 8.1, we start in Sec. 9.1 by calculating the electroweak corrections to the spin-independent direct detection cross section. In Sec. 9.2, the results are presented and discussed.

This chapter is based on ref. [3].

---

[1] Note that there are other planned direct detection experiments such as SuperCDMS [420], just to name an example. We have taken DARWIN as a prototype for future DD experiment.

[2] The only difference is that, in this analysis we do not take into account constraints from the indirect detection of DM, because these constraints are only relevant in a narrow mass window of the DM below $m_\chi \lesssim 100$ GeV [73], and the application of the indirect detection constraints relies on a Monte-Carlo simulation which is computationally quite expensive (see Chapter 8 for details).

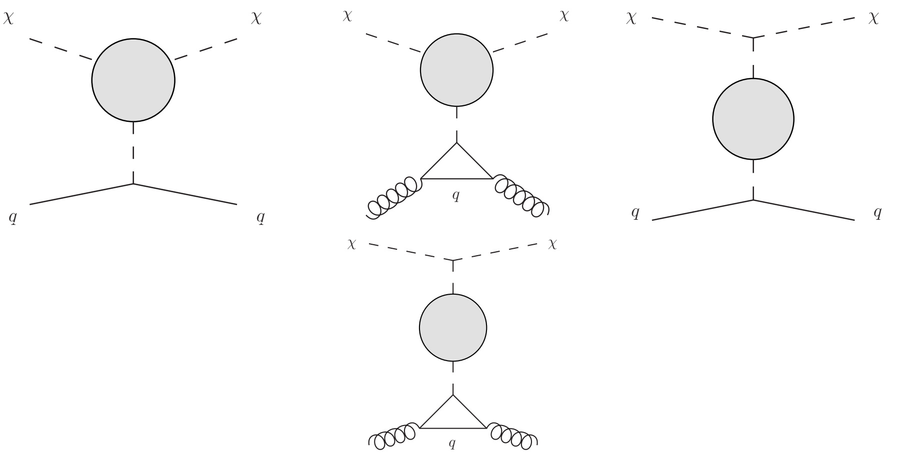

Figure 9.1: Schematic diagrams with upper vertex corrections and propagator corrections.

9.1 Calculation of DM-nucleon scattering cross section

In this section we discuss the calculation of the radiative corrections, where we include the dominant contributions at the one-loop level stemming from diagrams with the scalar states in the loops. Our procedure is an extension of the calculation performed in Ref. [62]. In Sect. 9.2 we will then present the numerical discussion of the loop-corrected scattering cross sections in order to answer the question whether the presence of the pNG DM state χ is testable at direct-detection experiments.

9.1.1 One-loop contributions to Wilson coefficients

The tree level diagram is just a t-channel $\chi q \to \chi q$ scattering where q is a quark belonging to the nucleon. The one-loop contributions to this process can be divided in three main contributions: upper vertex, lower vertex and mediator corrections. There are also box corrections that do not fit in this classification. Finally, although of higher order, the gluon initiated processes play a major role in the calculation. The one-loop contributions considered are the ones given by the topologies schematically shown in Fig. 9.1. These include only upper vertex and mediator corrections. Let us now discuss in detail why the remaining contributions were discarded.

The tree-level $\chi q \to \chi q$ amplitude vanishes in the limit of zero momentum transfer (the explicit expression is given in Sect. 7.1). Hence, the one-loop amplitude has to be finite in the same limit, that is, there is no need for a renormalization prescription nor for any counterterm. This was already proven in Ref. [62] for the singlet extension and again checked for our model. We explicitly verified the cancellation of the counterterm diagrams which can be carried out without specifying the individual counterterms, and thus in a generic fashion that is valid for all four Yukawa types of the S2HDM (counterterms insertions are shown in Fig. 9.2). As a consequence, the sum of all amplitudes is UV-finite (without the addition of counterterm diagrams), and the sum is also independent of the

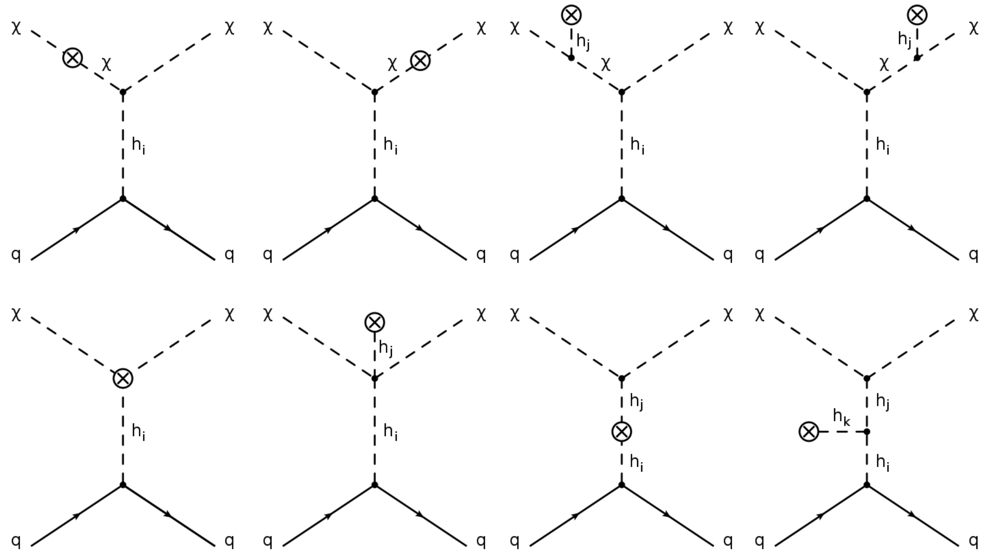

Figure 9.2: Counter-term insertion diagrams for the DM-nucleon scattering ($i, j \in \{1, 2, 3\}$).

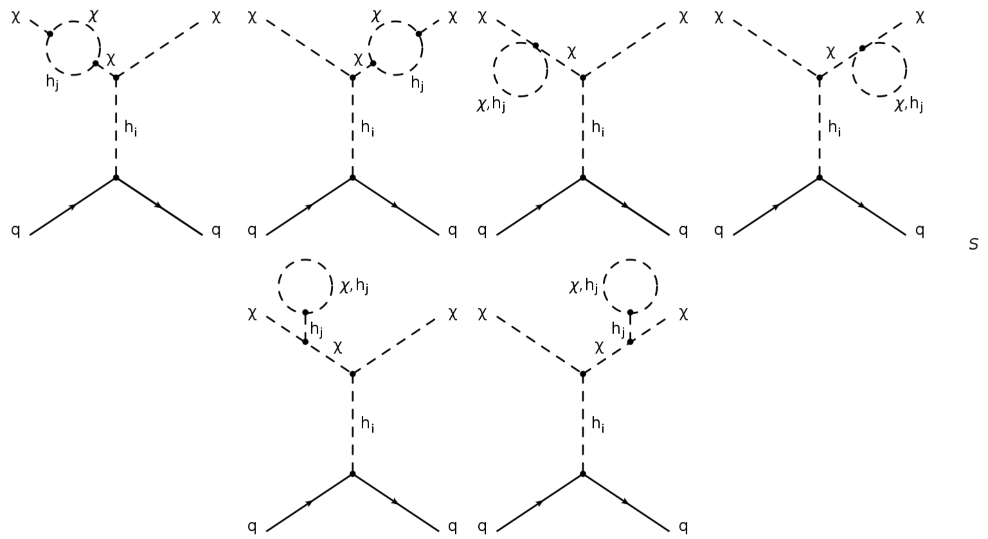

Figure 9.3: External leg corrections to the DM-nucleon scattering with $i, j, k \in \{1, 2, 3\}$

renormalization scale, which we verified numerically. Our analysis of the UV-finitenes of the one-loop amplitude is specific to the S2HDM, although we expect the same result to hold in a broad class of models which feature a vanishing tree-level amplitude in the limit of zero momentum transfer, because then there is no counterterm that could cancel a UV-divergent contribution at one-loop level.

In Fig. 9.3 we show the corrections on the external χ-legs. These corrections vanish in the limit of zero-momentum transfer, since the corresponding amplitudes are proportional to the tree-level amplitude which themselves vanish by means of the U(1) symmetry, such that the corresponding diagrams do not have to be considered. Finally we present in Fig. 9.4

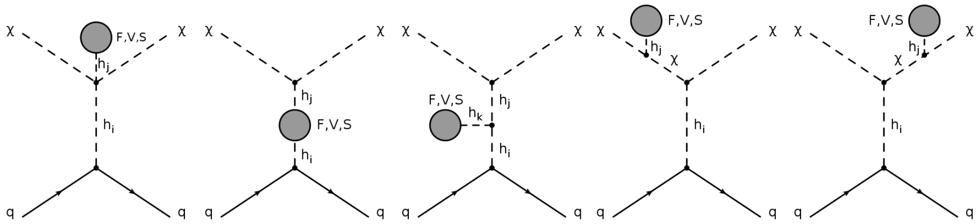

Figure 9.4: One-loop diagrams with loops containing SM particles, A or $H^{\pm}$ with $F \in \{u, c, s, c, b, t\}$, $V \in \{Z, W\}$ and $S \in \{G_0, G_{\pm}, A, H^{\pm}\}$

the set of diagrams with all SM particles, the charged scalars and the pseudoscalar in self-energies and tadpole loops. We explicitly verified that only diagrams with the neutral CP-even Higgs bosons and the DM state χ in the loops give rise to non-zero contributions, whereas the diagrams with the fermions, the gauge bosons, the pseudoscalar, the charged Higgs bosons and their corresponding Goldstone bosons in the loop cancel due to the proportionality to the tree-level amplitude. We note that again this was also shown to be true for the complex scalar extension [62], but in the S2HDM there are new particles in the scalar sector and the proportionality to the tree-level amplitude is not obvious. As a consequence of this result, the one-loop corrections to the scattering cross section considered in our analysis are independent of the gauge fixing, which we also explicitly verified by calculating the amplitudes in the R_ξ-gauge and varying the gauge-fixing parameter.

A set of diagrams that we did not take into account are the box contributions for the process $\chi q \to \chi q$. This is not because the amplitudes are proportional to the tree-level amplitude but rather because their contribution is at least one order of magnitude smaller than the vertex and mediator contributions. This was checked for two different models [69, 371, 421] and is mainly related to the fact that the amplitude is proportional to product of two Yukawa couplings to light quarks.

With all the above considerations the set of diagrams that actually contribute to the one-loop cross-section is the one with the topologies depicted in Fig. 9.5, containing the upper $h_i\chi\chi$-vertex and the h_i-propagators corrections. As discussed before, the only particles that have to be considered in the loops are the neutral CP-even Higgs bosons $h_{1,2,3}$ and the DM particle χ, since the diagrams with the other particles cancel each other out as a result of the U(1) symmetry.

Moreover, the above considerations lead us to consider only the effective scalar operator for the computation of the scattering cross sections of the DM on nucleons,

$$\mathcal{L}_{\text{eff}} = m_q C_q^s \chi\chi\bar{q}q \ , \tag{9.1}$$

where m_q is mass of the quark, and C_q^s is the Wilson coefficient that is determined order by order in perturbation theory from the matching to the full model. Since one has to consider the scattering on both up-type quarks and down-type quarks, there are important differences between the different Yukawa types of the S2HDM. In the type I and the type LS (Lepton Specific), only the doublet field ϕ_2 is coupled to the quarks, independently of the

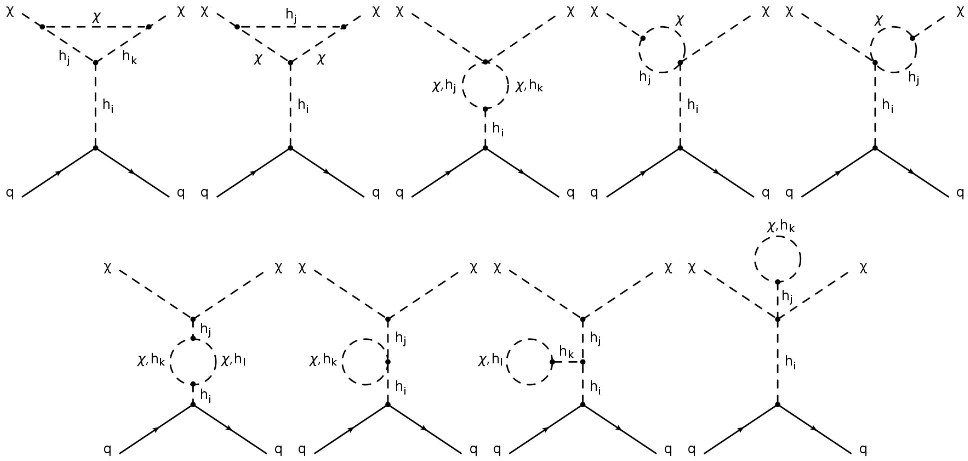

Figure 9.5: One-loop topologies that contribute to the DM-nucleon scattering cross section in our approximation with $q \in \{u,d,c,s,b,t\}$ and $i,j,k,l \in \{1,2,3\}$.

quark flavour. As a result of the fact that the dependence on the mass of the different quarks is factored out of the Wilson coefficients C_q^s as shown in 9.1, in these types C_q^s is identical for all six quark flavours, i.e.

$$C_q^{\text{I,LS}} = C_{u,d,c,s,b,t}^s \ . \tag{9.2}$$

In contrast, in the Yukawa types II and F (Flipped) the doublet field ϕ_2 is coupled to up-type quarks, and the field ϕ_1 is coupled to down-type quarks. This gives rise to the fact that the amplitudes are different depending on whether the DM particle χ scatters on up-type quarks or down-type quarks.[3] Consequently, one finds two different Wilson coefficients which we denote

$$C_u^{\text{II,F}} = C_{u,c,t}^s (= C_q^{\text{I,LS}}) \quad \text{and} \quad C_d^{\text{II,F}} = C_{d,s,b}^s \ , \tag{9.3}$$

in the following.

The calculations of the one-loop corrections as described above were performed using `FeynRules 2.3.48` [390, 392, 395], `FeynArts 3.10` [422, 423] and `FeynCalc 10.0.0` [424, 425]. An independent calculation was performed using `SARAH 4.14.3` [347, 426–429], `FeynArts 3.11` and `FormCalc 9.9` [430] All loop integrals were computed using LoopTools [431, 432]. We found agreement between both results. As a consequence of the fact that the total number of diagrams is large, we refrain from giving analytic expressions for the Wilson coefficients $C_q^{\text{I,LS}}$ and $C_q^{\text{II,F}}$ here, but instead discuss their numerical impact in terms of the DM-nucleon scattering cross sections, as discussed in the following. However, we make the obtained expressions for the Wilson coefficients available to the public as `Fortran` and `python` routines.[4]

---

[3] Also the tree-level amplitudes given in Eq. (7.1) are different in type II and type F depending on whether χ scatters on up-type or down-type quarks. However, at tree-level both amplitudes vanish in the limit of zero momentum transfer.

[4] The routines are available at `https://gitlab.com/thomas.biekoetter/dds2hdm`. The computation of

9.1.2 From amplitudes to cross sections

Following the discussion in Sect. 7.2, the DM-nucleon scattering cross section is given by Eq. (7.18). Hence, with the Wilson coefficients discussed above we can directly determine the DM-nucleon scattering cross section including the one-loop EW corrections.

As previously discussed, in our computation of C_q^s we only include the numerically dominant corrections to the upper vertex $h_i\chi\chi$ and the h_i-propagator corrections, according to the strategy also applied in Ref. [62] for the pNG DM model with a single Higgs doublet. In this approximation, in type II and type F the amplitudes C_q^s are different for the up-type quarks $q = u, c, t$ and the down-type quarks $q = d, s, b$, whereas in type I and type LS they are independent of the quark flavour. In the latter case, one can simplify 7.18 and write it as

$$\sigma_N = \frac{1}{\pi} \frac{m_N^4}{(m_N + m_\chi)^2} \left| C_q^s \right|^2 f_N^2 \ , \ \text{with } f_N = \sum_{q=u,d,s} f_{Tq}^N + 3\frac{2}{27} f_{Tg}^N = 0.27 \ , \tag{9.4}$$

where f_N is the nucleon form factor that was used in Ref. [62].

9.2 Numerical impact in light of current and future experiments

In this section we will present the numerical analysis of the DM direct-detection cross sections at the approximate one-loop level. We will start our discussion in Sect. 9.2.1 by analysing whether our expressions for the one-loop contributions fulfil some theoretical requirements that can be derived from symmetry arguments in order to cross check our results. In the second step, we present the results of two parameter scan projections in the type I and the type II of the S2HDM with the goal of determining whether the DM scattering cross sections are sufficiently enhanced at the loop level such that the presence of the DM state χ could be probed at DM direct-detection experiments.

9.2.1 General considerations

Due to the large number of diagrams that give rise to finite contributions to the DM-nuclei scattering cross sections in the limit of zero-momentum transfer, as discussed in Sect. 9.1, the complete expressions for the loop corrections are rather lengthy and complicated, such that they can only be evaluated numerically. Nevertheless, the expressions have to fulfil some basic requirements that can be derived by means of symmetry arguments (see Ref. [62] for a discussion in the pNG DM model with one Higgs doublet). We will discuss here if these requirements are met by our result. This will also provide us with a first insight about the order of magnitudes of the cross sections that can be achieved in the S2HDM beyond tree-level. A more complete assessment of the phenomenological impact can be found in Sect. 9.2.2, where we will discuss two parameter scan projections in which we take into

---

the DM-nucleon scattering cross sections will is also be implemented in the new version of the public code `s2hdmTools` [2].

Figure 9.6: DM-proton scattering cross section $\sigma_{\chi p}$ in dependence of the DM mass m_χ for different values of the singlet vev v_S in type 2. The other parameters are fixed to the values shown on the right. Also shown are the current upper limits on the 95% confidence level from XENON1T [95] (blue dashed), PandasX-4T [94] (red dashed) and LZ [97] (green dashed), and the projected upper limit from Darwin [419] (dotted). The gray area indicates the neutrino floor [433].

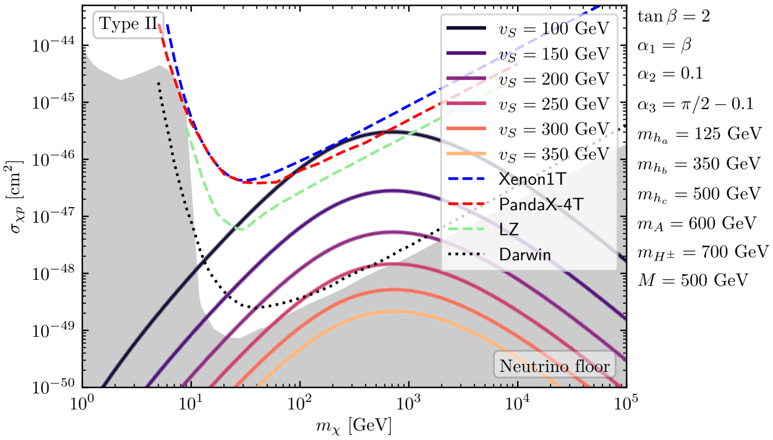

account the whole list of theoretical and experimental constraints mentioned in Sect. 8.1.1 and Sect. 8.1.2, respectively.

The presence of non-vanishing corrections to the scattering cross sections at the loop level is related to the fact that the U(1) symmetry, under which the singlet field ϕ_S is charged, is softly broken in order to give rise to a mass for the DM state χ. If the U(1) symmetry would be exact, the cancellation mechanism for the t-channel Higgs-boson exchange between χ and the quarks would hold at all orders in perturbation theory. A condition that the one-loop corrections have to fulfil is therefore that in the limit of $m_\chi \to 0$, i.e. in the limit in which the U(1) symmetry is restored, the corrections have to vanish as well. On the other hand, if the DM mass becomes much larger than the masses of the Higgs bosons, i.e. $m_\chi \gg m_{h_i}$, the cross sections become smaller as a result of the factor $1/m_\chi^2$ in 7.18.

In Fig. 9.6 we show the predictions for the cross sections of the scattering of χ on protons $\sigma_{\chi p}$ as a function of m_χ in the type II S2HDM. We show $\sigma_{\chi p}$ for different values of the singlet vev v_S, where the value of the latter is indicated by the colour coding of the lines. The values of the remaining free parameters are given next to the plot on the right-hand side. The parameter values were chosen such that the theoretical constraints discussed in Sect. 8.1.1, in particular the perturbative-unitarity constraints, are respected. However, we did not apply the experimental constraints on the Higgs sector and the DM sector. Also shown with the dashed lines are the exclusion limits at the 95% confidence level from the XENON1T experiment [95] (blue), the PandaX-4T experiment [94] (red) and the LZ experiment [97], respectively, and the dotted line indicates the future projected exclusion limits from the Darwin experiment [419]. The gray shaded area indicates the neutrino floor [433]. As expected based on the discussion above, the cross sections vanish in the limit $m_\chi \to 0$ independently of the value of v_S. $\sigma_{\chi p}$ reaches the maximum value for DM masses that are close to the masses of the CP-even Higgs bosons h_i. For DM masses that are much larger the cross sections drop again until they fall below the neutrino floor at $m_\chi \gtrsim 10$ TeV for the smallest values of v_S considered, whereas for the largest values of

Figure 9.7: DM-proton scattering cross section $\sigma_{\chi P}$ in dependence of the mass of one of the CP-even Higgs bosons m_{h_b} for different values of the singlet vev v_S in type 1. The other parameters are fixed to the values shown on the right.

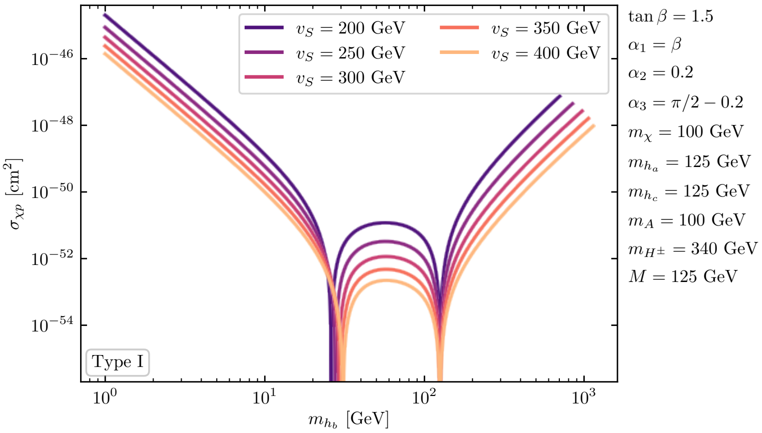

v_S the predictions are always within the neutrino floor. One can also observe that overall larger values of $\sigma_{\chi p}$ can be achieved for smaller values of v_S. This is due to the fact that for fixed values of the masses m_{h_i} smaller values of v_S give rise to larger values of the quartic couplings $\lambda_{6,7,8}$. These couplings act as the portal couplings between the visible and the dark sector, such that larger values of $\lambda_{6,7,8}$ give rise to larger values of the scattering cross sections. However, larger values of the quartic couplings also yield larger values of the annihilation cross sections and, therefore, smaller values of the predicted relic abundance. As a consequence, the parameter points with the largest values of $\sigma_{\chi p}$ can be expected to predict a relic abundance which is smaller than the measured DM relic abundance. The impact of the predicted DM density on the prospects of probing the S2HDM at DD experiments will be discussed in more detail in Sect. 9.2.2.

By comparing the theoretical predictions with the upper limit from XENON1T PandaX-4T and LZ, one can see that only for the smallest value of $v_S = 100$ GeV considered here the current DD experiments have the potential of probing the S2HDM parameter space. It should be noted that even smaller values of v_S, for which $\sigma_{\chi p}$ would become even larger, are excluded in this scenario as a consequence of the tree-level perturbative unitarity constraints. This emphasises the importance of taking into account such theoretical constraints in order to give an accurate estimate of the maximum values of $\sigma_{\chi N}$ that can be achieved in the S2HDM. While the current upper limits from XENON1T PandaX-4T, and LZ barely constrain the parameter points shown in Fig. 9.6, large parts of the interval of DM masses that are shown can be probed in the future by Darwin. For instance, assuming a value of $v_S = 200$ GeV, the expected limits from Darwin would exclude the DM mass range 30 GeV $\lesssim m_\chi \lesssim$ 1.8 TeV. In general it is interesting to note that the scattering cross sections peak for DM masses of the order of the masses of the Higgs boson. The presence of the BSM Higgs bosons can be tested at the LHC if they are not too heavy to be produced. In this case the S2HDM can be probed in a complementary way by DD experiments and colliders.

Another theoretical requirement which has to be fulfilled by the one-loop corrections that we take into account is that the cancellation mechanism only holds in the limit of vanishing momentum transfer. As a result, the cancellation mechanism breaks down if the mass of one of the Higgs bosons is not much larger than the momentum that is transferred in the scattering process. In order to demonstrate that our result also complies with this condition, we show in Fig. 9.7 the predictions for $\sigma_{\chi p}$ as a function of the mass of one of the Higgs bosons h_b, with the remaining parameters fixed to the values shown on the right-hand side of the plot, and where we show here the predictions of the type I S2HDM. One can see that, as expected, $\sigma_{\chi p}$ increases drastically in the limit $m_{h_b} \to 0$, independently of the value of v_S as indicated by the colour coding of the lines. As before, we applied only the theoretical constraints in order to produce the results shown in Fig. 9.7, whereas the experimental constraints were not applied. This is important to note because values of $m_{h_b} \ll 125/2$ GeV would be excluded due to constraints from the signal-rate measurements of h_{125} in combination with the condition of not overclosing the universe [2]. As a result, although the direct-detection cross sections can be very large if the singlet-like Higgs boson (here h_b) is much lighter than 125 GeV, DM direct-detection experiments cannot provide additional exclusion limits in this region of the parameter space.

In the opposite limit with $m_{h_b} \gg m_\chi$, one can observe in Fig. 9.7 that $\sigma_{\chi p}$ instead increases with increasing value of m_{h_b}. This behaviour has its origin in the fact that for fixed values of v_S the quartic couplings $\lambda_{6,7,8}$ grow with increasing value of the singlet-like Higgs-boson mass m_{h_b}. As already mentioned, larger absolute values of the quartic couplings give then rise to larger scattering cross sections. The absolute values of the quartic couplings are ultimately bounded from above by the constraints from perturbative unitarity. The predictions in Fig. 9.7 are shown for each value of v_S up the maximum value of m_{h_b} for which the parameter points were still in agreement with these bounds. Consequently, the maximum values of $\sigma_{\chi p}$ that are achieved here in a parameter region that is potentially not yet excluded by other experimental constraints are of the order of $\sigma_{\chi P} \sim 10^{-48}$ cm^2, which is well within the range that can be tested at future DD experiments like Darwin.

Another interesting feature that can be observed in Fig. 9.7 is the appearance of *blind-spots* at certain values of m_{h_b} where $\sigma_{\chi p}$ drops to zero. Such blind-spot regions were also observed in the simpler case of the pNG DM model with only one Higgs doublet [62]. The presence of the blind-spots is a result of a cancellation between the amplitudes of different loop diagrams, giving rise to the fact that the sum of all amplitudes, and thus the Wilson coefficients C_q^s, vanish. For the blind-spot on the right-hand side it is easy to see that it appears at the point at which all CP-even Higgs bosons are mass degenerate, with $m_{h_{a,b,c}} = 125$ GeV. Even though it is questionable whether such a situation is phenomenologically viable in light of constraints from the LHC measurements, it is still an interesting observation that approximately mass-degenerate scalar states could yield a highly suppressed DM-nucleon scattering cross section. A second blind-spot can be observed at roughly $m_{h_b} \sim 30$ GeV, where the precise location depends on the value of v_S. In addition, the location of this additional blind-spot also depends in a non-trivial way on the choice of the masses $m_{h_{a,b,c}}$ and the mixing angles $\alpha_{1,2,3}$. For both blind-spots, it might be interesting to compute corrections beyond the one-loop level in order to analyse whether they would remain, in which case their presence would be related to an accidental

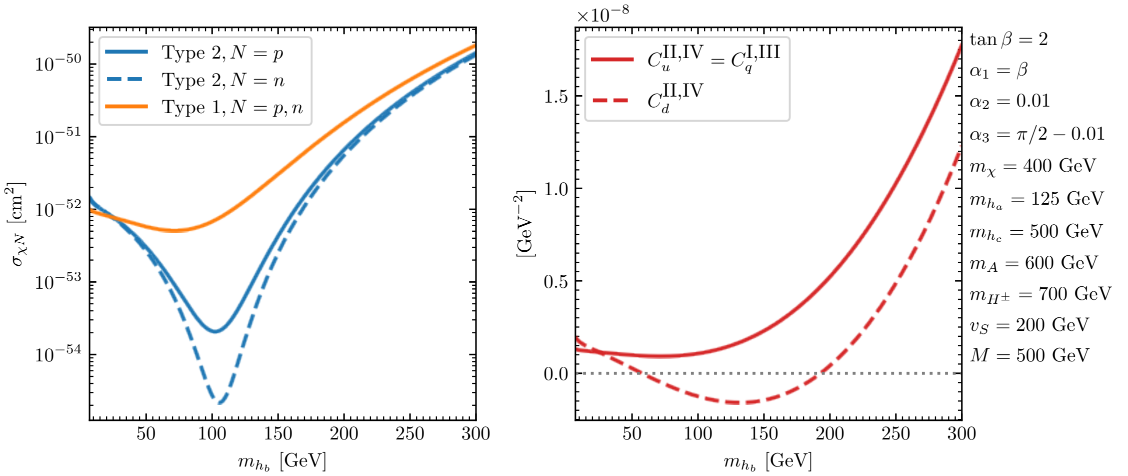

Figure 9.8: Left: Cross sections for the scattering of χ on protons ($N = p$) and neutrons ($N = n$) as a function of m_{h_b} in type I (orange) and type II (blue). Right: Wilson coefficients as defined in 9.2 and 9.3 as a function of m_{h_b}. The remaining parameters are fixed to the values shown on the right.

symmetry, or whether the higher-order corrections eliminate the blind-spots, in which case their presence relies on a purely accidental choice of parameters.

In addition to the blind-spots that appear due to vanishing scattering amplitudes between the DM state χ and the quarks, as discussed above, in the type II and the type F S2HDM further blind-spots can appear as a result of a cancellation between the different terms in the sum over the quark contributions as shown in 7.18. As discussed in Sect. 9.1.1, in type I and type LS (at the one-loop level) there is only a single Wilson coefficient $C_q^{\mathrm{I,LS}}$ that enters in this sum. However, in type II and type F there are two independent coefficients $C_u^{\mathrm{II,F}}$ and $C_d^{\mathrm{II,F}}$ (see 9.3 and the related discussion) for the scattering on up-type and down-type quarks, respectively. If these two coefficients have the opposite sign, the sum in 7.18 can be suppressed even though the individual terms are unsuppressed.

In order to demonstrate this feature, we show in the left plot of Fig. 9.8 the cross sections for the scattering of the DM state χ on protons and neutrons in type I (orange line) and type II (blue lines) for a representative benchmark scenario. As before, we applied here only the theoretical constraints in order to ensure that the scalar potential is well behaved. One can see that at values of $m_{h_b} \sim 100$ GeV the scattering cross sections in type II decrease by two orders of magnitude, whereas the cross sections in the type I remains almost constant. Moreover, it should be noted that in this interval of m_{h_b} the cross sections in type II are substantially different for the scattering on protons (solid blue line) and neutrons (dashed blue line). On the other hand, in type I both cross sections are practically equal, and consequently only one line for both the scattering on protons and on neutrons is shown. As a phenomenological consequence, one can notice that since different nuclei are composed out of a different number of neutrons and protons, a hypothetical measurement of the scattering cross sections on different kinds of nuclei could be utilised to distinguish between a DM candidate χ as predicted by the types I/LS or the types II,F, respectively.

The suppression of the cross sections in type II can be understood by the fact that one of the Wilson coefficients $C_u^{\mathrm{II,F}}$ or $C_d^{\mathrm{II,F}}$ changes the sign at the corresponding mass interval of h_b. In the right plot of Fig. 9.8 we show the Wilson coefficients as a function of m_{h_b} for the same benchmark scenario as was used in the left plot of Fig. 9.8. As expected, one can see that the coefficient $C_d^{\mathrm{II,F}}$ (dashed line) becomes negative in the mass range $50\ \mathrm{GeV} \lesssim m_{h_b} \lesssim 200\ \mathrm{GeV}$, where the mass range coincides with the one in the left plot in which the cross sections in type II are strongly suppressed. Since in type I there is only one Wilson coefficient $C_q^{\mathrm{I,LS}}$, which is identical to the coefficient $C_u^{\mathrm{II,IV}}$ in type II (solid line), the change of the sign of $C_d^{\mathrm{II,F}}$ has no impact on the cross sections in type I. Finally, we note that the precise location of the blind-spot visible for type II and also the amount of the suppression of the cross sections depend on the nucleon form factors $f_{T_q}^N$, which are only known approximately as they are determined from lattice simulations and from experimental data. As a consequence, in the parameter regions in which the scattering cross sections are suppressed due to the accidental cancellation of contributions from different quark types with opposite sign, the relative uncertainty of the cross-section predictions associated to the uncertainty of the form factors should be regarded as larger compared to other parameter space regions in which no such cancellation takes place.

As a summary of the discussion in this section, one can conclude that the one-loop corrections included in our computation fulfil the theoretical requirements that can be derived from symmetry arguments, which serves as a non-trivial cross check of our results. Moreover, we have demonstrated that the cross sections as predicted at the one-loop level can be well within the reach of future DM direct-detection experiments. It should be noted that we did not apply here the experimental constraints on the model parameters as introduced in Sect. 8.1.2. In order to verify whether the future sensitivity of DM direct-detection experiments is capable of probing parameter space regions that are not yet excluded by other experimental constraints on the Higgs sector and the DM sector of the S2HDM, we will discuss in the following section two parameter scans in the type I and the type II S2HDM in which the experimental constraints will be taken into account.

9.2.2 Parameter scans in type I and type II

In order to estimate the relevance of the loop-corrected predictions for the cross sections of the scattering of the DM state χ on nuclei, we present here the predictions in two parameter scan projections in the S2HDM type I and type II in which we take into account all the theoretical and experimental constraints discussed in Sect. 8.1.1 and Sect. 8.1.2, respectively. We note here that the Yukawa sectors of type I and type LS as well as the Yukawa sectors of type II and type F only differ in the couplings of the Higgs bosons to leptons. Consequently, the cross-section predictions for the DM-nucleon scattering in the type I are identical to the predictions in the type LS, and the predictions in the type II are identical to the ones in the type F. Accordingly, apart from the different collider constraints that have to be applied, the results using type I and II presented in the following also provide a good understanding of the importance of future DM DD experiments in the type LS and the type F.

Type	m_{h_a}	$m_{h_b}, m_{h_c}, m_A, m_\chi$	$m_{H^\pm}$	$\alpha_{1,2,3}$	$\tan\beta$	M	v_S
I	125.09	[30,1000]	[150,1000]	$[-\pi/2, \pi 2]$	[1.5,10]	[20, 1000]	[30,1000]

Type	m_{h_a}	m_{h_b, m_A}	$m_{H^\pm}$	$m_{h_c, \chi}$	$\alpha_{1,2,3}$	$\tan\beta$	M	v_S
II	125.09	[200,1000]	[650,1000]	[30,1000]	$[-\pi/2, \pi 2]$	[1.5,10]	[450, 1000]	[30,1000]

Table 9.1: Values of the free parameters for the scan in type I (top) and type II (bottom). Dimensionful parameters are given in GeV.

In our scans we used values for the free parameters as shown in Tab. 9.1. We fixed $m_{h_a} = 125.09$ GeV in order to account for a scalar state that could, depending on its couplings, behave in agreement with the experimental measurements with regards to the discovered Higgs boson. The masses of the BSM scalars were scanned up to values of 1 TeV, corresponding to a range that is potentially in reach of the LHC. It should be noted here that for the scan in type II we used a lower limit of $m_{H^\pm} > 650$ GeV in order to bypass constraints from flavour-physics observables, whereas in type I we used a lower limit of $m_{H^\pm} > 150$ GeV since the flavour constraints are much weaker (see also the discussion in Sect. 8.1.2). In combination with the theoretical constraints on the quartic scalar couplings and constraints from the EWPO, also the lower limits on the mass scale M and the masses m_{h_b} and m_A of one of the CP-even scalars h_b and the pseudoscalar A, respectively, are pushed to larger values in type II in order to account for the fact that the differences between these parameters and $m_{H^\pm}$ cannot be too large. The mixing angles were scanned over all physically distinguishable parameter space, and the lower limit on $\tan\beta$ was chosen according to constraints from flavour physics. Finally, the singlet vev v_S is varied within the scan range of the BSM scalars. We note that due to its pNG nature the DM state χ can be light even though the global U(1) symmetry breaking has its origin at energy scales much larger than the TeV scale, such that also values of $v_S \gg 1$ TeV would be physically reasonable. However, as we demonstrated in Sect. 9.2.1, sizable values of the cross sections for the scattering of the χ on nuclei are present only if v_S is of the order of the masses of the CP-even Higgs bosons or smaller. Therefore, for the purpose of determining the largest scattering cross sections that can be realised in the S2HDM it is sufficient to scan only a range in which v_S is of the order of $m_{h_{a,b,c}}$ (or smaller).

We have generated parameter points by scanning uniformly over the given parameter ranges. For each parameter point generated in this way, we have applied the theoretical and experimental constraints discussed above, and we have discarded the parameter points for which one of the constraints was violated. For the remaining parameter points, we have calculated the predictions for the DM-nucleon scattering cross sections. We have then compared the theoretical predictions against the current and future DM direct-detection constraints from the XENON1T, PandaX-4T, LZ and the Darwin experiment, respectively. Finally, we have also taken into account the predicted value of the DM density as obtained by assuming the standard freeze-out mechanism in order to answer the question whether

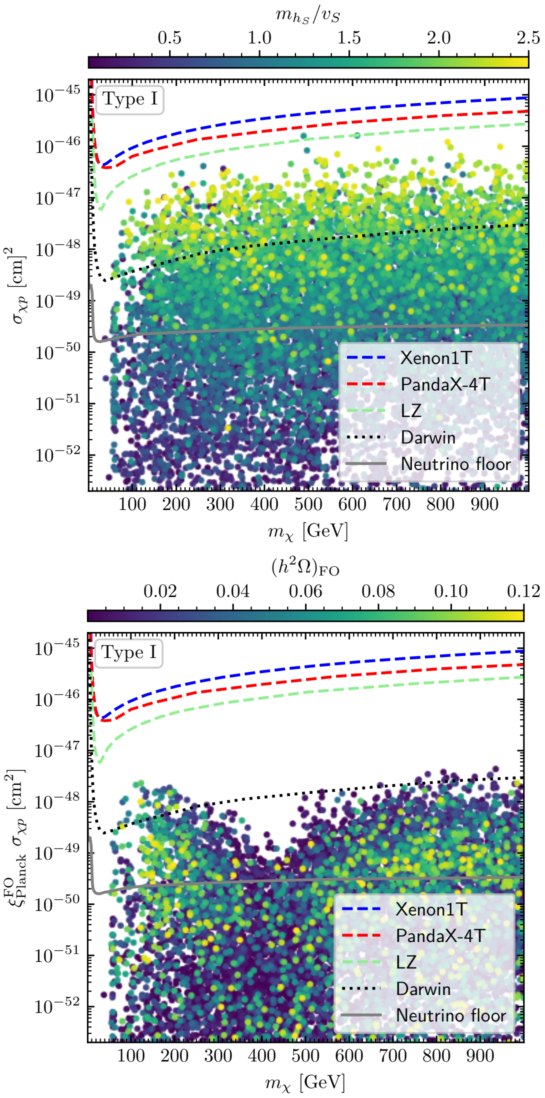

Figure 9.9: Parameter points of the scan in type I (left) and type I (right) in the (m_χ,$\sigma_{\chi P}$) plane (top) and in the (m_χ,$\xi^{FO}_{\text{Planck}}\sigma_{\chi P}$) plane (bottom). The colour coding of the points indicates the value of m_{h_S}/v_S (top) and the value of $(h^2\Omega)_{\text{FO}}$ (bottom). Also shown are the current upper limits on the 95% confidence level from XENON1T [95] (blue dashed line), from PandaX-4T [94] (red dashed line) and from LZ [97] (dashed green line), and the projected upper limit from Darwin [419] (dotted line). The gray solid line indicates the neutrino floor [433].

the parameter points that could be probed by DD experiments would also predict a sizeable fraction of the measured DM relic abundance. Moreover, in case the predicted relic abundance is substantially smaller, we address how much this reduces the prospects of probing the corresponding S2HDM parameter space by means of DD experiments.

In the top row of Fig. 9.9 we show the scan points in type I (left) and type II (right) with the DM mass m_χ on the horizontal axis and the DM-proton scattering cross section $\sigma_{\chi p}$ on the vertical axis. The colour coding of the points indicates the value of m_{h_S}/v_S, where

h_S is defined as the CP-even scalar h_i with the largest singlet admixture given by R_{i3}^2 (see Sect. 3.1.3). Also indicated are the cross section limits at the 95% confidence level from the XENON1T [95], the PandaX-4T [94] and the LZ [97] experiments with blue, red and green dashed lines, respectively, and the projected future limits from the Darwin experiment [419] with the black dashed line. Finally, the gray solid line indicates the neutrino floor [433]. One can see that we find points which predict values of $\sigma_{\chi p}$ that are within the reach of Darwin, whereas the current experimental sensitivity by XENON1T PandaX-4T and LZ are not sufficient to probe the S2HDM parameter space in a significant way. On the other hand, the largest fractions of parameter points feature values of $\sigma_{\chi p}$ that are substantially below the Darwin sensitivity, and many points are within the neutrino floor in which case a possible DM detection is not very promising even in the distant future. We note here that the range of the vertical axis for $\sigma_{\chi p}$ was set to 10^{-52} cm^2 for a better visibility of the relevant range of $\sigma_{\chi p}$ for which there is experimental sensitivity, although there are parameter points featuring values of $\sigma_{\chi p}$ that are orders of magnitude smaller. Finally, we emphasise that overall larger values of the DM-proton scattering cross section are correlated with larger values of the ratio m_{h_S}/v_S, which is in agreement with the observations discussed in Sect. 9.2.1.

The cross-section limits from XENON1T, PandaX-4T, LZ and Darwin, as shown in the top row of Fig. 9.9, were derived under the assumption that the DM particle under consideration accounts for the entire measured DM relic density as measured by Planck. However, in the S2HDM one can predict the DM relic abundance composed of the state χ assuming the standard freeze-out scenario, and in the parameter scans we only demanded that the predicted DM relic abundance is not larger than the measured value, thus leaving room for additional sources that contribute to the DM relic abundance. If the predicted abundance of the DM state χ is smaller than the measured value, the prospects for the DD of DM decrease, since the number of scattering events in the detector is smaller compared to the number of scattering events expected based on the measured DM density. In order to account for the impact of the predicted relic abundance, it is illustrative to compare the upper limits on the scattering cross section from the DM DD experiments against the predicted scattering cross section $\sigma_{\chi p}$ times a scaling factor

$$\xi_{\text{Planck}}^{\text{FO}} = \frac{(h^2\Omega)_{\text{FO}}}{(h^2\Omega)_{\text{Planck}}} \,, \tag{9.5}$$

where $(h^2\Omega)_{\text{FO}}$ is the theoretical prediction for the today's DM relic abundance based on the freeze-out mechanism (obtained with the help of `MicrOmegas`), and $(h^2\Omega)_{\text{Planck}} = (0.119 \pm 0.003)$ is the value as measured by the Planck sattelite [72].

In the bottom row of Fig. 9.9 we show the rescaled cross sections $\xi_{\text{Planck}}^{\text{FO}}\sigma_{\chi p}$ in dependence of the DM mass m_χ for type I on the left and for type II on the right, respectively. Here the colour coding indicates the value of the predicted DM relic abundance $(h^2\Omega)_{\text{FO}}$. Since we demanded $(h^2\Omega)_{\text{FO}} \leq (h^2\Omega)_{\text{Planck}}$ (see Sect. 8.1.2), the parameter points all feature $\xi_{\text{Planck}}^{\text{FO}} \leq 1$. Thus, compared to the plots in the upper row of Fig. 9.9, the points move towards the neutrino floor and away from the experimental upper limits on the DM-nucleon scattering cross section. Nevertheless, we find a mass interval 60 GeV $\lesssim m_\chi \lesssim$ 300 GeV in which Darwin has the potential to probe the S2HDM parameter space in both type I and type II. One should note that many of the parameter points in this interval of m_χ predict a sizable fraction (or all) of the measured DM relic abundance. Hence, the DD constraints will have the potential to probe regions of the parameter space that are especially interesting in view of the predictions for $(h^2\Omega)_{\mathrm{FO}}$.[5] For larger DM masses, additional DM annihilation channels, for instance into pairs of on-shell vector bosons, top quarks or Higgs bosons h_i, become kinematically open. As a consequence, in the range 200 GeV $\lesssim m_\chi \lesssim$ 500 GeV we find a strong suppression of $(h^2\Omega)_{\mathrm{FO}}$, and therefore $\xi^{\mathrm{FO}}_{\mathrm{Planck}} \ll 1$. This gives rise to the fact that in this range of m_χ almost no points are found above the projected upper limit of Darwin. For values of $m_\chi \gtrsim$ 500 GeV, one can see that parameter points featuring sizable values of $(h^2\Omega)_{\mathrm{FO}}$ can be found above the neutrino floor, however also here the projected sensitivity of Darwin is small and limited to parameter points for which the DM state χ does not account for the whole DM relic abundance. Finally, we note that no large differences between both Yukawa types can be found. Accordingly, the prospects for probing the S2HDM parameter space at future DM direct-detection experiments can be expected to be fairly similar.

---

[5] DM masses of 63 GeV $\lesssim m_\chi \lesssim$ 67 GeV were also shown to be favoured for a simultaneous description of the Fermi-LAT galactic-center excess and the AMS antiproton excess in the S2HDM [2].

Chapter 10

Conclusions

> Nature rarer uses yellow
> Than another hue;
> Saves she all of that for sunsets,–
> Prodigal of blue
>
> Emily Dickinson

There are exciting times ahead. The discovery of a Higgs boson in 2012 and the first detection of GW signals in 2015 opened new windows to look into the unresolved mysteries of particle physics and cosmology.

Among the near future experimental achievements, we expect the recently started Run 3 of the LHC to explore new territory in the search for new physics with the increased data samples and higher collision energy [434]. With the HL-LHC upgrade, which is projected to be operational in 2029 [435], we will be granted further opportunities to study known mechanisms in detail, and observe new phenomena. In particular, these experiments will aim at probing the nature of the Higgs boson with unprecedented precision. Deviations from the SM might be found in its production or decay modes, through the searches for rare decays of the Higgs boson, or via the measurements of the strength of its self-interaction. Aside from the perspectives in collider physics, the first space-based GW interferometer will be launched towards the end of the 30s [436]. LISA will be the first experiment to measure GWs in the milli-Hertz frequency range. Among the possible signals in this frequency band, the stochastic GW background from a strong FOEWPT in the early Universe exemplifies a well-motivated scenario that is expected in many models of physics BSM [26, 27].

Another experimental milestone consists of various indications for the existence of DM gathered since the first hints of its presence were reported almost 100 years ago. If DM has a particle nature, we need to probe its mass and couplings to the SM particles at direct detection experiments. Developments in this direction are being pursued, and future facilities, such as DARWIN [419], project sensitivities close to the neutrino floor.

Parallel to the progress on the experimental side, a blooming landscape of theoretical ideas aims at curing the shortcomings of the SM while making testable predictions for those present and near future experiments. This thesis represents an example of the theory efforts to tackle two of the major questions in particle physics that still remain unanswered:

- How did the Higgs field acquire its vacuum expectation value in the early Universe? (addressed in Chapters 5 and 6)

- What is the nature of dark matter? (addressed in Chapters 8 and 9).

Original results addressing these two questions followed from the analysis of three well-motivated scalar extensions of the SM: the 2HDM, the N2HDM and the S2HDM. A common feature of all the studies gathered in this dissertation is the interplay between Higgs physics and early Universe cosmology. Further similarities are the central role that the predictions for future experiments play, and the approach of combining multiple sources of experimental data as a valuable tool to probe BSM scenarios. In the following, we summarise the main conclusions drawn as a result of each one of the four studies.

10.1 The electroweak symmetry in the early Universe

In Chapters 5 and 6, we studied the 2HDM and the N2HDM, respectively. We have shown how scalar extensions of the SM allow for a rich cosmological history associated to the thermal evolution of the scalar potential in the early Universe. Besides the possibility of a FOEWPT, which has been studied in depth for all these scenarios, we encountered other interesting finite-temperature evolutions: vacuum trapping and EW SnR. The striking feature of vacuum trapping is that it triggers a situation in which the Universe remains in an unbroken EW phase, although the EW vacuum is the deepest one at $T = 0$. Such a situation is not phenomenologically viable, and parameter regions featuring vacuum trapping can, therefore, be excluded. On the other hand, contrary to the commonly expected picture predicted by the SM, in the presence of EW SnR, the vacuum adopted at high temperature is not the EW symmetric one. The viability of those scenarios depend on the details of the thermal evolution of the Universe at high temperatures.

In the analyses of both models, we demonstrated that relying merely on the presence of a critical temperature, at which the co-existing symmetric vacuum and the EW vacuum are degenerate, does not account for the effect of vacuum trapping, and erroneously assigns the strongest FOEWPTs to regions of the (N)2HDM parameter space in which actually no EW phase transition can take place. We also found that the occurrence of EW SnR in both models is driven by contributions from the resummation of daisy diagrams, and is expected to happen in other BSM extensions of the SM as well.

Overall, the results of both studies suggest that the combination of constraints from collider experiments, from the evolution of the early Universe and from future astrophysical experiments, such as GW interferometers, will be indispensable for probing the parameter space of BSM models featuring an extended Higgs sector.

Chapter 5 In the **2HDM**, our analysis was performed in a well-motivated benchmark scenario, which, in order to facilitate a FOEWPT, is characterised by the alignment limit ($c_{\beta-\alpha} = 0$) and sizeable mass splitting between the second CP-even state H and the CP-odd and the charged Higgs bosons A and $H^{\pm}$. The light CP-even Higgs-boson mass was set to 125.09 GeV, and the heavy CP-even Higgs-boson mass as well as the mass of the CP-odd Higgs-boson, assumed to be equal to the mass of the charged Higgs-bosons, are free parameters, whereas the soft Z_2-breaking parameter was fixed by the relation $m_{12}^2 = m_H^2 s_\beta c_\beta$, and we chose $\tan\beta = 3$.

Concerning the **production of GWs**, we found that even with optimistic assumptions (bubble wall velocity of $v_\mathrm{w} = 0.6$ and a mission time for LISA measurements of 7yrs), the part of the 2HDM type II parameter space that results in a SNR larger than 1 is very restricted. Most parts of the parameter space featuring a strong FOEWPT predict an associated stochastic GW background that is too weak to be detectable with LISA. Potentially detectable GW signals are found for a relatively fine-tuned interval of mass splittings between the additional CP-even state H and the CP-odd state A at the level of 200 GeV $\lesssim m_A - m_H \lesssim$ 250 GeV. We also demonstrated that parameter points with substantially larger mass splittings either feature SnR, or they feature unphysical thermal histories because of, for instance, vacuum trapping or a short-lived EW vacuum at zero temperature.

Concerning the **collider phenomenology**, based on the RGE evolution of the quartic scalar couplings and the TeV-scale energy cut-off of the parameter points featuring a detectable GW signal, we demonstrated that in these parameter regions new-physics effects are expected to be observable at the (HL-)LHC. As one of the promising examples for how such new-physics might arise at colliders, we discussed that the relevant parameter regions will, to a large extent, be probed at the high-luminosity phase of the LHC via the **"smoking gun signature"** $pp \to A \to ZH$ with subsequent decay of $H \to t\bar{t}$.

In the second HL-LHC analysis we focused on the **trilinear coupling** of the Higgs boson at $\sim$ 125 GeV, λ_{hhh}. Regions in the 2HDM parameter space that can give rise to large GW signals are associated with relatively large values of $\kappa_\lambda := \lambda_{hhh}/\lambda_{hhh}^\mathrm{SM} \sim 2$, which are within the 95% confidence-level upper limits that are expected to be reachable via the measurement of the non-resonant Higgs-boson pair-production at the HL-LHC. Even larger values of κ_λ are found for SnR, such that parameter regions giving rise to this phenomenon will also be probed at the HL-LHC.

The precision with which κ_λ can be measured sensitively depends on its precise value. $\kappa_\lambda \sim 2$ leads to a strongly reduced sensitivity at the HL-LHC with a resolution of only $\sim$ 70%, due to the enhanced negative interference of signal and background diagrams. The situation is reversed at the ILC operating at $\sqrt{s}$ = 500 GeV. For $\kappa_\lambda \sim 2$, the precision increases to $\sim$ 10% due to an enhanced positive interference between signal and background diagrams. Since a FOEWPT is naturally connected to values of $\kappa_\lambda > 1$, the general prospects for the HL-LHC to measure the trilinear couplings of the Higgs boson are worse than in the SM, whereas they improve substantially for the ILC.

As a final conclusion of our work on these subjects, we stress that in the 2HDM type II the parameter points accommodating a primordial GW background in reach of LISA are confined to contrived regions of the parameter space. Moreover, these regions of the parameter space imply the observation of new physics at energy scales accessible at the LHC. As a consequence, the hypothetical scenario of the absence of any indications for new-physics at the LHC, in particular during the high-luminosity phase, would put severe limitations on the prospects of a detection of a GW background at LISA within the considered model.

Chapter 6 For the **N2HDM**, we have identified the key quantities that can be used to analytically determine the restoration or **non-restoration** of the EW symmetry at high temperature, summarised in Eqs. (6.19)–(6.21) and (6.23). Previous studies in the literature [47–49] have shown that the presence of at least $O(100)$ thermalised scalars with negative quartic Higgs-portal couplings can keep the electroweak symmetry broken at temperatures well above the electroweak scale.[1] In this dissertation, a new mechanism to realise the non-restoration of the EW symmetry in the early Universe has been presented. Contrary to these earlier works, the presence of negative quartic couplings is not a necessary condition to achieve a persisting broken EW phase at high temperature. Instead, contributions to the scalar potential from the resummation of daisy diagrams are responsible for driving the thermal mass of the CP-even doublet-like scalars negative. Avoiding the necessity of negative quartic couplings facilitates achieving a stable scalar potential while realising EW symmetry non-restoration with an $O(1)$ number of additional degrees of freedom. We have supplemented our analytical investigation with a numerical analysis of the N2HDM thermal history with the help of the code `CosmoTransitions` tracking in each case the local minima of the potential as a function of temperature. Furthermore, we have shown that it is possible for a scenario with an unrestored EW symmetry at high temperatures to still feature a FOEWPT, since the EW symmetry can be restored in an intermediate temperature regime. The occurrence of both effects within the same thermal evolution was studied in detail for the N2HDM, but, in principle, this could also happen in similar models like the 2HDM.

In a further step, we have demonstrated that **vacuum trapping** leads to unphysical regions of the N2HDM parameter space despite the presence of a global EW minimum of the scalar potential at $T = 0$.

Finally, we have analysed the connection of these early Universe phenomena to the predicted phenomenology of the N2HDM at the **LHC**. We have shown that the patterns of the thermal history of the early Universe can be linked to characteristic signatures in the N2HDM which have no equivalent in other models like the 2HDM. While in the 2HDM in the alignment limit only the decay $A \to ZH$ is possible if kinematically allowed, in the N2HDM the two decays $A \to Zh_2$ and $A \to Zh_3$ can occur, whose branching ratios depend on both the singlet component and the masses of $h_{2,3}$. We have also shown that in the N2HDM a departure from the alignment limit does not necessarily diminish the prospects for a FOEWPT, in contrast to the case of the 2HDM [172].

10.2 Pseudo-Nambu-Goldstone dark matter

In Chapters 8 and 9, we studied the S2HDM, a complex singlet extension of the 2HDM, that provides a DM candidate through a $U(1)$ symmetry softly broken by dimension-two terms. The tree-level amplitude of the DM-nucleon scattering process is proportional to

---

[1] In Ref. [49], the possibility of reducing the additional number of degrees of freedom required to achieve EW symmetry non-restoration by considering an extra EW doublet was for the first time discussed.

the DM velocity, and thus negligible for direct-detection experiments. This is a feature of a class of models with a pseudo Nambu-Goldstone boson as the DM candidate.

In Chapter 8, we performed a detailed treatment of the S2HDM, taking into account a large number of experimental and theoretical constraints. Direct-detection constraints were not considered, due to the fact that the tree-level scattering amplitudes vanish in the limit of zero momentum transfer. Since non-vanishing scattering cross sections arise at the loop level, we studied a specific parameter space region were the contributions from those radiative corrections are expected to be small.

As a continuation of this analysis, in Chapter 9 we calculated the one-loop EW corrections to the DM-nucleon scattering cross section for a general choice of the parameter space. We profited from all the tools developed for the former study, in order to implement the multiple constraints and shape the physically allowed parameter space of the model.

Chapter 8 For the analysis of the S2HDM in this Chapter, we focused on the range of DM masses in the Higgs funnel region, i.e. 40 GeV $\leq m_\chi \leq$ 80 GeV., were most (or all) of the observed DM relic abundance can be accounted for via the thermal freeze-out of χ through resonant DM annihilation via s-channel diagrams mediated by the SM-like Higgs boson. This mass region is also interesting due to the increasing sensitivity in this regime of indirect detection experiments to probe those DM annihiliation cross sections, which are required to yield the correct relic abundance. Additionally, the corresponding parameter space is also suitable to realise the excess of gamma rays from the galactic center observed by Fermi LAT. At the same time, the Alpha Magnetic Spectrometer, reported an excess over the expected flux of cosmic ray antiprotons, which is also consistent with DM annihilating into b-quark pairs with a similar range of DM masses.

We performed the first analysis in this model that considers simultaneously all the **constraints** listed in the following. We required the scalar potential to be well-behaved up to energy scales of 1 TeV, i.e. to be bounded-from-below, to feature a stable EW vacuum and to fulfil conditions derived from perturbative unitarity. We also ensured that the parameter points were in agreement with measurements of EWPO, flavour physics, properties of the discovered Higgs boson at 125 GeV, searches for additional scalar states and with the DM observables (measured DM relic abundance and indirect detection constraints).

We focused on **two benchmark scenarios**. Firstly, we performed a broad parameter scan assuming that the SM-like Higgs boson h_{125} was the lightest of the three CP-even Higgs bosons. Secondly, we studied a scenario featuring a singlet-like CP-even state h_{96} at 96 GeV, where the presence of h_{96} gives rise to a second s-channel contribution to the thermal freeze-out cross section, apart from the one mediated by the SM-like Higgs.

In the **first scenario**, DM masses 62.5 GeV $\lesssim m_\chi \lesssim$ 67 GeV were found to be able to explain the Fermi LAT galactic center and antiproton excesses, while simultaneously also predicting values of the DM relic abundance in agreement with the observations by the Planck collaboration. However, these parameter regions are in tension with indirect-detection limits derived from observations of dwarf spheroidal galaxies, which are still subject to uncertainties with regards to the astrophysical modelling of the spectral curves.

In the **second scenario**, we studied whether the S2HDM could offer an explanation for the collider excesses observed at about 96 GeV at LEP and CMS in the $b\bar{b}$ and the diphoton final state, respectively. Here we found that a singlet-like CP-even Higgs boson at 96 GeV can reproduce both collider excesses under the constraint that $m_\chi > m_{h_{125}}/2$. Furthermore, it is possible to accommodate at the same time a large fraction or all of the measured DM relic abundance. Finally, we found that the simultaneous explanation of the cosmic-ray excesses and the collider excess at 96 GeV is in principle possible, but, as in the first scenario, the parameter regions are also in tension with limits arising from observations of dwarf spheroidal galaxies.

To summarise, we demonstrated that the S2HDM is an attractive model that can accommodate a rich phenomenology and an interesting interplay between the DM sector and the Higgs sector. We also showed that it is crucial to take into account the various theoretical and experimental constraints on the model parameters. We made our implementation of the model predictions and the application of the constraints available to the public in the form of a `python` package called `s2hdmTools`[2].

Chapter 9 For the analysis of the S2HDM in this Chapter, we calculated the one-loop EW corrections to the DM-nucleon scattering cross section.

The calculation was verified by two independent calculations. From the theoretical point of view, the Nambu-Goldstone nature of the DM particle has to be reflected in a zero cross section in the limit where the exact $U(1)$ symmetry is recovered. Another check was the fact that there was no need to introduce counterterms as the process is zero at tree-level in the limit of zero DM velocity. We have verified explicitly that all these features are fulfilled by the loop-corrected scattering amplitudes.

A scan of the model parameters has been performed taking into account all theoretical and experimental constraints discussed in the analysis of Chapter 8, except for DM indirect detection constraints. No parameter points have been found that could be probed by present direct detection experiments such as XENON1T, PandaX-4T or LZ, while at the same time predicting a sizeable fraction of the measured DM relic abundance. However, we have found such parameter points within the reach of future experiments such as DARWIN.

---

[2] More instructions regarding the installation and the usage of the package can be found in the documentation under the link `https://www.desy.de/~biek/s2hdmtoolsdocu/site/`

Appendix A

Change of basis in the S2HDM

In the following we give the transformation formulae between the basis of the Lagrangian parameters and the physical basis chosen to scan the parameter space of the S2HDM defined in Eq. (3.46). The quartic couplings λ_i can be written in terms of the physical basis as

$$\lambda_1 = \frac{1}{v^2 c_\beta^2}\left(-M^2 s_\beta^2 + \sum_{n=1}^{3} m_{h_i}^2 R_{i1}^2\right) , \tag{A.1}$$

$$\lambda_2 = \frac{1}{v^2 s_\beta^2}\left(-M^2 c_\beta^2 + \sum_{n=1}^{3} m_{h_i}^2 R_{i2}^2\right) , \tag{A.2}$$

$$\lambda_3 = -M^2 + \frac{1}{v^2}\left(\frac{1}{c_\beta s_\beta}\left(\sum_{n=1}^{3} m_{h_i}^2 R_{i1}^2 R_{i2}^2\right) + 2m_{H^\pm}\right) , \tag{A.3}$$

$$\lambda_4 = \frac{1}{v^2}\left(M^2 + m_A^2 - 2m_{H^\pm}\right) , \tag{A.4}$$

$$\lambda_5 = \frac{1}{v^2}\left(M^2 - m_A^2\right) , \tag{A.5}$$

$$\lambda_6 = \frac{1}{v_S^2}\left(\sum_{n=1}^{3} m_{h_i}^2 R_{i3}^2\right) , \tag{A.6}$$

$$\lambda_7 = \frac{1}{v v_S c_\beta}\left(\sum_{n=1}^{3} m_{h_i}^2 R_{i1} R_{i3}\right) , \tag{A.7}$$

$$\lambda_8 = \frac{1}{v v_S s_\beta}\left(\sum_{n=1}^{3} m_{h_i}^2 R_{i2} R_{i3}\right) , \tag{A.8}$$

where the matrix elements R_{ij} have been defined in terms of the mixing angles $\alpha_{1,2,3}$ in Eq. (3.45). With the previous transformations, one can also compute the mass parameters in the scalar potential using the tadpole equations as follows,

$$\mu_{11}^2 = m_{12}^2 \tan\beta - \frac{1}{2}\left(\lambda_1 v^2 c_\beta^2 + (\lambda_3+\lambda_4+\lambda_5) v^2 s_\beta^2 + \lambda_7 v_S^2\right) , \tag{A.9}$$

$$\mu_{22}^2 = \frac{m_{12}^2}{\tan\beta} - \frac{1}{2}\left(\lambda_2 v^2 s_\beta^2 + (\lambda_3+\lambda_4+\lambda_5) v^2 c_\beta^2 + \lambda_8 v_S^2\right) , \tag{A.10}$$

$$\mu_\chi^2 = m_\chi^2 , \tag{A.11}$$

$$\mu_S^2 = m_\chi^2 - \left(\lambda_7 v^2 c_\beta^2 + \lambda_8 v^2 s_\beta^2 + \lambda_6 v_S^2\right) . \tag{A.12}$$

References

Citing pages are listed in square brackets after each reference.

[1] T. Biekötter, S. Heinemeyer, J. M. No, M. O. Olea and G. Weiglein, *Fate of electroweak symmetry in the early Universe: Non-restoration and trapped vacua in the N2HDM*, *JCAP* **06** (2021) 018 [`2103.12707`]. [pp. v, 79, 80, 90, and 97]

[2] T. Biekötter and M. O. Olea-Romacho, *Reconciling Higgs physics and pseudo-Nambu-Goldstone dark matter in the S2HDM using a genetic algorithm*, *JHEP* **10** (2021) 215 [`2108.10864`]. [pp. v, 137, 170, 173, and 179]

[3] T. Biekötter, P. Gabriel, M. O. Olea-Romacho and R. Santos, *Direct detection of pseudo-Nambu-Goldstone dark matter in a two Higgs doublet plus singlet extension of the SM*, `2207.04973`. [pp. v and 165]

[4] T. Biekötter, S. Heinemeyer, J. M. No, M. O. Olea-Romacho and G. Weiglein, *The trap in the early Universe: impact on the interplay between gravitational waves and LHC physics in the 2HDM*, `2208.14466`. [pp. v and 71]

[5] H. S. Kragh, *Conceptions of cosmos: From myths to the accelerating universe. A history of cosmology.* 2007. [p. 3]

[6] A. Einstein, *The Field Equations of Gravitation*, *Sitzungsber. Preuss. Akad. Wiss. Berlin (Math. Phys.)* **1915** (1915) 844. [p. 3]

[7] A. Einstein, *Cosmological Considerations in the General Theory of Relativity*, *Sitzungsber. Preuss. Akad. Wiss. Berlin (Math. Phys.)* **1917** (1917) 142. [p. 3]

[8] E. Hubble and M. L. Humason, *The Velocity-Distance Relation among Extra-Galactic Nebulae*, *Astrophys. J.* **74** (1931) 43. [p. 3]

[9] G. Lemaitre, *The expanding universe*, *Annales Soc. Sci. Bruxelles A* **53** (1933) 51. [p. 3]

[10] Particle Data Group collaboration, P. A. Zyla et al., *Review of Particle Physics*, *PTEP* **2020** (2020) 083C01. [pp. 3, 4, 10, 13, 19, 22, 37, and 45]

[11] L. Perivolaropoulos and F. Skara, *Challenges for* Λ*CDM: An update*, `2105.05208`. [p. 3]

[12] P. Huet and E. Sather, *Electroweak baryogenesis and standard model CP violation*, *Phys. Rev. D* **51** (1995) 379 [`hep-ph/9404302`]. [p. 4]

[13] M. B. Gavela, M. Lozano, J. Orloff and O. Pene, *Standard model CP violation and baryon asymmetry. Part 1: Zero temperature*, *Nucl. Phys. B* **430** (1994) 345 [`hep-ph/9406288`]. [p. 4]

[14] M. B. Gavela, P. Hernandez, J. Orloff, O. Pene and C. Quimbay, *Standard model CP violation and baryon asymmetry. Part 2: Finite temperature*, *Nucl. Phys. B* **430** (1994) 382 [`hep-ph/9406289`]. [p. 4]

[15] PLANCK collaboration, N. Aghanim et al., *Planck 2018 results. VI. Cosmological parameters*, *Astron. Astrophys.* **641** (2020) A6 [`1807.06209`]. [p. 4]

[16] J. R. Espinosa and M. Quiros, *The Electroweak phase transition with a singlet*, *Phys. Lett. B* **305** (1993) 98 [`hep-ph/9301285`]. [pp. 4 and 16]

[17] S. Profumo, M. J. Ramsey-Musolf and G. Shaughnessy, *Singlet Higgs phenomenology and the electroweak phase transition*, *JHEP* **08** (2007) 010 [`0705.2425`]. [pp. 4 and 16]

[18] J. R. Espinosa and M. Quiros, *Novel Effects in Electroweak Breaking from a Hidden Sector*, *Phys. Rev. D* **76** (2007) 076004 [`hep-ph/0701145`]. [pp. 4 and 16]

[19] J. R. Espinosa, T. Konstandin and F. Riva, *Strong Electroweak Phase Transitions in the Standard Model with a Singlet*, *Nucl. Phys. B* **854** (2012) 592 [`1107.5441`]. [pp. 4 and 16]

[20] D. Curtin, P. Meade and C.-T. Yu, *Testing Electroweak Baryogenesis with Future Colliders*, *JHEP* **11** (2014) 127 [`1409.0005`]. [pp. 4 and 16]

[21] G. Kurup and M. Perelstein, *Dynamics of Electroweak Phase Transition In Singlet-Scalar Extension of the Standard Model*, *Phys. Rev. D* **96** (2017) 015036 [`1704.03381`]. [pp. 4 and 16]

[22] S. W. Ham, Y. S. Jeong and S. K. Oh, *Electroweak phase transition in an extension of the standard model with a real Higgs singlet*, *J. Phys. G* **31** (2005) 857 [`hep-ph/0411352`]. [pp. 4 and 16]

[23] V. Barger, P. Langacker, M. McCaskey, M. Ramsey-Musolf and G. Shaughnessy, *Complex Singlet Extension of the Standard Model*, *Phys. Rev. D* **79** (2009) 015018 [`0811.0393`]. [pp. 4, 6, 16, and 141]

[24] A. D. Sakharov, *Violation of CP Invariance, C asymmetry, and baryon asymmetry of the universe*, *Pisma Zh. Eksp. Teor. Fiz.* **5** (1967) 32. [pp. 4, 15, and 61]

[25] C. Caprini et al., *Science with the space-based interferometer eLISA. II: Gravitational waves from cosmological phase transitions*, *JCAP* **04** (2016) 001 [`1512.06239`]. [p. 4]

[26] C. Caprini et al., *Detecting gravitational waves from cosmological phase transitions with LISA: an update*, *JCAP* **03** (2020) 024 [`1910.13125`]. [pp. 4, 60, 61, 67, 68, 69, 70, 88, and 181]

[27] P. Auclair et al., *Cosmology with the Laser Interferometer Space Antenna*, `2204.05434`. [pp. 4, 60, 61, 67, and 181]

[28] ATLAS collaboration, *Observation of a new particle in the search for the Standard Model Higgs boson with the ATLAS detector at the LHC*, *Phys. Lett. B* **716** (2012) 1 [`1207.7214`]. [p. 4]

[29] CMS collaboration, *Observation of a New Boson at a Mass of 125 GeV with the CMS Experiment at the LHC*, *Phys. Lett. B* **716** (2012) 30 [`1207.7235`]. [p. 4]

[30] ATLAS, CMS collaboration, G. Aad et al., *Measurements of the Higgs boson production and decay rates and constraints on its couplings from a combined ATLAS and CMS analysis of the LHC pp collision data at $\sqrt{s} = 7$ and 8 TeV*, *JHEP* **08** (2016) 045 [`1606.02266`]. [p. 5]

[31] ATLAS collaboration, *Combined measurements of Higgs boson production and decay using up to* 80 *fb*$^{-1}$ *of proton-proton collision data at $\sqrt{s} = 13$ TeV collected with the ATLAS experiment*, *Phys. Rev. D* **101** (2020) 012002 [`1909.02845`]. [p. 5]

[32] CMS collaboration, *Combined measurements of Higgs boson couplings in proton–proton collisions at $\sqrt{s} = 13$ TeV*, *Eur. Phys. J. C* **79** (2019) 421 [`1809.10733`]. [p. 5]

[33] T. D. Lee, *A Theory of Spontaneous T Violation*, *Phys. Rev. D* **8** (1973) 1226. [pp. 5 and 20]

[34] J. E. Kim, *Weak Interaction Singlet and Strong CP Invariance*, *Phys. Rev. Lett.* **43** (1979) 103. [p. 5]

[35] F. Wilczek, *Problem of Strong P and T Invariance in the Presence of Instantons*, *Phys. Rev. Lett.* **40** (1978) 279. [p. 5]

[36] J. M. Cline and P.-A. Lemieux, *Electroweak phase transition in two Higgs doublet models*, *Phys. Rev. D* **55** (1997) 3873 [`hep-ph/9609240`]. [pp. 5 and 102]

[37] L. Fromme, S. J. Huber and M. Seniuch, *Baryogenesis in the two-Higgs doublet model*, *JHEP* **11** (2006) 038 [`hep-ph/0605242`]. [p. 5]

[38] J. M. Cline, K. Kainulainen and M. Trott, *Electroweak Baryogenesis in Two Higgs Doublet Models and B meson anomalies*, *JHEP* **11** (2011) 089 [`1107.3559`]. [p. 5]

[39] G. C. Dorsch, S. J. Huber, T. Konstandin and J. M. No, *A Second Higgs Doublet in the Early Universe: Baryogenesis and Gravitational Waves*, *JCAP* **05** (2017) 052 [`1611.05874`]. [pp. 5, 16, 61, 67, 74, 81, 83, 85, 115, and 120]

[40] K. Kajantie, M. Laine, K. Rummukainen and M. E. Shaposhnikov, *Is there a hot electroweak phase transition at $m_H \gtrsim m_W$?*, *Phys. Rev. Lett.* **77** (1996) 2887 [`hep-ph/9605288`]. [pp. 5, 61, and 77]

[41] F. Karsch, T. Neuhaus, A. Patkos and J. Rank, *Critical Higgs mass and temperature dependence of gauge boson masses in the SU(2) gauge Higgs model*, *Nucl. Phys. B Proc. Suppl.* **53** (1997) 623 [`hep-lat/9608087`]. [pp. 5 and 61]

[42] Y. Aoki, *Four-dimensional simulation of the hot electroweak phase transition with the SU(2) gauge Higgs model*, *Phys. Rev. D* **56** (1997) 3860 [`hep-lat/9612023`]. [pp. 5 and 61]

[43] M. Gurtler, E.-M. Ilgenfritz and A. Schiller, *Where the electroweak phase transition ends*, *Phys. Rev. D* **56** (1997) 3888 [`hep-lat/9704013`]. [pp. 5 and 61]

[44] M. D'Onofrio and K. Rummukainen, *Standard model cross-over on the lattice*, *Phys. Rev. D* **93** (2016) 025003 [`1508.07161`]. [pp. 5 and 61]

[45] S. Weinberg, *Gauge and Global Symmetries at High Temperature*, *Phys. Rev. D* **9** (1974) 3357. [p. 5]

[46] J. R. Espinosa, M. Losada and A. Riotto, *Symmetry nonrestoration at high temperature in little Higgs models*, *Phys. Rev. D* **72** (2005) 043520 [`hep-ph/0409070`]. [pp. 5 and 62]

[47] P. Meade and H. Ramani, *Unrestored Electroweak Symmetry*, *Phys. Rev. Lett.* **122** (2019) 041802 [`1807.07578`]. [pp. 5, 62, 63, 79, 109, and 184]

[48] I. Baldes and G. Servant, *High scale electroweak phase transition: baryogenesis \& symmetry non-restoration*, *JHEP* **10** (2018) 053 [`1807.08770`]. [pp. 5, 62, 79, 109, and 184]

[49] A. Glioti, R. Rattazzi and L. Vecchi, *Electroweak Baryogenesis above the Electroweak Scale*, *JHEP* **04** (2019) 027 [`1811.11740`]. [pp. 5, 62, 79, and 184]

[50] O. Matsedonskyi and G. Servant, *High-Temperature Electroweak Symmetry Non-Restoration from New Fermions and Implications for Baryogenesis*, *JHEP* **09** (2020) 012 [`2002.05174`]. [pp. 5, 62, and 79]

[51] M. J. Ramsey-Musolf, P. Winslow and G. White, *Color Breaking Baryogenesis*, *Phys. Rev. D* **97** (2018) 123509 [`1708.07511`]. [pp. 5 and 62]

[52] V. A. Kuzmin, V. A. Rubakov and M. E. Shaposhnikov, *On the Anomalous Electroweak Baryon Number Nonconservation in the Early Universe*, *Phys. Lett. B* **155** (1985) 36. [pp. 5 and 61]

[53] B. Patt and F. Wilczek, *Higgs-field portal into hidden sectors*, `hep-ph/0605188`. [pp. 6 and 17]

[54] R. Barbieri, L. J. Hall and V. S. Rychkov, *Improved naturalness with a heavy Higgs: An Alternative road to LHC physics*, *Phys. Rev. D* **74** (2006) 015007 [`hep-ph/0603188`]. [pp. 6 and 17]

[55] M. Schumann, *Direct Detection of WIMP Dark Matter: Concepts and Status*, *J. Phys. G* **46** (2019) 103003 [`1903.03026`]. [p. 6]

[56] V. Barger, M. McCaskey and G. Shaughnessy, *Complex Scalar Dark Matter vis-\‘a-vis CoGeNT, DAMA/LIBRA and XENON100*, *Phys. Rev. D* **82** (2010) 035019 [`1005.3328`]. [p. 6]

[57] D. Barducci, A. Bharucha, N. Desai, M. Frigerio, B. Fuks, A. Goudelis et al., *Monojet searches for momentum-dependent dark matter interactions*, *JHEP* **01** (2017) 078 [`1609.07490`]. [p. 6]

[58] C. Gross, O. Lebedev and T. Toma, *Cancellation Mechanism for Dark-Matter–Nucleon Interaction*, *Phys. Rev. Lett.* **119** (2017) 191801 [`1708.02253`]. [pp. 6 and 7]

[59] R. Balkin, M. Ruhdorfer, E. Salvioni and A. Weiler, *Dark matter shifts away from direct detection*, *JCAP* **11** (2018) 050 [`1809.09106`]. [p. 6]

[60] K. Huitu, N. Koivunen, O. Lebedev, S. Mondal and T. Toma, *Probing pseudo-Goldstone dark matter at the LHC*, *Phys. Rev. D* **100** (2019) 015009 [`1812.05952`]. [p. 6]

[61] D. Karamitros, *Pseudo Nambu-Goldstone Dark Matter: Examples of Vanishing Direct Detection Cross Section*, *Phys. Rev. D* **99** (2019) 095036 [`1901.09751`]. [p. 6]

[62] D. Azevedo, M. Duch, B. Grzadkowski, D. Huang, M. Iglicki and R. Santos, *One-loop contribution to dark-matter-nucleon scattering in the pseudo-scalar dark matter model*, *JHEP* **01** (2019) 138 [`1810.06105`]. [pp. 6, 141, 166, 168, 170, and 173]

[63] K. Ishiwata and T. Toma, *Probing pseudo Nambu-Goldstone boson dark matter at loop level*, *JHEP* **12** (2018) 089 [`1810.08139`]. [pp. 6 and 141]

[64] C. Arina, A. Beniwal, C. Degrande, J. Heisig and A. Scaffidi, *Global fit of pseudo-Nambu-Goldstone Dark Matter*, *JHEP* **04** (2020) 015 [`1912.04008`]. [pp. 6, 141, 152, and 153]

[65] C.-W. Chiang and B.-Q. Lu, *First-order electroweak phase transition in a complex singlet model with $\mathbb{Z}_3$ symmetry*, *JHEP* **07** (2020) 082 [`1912.12634`]. [p. 6]

[66] J. M. Cline and T. Toma, *Pseudo-Goldstone dark matter confronts cosmic ray and collider anomalies*, *Phys. Rev. D* **100** (2019) 035023 [`1906.02175`]. [pp. 6, 141, 156, 157, 158, and 159]

[67] A. Ahmed, S. Najjari and C. B. Verhaaren, *A Minimal Model for Neutral Naturalness and pseudo-Nambu-Goldstone Dark Matter*, *JHEP* **06** (2020) 007 [`2003.08947`]. [p. 6]

[68] Y. Abe, Y. Hamada, T. Ohata, K. Suzuki and K. Yoshioka, *TeV-scale Majorogenesis*, *JHEP* **07** (2020) 105 [`2004.00599`]. [p. 6]

[69] S. Glaus, M. Mühlleitner, J. Müller, S. Patel, T. Römer and R. Santos, *Electroweak Corrections in a Pseudo-Nambu Goldstone Dark Matter Model Revisited*, *JHEP* **12** (2020) 034 [`2008.12985`]. [pp. 6, 134, 141, and 168]

[70] Z. Zhang, C. Cai, X.-M. Jiang, Y.-L. Tang, Z.-H. Yu and H.-H. Zhang, *Phase transition gravitational waves from pseudo-Nambu-Goldstone dark matter and two Higgs doublets*, *JHEP* **05** (2021) 160 [`2102.01588`]. [pp. 6, 141, and 150]

[71] U. Haisch, G. Polesello and S. Schulte, *Searching for pseudo Nambu-Goldstone boson dark matter production in association with top quarks*, `2107.12389`. [p. 6]

[72] Planck collaboration, N. Aghanim et al., *Planck 2018 results. VI. Cosmological parameters*, *Astron. Astrophys.* **641** (2020) A6 [`1807.06209`]. [pp. 6, 15, 17, 141, and 178]

[73] Fermi-LAT, DES collaboration, A. Albert et al., *Searching for Dark Matter Annihilation in Recently Discovered Milky Way Satellites with Fermi-LAT*, *Astrophys. J.* **834** (2017) 110 [`1611.03184`]. [pp. 6, 142, and 165]

[74] Fermi-LAT collaboration, M. Ackermann et al., *The Fermi Galactic Center GeV Excess and Implications for Dark Matter*, *Astrophys. J.* **840** (2017) 43 [`1704.03910`]. [pp. 6 and 157]

[75] Fermi-LAT collaboration, M. Ajello et al., *Fermi-LAT Observations of High-Energy γ-Ray Emission Toward the Galactic Center*, *Astrophys. J.* **819** (2016) 44 [`1511.02938`]. [pp. 6 and 157]

[76] D. Hooper and L. Goodenough, *Dark Matter Annihilation in The Galactic Center As Seen by the Fermi Gamma Ray Space Telescope*, *Phys. Lett. B* **697** (2011) 412 [`1010.2752`]. [p. 6]

[77] D. Hooper and T. Linden, *On The Origin Of The Gamma Rays From The Galactic Center*, *Phys. Rev. D* **84** (2011) 123005 [`1110.0006`]. [p. 6]

[78] D. Hooper and T. R. Slatyer, *Two Emission Mechanisms in the Fermi Bubbles: A Possible Signal of Annihilating Dark Matter*, *Phys. Dark Univ.* **2** (2013) 118 [`1302.6589`]. [p. 6]

[79] T. Daylan, D. P. Finkbeiner, D. Hooper, T. Linden, S. K. N. Portillo, N. L. Rodd et al., *The characterization of the gamma-ray signal from the central Milky Way: A case for annihilating dark matter*, *Phys. Dark Univ.* **12** (2016) 1 [`1402.6703`]. [p. 6]

[80] F. Calore, I. Cholis and C. Weniger, *Background Model Systematics for the Fermi GeV Excess*, *JCAP* **03** (2015) 038 [`1409.0042`]. [pp. 6 and 163]

[81] B. Zhou, Y.-F. Liang, X. Huang, X. Li, Y.-Z. Fan, L. Feng et al., *GeV excess in the Milky Way: The role of diffuse galactic gamma-ray emission templates*, *Phys. Rev. D* **91** (2015) 123010 [`1406.6948`]. [p. 6]

[82] K. N. Abazajian, N. Canac, S. Horiuchi and M. Kaplinghat, *Astrophysical and Dark Matter Interpretations of Extended Gamma-Ray Emission from the Galactic Center*, *Phys. Rev. D* **90** (2014) 023526 [`1402.4090`]. [p. 6]

[83] J. F. Navarro, C. S. Frenk and S. D. M. White, *A Universal density profile from hierarchical clustering*, *Astrophys. J.* **490** (1997) 493 [`astro-ph/9611107`]. [p. 6]

[84] M. Kaplinghat, R. E. Keeley, T. Linden and H.-B. Yu, *Tying Dark Matter to Baryons with Self-interactions*, *Phys. Rev. Lett.* **113** (2014) 021302 [`1311.6524`]. [p. 6]

[85] AMS collaboration, M. Aguilar et al., *Antiproton Flux, Antiproton-to-Proton Flux Ratio, and Properties of Elementary Particle Fluxes in Primary Cosmic Rays Measured with the Alpha Magnetic Spectrometer on the International Space Station*, *Phys. Rev. Lett.* **117** (2016) 091103. [pp. 6 and 157]

[86] M. Cirelli, D. Gaggero, G. Giesen, M. Taoso and A. Urbano, *Antiproton constraints on the GeV gamma-ray excess: a comprehensive analysis*, *JCAP* **12** (2014) 045 [`1407.2173`]. [p. 6]

[87] A. Cuoco, M. Krämer and M. Korsmeier, *Novel Dark Matter Constraints from Antiprotons in Light of AMS-02*, *Phys. Rev. Lett.* **118** (2017) 191102 [`1610.03071`]. [p. 6]

[88] M.-Y. Cui, Q. Yuan, Y.-L. S. Tsai and Y.-Z. Fan, *Possible dark matter annihilation signal in the AMS-02 antiproton data*, *Phys. Rev. Lett.* **118** (2017) 191101 [`1610.03840`]. [p. 6]

[89] I. Cholis, T. Linden and D. Hooper, *A Robust Excess in the Cosmic-Ray Antiproton Spectrum: Implications for Annihilating Dark Matter*, *Phys. Rev. D* **99** (2019) 103026 [`1903.02549`]. [pp. 6, 156, 157, and 163]

[90] S.-J. Lin, X.-J. Bi and P.-F. Yin, *Investigating the dark matter signal in the cosmic ray antiproton flux with the machine learning method*, *Phys. Rev. D* **100** (2019) 103014 [`1903.09545`]. [p. 6]

[91] M. Carena, J. Osborne, N. R. Shah and C. E. M. Wagner, *Return of the WIMP: Missing energy signals and the Galactic Center excess*, *Phys. Rev. D* **100** (2019) 055002 [`1905.03768`]. [p. 6]

[92] LEP Working Group for Higgs boson searches, ALEPH, DELPHI, L3, OPAL collaboration, R. Barate et al., *Search for the standard model Higgs boson at LEP*, *Phys. Lett. B* **565** (2003) 61 [`hep-ex/0306033`]. [pp. 6 and 159]

[93] CMS collaboration, *Search for a standard model-like Higgs boson in the mass range between 70 and 110 GeV in the diphoton final state in proton-proton collisions at* $\sqrt{s} = 8$ *and 13 TeV*, *Phys. Lett. B* **793** (2019) 320 [`1811.08459`]. [pp. 7 and 159]

[94] PandaX-4T collaboration, Y. Meng et al., *Dark Matter Search Results from the PandaX-4T Commissioning Run*, *Phys. Rev. Lett.* **127** (2021) 261802 [`2107.13438`]. [pp. 7, 165, 171, 177, and 178]

[95] XENON collaboration, E. Aprile et al., *Dark Matter Search Results from a One Ton-Year Exposure of XENON1T*, *Phys. Rev. Lett.* **121** (2018) 111302 [`1805.12562`]. [pp. 7, 165, 171, 177, and 178]

[96] LZ collaboration, D. S. Akerib et al., *Projected sensitivities of the LUX-ZEPLIN experiment to new physics via low-energy electron recoils*, *Phys. Rev. D* **104** (2021) 092009 [`2102.11740`]. [p. 7]

[97] LZ collaboration, *First Dark Matter Search Results from the LUX-ZEPLIN (LZ) Experiment*, 2022. [pp. 7, 165, 171, 177, and 178]

[98] "Stanford Encyclopedia of Philosophy." `https://plato.stanford.edu/entries/symmetry-breaking/`. [p. 9]

[99] D. Hanneke, S. Fogwell and G. Gabrielse, *New Measurement of the Electron Magnetic Moment and the Fine Structure Constant*, *Phys. Rev. Lett.* **100** (2008) 120801 [`0801.1134`]. [p. 9]

[100] S. L. Glashow, *Partial Symmetries of Weak Interactions*, *Nucl. Phys.* **22** (1961) 579. [p. 9]

[101] A. Salam, *Weak and Electromagnetic Interactions*, *Conf. Proc. C* **680519** (1968) 367. [p. 9]

[102] S. Weinberg, *A Model of Leptons*, *Phys. Rev. Lett.* **19** (1967) 1264. [p. 9]

[103] C.-N. Yang and R. L. Mills, *Conservation of Isotopic Spin and Isotopic Gauge Invariance*, *Phys. Rev.* **96** (1954) 191. [p. 9]

[104] P. A. M. Dirac, *Quantum theory of emission and absorption of radiation*, *Proc. Roy. Soc. Lond. A* **114** (1927) 243. [p. 9]

[105] P. Jordan and W. Pauli, *Zur quantenelektrodynamik ladungsfreier felder*, *Zeitschrift für Physik* **47** 151. [p. 9]

[106] W. Heisenberg and W. Pauli, *Zur quantendynamik der wellenfelder*, *Zeitschrift für Physik* **56** 1. [p. 9]

[107] S. Tomonaga, *On a relativistically invariant formulation of the quantum theory of wave fields*, *Prog. Theor. Phys.* **1** (1946) 27. [p. 9]

[108] J. S. Schwinger, *On Quantum electrodynamics and the magnetic moment of the electron*, *Phys. Rev.* **73** (1948) 416. [p. 9]

[109] R. P. Feynman, *Space - time approach to quantum electrodynamics*, *Phys. Rev.* **76** (1949) 769. [p. 9]

[110] E. Fermi, *An attempt of a theory of beta radiation. 1.*, *Z. Phys.* **88** (1934) 161. [p. 9]

[111] R. P. Feynman and M. Gell-Mann, *Theory of Fermi interaction*, *Phys. Rev.* **109** (1958) 193. [p. 9]

[112] M. Gell-Mann, *A Schematic Model of Baryons and Mesons*, *Phys. Lett.* **8** (1964) 214. [p. 9]

[113] H. Fritzsch, M. Gell-Mann and H. Leutwyler, *Advantages of the Color Octet Gluon Picture*, *Phys. Lett. B* **47** (1973) 365. [p. 9]

[114] G. Zweig, *An SU(3) model for strong interaction symmetry and its breaking. Version 1*, . [p. 9]

[115] G. Zweig, *An SU(3) model for strong interaction symmetry and its breaking. Version 2*, pp. 22–101. 2, 1964. [p. 9]

[116] H. D. Politzer, *Reliable Perturbative Results for Strong Interactions?*, *Phys. Rev. Lett.* **30** (1973) 1346. [p. 9]

[117] D. J. Gross and F. Wilczek, *Ultraviolet Behavior of Nonabelian Gauge Theories*, *Phys. Rev. Lett.* **30** (1973) 1343. [p. 9]

[118] P. W. Higgs, *Broken Symmetries and the Masses of Gauge Bosons*, *Phys. Rev. Lett.* **13** (1964) 508. [p. 9]

[119] P. W. Higgs, *Spontaneous Symmetry Breakdown without Massless Bosons*, *Phys. Rev.* **145** (1966) 1156. [p. 9]

[120] F. Englert and R. Brout, *Broken Symmetry and the Mass of Gauge Vector Mesons*, *Phys. Rev. Lett.* **13** (1964) 321. [p. 9]

[121] G. S. Guralnik, C. R. Hagen and T. W. B. Kibble, *Global Conservation Laws and Massless Particles*, *Phys. Rev. Lett.* **13** (1964) 585. [p. 9]

[122] T. W. B. Kibble, *Symmetry breaking in nonAbelian gauge theories*, *Phys. Rev.* **155** (1967) 1554. [p. 9]

[123] A. Djouadi, *The Anatomy of electro-weak symmetry breaking. I: The Higgs boson in the standard model*, *Phys. Rept.* **457** (2008) 1 [`hep-ph/0503172`]. [p. 10]

[124] J. Ellis, *Topics in Higgs Physics*, *CERN Yellow Rep. School Proc.* **2** (2018) 1 [`1702.05436`]. [p. 10]

[125] S. Heinemeyer, *Higgs and Electroweak Physics*, in *65th Scottish Universities Summer School in Physics: LHC Physics*, pp. 37–67, 12, 2009, `0912.0361`, DOI. [p. 10]

[126] S. Dawson, C. Englert and T. Plehn, *Higgs Physics: It ain't over till it's over*, *Phys. Rept.* **816** (2019) 1 [`1808.01324`]. [pp. 10 and 16]

[127] N. Cabibbo, *Unitary Symmetry and Leptonic Decays*, *Phys. Rev. Lett.* **10** (1963) 531. [p. 12]

[128] M. Kobayashi and T. Maskawa, *CP Violation in the Renormalizable Theory of Weak Interaction*, *Prog. Theor. Phys.* **49** (1973) 652. [p. 12]

[129] LHC Higgs Cross Section Working Group collaboration, J. R. Andersen et al., *Handbook of LHC Higgs Cross Sections: 3. Higgs Properties*, `1307.1347`. [pp. 13 and 14]

[130] "LHC Higgs Working Group." `https://twiki.cern.ch/twiki/bin/view/LHCPhysics/LHCHWG`. [p. 14]

[131] T. Plehn and M. Rauch, *The quartic higgs coupling at hadron colliders*, *Phys. Rev. D* **72** (2005) 053008 [`hep-ph/0507321`]. [p. 14]

[132] J. de Blas et al., *Higgs Boson Studies at Future Particle Colliders*, *JHEP* **01** (2020) 139 [`1905.03764`]. [p. 14]

[133] ATLAS collaboration, *Constraining the Higgs boson self-coupling from single- and double-Higgs production with the ATLAS detector using pp collisions at $\sqrt{s} = 13$ TeV*, Tech. Rep. ATLAS-CONF-2022-050, Jul, 2022. [pp. 14, 41, and 93]

[134] M. Cepeda et al., *Report from Working Group 2: Higgs Physics at the HL-LHC and HE-LHC*, *CERN Yellow Rep. Monogr.* **7** (2019) 221 [`1902.00134`]. [pp. 15, 93, and 95]

[135] K. Fujii et al., *Physics Case for the 250 GeV Stage of the International Linear Collider*, `1710.07621`. [p. 15]

[136] R. Contino et al., *Physics at a 100 TeV pp collider: Higgs and EW symmetry breaking studies*, `1606.09408`. [p. 15]

[137] T. Golling et al., *Physics at a 100 TeV pp collider: beyond the Standard Model phenomena*, `1606.00947`. [p. 15]

[138] M. J. G. Veltman, *The Infrared - Ultraviolet Connection*, *Acta Phys. Polon. B* **12** (1981) 437. [pp. 15 and 19]

[139] S. Dimopoulos and H. Georgi, *Softly Broken Supersymmetry and SU(5)*, *Nucl. Phys. B* **193** (1981) 150. [pp. 15 and 19]

[140] E. Witten, *Dynamical Breaking of Supersymmetry*, *Nucl. Phys. B* **188** (1981) 513. [pp. 15 and 19]

[141] Super-Kamiokande collaboration, Y. Fukuda et al., *Evidence for oscillation of atmospheric neutrinos*, *Phys. Rev. Lett.* **81** (1998) 1562 [`hep-ex/9807003`]. [p. 15]

[142] `https://www.cosmos.esa.int/web/lisa/lisa-documents`.. [pp. 16 and 70]

[143] C. Grojean, G. Servant and J. D. Wells, *First-order electroweak phase transition in the standard model with a low cutoff*, *Phys. Rev. D* **71** (2005) 036001 [`hep-ph/0407019`]. [p. 16]

[144] M. Reichert, A. Eichhorn, H. Gies, J. M. Pawlowski, T. Plehn and M. M. Scherer, *Probing baryogenesis through the Higgs boson self-coupling*, *Phys. Rev. D* **97** (2018) 075008 [`1711.00019`]. [p. 16]

[145] D. Gonçalves, A. Kaladharan and Y. Wu, *Electroweak phase transition in the 2HDM: collider and gravitational wave complementarity*, `2108.05356`. [pp. 16, 60, 62, 71, 74, 80, 83, and 94]

[146] M. Aoki, T. Komatsu and H. Shibuya, *Possibility of multi-step electroweak phase transition in the two Higgs doublet models*, `2106.03439`. [pp. 16 and 74]

[147] F. Zwicky, *Die Rotverschiebung von extragalaktischen Nebeln*, *Helv. Phys. Acta* **6** (1933) 110. [p. 17]

[148] V. C. Rubin and W. K. Ford, Jr., *Rotation of the Andromeda Nebula from a Spectroscopic Survey of Emission Regions*, *Astrophys. J.* **159** (1970) 379. [p. 17]

[149] R. Massey, T. Kitching and J. Richard, *The dark matter of gravitational lensing*, *Rept. Prog. Phys.* **73** (2010) 086901 [`1001.1739`]. [p. 17]

[150] D. Clowe, M. Bradac, A. H. Gonzalez, M. Markevitch, S. W. Randall, C. Jones et al., *A direct empirical proof of the existence of dark matter*, *Astrophys. J. Lett.* **648** (2006) L109 [`astro-ph/0608407`]. [p. 17]

[151] A. De Simone, *Introduction to cosmology and dark matter*, *CERN Yellow Rep. School Proc.* **6** (2019) 145. [p. 17]

[152] S. Davidson, S. Hannestad and G. Raffelt, *Updated bounds on millicharged particles*, *JHEP* **05** (2000) 003 [`hep-ph/0001179`]. [p. 17]

[153] J. E. Kim, *Light Pseudoscalars, Particle Physics and Cosmology*, *Phys. Rept.* **150** (1987) 1. [p. 19]

[154] P. Fayet, *U boson interpolating between a generalized dark photon or dark Z , an axial boson, and an axionlike particle*, *Phys. Rev. D* **103** (2021) 035034 [`2010.04673`]. [p. 19]

[155] M. Frigerio, A. Pomarol, F. Riva and A. Urbano, *Composite Scalar Dark Matter*, *JHEP* **07** (2012) 015 [`1204.2808`]. [p. 19]

[156] J. Mrazek, A. Pomarol, R. Rattazzi, M. Redi, J. Serra and A. Wulzer, *The Other Natural Two Higgs Doublet Model*, *Nucl. Phys. B* **853** (2011) 1 [`1105.5403`]. [p. 19]

[157] S. De Curtis, S. Moretti, K. Yagyu and E. Yildirim, *LHC Phenomenology of Composite 2-Higgs Doublet Models*, *Eur. Phys. J. C* **77** (2017) 513 [`1610.02687`]. [p. 19]

[158] S. De Curtis, L. Delle Rose, S. Moretti and K. Yagyu, *A Concrete Composite 2-Higgs Doublet Model*, *JHEP* **12** (2018) 051 [`1810.06465`]. [p. 19]

[159] T. Vieu, A. P. Morais and R. Pasechnik, *Electroweak phase transitions in multi-Higgs models: the case of Trinification-inspired THDSM*, *JCAP* **07** (2018) 014 [`1801.02670`]. [p. 19]

[160] L. Lopez Honorez, E. Nezri, J. F. Oliver and M. H. G. Tytgat, *The Inert Doublet Model: An Archetype for Dark Matter*, *JCAP* **02** (2007) 028 [`hep-ph/0612275`]. [p. 19]

[161] I. Engeln, P. Ferreira, M. M. Mühlleitner, R. Santos and J. Wittbrodt, *The Dark Phases of the N2HDM*, *JHEP* **08** (2020) 085 [`2004.05382`]. [p. 19]

[162] A. Berlin, S. Gori, T. Lin and L.-T. Wang, *Pseudoscalar Portal Dark Matter*, *Phys. Rev. D* **92** (2015) 015005 [`1502.06000`]. [p. 19]

[163] N. F. Bell, G. Busoni and I. W. Sanderson, *Two Higgs Doublet Dark Matter Portal*, *JCAP* **01** (2018) 015 [`1710.10764`]. [p. 19]

[164] E. Ma, *Verifiable radiative seesaw mechanism of neutrino mass and dark matter*, *Phys. Rev. D* **73** (2006) 077301 [`hep-ph/0601225`]. [p. 19]

[165] G. C. Branco, P. M. Ferreira, L. Lavoura, M. N. Rebelo, M. Sher and J. P. Silva, *Theory and phenomenology of two-Higgs-doublet models*, *Phys. Rept.* **516** (2012) 1 [`1106.0034`]. [pp. 20, 22, 24, and 27]

[166] J. F. Gunion, H. E. Haber and J. Wudka, *Sum rules for Higgs bosons*, *Phys. Rev. D* **43** (1991) 904. [p. 22]

[167] J. F. Gunion and H. E. Haber, *The CP conserving two Higgs doublet model: The Approach to the decoupling limit*, *Phys. Rev. D* **67** (2003) 075019 [`hep-ph/0207010`]. [p. 22]

[168] P. S. B. Dev and A. Pilaftsis, *Natural Standard Model Alignment in the Two Higgs Doublet Model*, *J. Phys. Conf. Ser.* **631** (2015) 012030 [`1503.09140`]. [p. 22]

[169] P. S. Bhupal Dev and A. Pilaftsis, *Natural Alignment in the Two Higgs Doublet Model*, *J. Phys. Conf. Ser.* **873** (2017) 012008 [`1703.05730`]. [p. 22]

[170] S. L. Glashow, J. Iliopoulos and L. Maiani, *Weak Interactions with Lepton-Hadron Symmetry*, *Phys. Rev. D* **2** (1970) 1285. [p. 23]

[171] A. G. Akeroyd et al., *Prospects for charged Higgs searches at the LHC*, *Eur. Phys. J. C* **77** (2017) 276 [`1607.01320`]. [p. 24]

[172] G. Dorsch, S. Huber, K. Mimasu and J. No, *Echoes of the Electroweak Phase Transition: Discovering a second Higgs doublet through $A_0 \to ZH_0$*, *Phys. Rev. Lett.* **113** (2014) 211802 [`1405.5537`]. [pp. 24, 28, 71, 74, 82, 83, 90, 115, 119, 122, and 184]

[173] CMS collaboration, *Search for neutral resonances decaying into a Z boson and a pair of b jets or τ leptons*, *Phys. Lett. B* **759** (2016) 369 [`1603.02991`]. [pp. 24 and 90]

[174] ATLAS collaboration, *Search for a heavy Higgs boson decaying into a Z boson and another heavy Higgs boson in the $\ell\ell bb$ and $\ell\ell WW$ final states in pp collisions at $\sqrt{s} = 13$ TeV with the ATLAS detector*, *Eur. Phys. J. C* **81** (2021) 396 [`2011.05639`]. [pp. 24, 39, and 40]

[175] CMS collaboration, *Search for new neutral Higgs bosons through the $H\to ZA \to \ell^+\ell^-\mathrm{b}\bar{\mathrm{b}}$ process in pp collisions at $\sqrt{s} =$ 13 TeV*, *JHEP* **03** (2020) 055 [`1911.03781`]. [pp. 24 and 90]

[176] M. Muhlleitner, M. O. P. Sampaio, R. Santos and J. Wittbrodt, *The N2HDM under Theoretical and Experimental Scrutiny*, *JHEP* **03** (2017) 094 [`1612.01309`]. [pp. 25, 32, 35, 100, 101, 107, 122, 123, 138, 140, and 151]

[177] X.-G. He, T. Li, X.-Q. Li, J. Tandean and H.-C. Tsai, *Constraints on Scalar Dark Matter from Direct Experimental Searches*, *Phys. Rev. D* **79** (2009) 023521 [`0811.0658`]. [p. 25]

[178] B. Grzadkowski and P. Osland, *Tempered Two-Higgs-Doublet Model*, *Phys. Rev. D* **82** (2010) 125026 [`0910.4068`]. [p. 25]

[179] M. S. Boucenna and S. Profumo, *Direct and Indirect Singlet Scalar Dark Matter Detection in the Lepton-Specific two-Higgs-doublet Model*, *Phys. Rev. D* **84** (2011) 055011 [`1106.3368`]. [p. 25]

[180] X.-G. He, B. Ren and J. Tandean, *Hints of Standard Model Higgs Boson at the LHC and Light Dark Matter Searches*, *Phys. Rev. D* **85** (2012) 093019 [`1112.6364`]. [p. 25]

[181] Y. Bai, V. Barger, L. L. Everett and G. Shaughnessy, *Two-Higgs-doublet-portal dark-matter model: LHC data and Fermi-LAT 135 GeV line*, *Phys. Rev. D* **88** (2013) 015008 [`1212.5604`]. [p. 25]

[182] Y. Cai and T. Li, *Singlet dark matter in a type II two Higgs doublet model*, *Phys. Rev. D* **88** (2013) 115004 [`1308.5346`]. [p. 25]

[183] C.-Y. Chen, M. Freid and M. Sher, *Next-to-minimal two Higgs doublet model*, *Phys. Rev. D* **89** (2014) 075009 [`1312.3949`]. [p. 25]

[184] A. Drozd, B. Grzadkowski, J. F. Gunion and Y. Jiang, *Extending two-Higgs-doublet models by a singlet scalar field - the Case for Dark Matter*, *JHEP* **11** (2014) 105 [`1408.2106`]. [p. 25]

[185] T. Plehn, *Lectures on LHC Physics*, *Lect. Notes Phys.* **844** (2012) 1 [`0910.4182`]. [p. 30]

[186] H. G. J. Veltman, *The Equivalence Theorem*, *Phys. Rev. D* **41** (1990) 2294. [p. 31]

[187] P. Fayet, *On the Search for a New Spin 1 Boson*, *Nucl. Phys. B* **187** (1981) 184. [p. 31]

[188] G. Bhattacharyya and D. Das, *Scalar sector of two-Higgs-doublet models: A minireview*, *Pramana* **87** (2016) 40 [`1507.06424`]. [pp. 31 and 34]

[189] A. G. Akeroyd, A. Arhrib and E.-M. Naimi, *Note on tree level unitarity in the general two Higgs doublet model*, *Phys. Lett. B* **490** (2000) 119 [`hep-ph/0006035`]. [pp. 31 and 34]

[190] K. G. Klimenko, *On Necessary and Sufficient Conditions for Some Higgs Potentials to Be Bounded From Below*, *Theor. Math. Phys.* **62** (1985) 58. [pp. 32, 35, and 100]

[191] M. Maniatis, A. von Manteuffel, O. Nachtmann and F. Nagel, *Stability and symmetry breaking in the general two-Higgs-doublet model*, *Eur. Phys. J. C* **48** (2006) 805 [`hep-ph/0605184`]. [p. 32]

[192] S. R. Coleman, *The Fate of the False Vacuum. 1. Semiclassical Theory*, *Phys. Rev. D* **15** (1977) 2929. [pp. 32 and 59]

[193] C. G. Callan, Jr. and S. R. Coleman, *The Fate of the False Vacuum. 2. First Quantum Corrections*, *Phys. Rev. D* **16** (1977) 1762. [pp. 32 and 59]

[194] M. Shifman, *Advanced topics in quantum field theory.: A lecture course.* Cambridge Univ. Press, Cambridge, UK, 2, 2012. [p. 33]

[195] V. A. Rubakov, *Classical theory of gauge fields.* Princeton University Press, Princeton, New Jersey, 5, 2002. [p. 33]

[196] C. L. Wainwright, *CosmoTransitions: Computing Cosmological Phase Transition Temperatures and Bubble Profiles with Multiple Fields*, *Comput. Phys. Commun.* **183** (2012) 2006 [`1109.4189`]. [pp. 33, 74, 103, and 110]

[197] J. Wittbrodt, *Exploring Models of Electroweak Symmetry Breaking at the LHC and Beyond*, Ph.D. thesis, Hamburg U., Hamburg, 2019. 10.3204/PUBDB-2019-03809. [p. 34]

[198] W. G. Hollik, G. Weiglein and J. Wittbrodt, *Impact of Vacuum Stability Constraints on the Phenomenology of Supersymmetric Models*, *JHEP* **03** (2019) 109 [`1812.04644`]. [pp. 34 and 100]

[199] P. M. Ferreira, M. Mühlleitner, R. Santos, G. Weiglein and J. Wittbrodt, *Vacuum Instabilities in the N2HDM*, *JHEP* **09** (2019) 006 [`1905.10234`]. [pp. 34, 35, 119, and 138]

[200] N. G. Deshpande and E. Ma, *Pattern of Symmetry Breaking with Two Higgs Doublets*, *Phys. Rev. D* **18** (1978) 2574. [p. 34]

[201] A. Barroso, P. M. Ferreira, I. P. Ivanov and R. Santos, *Metastability bounds on the two Higgs doublet model*, *JHEP* **06** (2013) 045 [`1303.5098`]. [pp. 34, 35, and 76]

[202] F. Staub, *Reopen parameter regions in Two-Higgs Doublet Models*, *Phys. Lett. B* **776** (2018) 407 [`1705.03677`]. [pp. 36 and 75]

[203] K. Matchev, *TASI lectures on precision electroweak physics*, in *Theoretical Advanced Study Institute in Elementary Particle Physics (TASI 2002): Particle Physics and Cosmology: The Quest for Physics Beyond the Standard Model(s)*, pp. 51–98, 1, 2004, `hep-ph/0402031`. [p. 37]

[204] M. E. Peskin and T. Takeuchi, *A New constraint on a strongly interacting Higgs sector*, *Phys. Rev. Lett.* **65** (1990) 964. [pp. 37 and 101]

[205] M. E. Peskin and T. Takeuchi, *Estimation of oblique electroweak corrections*, *Phys. Rev. D* **46** (1992) 381. [pp. 37 and 101]

[206] W. Grimus, L. Lavoura, O. M. Ogreid and P. Osland, *A Precision constraint on multi-Higgs-doublet models*, *J. Phys. G* **35** (2008) 075001 [`0711.4022`]. [pp. 37, 72, 102, and 140]

[207] W. Grimus, L. Lavoura, O. M. Ogreid and P. Osland, *The Oblique parameters in multi-Higgs-doublet models*, *Nucl. Phys. B* **801** (2008) 81 [`0802.4353`]. [pp. 37, 72, 102, and 140]

[208] CDF collaboration, T. Aaltonen et al., *High-precision measurement of the W boson mass with the CDF II detector*, *Science* **376** (2022) 170. [pp. 38 and 72]

[209] A. Arbey, F. Mahmoudi, O. Stal and T. Stefaniak, *Status of the Charged Higgs Boson in Two Higgs Doublet Models*, *Eur. Phys. J. C* **78** (2018) 182 [`1706.07414`]. [p. 38]

[210] J. Haller, A. Hoecker, R. Kogler, K. Mönig, T. Peiffer and J. Stelzer, *Update of the global electroweak fit and constraints on two-Higgs-doublet models*, *Eur. Phys. J. C* **78** (2018) 675 [`1803.01853`]. [pp. 38, 72, 74, 100, 102, 115, 140, 141, 149, and 152]

[211] M. Misiak and M. Steinhauser, *Weak radiative decays of the B meson and bounds on $M_{H^\pm}$ in the Two-Higgs-Doublet Model*, *Eur. Phys. J. C* **77** (2017) 201 [`1702.04571`]. [p. 38]

[212] ATLAS collaboration, *Search for low-mass resonances decaying into two jets and produced in association with a photon using pp collisions at $\sqrt{s} = 13$ TeV with the ATLAS detector*, *Phys. Lett. B* **795** (2019) 56 [`1901.10917`]. [p. 39]

[213] CMS collaboration, *Search for heavy Higgs bosons decaying to a top quark pair in proton-proton collisions at $\sqrt{s} = 13$ TeV*, *JHEP* **04** (2020) 171 [`1908.01115`]. [pp. 39 and 40]

[214] CMS collaboration, *Search for a new scalar resonance decaying to a pair of Z bosons in proton-proton collisions at $\sqrt{s} = 13$ TeV*, *JHEP* **06** (2018) 127 [`1804.01939`]. [pp. 39 and 40]

[215] CMS collaboration, *Update on the search for the standard model Higgs boson in pp collisions at the LHC decaying to W + W in the fully leptonic final state*, . [p. 39]

[216] ALEPH, DELPHI, L3, OPAL, LEP WORKING GROUP FOR HIGGS BOSON SEARCHES collaboration, S. Schael et al., *Search for neutral MSSM Higgs bosons at LEP*, *Eur. Phys. J. C* **47** (2006) 547 [`hep-ex/0602042`]. [p. 40]

[217] ATLAS collaboration, *Combination of searches for heavy resonances decaying into bosonic and leptonic final states using 36 fb^{-1} of proton-proton collision data at $\sqrt{s} = 13$ TeV with the ATLAS detector*, *Phys. Rev. D* **98** (2018) 052008 [`1808.02380`]. [p. 40]

[218] CMS collaboration, *Search for a Higgs boson in the mass range from 145 to 1000 GeV decaying to a pair of W or Z bosons*, *JHEP* **10** (2015) 144 [`1504.00936`]. [p. 40]

[219] ATLAS collaboration, *Search for heavy ZZ resonances in the $\ell^+\ell^-\ell^+\ell^-$ and $\ell^+\ell^-\nu\bar{\nu}$ final states using proton–proton collisions at $\sqrt{s} = 13$ TeV with the ATLAS detector*, *Eur. Phys. J. C* **78** (2018) 293 [`1712.06386`]. [p. 40]

[220] ATLAS collaboration, *Search for heavy Higgs bosons decaying into two tau leptons with the ATLAS detector using pp collisions at $\sqrt{s} = 13$ TeV*, *Phys. Rev. Lett.* **125** (2020) 051801 [`2002.12223`]. [p. 40]

[221] ATLAS collaboration, *Search for pair production of Higgs bosons in the $b\bar{b}b\bar{b}$ final state using proton-proton collisions at $\sqrt{s} = 13$ TeV with the ATLAS detector*, *JHEP* **01** (2019) 030 [`1804.06174`]. [p. 40]

[222] CMS collaboration, *Search for a heavy pseudoscalar boson decaying to a Z and a Higgs boson at $\sqrt{s} = 13$ TeV*, *Eur. Phys. J. C* **79** (2019) 564 [`1903.00941`]. [p. 40]

[223] ATLAS collaboration, *Search for charged Higgs bosons decaying into a top quark and a bottom quark at $\sqrt{\mathrm{s}} = 13$ TeV with the ATLAS detector*, *JHEP* **06** (2021) 145 [`2102.10076`]. [pp. 40 and 151]

[224] ATLAS collaboration, *Combination of searches for Higgs boson pairs in pp collisions at $\sqrt{s}$ =13 TeV with the ATLAS detector*, *Phys. Lett. B* **800** (2020) 135103 [`1906.02025`]. [p. 40]

[225] ATLAS collaboration, *Observation of a new particle in the search for the Standard Model Higgs boson with the ATLAS detector at the LHC*, *Phys. Lett. B* **716** (2012) 1 [`1207.7214`]. [p. 40]

[226] CMS collaboration, *Observation of a New Boson at a Mass of 125 GeV with the CMS Experiment at the LHC*, *Phys. Lett. B* **716** (2012) 30 [`1207.7235`]. [p. 40]

[227] ATLAS, CMS collaboration, M. Moreno Llácer, *Higgs CP studies at ATLAS and CMS experiments*, *PoS* **LHCP2021** (2021) 071. [p. 40]

[228] CMS collaboration, *A portrait of the Higgs boson by the CMS experiment ten years after the discovery*, *Nature* **607** (2022) 60 [`2207.00043`]. [pp. 41 and 93]

[229] ATLAS collaboration, *Combination of searches for invisible Higgs boson decays with the ATLAS experiment*, *ATLAS-CONF-2020-052* (2020) . [pp. 41, 140, and 153]

[230] LIGO Scientific, Virgo collaboration, B. P. Abbott et al., *Observation of Gravitational Waves from a Binary Black Hole Merger*, *Phys. Rev. Lett.* **116** (2016) 061102 [`1602.03837`]. [p. 45]

[231] LIGO Scientific, Virgo collaboration, B. P. Abbott et al., *GW170817: Observation of Gravitational Waves from a Binary Neutron Star Inspiral*, *Phys. Rev. Lett.* **119** (2017) 161101 [`1710.05832`]. [p. 45]

[232] LIGO Scientific, Virgo collaboration, B. P. Abbott et al., *GW151226: Observation of Gravitational Waves from a 22-Solar-Mass Binary Black Hole Coalescence*, *Phys. Rev. Lett.* **116** (2016) 241103 [`1606.04855`]. [p. 45]

[233] M. E. Shaposhnikov, *Finite temperature effective theories*, *Subnucl. Ser.* **34** (1997) 360 [`hep-ph/9610247`]. [pp. 45, 48, and 54]

[234] H. Lehmann, K. Symanzik and W. Zimmermann, *On the formulation of quantized field theories*, *Nuovo Cim.* **1** (1955) 205. [p. 46]

[235] G. Arutyunov, *Quantizing Fields.* 2021. [p. 46]

[236] M. Quiros, *Finite temperature field theory and phase transitions*, in *ICTP Summer School in High-Energy Physics and Cosmology*, pp. 187–259, 1, 1999, `hep-ph/9901312`. [pp. 48, 50, 53, 54, 82, and 120]

[237] C. Scrucca, *Advanced Quantum Field Theory.* [p. 48]

[238] N. P. Landsman and C. G. van Weert, *Real and Imaginary Time Field Theory at Finite Temperature and Density*, *Phys. Rept.* **145** (1987) 141. [p. 48]

[239] C. Delaunay, C. Grojean and J. D. Wells, *Dynamics of Non-renormalizable Electroweak Symmetry Breaking*, *JHEP* **04** (2008) 029 [`0711.2511`]. [pp. 48 and 55]

[240] S. R. Coleman and E. J. Weinberg, *Radiative Corrections as the Origin of Spontaneous Symmetry Breaking*, *Phys. Rev. D* **7** (1973) 1888. [p. 52]

[241] N. Nielsen, *On the Gauge Dependence of Spontaneous Symmetry Breaking in Gauge Theories*, *Nucl. Phys. B* **101** (1975) 173. [p. 53]

[242] I. Aitchison and C. Fraser, *Gauge Invariance and the Effective Potential*, *Annals Phys.* **156** (1984) 1. [p. 53]

[243] H. H. Patel and M. J. Ramsey-Musolf, *Baryon Washout, Electroweak Phase Transition, and Perturbation Theory*, *JHEP* **07** (2011) 029 [`1101.4665`]. [pp. 53, 73, 82, and 88]

[244] P. Basler, M. Krause, M. Muhlleitner, J. Wittbrodt and A. Wlotzka, *Strong First Order Electroweak Phase Transition in the CP-Conserving 2HDM Revisited*, *JHEP* **02** (2017) 121 [`1612.04086`]. [pp. 53, 71, 74, 82, 102, 103, 119, 121, 122, 125, and 127]

[245] P. Basler, M. Mühlleitner and J. Müller, *Electroweak Phase Transition in Non-Minimal Higgs Sectors*, *JHEP* **05** (2020) 016 [`1912.10477`]. [pp. 53, 82, 103, 104, 120, and 121]

[246] J. E. Camargo-Molina, A. P. Morais, R. Pasechnik, M. O. P. Sampaio and J. Wessén, *All one-loop scalar vertices in the effective potential approach*, *JHEP* **08** (2016) 073 [`1606.07069`]. [p. 53]

[247] L. Dolan and R. Jackiw, *Symmetry Behavior at Finite Temperature*, *Phys. Rev. D* **9** (1974) 3320. [pp. 53 and 73]

[248] M. Carrington, *The Effective potential at finite temperature in the Standard Model*, *Phys. Rev. D* **45** (1992) 2933. [pp. 54 and 102]

[249] D. J. Gross, R. D. Pisarski and L. G. Yaffe, *QCD and Instantons at Finite Temperature*, *Rev. Mod. Phys.* **53** (1981) 43. [p. 54]

[250] R. R. Parwani, *Resummation in a hot scalar field theory*, *Phys. Rev. D* **45** (1992) 4695 [`hep-ph/9204216`]. [p. 54]

[251] P. B. Arnold and O. Espinosa, *The Effective potential and first order phase transitions: Beyond leading-order*, *Phys. Rev. D* **47** (1993) 3546 [`hep-ph/9212235`]. [pp. 54, 55, and 102]

[252] D. Croon, O. Gould, P. Schicho, T. V. I. Tenkanen and G. White, *Theoretical uncertainties for cosmological first-order phase transitions*, `2009.10080`. [p. 56]

[253] P. M. Schicho, T. V. I. Tenkanen and J. Österman, *Robust approach to thermal resummation: Standard Model meets a singlet*, `2102.11145`. [p. 56]

[254] V. A. Rubakov and D. S. Gorbunov, *Introduction to the Theory of the Early Universe: Hot big bang theory*. World Scientific, Singapore, 2017, 10.1142/10447. [p. 58]

[255] M. Gleiser and A. F. Heckler, *Nonperturbative effects on nucleation*, *Phys. Rev. Lett.* **76** (1996) 180 [`hep-ph/9509347`]. [p. 58]

[256] M. Hindmarsh, S. J. Huber, K. Rummukainen and D. J. Weir, *Numerical simulations of acoustically generated gravitational waves at a first order phase transition*, *Phys. Rev. D* **92** (2015) 123009 [`1504.03291`]. [pp. 59 and 68]

[257] D. J. Weir, *Gravitational waves from a first order electroweak phase transition: a brief review*, *Phil. Trans. Roy. Soc. Lond. A* **376** (2018) 20170126 [`1705.01783`]. [p. 59]

[258] A. D. Linde, *Fate of the False Vacuum at Finite Temperature: Theory and Applications*, *Phys. Lett. B* **100** (1981) 37. [p. 59]

[259] A. D. Linde, *Decay of the False Vacuum at Finite Temperature*, *Nucl. Phys. B* **216** (1983) 421. [p. 59]

[260] J. Espinosa, T. Konstandin, J. No and M. Quiros, *Some Cosmological Implications of Hidden Sectors*, *Phys. Rev. D* **78** (2008) 123528 [`0809.3215`]. [p. 59]

[261] S. Kanemura and M. Tanaka, *Strongly first-order electroweak phase transition by relatively heavy additional Higgs bosons*, `2201.04791`. [p. 60]

[262] F. Giese, T. Konstandin and J. van de Vis, *Model-independent energy budget of cosmological first-order phase transitions—A sound argument to go beyond the bag model*, *JCAP* **07** (2020) 057 [`2004.06995`]. [p. 60]

[263] J. Ellis, M. Lewicki and J. M. No, *On the Maximal Strength of a First-Order Electroweak Phase Transition and its Gravitational Wave Signal*, *JCAP* **04** (2019) 003 [`1809.08242`]. [pp. 60 and 89]

[264] D. Bodeker and G. D. Moore, *Can electroweak bubble walls run away?*, *JCAP* **05** (2009) 009 [`0903.4099`]. [p. 60]

[265] D. Bodeker and G. D. Moore, *Electroweak Bubble Wall Speed Limit*, *JCAP* **05** (2017) 025 [`1703.08215`]. [p. 60]

[266] S. Höche, J. Kozaczuk, A. J. Long, J. Turner and Y. Wang, *Towards an all-orders calculation of the electroweak bubble wall velocity*, *JCAP* **03** (2021) 009 [`2007.10343`]. [p. 60]

[267] G. D. Moore and T. Prokopec, *How fast can the wall move? A Study of the electroweak phase transition dynamics*, *Phys. Rev. D* **52** (1995) 7182 [`hep-ph/9506475`]. [p. 61]

[268] T. Konstandin, G. Nardini and I. Rues, *From Boltzmann equations to steady wall velocities*, *JCAP* **09** (2014) 028 [`1407.3132`]. [p. 61]

[269] J. Kozaczuk, *Bubble Expansion and the Viability of Singlet-Driven Electroweak Baryogenesis*, *JHEP* **10** (2015) 135 [`1506.04741`]. [p. 61]

[270] G. C. Dorsch, S. J. Huber and T. Konstandin, *Bubble wall velocities in the Standard Model and beyond*, *JCAP* **12** (2018) 034 [`1809.04907`]. [p. 61]

[271] M. Barroso Mancha, T. Prokopec and B. Swiezewska, *Field-theoretic derivation of bubble-wall force*, *JHEP* **01** (2021) 070 [`2005.10875`]. [p. 61]

[272] B. Laurent and J. M. Cline, *Fluid equations for fast-moving electroweak bubble walls*, *Phys. Rev. D* **102** (2020) 063516 [`2007.10935`]. [p. 61]

[273] G. C. Dorsch, S. J. Huber and T. Konstandin, *A sonic boom in bubble wall friction*, *JCAP* **04** (2022) 010 [`2112.12548`]. [p. 61]

[274] W.-Y. Ai, B. Garbrecht and C. Tamarit, *Bubble wall velocities in local equilibrium*, *JCAP* **03** (2022) 015 [`2109.13710`]. [p. 61]

[275] M. Lewicki, M. Merchand and M. Zych, *Electroweak bubble wall expansion: gravitational waves and baryogenesis in Standard Model-like thermal plasma*, *JHEP* **02** (2022) 017 [`2111.02393`]. [pp. 61 and 70]

[276] B. Laurent and J. M. Cline, *First principles determination of bubble wall velocity*, `2204.13120`. [pp. 61 and 70]

[277] D. E. Morrissey and M. J. Ramsey-Musolf, *Electroweak baryogenesis*, *New J. Phys.* **14** (2012) 125003 [`1206.2942`]. [p. 61]

[278] M. Garny and T. Konstandin, *On the gauge dependence of vacuum transitions at finite temperature*, *JHEP* **07** (2012) 189 [`1205.3392`]. [pp. 62 and 73]

[279] S. Baum, M. Carena, N. R. Shah, C. E. Wagner and Y. Wang, *Nucleation is More than Critical – A Case Study of the Electroweak Phase Transition in the NMSSM*, `2009.10743`. [pp. 62, 73, 80, 104, and 121]

[280] J. M. Cline, G. D. Moore and G. Servant, *Was the electroweak phase transition preceded by a color broken phase?*, *Phys. Rev. D* **60** (1999) 105035 [`hep-ph/9902220`]. [p. 62]

[281] M. Carena, C. Krause, Z. Liu and Y. Wang, *New approach to electroweak symmetry nonrestoration*, *Phys. Rev. D* **104** (2021) 055016 [`2104.00638`]. [pp. 62, 73, and 79]

[282] J. A. Harvey, E. W. Kolb, D. B. Reiss and S. Wolfram, *Calculation of Cosmological Baryon Asymmetry in Grand Unified Gauge Models*, *Nucl. Phys. B* **201** (1982) 16. [p. 63]

[283] S. Weinberg, *Cosmological Production of Baryons*, *Phys. Rev. Lett.* **42** (1979) 850. [p. 63]

[284] D. V. Nanopoulos and S. Weinberg, *Mechanisms for Cosmological Baryon Production*, *Phys. Rev. D* **20** (1979) 2484. [p. 63]

[285] A. Y. Ignatiev, N. V. Krasnikov, V. A. Kuzmin and A. N. Tavkhelidze, *Universal CP Noninvariant Superweak Interaction and Baryon Asymmetry of the Universe*, *Phys. Lett. B* **76** (1978) 436. [p. 63]

[286] M. Yoshimura, *Origin of Cosmological Baryon Asymmetry*, *Phys. Lett. B* **88** (1979) 294. [p. 63]

[287] C. Caprini and D. G. Figueroa, *Cosmological Backgrounds of Gravitational Waves*, *Class. Quant. Grav.* **35** (2018) 163001 [`1801.04268`]. [p. 63]

[288] M. Kamionkowski, A. Kosowsky and M. S. Turner, *Gravitational radiation from first order phase transitions*, *Phys. Rev. D* **49** (1994) 2837 [`astro-ph/9310044`]. [p. 66]

[289] R. Caldwell et al., *Detection of Early-Universe Gravitational Wave Signatures and Fundamental Physics*, `2203.07972`. [p. 67]

[290] M. Hindmarsh, S. J. Huber, K. Rummukainen and D. J. Weir, *Shape of the acoustic gravitational wave power spectrum from a first order phase transition*, *Phys. Rev. D* **96** (2017) 103520 [`1704.05871`]. [p. 68]

[291] M. Hindmarsh, *Sound shell model for acoustic gravitational wave production at a first-order phase transition in the early Universe*, *Phys. Rev. Lett.* **120** (2018) 071301 [`1608.04735`]. [p. 68]

[292] M. Hindmarsh and M. Hijazi, *Gravitational waves from first order cosmological phase transitions in the Sound Shell Model*, *JCAP* **12** (2019) 062 [`1909.10040`]. [p. 68]

[293] J. R. Espinosa, T. Konstandin, J. M. No and G. Servant, *Energy Budget of Cosmological First-order Phase Transitions*, *JCAP* **06** (2010) 028 [`1004.4187`]. [p. 68]

[294] J. Ellis, M. Lewicki and J. M. No, *Gravitational waves from first-order cosmological phase transitions: lifetime of the sound wave source*, *JCAP* **07** (2020) 050 [`2003.07360`]. [p. 68]

[295] C. Caprini, R. Durrer and G. Servant, *The stochastic gravitational wave background from turbulence and magnetic fields generated by a first-order phase transition*, *JCAP* **12** (2009) 024 [`0909.0622`]. [p. 69]

[296] A. Brandenburg, T. Kahniashvili, S. Mandal, A. Roper Pol, A. G. Tevzadze and T. Vachaspati, *Evolution of hydromagnetic turbulence from the electroweak phase transition*, *Phys. Rev. D* **96** (2017) 123528 [`1711.03804`]. [p. 69]

[297] A. Roper Pol, S. Mandal, A. Brandenburg, T. Kahniashvili and A. Kosowsky, *Numerical simulations of gravitational waves from early-universe turbulence*, *Phys. Rev. D* **102** (2020) 083512 [`1903.08585`]. [p. 69]

[298] P. Auclair, C. Caprini, D. Cutting, M. Hindmarsh, K. Rummukainen, D. A. Steer et al., *Generation of gravitational waves from freely decaying turbulence*, `2205.02588`. [p. 69]

[299] D. Cutting, M. Hindmarsh and D. J. Weir, *Vorticity, kinetic energy, and suppressed gravitational wave production in strong first order phase transitions*, *Phys. Rev. Lett.* **125** (2020) 021302 [`1906.00480`]. [p. 69]

[300] E. Thrane and J. D. Romano, *Sensitivity curves for searches for gravitational-wave backgrounds*, *Phys. Rev. D* **88** (2013) 124032 [`1310.5300`]. [p. 69]

[301] G. Dorsch, S. Huber and J. No, *A strong electroweak phase transition in the 2HDM after LHC8*, *JHEP* **10** (2013) 029 [`1305.6610`]. [pp. 71, 115, 119, and 122]

[302] G. Dorsch, S. Huber, K. Mimasu and J. No, *The Higgs Vacuum Uplifted: Revisiting the Electroweak Phase Transition with a Second Higgs Doublet*, *JHEP* **12** (2017) 086 [`1705.09186`]. [pp. 71, 82, 83, 93, 115, 122, and 127]

[303] J. Bernon, L. Bian and Y. Jiang, *A new insight into the phase transition in the early Universe with two Higgs doublets*, *JHEP* **05** (2018) 151 [`1712.08430`]. [pp. 71, 82, 119, and 125]

[304] A. Noble and M. Perelstein, *Higgs self-coupling as a probe of electroweak phase transition*, *Phys. Rev. D* **78** (2008) 063518 [`0711.3018`]. [pp. 71 and 92]

[305] P. Huang, A. Joglekar, B. Li and C. E. M. Wagner, *Probing the Electroweak Phase Transition at the LHC*, *Phys. Rev. D* **93** (2016) 055049 [`1512.00068`]. [pp. 71 and 92]

[306] R. Coimbra, M. O. Sampaio and R. Santos, *ScannerS: Constraining the phase diagram of a complex scalar singlet at the LHC*, *Eur. Phys. J. C* **73** (2013) 2428 [`1301.2599`]. [pp. 72 and 99]

[307] M. Mühlleitner, M. O. Sampaio, R. Santos and J. Wittbrodt, *ScannerS: Parameter Scans in Extended Scalar Sectors*, `2007.02985`. [pp. 72, 99, and 100]

[308] P. Bechtle, S. Heinemeyer, O. Stål, T. Stefaniak and G. Weiglein, *HiggsSignals: Confronting arbitrary Higgs sectors with measurements at the Tevatron and the LHC*, *Eur. Phys. J.* **C74** (2014) 2711 [`1305.1933`]. [pp. 72, 101, and 139]

[309] O. Stål and T. Stefaniak, *Constraining extended Higgs sectors with HiggsSignals*, *PoS* **EPS-HEP2013** (2013) 314 [`1310.4039`]. [pp. 72, 101, and 139]

[310] P. Bechtle, S. Heinemeyer, O. Stål, T. Stefaniak and G. Weiglein, *Probing the Standard Model with Higgs signal rates from the Tevatron, the LHC and a future ILC*, *JHEP* **11** (2014) 039 [`1403.1582`]. [pp. 72, 101, and 139]

[311] P. Bechtle, S. Heinemeyer, T. Klingl, T. Stefaniak, G. Weiglein and J. Wittbrodt, *HiggsSignals-2: Probing new physics with precision Higgs measurements in the LHC 13 TeV era*, `2012.09197`. [pp. 72, 101, and 139]

[312] P. Bechtle, O. Brein, S. Heinemeyer, G. Weiglein and K. E. Williams, *HiggsBounds: Confronting Arbitrary Higgs Sectors with Exclusion Bounds from LEP and the Tevatron*, *Comput. Phys. Commun.* **181** (2010) 138 [`0811.4169`]. [pp. 72, 101, and 139]

[313] P. Bechtle, O. Brein, S. Heinemeyer, G. Weiglein and K. E. Williams, *HiggsBounds 2.0.0: Confronting Neutral and Charged Higgs Sector Predictions with Exclusion Bounds from LEP and the Tevatron*, *Comput. Phys. Commun.* **182** (2011) 2605 [`1102.1898`]. [pp. 72, 101, and 139]

[314] P. Bechtle, O. Brein, S. Heinemeyer, O. Stål, T. Stefaniak, G. Weiglein et al., *Recent Developments in HiggsBounds and a Preview of HiggsSignals*, *PoS* **CHARGED2012** (2012) 024 [`1301.2345`]. [pp. 72, 101, and 139]

[315] P. Bechtle, O. Brein, S. Heinemeyer, O. Stål, T. Stefaniak, G. Weiglein et al., HiggsBounds − 4*: Improved Tests of Extended Higgs Sectors against Exclusion Bounds from LEP, the Tevatron and the LHC*, *Eur. Phys. J.* **C74** (2014) 2693 [`1311.0055`]. [pp. 72, 101, and 139]

[316] P. Bechtle, D. Dercks, S. Heinemeyer, T. Klingl, T. Stefaniak, G. Weiglein et al., *HiggsBounds-5: Testing Higgs Sectors in the LHC 13 TeV Era*, *Eur. Phys. J. C* **80** (2020) 1211 [`2006.06007`]. [pp. 72 and 139]

[317] R. V. Harlander, S. Liebler and H. Mantler, *SusHi: A program for the calculation of Higgs production in gluon fusion and bottom-quark annihilation in the Standard Model and the MSSM*, *Comput. Phys. Commun.* **184** (2013) 1605 [`1212.3249`]. [pp. 72, 91, and 122]

[318] I. Engeln, M. Mühlleitner and J. Wittbrodt, *N2HDECAY: Higgs Boson Decays in the Different Phases of the N2HDM*, *Comput. Phys. Commun.* **234** (2019) 256 [`1805.00966`]. [pp. 72, 91, 101, 122, and 140]

[319] P. Basler and M. Mühlleitner, *BSMPT (Beyond the Standard Model Phase Transitions): A tool for the electroweak phase transition in extended Higgs sectors*, *Comput. Phys. Commun.* **237** (2019) 62 [`1803.02846`]. [pp. 72, 98, 103, and 104]

[320] P. Basler, M. Muhlleitner and J. Müller, *BSMPT v2 A Tool for the Electroweak Phase Transition and the Baryon Asymmetry of the Universe in Extended Higgs Sectors*, `2007.01725`. [p. 72]

[321] C. Wainwright, S. Profumo and M. J. Ramsey-Musolf, *Gravity Waves from a Cosmological Phase Transition: Gauge Artifacts and Daisy Resummations*, *Phys. Rev. D* **84** (2011) 023521 [`1104.5487`]. [p. 73]

[322] J. Oredsson, *2HDME : Two-Higgs-Doublet Model Evolver*, *Comput. Phys. Commun.* **244** (2019) 409 [`1811.08215`]. [p. 73]

[323] L. Niemi, M. J. Ramsey-Musolf, T. V. I. Tenkanen and D. J. Weir, *Thermodynamics of a Two-Step Electroweak Phase Transition*, *Phys. Rev. Lett.* **126** (2021) 171802 [`2005.11332`]. [p. 77]

[324] O. Matsedonskyi, *High-Temperature Electroweak Symmetry Breaking by SM Twins*, *JHEP* **04** (2021) 036 [`2008.13725`]. [p. 79]

[325] D. Bodeker and W. Buchmuller, *Baryogenesis from the weak scale to the grand unification scale*, *Rev. Mod. Phys.* **93** (2021) 035004 [`2009.07294`]. [p. 79]

[326] O. Matsedonskyi, J. Unwin and Q. Wang, *Electroweak symmetry non-restoration from dark matter*, *JHEP* **12** (2021) 167 [`2107.07560`]. [p. 79]

[327] J. M. Cline and K. Kainulainen, *Improved Electroweak Phase Transition with Subdominant Inert Doublet Dark Matter*, *Phys. Rev. D* **87** (2013) 071701 [`1302.2614`]. [p. 82]

[328] P. Basler, M. Mühlleitner and J. Wittbrodt, *The CP-Violating 2HDM in Light of a Strong First Order Electroweak Phase Transition and Implications for Higgs Pair Production*, *JHEP* **03** (2018) 061 [`1711.04097`]. [p. 82]

[329] S. Fabian, F. Goertz and Y. Jiang, *Dark matter and nature of electroweak phase transition with an inert doublet*, *JCAP* **09** (2021) 011 [`2012.12847`]. [p. 82]

[330] W. Su, A. G. Williams and M. Zhang, *Strong first order electroweak phase transition in 2HDM confronting future Z & Higgs factories*, *JHEP* **04** (2021) 219 [`2011.04540`]. [p. 82]

[331] M. Gabelmann, M. M. Mühlleitner and J. Müller, *Electroweak phase transitions with BSM fermions*, *JHEP* **01** (2022) 012 [`2107.09617`]. [p. 82]

[332] O. Atkinson, M. Black, A. Lenz, A. Rusov and J. Wynne, *Cornering the Two Higgs Doublet Model Type II*, `2107.05650`. [p. 82]

[333] O. Atkinson, M. Black, C. Englert, A. Lenz, A. Rusov and J. Wynne, *The Flavourful Present and Future of 2HDMs at the Collider Energy Frontier*, `2202.08807`. [p. 82]

[334] L. S. Friedrich, M. J. Ramsey-Musolf, T. V. I. Tenkanen and V. Q. Tran, *Addressing the Gravitational Wave - Collider Inverse Problem*, `2203.05889`. [p. 85]

[335] P. Basler, P. M. Ferreira, M. Mühlleitner and R. Santos, *High scale impact in alignment and decoupling in two-Higgs doublet models*, *Phys. Rev. D* **97** (2018) 095024 [`1710.10410`]. [pp. 89 and 99]

[336] ATLAS collaboration, *Search for a heavy Higgs boson decaying into a Z boson and another heavy Higgs boson in the $\ell\ell bb$ final state in pp collisions at $\sqrt{s} = 13$ TeV with the ATLAS detector*, *Phys. Lett. B* **783** (2018) 392 [`1804.01126`]. [p. 90]

[337] U. Haisch and G. Polesello, *Searching for heavy Higgs bosons in the $t\bar{t}Z$ and tbW final states*, *JHEP* **09** (2018) 151 [`1807.07734`]. [pp. 90 and 123]

[338] D. Gonçalves, A. Kaladharan and Y. Wu, *Resonant top pair searches at the LHC: a window to electroweak phase transition*, `2206.08381`. [p. 90]

[339] R. Kuesters, T. Moskalets and S. Argyropoulos, *Search for $A \to ZH \to \ell\ell tt$ at $\sqrt{2} = 13$ TeV with the ATLAS detector, Contribution to: DPG Spring Meeting*, 2022. [p. 91]

[340] D. Hundhausen, K. De Leo, Y. Fischer, J. Haller and M. Schroeder, *Search for heavy Higgs bosons in the $Z + t\bar{t}$ final state with CMS, Contribution to: DPG Spring Meeting*, 2022. [p. 91]

[341] Y. Fischer, *Search for heavy Higgs bosons in the $Z + t\bar{t}$ final state with the CMS detector*, Master's thesis, Universität Hamburg, 2021. [p. 91]

[342] A. Ashoorioon and T. Konstandin, *Strong electroweak phase transitions without collider traces*, *JHEP* **07** (2009) 086 [`0904.0353`]. [p. 92]

[343] C. F. Dürig, *Measuring the Higgs Self-coupling at the International Linear Collider*, Ph.D. thesis, Hamburg U., Hamburg, 2016. 10.3204/PUBDB-2016-04283. [pp. 93, 95, and 96]

[344] H. Bahl, J. Braathen and G. Weiglein, *New constraints on extended Higgs sectors from the trilinear Higgs coupling*, `2202.03453`. [p. 95]

[345] R. Frederix, S. Frixione, V. Hirschi, F. Maltoni, O. Mattelaer, P. Torrielli et al., *Higgs pair production at the LHC with NLO and parton-shower effects*, *Phys. Lett. B* **732** (2014) 142 [`1401.7340`]. [p. 95]

[346] LCC PHYSICS WORKING GROUP collaboration, K. Fujii et al., *Tests of the Standard Model at the International Linear Collider*, `1908.11299`. [p. 96]

[347] F. Staub, *SARAH 4 : A tool for (not only SUSY) model builders*, *Comput. Phys. Commun.* **185** (2014) 1773 [`1309.7223`]. [pp. 99, 139, and 169]

[348] I. Schienbein, F. Staub, T. Steudtner and K. Svirina, *Revisiting RGEs for general gauge theories*, *Nucl. Phys. B* **939** (2019) 1 [`1809.06797`]. [pp. 99 and 139]

[349] M. E. Machacek and M. T. Vaughn, *Two Loop Renormalization Group Equations in a General Quantum Field Theory. 1. Wave Function Renormalization*, *Nucl. Phys. B* **222** (1983) 83. [pp. 99 and 139]

[350] M. E. Machacek and M. T. Vaughn, *Two Loop Renormalization Group Equations in a General Quantum Field Theory. 2. Yukawa Couplings*, *Nucl. Phys. B* **236** (1984) 221. [pp. 99 and 139]

[351] M. E. Machacek and M. T. Vaughn, *Two Loop Renormalization Group Equations in a General Quantum Field Theory. 3. Scalar Quartic Couplings*, *Nucl. Phys. B* **249** (1985) 70. [pp. 99 and 139]

[352] L. Sartore and I. Schienbein, *PyR@TE 3*, `2007.12700`. [pp. 99 and 139]

[353] P. Ferreira, H. E. Haber and E. Santos, *Preserving the validity of the Two-Higgs Doublet Model up to the Planck scale*, *Phys. Rev. D* **92** (2015) 033003 [`1505.04001`]. [p. 99]

[354] T. Robens, T. Stefaniak and J. Wittbrodt, *Two-real-scalar-singlet extension of the SM: LHC phenomenology and benchmark scenarios*, *Eur. Phys. J. C* **80** (2020) 151 [`1908.08554`]. [p. 100]

[355] M. Carena, Z. Liu and Y. Wang, *Electroweak Phase Transition with Spontaneous Z_2-Breaking*, `1911.10206`. [p. 104]

[356] Y. Bai, S. J. Lee, M. Son and F. Ye, *Global Electroweak Symmetric Vacuum*, `2103.09819`. [p. 110]

[357] A. Fowlie, *A fast C++ implementation of thermal functions*, *Comput. Phys. Commun.* **228** (2018) 264 [`1802.02720`]. [p. 111]

[358] M. Laine, M. Meyer and G. Nardini, *Thermal phase transition with full 2-loop effective potential*, *Nucl. Phys. B* **920** (2017) 565 [`1702.07479`]. [p. 114]

[359] K. Kainulainen, V. Keus, L. Niemi, K. Rummukainen, T. V. Tenkanen and V. Vaskonen, *On the validity of perturbative studies of the electroweak phase transition in the Two Higgs Doublet model*, *JHEP* **06** (2019) 075 [`1904.01329`]. [p. 114]

[360] S. Weinberg, *Does Gravitation Resolve the Ambiguity Among Supersymmetry Vacua?*, *Phys. Rev. Lett.* **48** (1982) 1776. [p. 120]

[361] B. Bajc, *High temperature symmetry nonrestoration*, in *3rd International Conference on Particle Physics and the Early Universe*, pp. 247–253, 2000, `hep-ph/0002187`, DOI. [p. 120]

[362] A. H. Guth and E. J. Weinberg, *Could the Universe Have Recovered from a Slow First Order Phase Transition?*, *Nucl. Phys. B* **212** (1983) 321. [p. 120]

[363] R. V. Harlander, S. Liebler and H. Mantler, *SusHi Bento: Beyond NNLO and the heavy-top limit*, *Comput. Phys. Commun.* **212** (2017) 239 [`1605.03190`]. [p. 122]

[364] CMS collaboration, *Search for neutral resonances decaying into a Z boson and a pair of b jets or τ leptons*, *Phys. Lett. B* **759** (2016) 369 [`1603.02991`]. [p. 122]

[365] ATLAS collaboration, *Search for a heavy Higgs boson decaying into a Z boson and another heavy Higgs boson in the $\ell\ell bb$ final state in pp collisions at $\sqrt{s} = 13$ TeV with the ATLAS detector*, *Phys. Lett. B* **783** (2018) 392 [`1804.01126`]. [p. 122]

[366] CMS collaboration, *Search for new neutral Higgs bosons through the $H \to ZA \to \ell^+\ell^-\mathrm{b\bar{b}}$ process in pp collisions at $\sqrt{s} =$ 13 TeV*, *JHEP* **03** (2020) 055 [`1911.03781`]. [p. 122]

[367] T. Biekötter, M. Chakraborti and S. Heinemeyer, *A 96 GeV Higgs boson in the N2HDM*, *Eur. Phys. J. C* **80** (2020) 2 [`1903.11661`]. [pp. 123 and 159]

[368] CMS collaboration, *Search for a new scalar resonance decaying to a pair of Z bosons in proton-proton collisions at* $\sqrt{s} = 13$ *TeV*, *JHEP* **06** (2018) 127 [`1804.01939`]. [p. 124]

[369] LEP Working Group for Higgs boson searches, ALEPH, DELPHI, L3, OPAL collaboration, R. Barate et al., *Search for the standard model Higgs boson at LEP*, *Phys. Lett. B* **565** (2003) 61 [`hep-ex/0306033`]. [p. 125]

[370] D. G. Cerdeno and A. M. Green, *Direct detection of WIMPs*, `1002.1912`. [pp. 132, 133, and 135]

[371] S. Glaus, M. Mühlleitner, J. Müller, S. Patel and R. Santos, *NLO corrections to Vector Dark Matter Direct Detection - An update*, *PoS* **CORFU2019** (2020) 046 [`2005.11540`]. [pp. 132 and 168]

[372] T. Marrodán Undagoitia and L. Rauch, *Dark matter direct-detection experiments*, *J. Phys. G* **43** (2016) 013001 [`1509.08767`]. [p. 132]

[373] P. N. Steppeler, *Radiative corrections for the direct detection of neutralino dark matter and its relic density*, Ph.D. thesis, Munster U., ITP, 2016. [pp. 132, 133, and 134]

[374] T. Piffl et al., *The RAVE survey: the Galactic escape speed and the mass of the Milky Way*, *Astron. Astrophys.* **562** (2014) A91 [`1309.4293`]. [p. 132]

[375] T. Lin, *Dark matter models and direct detection*, *PoS* **333** (2019) 009 [`1904.07915`]. [p. 132]

[376] M. A. Shifman, A. I. Vainshtein and V. I. Zakharov, *Remarks on Higgs Boson Interactions with Nucleons*, *Phys. Lett. B* **78** (1978) 443. [p. 134]

[377] J. Hisano, K. Ishiwata and N. Nagata, *Direct Search of Dark Matter in High-Scale Supersymmetry*, *Phys. Rev. D* **87** (2013) 035020 [`1210.5985`]. [p. 134]

[378] R. D. Young and A. W. Thomas, *Octet baryon masses and sigma terms from an SU(3) chiral extrapolation*, *Phys. Rev. D* **81** (2010) 014503 [`0901.3310`]. [p. 134]

[379] J. Hisano, K. Ishiwata and N. Nagata, *QCD Effects on Direct Detection of Wino Dark Matter*, *JHEP* **06** (2015) 097 [`1504.00915`]. [p. 134]

[380] JLQCD collaboration, H. Ohki, K. Takeda, S. Aoki, S. Hashimoto, T. Kaneko, H. Matsufuru et al., *Nucleon strange quark content from* $N_f = 2 + 1$ *lattice QCD with exact chiral symmetry*, *Phys. Rev. D* **87** (2013) 034509 [`1208.4185`]. [p. 134]

[381] J. F. Owens, A. Accardi and W. Melnitchouk, *Global parton distributions with nuclear and finite-*Q^2 *corrections*, *Phys. Rev. D* **87** (2013) 094012 [`1212.1702`]. [p. 134]

[382] T. L. Lee, T. Y. Li and C. H. Tsai, *HOM4PS-2.0: a software package for solving polynomial systems by the ployhedral homotopy continuation method*, *Computing* **83** (2008) 109. [p. 138]

[383] P. Bechtle, S. Heinemeyer, O. Stal, T. Stefaniak and G. Weiglein, *Applying Exclusion Likelihoods from LHC Searches to Extended Higgs Sectors*, *Eur. Phys. J. C* **75** (2015) 421 [`1507.06706`]. [p. 139]

[384] A. Djouadi, J. Kalinowski and M. Spira, *HDECAY: A Program for Higgs boson decays in the standard model and its supersymmetric extension*, *Comput. Phys. Commun.* **108** (1998) 56 [`hep-ph/9704448`]. [p. 140]

[385] J. M. Butterworth et al., *THE TOOLS AND MONTE CARLO WORKING GROUP Summary Report from the Les Houches 2009 Workshop on TeV Colliders*, in *6th Les Houches Workshop on Physics at TeV Colliders*, 3, 2010, `1003.1643`. [p. 140]

[386] A. Djouadi, J. Kalinowski, M. Muehlleitner and M. Spira, *HDECAY: Twenty$_{++}$ years after*, *Comput. Phys. Commun.* **238** (2019) 214 [`1801.09506`]. [p. 140]

[387] M. Misiak, A. Rehman and M. Steinhauser, *Towards $\overline{B} \to X_s \gamma$ at the NNLO in QCD without interpolation in m_c*, *JHEP* **06** (2020) 175 [`2002.01548`]. [p. 141]

[388] SIMBA collaboration, F. U. Bernlochner, H. Lacker, Z. Ligeti, I. W. Stewart, F. J. Tackmann and K. Tackmann, *Precision Global Determination of the $B \to X_s \gamma$ Decay Rate*, `2007.04320`. [p. 141]

[389] X.-M. Jiang, C. Cai, Z.-H. Yu, Y.-P. Zeng and H.-H. Zhang, *Pseudo-Nambu-Goldstone dark matter and two-Higgs-doublet models*, *Phys. Rev. D* **100** (2019) 075011 [`1907.09684`]. [p. 141]

[390] N. D. Christensen and C. Duhr, *FeynRules - Feynman rules made easy*, *Comput. Phys. Commun.* **180** (2009) 1614 [`0806.4194`]. [pp. 141 and 169]

[391] N. D. Christensen, P. de Aquino, C. Degrande, C. Duhr, B. Fuks, M. Herquet et al., *A Comprehensive approach to new physics simulations*, *Eur. Phys. J. C* **71** (2011) 1541 [`0906.2474`]. [p. 141]

[392] A. Alloul, N. D. Christensen, C. Degrande, C. Duhr and B. Fuks, *FeynRules 2.0 - A complete toolbox for tree-level phenomenology*, *Comput. Phys. Commun.* **185** (2014) 2250 [`1310.1921`]. [pp. 141 and 169]

[393] A. Belyaev, N. D. Christensen and A. Pukhov, *CalcHEP 3.4 for collider physics within and beyond the Standard Model*, *Comput. Phys. Commun.* **184** (2013) 1729 [`1207.6082`]. [p. 141]

[394] G. Bélanger, F. Boudjema, A. Goudelis, A. Pukhov and B. Zaldivar, *micrOMEGAs5.0 : Freeze-in*, *Comput. Phys. Commun.* **231** (2018) 173 [`1801.03509`]. [p. 141]

[395] C. Degrande, C. Duhr, B. Fuks, D. Grellscheid, O. Mattelaer and T. Reiter, *UFO - The Universal FeynRules Output*, *Comput. Phys. Commun.* **183** (2012) 1201 [`1108.2040`]. [pp. 142 and 169]

[396] M. Backovic, K. Kong and M. McCaskey, *MadDM v.1.0: Computation of Dark Matter Relic Abundance Using MadGraph5*, *Physics of the Dark Universe* **5-6** (2014) 18 [`1308.4955`]. [p. 142]

[397] F. Ambrogi, C. Arina, M. Backovic, J. Heisig, F. Maltoni, L. Mantani et al., *MadDM v.3.0: a Comprehensive Tool for Dark Matter Studies*, *Phys. Dark Univ.* **24** (2019) 100249 [`1804.00044`]. [p. 142]

[398] J. Alwall, R. Frederix, S. Frixione, V. Hirschi, F. Maltoni, O. Mattelaer et al., *The automated computation of tree-level and next-to-leading order differential cross sections, and their matching to parton shower simulations*, *JHEP* **07** (2014) 079 [`1405.0301`]. [p. 142]

[399] M. Bauer and T. Plehn, *Yet Another Introduction to Dark Matter: The Particle Physics Approach*, vol. 959 of *Lecture Notes in Physics*. Springer, 2019, 10.1007/978-3-030-16234-4, [`1705.01987`]. [p. 143]

[400] F.-A. Fortin, F.-M. De Rainville, M.-A. Gardner, M. Parizeau and C. Gagné, *DEAP: Evolutionary algorithms made easy*, *Journal of Machine Learning Research* **13** (2012) 2171. [p. 144]

[401] S. von Buddenbrock, N. Chakrabarty, A. S. Cornell, D. Kar, M. Kumar, T. Mandal et al., *Phenomenological signatures of additional scalar bosons at the LHC*, *Eur. Phys. J. C* **76** (2016) 580 [`1606.01674`]. [p. 151]

[402] S. Baum and N. R. Shah, *Two Higgs Doublets and a Complex Singlet: Disentangling the Decay Topologies and Associated Phenomenology*, *JHEP* **12** (2018) 044 [`1808.02667`]. [p. 151]

[403] T. Binder, T. Bringmann, M. Gustafsson and A. Hryczuk, *Early kinetic decoupling of dark matter: when the standard way of calculating the thermal relic density fails*, *Phys. Rev. D* **96** (2017) 115010 [`1706.07433`]. [p. 154]

[404] T. Abe, *Early kinetic decoupling and a pseudo-Nambu-Goldstone dark matter model*, `2106.01956`. [p. 154]

[405] AMS collaboration, M. Aguilar et al., *The Alpha Magnetic Spectrometer (AMS) on the international space station: Part II — Results from the first seven years*, *Phys. Rept.* **894** (2021) 1. [p. 157]

[406] R. Bartels, S. Krishnamurthy and C. Weniger, *Strong support for the millisecond pulsar origin of the Galactic center GeV excess*, *Phys. Rev. Lett.* **116** (2016) 051102 [`1506.05104`]. [p. 157]

[407] S. K. Lee, M. Lisanti, B. R. Safdi, T. R. Slatyer and W. Xue, *Evidence for Unresolved γ-Ray Point Sources in the Inner Galaxy*, *Phys. Rev. Lett.* **116** (2016) 051103 [`1506.05124`]. [p. 157]

[408] F. Calore, M. Di Mauro, F. Donato, J. W. T. Hessels and C. Weniger, *Radio detection prospects for a bulge population of millisecond pulsars as suggested by Fermi LAT observations of the inner Galaxy*, *Astrophys. J.* **827** (2016) 143 [`1512.06825`]. [p. 157]

[409] J. Heisig, M. Korsmeier and M. W. Winkler, *Dark matter or correlated errors: Systematics of the AMS-02 antiproton excess*, *Phys. Rev. Res.* **2** (2020) 043017 [`2005.04237`]. [p. 157]

[410] M. Boudaud, Y. Génolini, L. Derome, J. Lavalle, D. Maurin, P. Salati et al., *AMS-02 antiprotons' consistency with a secondary astrophysical origin*, *Phys. Rev. Res.* **2** (2020) 023022 [`1906.07119`]. [p. 157]

[411] M. Di Mauro, *Characteristics of the Galactic Center excess measured with 11 years of Fermi-LAT data*, *Phys. Rev. D* **103** (2021) 063029 [`2101.04694`]. [p. 157]

[412] F. List, N. L. Rodd and G. F. Lewis, *Dim but not entirely dark: Extracting the Galactic Center Excess' source-count distribution with neural nets*, `2107.09070`. [p. 157]

[413] F. Kahlhoefer, M. Korsmeier, M. Krämer, S. Manconi and K. Nippel, *Constraining dark matter annihilation with cosmic ray antiprotons using neural networks*, `2107.12395`. [p. 157]

[414] M. Abdughani, Y.-Z. Fan, L. Feng, Y.-L. S. Tsai, L. Wu and Q. Yuan, *A common origin of muon g-2 anomaly, Galaxy Center GeV excess and AMS-02 anti-proton excess in the NMSSM*, *Sci. Bull.* **66** (2021) 2170 [`2104.03274`]. [p. 157]

[415] G. Beck, R. Temo, E. Malwa, M. Kumar and B. Mellado, *Connecting multi-lepton anomalies at the LHC and in Astrophysics with MeerKAT/SKA*, 2, 2021, `2102.10596`. [p. 157]

[416] FERMI-LAT collaboration, E. Charles et al., *Sensitivity Projections for Dark Matter Searches with the Fermi Large Area Telescope*, *Phys. Rept.* **636** (2016) 1 [`1605.02016`]. [p. 158]

[417] J. Cao, X. Guo, Y. He, P. Wu and Y. Zhang, *Diphoton signal of the light Higgs boson in natural NMSSM*, *Phys. Rev. D* **95** (2017) 116001 [`1612.08522`]. [p. 159]

[418] LHC HIGGS CROSS SECTION WORKING GROUP collaboration, D. de Florian et al., *Handbook of LHC Higgs Cross Sections: 4. Deciphering the Nature of the Higgs Sector*, `1610.07922`. [p. 160]

[419] DARWIN collaboration, J. Aalbers et al., *DARWIN: towards the ultimate dark matter detector*, *JCAP* **11** (2016) 017 [`1606.07001`]. [pp. 165, 171, 177, 178, and 181]

[420] SuperCDMS collaboration, M. F. Albakry et al., *A Strategy for Low-Mass Dark Matter Searches with Cryogenic Detectors in the SuperCDMS SNOLAB Facility*, in *2022 Snowmass Summer Study*, 3, 2022, `2203.08463`. [p. 165]

[421] S. Glaus, M. Mühlleitner, J. Müller, S. Patel and R. Santos, *Electroweak Corrections to Dark Matter Direct Detection in a Vector Dark Matter Model*, *JHEP* **10** (2019) 152 [`1908.09249`]. [p. 168]

[422] J. Kublbeck, M. Bohm and A. Denner, *Feyn Arts: Computer Algebraic Generation of Feynman Graphs and Amplitudes*, *Comput. Phys. Commun.* **60** (1990) 165. [p. 169]

[423] T. Hahn, *Generating Feynman diagrams and amplitudes with FeynArts 3*, *Comput. Phys. Commun.* **140** (2001) 418 [`hep-ph/0012260`]. [p. 169]

[424] R. Mertig, M. Bohm and A. Denner, *FEYN CALC: Computer algebraic calculation of Feynman amplitudes*, *Comput. Phys. Commun.* **64** (1991) 345. [p. 169]

[425] V. Shtabovenko, R. Mertig and F. Orellana, *New Developments in FeynCalc 9.0*, *Comput. Phys. Commun.* **207** (2016) 432 [`1601.01167`]. [p. 169]

[426] F. Staub, *From Superpotential to Model Files for FeynArts and CalcHep/CompHep*, *Comput. Phys. Commun.* **181** (2010) 1077 [`0909.2863`]. [p. 169]

[427] F. Staub, *Automatic Calculation of supersymmetric Renormalization Group Equations and Self Energies*, *Comput. Phys. Commun.* **182** (2011) 808 [`1002.0840`]. [p. 169]

[428] F. Staub, *SARAH 3.2: Dirac Gauginos, UFO output, and more*, *Comput. Phys. Commun.* **184** (2013) 1792 [`1207.0906`]. [p. 169]

[429] F. Staub, *Exploring new models in all detail with SARAH*, *Adv. High Energy Phys.* **2015** (2015) 840780 [`1503.04200`]. [p. 169]

[430] T. Hahn, S. Paßehr and C. Schappacher, *FormCalc 9 and Extensions*, *PoS* **LL2016** (2016) 068 [`1604.04611`]. [p. 169]

[431] T. Hahn and M. Perez-Victoria, *Automatized one loop calculations in four-dimensions and D-dimensions*, *Comput. Phys. Commun.* **118** (1999) 153 [`hep-ph/9807565`]. [p. 169]

[432] G. J. van Oldenborgh and J. A. M. Vermaseren, *New Algorithms for One Loop Integrals*, *Z. Phys. C* **46** (1990) 425. [p. 169]

[433] J. Billard, L. Strigari and E. Figueroa-Feliciano, *Implication of neutrino backgrounds on the reach of next generation dark matter direct detection experiments*, *Phys. Rev. D* **89** (2014) 023524 [`1307.5458`]. [pp. 171, 177, and 178]

[434] "Cern website." `https://home.web.cern.ch/press/2022/run-3`. [p. 181]

[435] "High Luminosity LHC Project."
`https://hilumilhc.web.cern.ch/article/ls3-schedule-change`. [p. 181]

[436] NASA LISA Study Team collaboration, J. Bellovary et al., *Getting Ready for LISA: The Data, Support and Preparation Needed to Maximize US Participation in Space-Based Gravitational Wave Science*, `2012.02650`. [p. 181]

Eidesstattliche Versicherung

Hiermit versichere ich an Eides statt, die vorliegende Dissertationsschrift selbst verfasst und keine anderen als die angegebenen Hilfsmittel und Quellen benutzt zu haben. Die eingereichte schriftliche Fassung entspricht der auf dem elektronischen Speichermedium. Die Dissertation wurde in der vorgelegten oder einer ähnlichen Form nicht schon einmal in einem früheren Promotionsverfahren angenommen oder als ungenügend beurteilt.

Hamburg, 25.07.2022

María Olalla Olea Romacho